

# **ELECTRO-OPTICAL BEHAVIOUR OF NON-SPHERICAL PARTICLES UNDER ALTERNATING FIELDS**

Programa Oficial de Doctorado en Física y Ciencias del Espacio



**TESIS DOCTORAL 2018**  
PALOMA ARENAS GUERRERO

**DIRECTOR Y DIRECTORA**  
ÁNGEL V. DELGADO MORA  
MARÍA L. JIMÉNEZ OLIVARES

Departamento de Física Aplicada  
Grupo de Física de Interfases y Sistemas Coloidales  
Universidad de Granada

Editor: Universidad de Granada. Tesis Doctorales  
Autor: Paloma Arenas Guerrero  
ISBN: 978-84-1306-022-4  
URI: <http://hdl.handle.net/10481/54067>





*A mi madre, a mi padre  
y a mis hermanos.*

*A todas las que luchan  
por una ciencia del y para el pueblo.*



# AGRADECIMIENTOS

La investigación que se presenta en esta tesis ha sido fruto de 4 años de trabajo en el grupo "Física de Interfases y Sistemas Coloidales" del departamento de Física Aplicada de la Universidad de Granada, y ha sido posible gracias a la financiación pública de la ciencia y al trabajo de muchas personas. Durante este tiempo hemos tenido días mejores y peores, pero podemos decir que esta tesis se ha hecho con ilusión y alegría, risas, compañerismo, galletas de las malas y dulces de celebración.

En esta página quiero expresar mi agradecimiento a mi director y directora de tesis, Ángel y Marisa, por su gran trabajo y su enorme paciencia, pero sobre todo por construir un grupo del que nunca queremos irnos. A Ángel le agradezco su dedicación y amor por la ciencia, su despacho siempre abierto y lleno de gente, y el cariño que pone en todo lo que hace. A Marisa le estaré siempre agradecida por su ejemplo, su valentía y sabiduría, por escucharme, guiarme y por estar siempre para todo lo que he podido necesitar. A Silvia le doy gracias por su infinita dulzura, su complicidad y su forma de reñirme. A Guillermo por sus chistes, y por enseñarnos que hay solución para todo, aunque tenga que hacerla con sus propias manos.

El trabajo que se desarrolla en este grupo está acompañado de muchas otras personas que ponen cariño y alegría por pasillos y despachos; a todas ellas gracias. En especial, a las/os compañeras/os del café: Laura, Kasia, Felisa, Ana Belén, María del Mar Senior, Fernando, Juande, Modesto, Alejandro, Arturo, Gerardo y Juan. También a María del Mar, por llenar de alegría y colores nuestro despacho, y por soñar juntas un mundo con miles de estrellas rojas. Por último, gracias a Emilia, Angélica, Natasha y Maite por alegrarnos las mañanas, y a Leo y a Irene por escucharme tantas veces.

Durante mi estancia de tres meses en Londres, agradezco a Kevin y a Ken por recibirme en su laboratorio y por las interesantes discusiones, y a Serena que me acogiese y me despertase con café italiano. También quiero agradecer la contribución de los coautores de este trabajo, F. Mantegazza y T. Bellini.

Y por último, gracias a mi familia, a mis amigas, a mis amigos, a mis compañeras/os de luchas, a nuestra tierra Andalucía y a sus gentes, que le dan la vida.

Financial support of this investigation by Junta de Andalucía, Spain (grant No. PE2012-FQM0694) and MICINN, Spain (project No. FIS2013-47666-C3-1-R) is gratefully acknowledged. The author thanks MEC, Spain for her FPU grant (FPU13/02364) and University of Granada, Spain, for her mobility grant.

*La ciencia es revolucionaria y contribuye a la liberación de la humanidad.*

G. Politzer

# Contents

<b>Contents</b>	<b>IX</b>
<b>1. INTRODUCTION</b>	<b>1</b>
1.1. Introduction and motivation . . . . .	3
1.2. Objectives and thesis outline . . . . .	5
<b>2. PARTICLE POLARIZATION AND ELECTRO-ORIENTATION</b>	<b>9</b>
2.1. Fundamentals of particle polarization . . . . .	11
2.2. Polarization of charged particles . . . . .	17
2.3. Polarization of metallic particles . . . . .	30
2.4. Non-spherical particle electro-orientation . . . . .	35
2.5. Non-spherical particle electro-optics . . . . .	45
<b>3. MATERIALS AND METHODS</b>	<b>53</b>
3.1. General information . . . . .	55
3.2. Materials . . . . .	55
3.3. Methods . . . . .	69
<b>4. ELECTRIC BIREFRINGENCE SPECTROSCOPY OF MONTMORILLONITE PARTICLES</b>	<b>77</b>
4.1. Introduction . . . . .	81
4.2. Theory . . . . .	82
4.3. Materials and Methods . . . . .	86
4.4. Results and Discussion . . . . .	88

---

4.5. Conclusions . . . . .	101
<b>5. ELECTRIC BIREFRINGENCE OF CARBON NANOTUBES: SINGLE- VS DOUBLE-WALLED</b>	<b>103</b>
5.1. Introduction . . . . .	107
5.2. Experimental . . . . .	112
5.3. Results and discussion . . . . .	115
5.4. Conclusion . . . . .	126
<b>6. DETERMINATION OF THE SIZE DISTRIBUTION OF NON-SPHERICAL NANOPARTICLES BY ELECTRIC BIREFRINGENCE-BASED METHODS</b>	<b>127</b>
6.1. Introduction . . . . .	131
6.2. Methods . . . . .	136
6.3. Results . . . . .	137
6.4. Discussion . . . . .	150
<b>7. ELECTRIC BIREFRINGENCE OF GOLD NANORODS: EFFECT OF SUR- FACTANT COATING</b>	<b>157</b>
7.1. Introduction . . . . .	161
7.2. Experimental section . . . . .	162
7.3. Results and discussion . . . . .	165
7.4. Conclusions . . . . .	176
<b>8. ELECTRO-ORIENTATION OF SILVER NANOWIRES IN ALTERNATING FIELDS</b>	<b>179</b>
8.1. Introduction . . . . .	183
8.2. Experimental Section . . . . .	184
8.3. Results and Discussion . . . . .	186
8.4. Summary and Conclusions . . . . .	199
<b>9. ANALYSIS OF THE ELECTRO-OPTICAL RESPONSE OF GRAPHENE OX- IDE DISPERSIONS UNDER ALTERNATING FIELDS</b>	<b>201</b>
9.1. Introduction . . . . .	205

---

9.2. Theoretical background . . . . .	205
9.3. Experimental section . . . . .	207
9.4. Results and discussion . . . . .	209
9.5. Conclusions . . . . .	219
<b>10. CONCLUSIONS</b>	<b>221</b>
<b>11. RESUMEN</b>	<b>229</b>
11.1. Introducción y objetivos . . . . .	231
11.2. Polarización y electro-orientación de partículas . . . . .	234
11.3. Principales resultados . . . . .	240
11.4. Conclusiones . . . . .	254
<b>List of Figures</b>	<b>257</b>
<b>List of Tables</b>	<b>269</b>
<b>Bibliography</b>	<b>303</b>



# 1

## INTRODUCTION



## 1.1. Introduction and motivation

Progress in nanoparticle science is bringing along the discovery of new systems with extraordinary properties, immediately followed by new applications in different branches of technology and in medicine. In fact, the potential of these particles is often glimpsed before their physical properties are completely understood. However, much work is still needed to achieve their full potential and, above all, to convert these advances in resources for the benefit of all, keeping their knowledge public and at the service of the people.

Although it is frequently assumed that particle size is the determining parameter in the properties and applications of nanoparticles, it is increasingly clear that, whereas essential, this is not the only relevant magnitude. Thus, particle shape has proven to exert a significant impact on the physics of the systems and their technical performance [1, 2]. For instance, it has been shown that the elongated shape of gold nanorods plays an essential role in their use in DNA biosensing, high density optical data storage or plasmon-enhanced Raman spectroscopy [3–5]. Other examples are the antibacterial activity of silver nanoparticles, the toxicity of carbon nanotubes, the rheological behaviour of sodium montmorillonite or the catalytic properties of platinum nanoparticles [6–9]. This is the basic hypothesis of the present work: nanoparticles with controlled size and non-spherical shape possess special characteristics, not sufficiently explored and susceptible of novel applications in diverse fields.

Particle shape is a determining parameter of the physical properties of colloidal systems and their potential applications.

Furthermore, the possibility to control the orientation of non-spherical particles opens up new possibilities, and has proven crucial for progress in applications which exploit directional properties. Examples of this can be found in the use of gold nanorods in metamaterials or particle traps, the fabrication of transparent conductive electrodes with silver nanowires, the implementation of carbon nanotubes as DNA sensors, microscopy nanoprobe or photodetectors, and the fabrication of graphene-based su-

percapacitors [10–16]. The use of electric fields has proven a simple and efficient route for the manipulation of micro and nanoparticles. Thus, for example, dielectrophoresis has been used in the separation of biological particles such as cells or bacteria, and in the separation of metallic and semiconducting carbon nanotubes [17–19]. Moreover, the controlled assembly and orientation of non-spherical particles of different nature, dispersed in liquid media, has been achieved by different techniques based on the applications of electric fields [20–23]. However, the mechanisms underlying electric field-driven alignment and assembly have yet to be fully understood, due to the complex nature of the electro-hydrodynamic processes.

In many cases, micro and nanoparticles are used in aqueous suspension, giving rise to interfacial phenomena which play an essential role in the macroscopic behaviour of the systems, further complicating their description. The present work focuses on the response of dispersions of non-spherical particles under the effect of alternating electric fields, paying special attention to the polarisation mechanisms of the particles and their electrical double layers. In the case of dielectric particles with simplified geometries, this problem has been tackled analytically by Shilov et al. [24, 25] and numerically by Fixman [26]. In the last decade, a number of experimental studies has also been reported [27–32]. The case of uncharged conducting particles in an electrolyte was studied originally by Murtsovkin, Dukhin et al. in the case of spheres [33, 34]. Recently, calculations were extended to other geometries [35, 36] and the experimental study of these particles is being addressed [37–41].

In this work, we study the polarisation of non-spherical particles in suspension under the effect of electric fields, via the analysis of the electro-optical phenomena. These consist in the modification of different optical properties of colloidal suspensions under the application of external electric fields [42, 43]. Here, we focus on two of them: Electric birefringence and linear dichroism, both related to non-spherical particle electro-orientation. The analysis of these effects can provide much useful information about the optical, electrical and geometrical properties of the particles in suspension, as well as about the electrokinetic phenomena taking place

at their interfaces. Hence, we have a double purpose: the understanding of the observed phenomena and the use of the electro-optical techniques for non-spherical particle characterisation.

In this respect, for example, transient electric birefringence has long been used to obtain information on the flexibility or the size of non-spherical particles in suspension [44–46]. However, only a few works are

The electro-optical phenomena are related to the modification of the optical properties of suspensions of non-spherical particles by the application of electric fields, and can be used for particle characterisation.

devoted to the analysis of the size distribution of polydisperse samples by this method [47, 48]. The electric birefringence decay depends on the third power of the particle size, which provides a very high sensitivity, making this a technique with a great potential. Furthermore, electric birefringence spectroscopy has been proposed as a powerful tool for the direct measurement of the electrical polarisability of dispersed non-spherical particles [49, 50]. Among other advantages, this technique is highly susceptible to particle anisotropy, unlike others such as electrophoresis or dielectric spectroscopy, which typically measure spatially-averaged magnitudes. Hence, it can provide information on the effect of particle shape and inhomogeneities in the charge distribution or the internal particle structure.

To summarise, this work is devoted to the experimental study of the electro-optical response of non-spherical particles of very different nature. From the analysis of the experimental results, information is extracted on the optical, electrical and geometrical properties of the dispersed particles, and their different polarisation mechanisms, which are related to the presence of the electrical double layer.

## 1.2. Objectives and thesis outline

In light of the former considerations, in this work we intend to carefully study the electro-optical behaviour of non-spherical particles in suspension, in order to analyse their polarization mechanisms and obtain information on their optical and geometrical characteristics. The main objec-

tives can be summarised as follows:

- The determination and understanding of the complete electro-optical phenomenology of non-spherical particles with very diverse properties.
- The progress in the understanding of the behaviour of metallic particles, barely studied in the literature.
- The advance in the use of electro-optical techniques for particle characterisation, especially regarding the size distributions of polydisperse suspensions.

Keeping in mind these goals, the thesis is arranged as follows. In **Chapter 2** we give an exhaustive account of the polarization mechanisms of non-spherical particles and their electrical double layers. A complete description of the electro-orientation process and the associated electro-optical phenomena is included in this chapter. Since no commercial devices are available for the determination of the electro-optic response of colloidal dispersions, a first step was the development of an experimental setup, described in **Chapter 3**, able to measure the electric birefringence and linear dichroism in a wide spectral range. In this chapter, we also describe the structure and main properties of the materials used in this work.

In **Chapter 4**, we analyse the electric birefringence phenomenology of sodium montmorillonite platelets under different experimental conditions. An extensive examination of the spectral response of the suspensions is carried out in order to study the electrical properties of the particles, the effect of the inhomogeneous charge distribution, the swelling of the material and the origin of the anomalous response at low field frequencies. In **Chapter 5**, we study the electro-optical behaviour of single- and double-walled carbon nanotubes in non-aqueous suspension, paying special attention to the negative signal of the latter. The thorough study of their birefringent phenomenology provides information about the electrical polarizability, the length of the tubes and their optical properties.

**Chapter 6** addresses the study of transient electric birefringence as a size characterisation technique for polydisperse suspensions of non-spherical

particles. Three approaches for the analysis of the birefringence decay are studied and applied to suspensions of six types of particles with very different geometries. The results are compared to electron microscopy and dynamic light scattering measurements.

The electro-optical behaviour of elongated metallic particles in aqueous dispersion is addressed in **Chapters 7 and 8**, devoted to the study of gold nanorods and silver nanowires. In both cases, the anomalous sign is analysed with additional flow birefringence measurements. The polarization mechanisms of the two types of particles and their diffusional properties are studied via the determination of the spectral and dynamic behaviour of the electric birefringence respectively. In the case of gold, special attention is paid to the effect of the surfactant coating on the properties of the system. For the silver wires, models for the polarisation of barely-charged metallic particles were used to understand the spectral response.

**Chapter 9** contains the experimental study of the linear dichroism of graphene oxide flakes in aqueous suspension. The models for silver nanowires are adapted to the case of planar geometries to understand the polarisation mechanisms of these particles. The absorptivity of the flakes and their size distribution are also obtained from the electro-optical behaviour. **Chapter 10** summarises the main conclusions of this work.



# 2

## PARTICLE POLARIZATION AND ELECTRO-ORIENTATION



## 2.1. Fundamentals of particle polarization

### 2.1.1. Electric double layer at equilibrium

When a surface is placed in a polar medium such as water, it normally acquires an electric charge by different possible mechanisms [51–54]. As a consequence, if ions are present in the medium, they redistribute near the surface to achieve electroneutrality. The surface charge and its compensating countercharge in solution compose the **Electric Double Layer** (EDL) [51, 55]. Although its existence is almost universal, the formation of this structure has more relevance to the physics of the system for high surface-to-volume ratios. Hence, the EDL acquires special significance in colloidal suspensions, in which particles are in the nano or microscale. Thus, properties as the stability of the dispersions, their response to external fields or structure formation in them, either spontaneously or field-induced, are closely related to the properties of the EDL [51, 52].

While the **EDL structure at equilibrium** has been extensively studied [56], direct experimental access to it is not possible, which makes theoretical approaches necessary for the understanding of colloidal systems. Figure 2.1 shows the most widely accepted theoretical model for the description of the EDL, which consists in the consideration of three regions inside it [52]:

- **Particle surface:** The surface charge, whose density is denoted as  $\sigma_0$ , is placed either on the material surface or on its immediate vicinity. The value of the potential on this layer, referred to the bulk solution, is known as surface potential  $\Psi_0$ .
- **Stern layer:** Because of ionic size, there exists a distance of closest approach of hydrated ions to the particle surface. The layer can be uncharged, although in some cases a charge density  $\sigma_i$  exists inside this region due to the presence of ions which, attracted by strong short-distance interactions (such as hydrophilic or hydrophobic forces or hydrogen bonds [54]), dehydrate partially and remain attached to the surface. Since thermal agitation is not capable to counteract these strong forces, a reasonable approximation is to consider the ions arranged on a single plane, at a distance or the order of the dehydrated

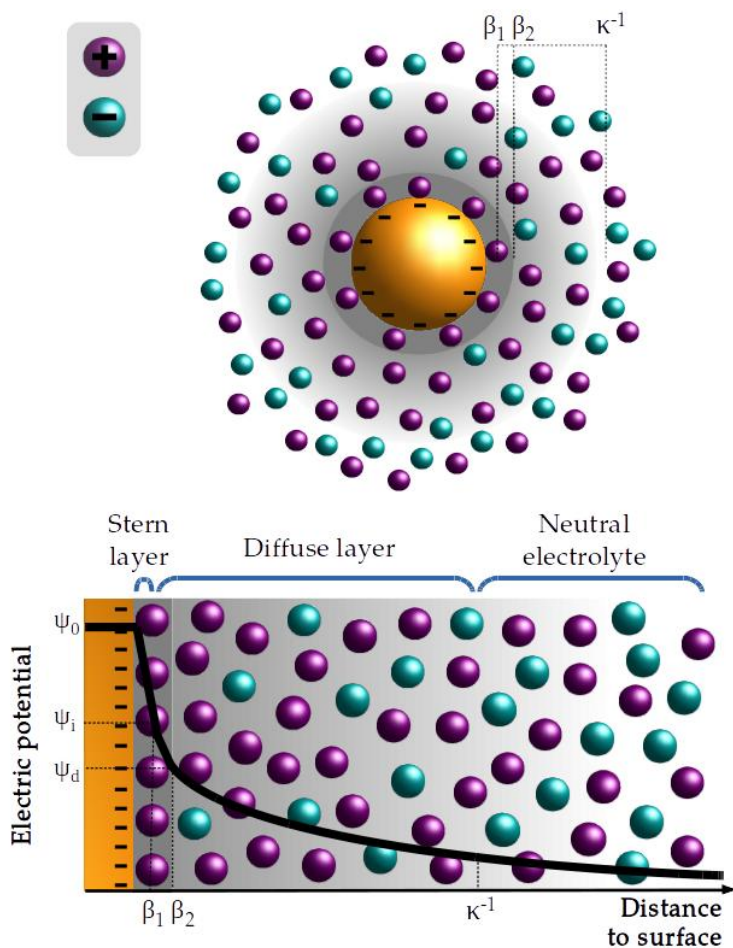


FIGURE 2.1: Schematic representation of the structure of the electric double layer of a negatively charged spherical colloidal particle.

ionic radius ( $\beta_1$ ). The potential on this plane, known as Helmholtz inner plane, is denoted as  $\Psi_1$ .

- Diffuse layer:** This region begins at the outer Helmholtz plane, at a distance  $\beta_2$  roughly corresponding to the radius of a hydrated ion, where the potential is  $\Psi_d$ . Here, the interaction with the particle surface is purely electrical, and hence the ionic distribution is the result

of a balance between the electric and diffusive forces. As a consequence, ions are not placed on a plane but rather a spatial charge distribution exists, which can stretch out to distances of the order of several particle diameters. In spite of this spacial distribution, it is usual to define  $\sigma_d$  as the surface charge density that would exist on the outer Helmholtz plane if all the charge of the diffuse layer were placed on it. Therefore, the total surface charge balance reads  $\sigma_0 + \sigma_i + \sigma_d = 0$ .

To study the charge distribution and the shape of the potential inside the **diffuse part of the EDL**, we can use as a first approximation the model proposed by Gouy and Chapman [52, 57, 58]. This approach considers that ions are point charges that do not interact amongst them, immersed in a structureless continuous medium. As mentioned, equilibrium is established between electrostatic attraction to the surface and ion diffusion tending to even the concentrations. Therefore, the number of ions of type  $k$  per unit volume follows a Boltzmann distribution:

$$n^k(\mathbf{r}) = n_0^k \exp\left(-\frac{z_k e \Psi(\mathbf{r})}{k_B T}\right) \quad (2.1)$$

where  $n_0^k$  is the ion concentration in the bulk solution (far from the interface),  $z_k$  the valence of the  $k$ -th ion,  $e$  the electron charge,  $k_B$  the Boltzmann constant and  $T$  the absolute temperature.  $\Psi(\mathbf{r})$  is the value of the electric potential at position  $\mathbf{r}$ , which satisfies Poisson's equation:

$$\nabla^2 \Psi(\mathbf{r}) = -\frac{\rho(\mathbf{r})}{\epsilon_0 \epsilon_m} = -\frac{1}{\epsilon_0 \epsilon_m} \sum_{k=1}^N z_k e n^k(\mathbf{r}) \quad (2.2)$$

where  $\epsilon_0$  is the vacuum permittivity,  $\epsilon_m$  the relative permittivity of the solvent and  $\rho(\mathbf{r})$  the volume charge density at position  $\mathbf{r}$ . From these expressions, the Poisson-Boltzmann equation is obtained:

$$\nabla^2 \Psi(\mathbf{r}) = -\frac{e}{\epsilon_0 \epsilon_m} \sum_{k=1}^N z_k n_0^k \exp\left(-\frac{z_k e \Psi(\mathbf{r})}{k_B T}\right) \quad (2.3)$$

This expression is completed by boundary conditions for the potential, which is equal to  $\Psi_0$  on the particle surface and 0 far from it. Although in general there is no analytic solution for this equation, in the case of a planar interface (a valid approximation for thin double layers, i.e, those whose width is small as compared to particle size) and using the Debye-Hückel approximation (low potentials,  $|z_k e \Psi| \ll k_B T$ ), an analytic expression of  $\Psi(\mathbf{r})$  is available. Under these conditions, the exponential function in Equation 2.3 can be expanded in power series up to the second term, which leads to the expression

$$\epsilon_0 \epsilon_m \frac{d^2 \Psi(z)}{dz^2} = \sum_{k=1}^N \frac{e^2 z_k^2 n_0^k}{k_B T} \Psi(z) \quad (2.4)$$

where  $z$  is the distance to the particle surface. The solution to this equation, introducing the previously mentioned boundary conditions, reads:

$$\Psi(r) = \Psi_0 e^{-\kappa z} \quad (2.5)$$

where  $\kappa$  is the inverse of the Debye length, a measure of the thickness of the diffuse part of the EDL:

$$\kappa^{-1} = \sqrt{\frac{\epsilon_0 \epsilon_m k_B T}{\sum n_0^k (z_k e)^2}} \quad (2.6)$$

For the **inner part of the EDL**, it is usual to employ the Stern model [52, 59] in its simplest version, which considers the region spanning from the particle surface to the inner Helmholtz plane, and the one between the inner and outer Helmholtz planes, as two parallel-plate capacitors. The capacitance values per unit interface area are, respectively,

$$\begin{aligned} C_1 &= \frac{\sigma_0}{\Psi_0 - \Psi_i} = \frac{\epsilon_0 \epsilon_1}{\beta_1} \\ C_2 &= \frac{\sigma_0 + \sigma_i}{\Psi_i - \Psi_d} = \frac{\epsilon_0 \epsilon_2}{\beta_2 - \beta_1} \end{aligned} \quad (2.7)$$

being  $\epsilon_1$  and  $\epsilon_2$  the relative dielectric constants in these two regions, although it must be pointed out that the meaning of  $\epsilon_1$ , in a volume of molecular width, is unclear.

All the quantities mentioned in this description are, strictly speaking, out of the reach of experimental determinations in the majority of cases. In contrast, there are a number of methods aimed at their indirect evaluation, jointly known as electrokinetic techniques. These are associated to the electrokinetic phenomena, which manifest when an external field (electrical, pressure, concentration or temperature gradient, etc) produces a relative movement between the particle and the solution containing the diffuse part of the EDL. Since both the ions and the fluid in the region adjacent to the surface are typically considered stuck to the particle, and hence immobile, they do not participate in the electrokinetics of the system. For all practical purposes, it is as if the interface were shifted out a certain distance to the region that is mobile. An ideal surface of separation, known as slipping plane, is assumed between both regions. The potential on this plane is the zeta potential,  $\zeta$ , which is the one actually detected by electrokinetics.

Although widely used, the existence of the slipping plane and the zeta potential itself is strictly an abstraction, since it is based on the hypothesis that the liquid viscosity is a spatially discontinuous function, which goes from an infinite value inside the Stern layer to a finite value in the diffuse layer. Normally, the slipping plane is identified with the boundary of the Stern layer, and  $\Psi_d$  and  $\zeta$  are considered identical, which is a reasonable assumption for low ionic strengths [60]. At high ionic concentrations, on the other hand, the thickness of the EDL is so small that the exact position of the slipping plane is needed to extract any information on  $\Psi_d$ .

### 2.1.2. Non-equilibrium structure of the EDL

As mentioned, experimental access to the properties of the EDL is generally not possible, and therefore indirect techniques based on the response of the particles in suspension to the application of external fields, which perturbate the EDL, are normally used. In this section, we describe the phenomena that take place in the double layer after the application of an **external electric field**, until the steady state is reached. Taking into account the usual EDL potential values (around 100 mV) and thickness (1-30 nm) of the EDLs, in most cases the electric fields inside it are of the order of

$10^7$  V/m, a value much higher than the external fields normally used to perturb this structure.

In this situation, it can be considered that the characteristic properties of the double layer are modified only by a first-order term in the potential, so that this can be written, assuming spherical symmetry, as:

$$\Psi(\mathbf{r}) = \Psi_0(\mathbf{r}) + \varphi(\mathbf{r}) \quad (2.8)$$

where  $\Psi_0(\mathbf{r})$  is the equilibrium potential at position  $\mathbf{r}$ , and  $\varphi(\mathbf{r})$  the perturbation term. The latter, in turn, includes the potential associated directly to the external field and a contribution related to the changes in the EDL structure [61]. For **spherical particles**, the perturbation term is dipolar, and Equation 2.8 can be written in spherical coordinates as:

OJO -> En las tesis ponía que puede ser considerado dipolar, pero es que ES dipolar (verdad en general cuando hay simetría azimutal). Corroborar.

$$\varphi(r, \theta) = -E_0 r \cos \theta + \frac{d}{4\pi\epsilon_m\epsilon_0 r^2} \cos \theta \quad (2.9)$$

where  $E_0$  is the field amplitude,  $\theta$  the angle between the position vector and the direction of the external field and  $d$  the dipole strength. Hereafter, we focus on **induced polarization** [62], for which the electric dipole reads:

$$\mathbf{d} = \alpha^e \mathbf{E} \quad (2.10)$$

Therefore,  $\mathbf{d}$  is proportional to the electric field and parallel to it. The proportionality constant,  $\alpha^e$ , is the electric polarizability of the spherical particle, which can in turn be expressed as

$$\alpha^e = 3V_p\epsilon_0\epsilon_m C \quad (2.11)$$

where  $V_p$  is the particle volume and  $C$  the dipolar coefficient, defined to contain all the information regarding the processes that take place in the polarisation of the particle and on the particle/solution interface.

## 2.2. Polarization of charged particles

### 2.2.1. Spherical particles under DC fields

Under the application of a step external electric field, there are several successive **polarization mechanisms** that can give rise to the formation of an induced dipole on the particles of a colloidal suspension. Moreover, the external field also causes electromigration flows and the subsequent charge accumulation which, in turn, provokes diffusive flows around the particles. All these processes, which take different times to be established, must be analysed to understand the behaviour of colloidal suspensions subjected to electric fields. Hereunder, we present the main particle polarization mechanisms ordered from shorter to longer characteristic times [62]:

- The first reaction of the particles in suspension to the application of an electric field, almost instantaneous, is the **polarization of the electron clouds** of the atoms or molecules [63]. Later, the orientation of the molecular dipoles of both the particles and the solvent will give rise to a polarization charge density, associated to the mismatch between their permittivities. This will take place typically 0.1 ns after the application of the field. For this mechanism, the value of the dipolar coefficient is [62]:

$$C_{\text{perm}} = \frac{\epsilon_p - \epsilon_m}{\epsilon_p + 2\epsilon_m} \quad (2.12)$$

where  $\epsilon_p$  is the relative permittivity of the particles. Figure 2.2a illustrates this process in the case of a spherical particle immersed in a medium of higher permittivity.

- For longer times, free charges are able to move under the action of the electric field, giving rise to a charge accumulation on the interface due to the contrast between the conductivities of the particle ( $K_p$ ) and the medium ( $K_m$ ). This process is known as **Maxwell-Wagner polarization** [64, 65], and is schematically represented in Figure 2.2b for the case of a medium less conducting than the particle.

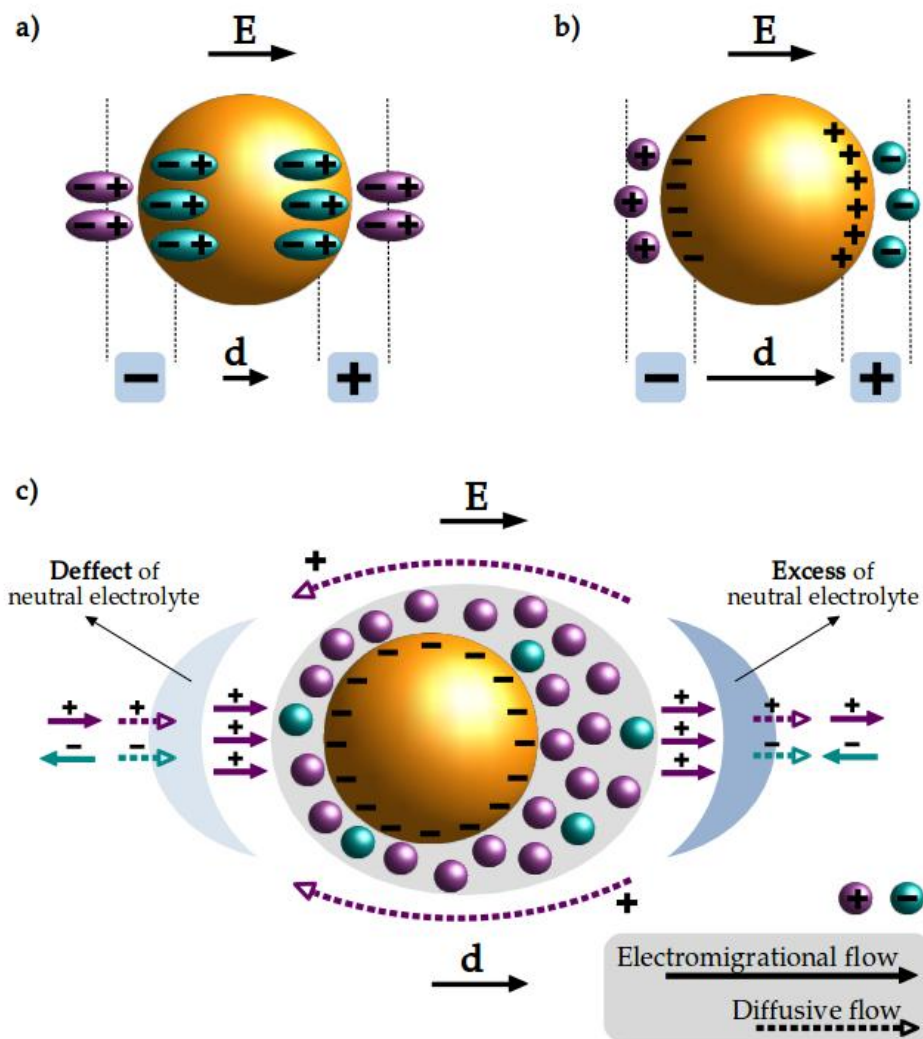


FIGURE 2.2: Schematic representation of a) molecular polarization, b) Maxwell-Wagner-O'Konski polarization and c) concentration polarization, of a negatively charged colloidal particle.

Note that when referring to particle conductivity, the effect of the presence of the EDL must be included. In general, the double layer introduces an additional conductivity at the interface which is not taken into account in the original Maxwell-Wagner approach, and

that accounts for the fact that this polarization mechanism is found even in dielectric materials. When the EDL is sufficiently thin, this contribution can be modelled as a surface conductivity  $K^\sigma$ , as first suggested by O’Konski [66]. Moreover, the excess conductivity, albeit located on the interface, can be attributed to the particle by means of an effective conductivity:

$$K_p^{\text{eff}} = 2K^\sigma/a \quad (2.13)$$

where  $a$  is the particle radius. This more realistic model, known as Maxwell-Wagner-O’Konski (MWO) theory, is based on the assumption that, for spherical nonconducting particles of radius  $a$ , the problem is equivalent to that of a uniform sphere with radius  $a + \kappa^{-1}$  and conductivity  $K_p^{\text{eff}}$  [61].

The dipolar coefficient for MWO polarization reads [62]:

$$C_{\text{cond}} = \frac{K_p^{\text{eff}} - K_m}{K_p^{\text{eff}} + 2K_m} \quad (2.14)$$

where the medium conductivity can be calculated as:

$$K_m = \sum_{k=1}^N \frac{(z_k e)^2 n_0^k N_A}{k_B T} D^k \quad (2.15)$$

being  $D^k$  the translational diffusion coefficient of the  $k$ -th ion and  $N_A$  the Avogadro number. The characteristic time for the establishment of this mechanism, associated to charge accumulation, is similar to that required for the charging of a capacitor:

$$\tau_{\text{MWO}} = \frac{\epsilon_0 \epsilon_p + \epsilon_0 \epsilon_m}{K_p^{\text{eff}} + K_m} \quad (2.16)$$

- The slowest contributing mechanism is **concentration polarization**, associated to deformations of the EDL due to unsymmetrical electromigrating and diffusive ion flows around the particle [52]. Coions

(ions with charge of the same sign than that of the particle surface) and counterions (with opposite charge) present practically identical transport numbers far from the EDL. However, their values differ inside it and, in fact, if the particle is sufficiently charged, near its surface the charge flows are almost exclusively associated to counterions. This produces a continuous increase of salt concentration on one side of the particle, and hence a reduction of the thickness of the EDL according to Equation 2.6, and a depletion on the other, with a subsequent increase in the EDL width. A steady state is reached when diffusive flows counterbalance these concentration polarization clouds. A schematic representation of this mechanism in the case of a negatively charged particle is displayed in Figure 2.2c, where the deformation of the EDL can be observed.

Concentration polarization leads to a reduction of the induced dipole for two reasons. First, the deformation of the EDL results in a small dipole opposite to the external field. Moreover, ion redistribution due to diffusive flows effectively lowers the MWO contribution. In the case of a thin double layer, and neglecting convective flows (which can be shown to barely affect), the following expression can be found for the contribution of this mechanism to the dipolar coefficient for non-conducting spherical particles, which must be added to  $C_{\text{cond}}$  [62]:

$$C_{\text{conc}} = -\frac{3}{2} \frac{K\sigma^2}{(2K\sigma + aK_m)(K\sigma + aK_m)} \quad (2.17)$$

The characteristic time for this process is determined by the establishment of diffusive flows along distances of the order of the particle radius:

$$\tau_\alpha = \frac{a^2}{2D_{\text{eff}}} \quad D_{\text{eff}} = \frac{2D^+D^-}{D^+ + D^-} \quad (2.18)$$

### 2.2.2. Polarization under alternating fields

The mechanisms just described in the time domain appear also in the **frequency domain**: as the period of the field sweeps the characteristic

times referred to above, frequency dispersion processes will be detected in the polarisation spectrum of the system. To study this spectral behaviour, we consider an alternating electric field of angular frequency  $\omega$ , given by  $E_0 e^{-i\omega t}$ , where  $i = \sqrt{-1}$ . Since the described processes for particle polarization are established in a finite time, they can have a retardation with respect to the external field, and therefore the dipolar coefficient is a complex quantity, which can be expressed as:

$$C(t) = C^*(\omega)e^{-i\omega t} \quad C^* = C' - iC'' \quad (2.19)$$

where  $C'$  and  $C''$  are real numbers. For our purposes, only the real part of the dipolar coefficient is needed [49], and hence we will refer to it simply as  $C$ .

In the frequency domain, the spectrum of the dipolar coefficient shows different relaxations, related to each polarization mechanism and its characteristic time [67]. Thus, the **frequency dependence** of  $C$  provides useful information on the processes that take place around the particle and its double layer. A **relaxation of the dipolar coefficient** occurs when the frequency of the applied field is so high that a determined process cannot be established in the time corresponding to two consecutive field inversions. As a consequence, the mentioned mechanism can no longer contribute to the value of  $C$ . The relaxation frequency of each process is the inverse to the characteristic time for its formation. According to this, two relaxations are expected for the frequencies typically tested in dielectric spectra determinations, namely between 1 kHz and a few MHz:

- **Maxwell-Wagner-O'Konski relaxation:** If the frequency of the applied field is much higher than  $\omega_{\text{MWO}} = 1/\tau_{\text{MWO}}$ , the electromigrational flows do not have enough time to redistribute the ions in the EDL, and hence the polarisation depends exclusively on the difference of the permittivities of the medium and the particle. For lower frequencies, in contrast, the displacement of the free charges dominates the behaviour of the system, and the dipolar coefficient  $C_{\text{cond}}$  depends on the contrast between the conductivities.
- **$\alpha$ -relaxation:** If the field frequency is further lowered, down to val-

ues below  $\omega_\alpha = 1/\tau_\alpha$ , diffusive flows have enough time to establish and the concentration polarization mechanism contributes to the value of the the dipolar coefficient, which then is  $C_{\text{cond}} + C_{\text{conc}}$ .

The Maxwell-Wagner relaxation can be in fact better understood if the problem is analysed directly in the frequency-domain, since in this framework it is possible to define a complex conductivity which includes the contribution of both the permittivity and the conductivity,  $K^* = K + i\omega\epsilon\epsilon_0$ . The dipolar coefficient of a spherical particle with complex conductivity  $K_p^*$  immersed in a medium with complex conductivity  $K_m^*$  is given by:

$$C^* = \frac{K_p^* - K_m^*}{K_p^* + 2K_m^*} \quad (2.20)$$

From this expression, the high and low frequency limits  $C_{\text{perm}}$  and  $C_{\text{cond}}$  can be obtained, together with the relaxation frequency  $\omega_{\text{MWO}}$ . The transition from one value to the other is typically described by a **Debye-type relaxation** [68]

$$C(\omega) = C_{\text{perm}} + \frac{C_{\text{cond}} - C_{\text{perm}}}{1 + \omega/\omega_{\text{MWO}}} \quad (2.21)$$

Figure 2.3 shows the spectrum of the real part of the dipolar coefficient corresponding to the particle represented in Figure 2.2, where the  $\alpha$  and MWO relaxations can be clearly observed.

Note that along this discussion, monodispersity of the dispersions was assumed, since the particle radius has been fixed. However, real nanoparticle suspensions present size distributions. The behaviour of these **polydisperse samples** can be better explained by **Cole-Cole-type relaxations** [69]:

$$C(\omega) = C_\infty + \frac{C_0 - C_\infty}{1 + (\omega/\omega_c)^{1-\gamma}} \quad (2.22)$$

where  $0 < \gamma < 1$  is a parameter related to polydispersity. The value  $\gamma = 0$  corresponds to the monodisperse case, for which the Debye-type relaxation is recovered.

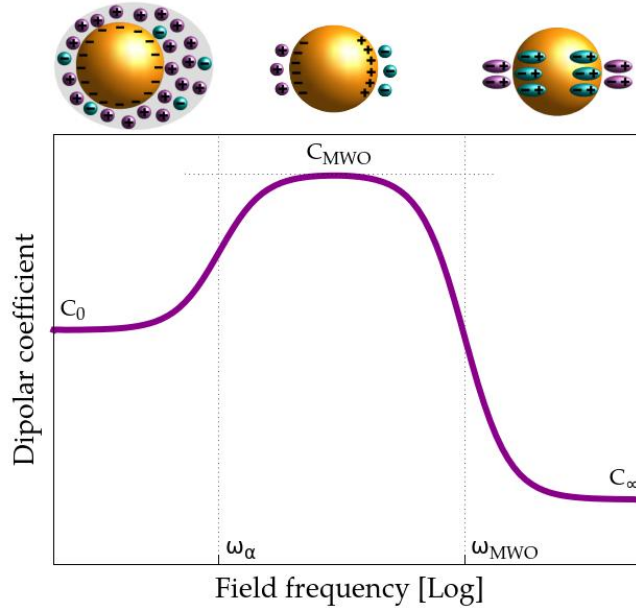


FIGURE 2.3: Dipolar coefficient spectrum for the particle represented in Figure 2.2.

### 2.2.3. The case of non-spherical particles

The polarization mechanisms just described are also observed for non-spherical particles, but the problem in this case presents further complexities. In the first place, the electric properties of the particles are inosotropic, and hence their electric polarizability and dipolar coefficient are not scalar quantities but tensors. Therefore, Equations 2.10 and 2.11 must be written in their general form [63]:

$$\mathbf{d} = \tilde{\alpha}^e \mathbf{E}_0 \quad \tilde{\alpha}^e = 3V_p \epsilon_0 \epsilon_m \tilde{C} \quad (2.23)$$

As a consequence, the polarization depends on the shape and orientation of the particles and, in general, the induced dipole is not parallel to the applied field. This fact further complicates the theoretical approaches, making the use of symmetry considerations and approximations normally necessary to model the polarization of non-spherical particles. Here, we will restrict ourselves to spheroidal geometries, schematically represented

in Figure 2.4.

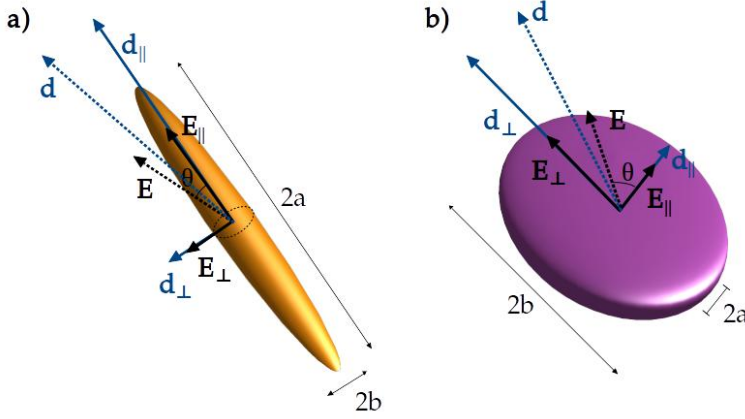


**FIGURE 2.4:** Representation of the geometry of a) a prolate and b) an oblate spheroid, together with the electric field and dipole moment components along the symmetry axis and perpendicular to it.

For spheroidal particles, if the principal axes are used as the reference frame, the electric polarizability (and analogously the dipolar coefficient) is diagonal, with only two independent non-zero terms,  $\alpha_{\parallel}^e$  and  $\alpha_{\perp}^e$ , referred to the directions parallel and perpendicular to the symmetry axis of the spheroid respectively. In this manner:

$$d_i = \alpha_i^e E_i \quad (2.24)$$

where  $i = \parallel / \perp$ . For an arbitrary orientation, in which the symmetry axis of the particle and the external electric field form an angle  $\theta$ , the superposition principle can be used to obtain the induced dipole, since polarization depends linearly on the applied field. As a result,

$$\mathbf{d} = \alpha_{\parallel}^e \cos \theta \hat{\mathbf{e}}_{\parallel} + \alpha_{\perp}^e \sin \theta \hat{\mathbf{e}}_{\perp} \quad (2.25)$$

where  $\hat{\mathbf{e}}_i$  is the unit vector along the parallel or perpendicular direction. In this manner, in the case of non-spherical axially-symmetric particles, the polarization mechanisms formerly explained must be analysed along the two main axes.

Moreover, the problem presents an additional complication, given by the fact that the electric field around a polarised spheroid is not purely dipolar, but rather presents different multipolar contributions. However, these do not affect the macroscopic response, and hence the dipolar approximation can still be used [24, 49]. Here we adopt this approach, taking into account that for spheroidal geometries the particle conductivity depends on its orientation with respect to the electric field:

$$K_{p,i}^* = K_p + K_{p,i}^{\text{eff}} + i\omega\epsilon_0\epsilon_p \quad (2.26)$$

where  $K_{p,i}^{\text{eff}}$  is an equivalent conductivity, analogous to that defined in the case of spheres, which for spheroidal geometries depend on particle orientation. The effective conductivities along the directions parallel and perpendicular to the symmetry axis can be obtained from the surface conductivity introduced by the EDL,  $K^\sigma$ , as  $K_{p,i} = K^\sigma g_i$ , where  $g_i$  are purely geometrical factors [25]:

$$g_{\parallel} = \begin{cases} \frac{3a}{2bh} \left( \frac{a^2-2b^2}{h^2} \arctan \frac{h}{b} + \frac{b}{h} \right) & \text{for prolate spheroids } (h = \sqrt{a^2 - b^2}) \\ \frac{3a}{2bh} \left( \frac{2b^2-a^2}{h^2} \ln \frac{h+b}{a} - \frac{b}{h} \right) & \text{for oblate spheroids } (h = \sqrt{b^2 - a^2}) \end{cases}$$

$$g_{\perp} = \begin{cases} \frac{3a}{2bh} \left( \frac{a^2}{2h^2} \operatorname{arccot} \frac{b}{h} + \frac{ba^2-2b^3}{2a^2h} \right) & \text{for prolate spheroids} \\ \frac{3h}{2ba} \left( \frac{2b^3-ba^2}{2h^3} - \frac{a^4}{2h^4} \ln \frac{h+b}{a} \right) & \text{for oblate spheroids} \end{cases} \quad (2.27)$$

Similarly to the case of spheres, the dipolar coefficient of spheroidal particles can be obtained from the mismatch between the complex conductivities of the medium and the particle, taking into account the shape effects. In this manner [63]:

$$C_i^*(\omega) = \frac{1}{3} \frac{K_{p,i}^* - K_m^*}{K_m^* + (K_{p,i}^* - K_m^*)L_i} \quad (2.28)$$

where  $L_{\parallel/\perp}$  are the depolarization factors, purely geometrical coefficients which describe the electric field created inside a particle with a determined

shape by an external electric field. In our case, the internal field is homogeneous and given by [63]

$$\mathbf{E}_i^{\text{int}} = \frac{\mathbf{E}}{1 + (K_p^*/K_m^* - 1)L_i} \quad (2.29)$$

For spheroidal geometries, the depolarization factors read [25]:

$$L_{\parallel} = \frac{ab^2}{h^3} \begin{cases} (\operatorname{atanh} \frac{h}{a} - \frac{h}{a}) & \text{for prolate spheroids} \\ (\frac{h}{a} - \operatorname{atan} \frac{h}{a}) & \text{for oblate spheroids} \end{cases} \quad (2.30)$$

$$L_{\perp} = \frac{1 - L_{\parallel}}{2}$$

Finally, operating in Equation 2.28, a Debye-type MWO relaxation is found for each orientation:

$$C_{\text{MWO},i}^*(\omega) = C_{\text{MWO},i}^{\infty} + \frac{C_{\text{MWO},i}^0 - C_{\text{MWO},i}^{\infty}}{1 + i\omega\tau_{\text{MWO},i}}$$

$$\tau_{\text{MWO},i} = \epsilon_0 \frac{(1 - L_i)\epsilon_m + L_i\epsilon_p}{(1 - L_i)K_m + L_iK_{p,i}} \quad (2.31)$$

$$C_{\text{MWO},i}^{\infty} = \frac{1}{3} \frac{\epsilon_p - \epsilon_m}{\epsilon_m + (\epsilon_p - \epsilon_m)L_i}$$

$$C_{\text{MWO},i}^0 = \frac{1}{3} \frac{K_{p,i} - K_m}{K_m + (K_{p,i} - K_m)L_i}$$

The analysis of **concentration polarization** in the case of non-spherical particles is further complicated by the fact that there is not a single characteristic dimension. In particular, for spheroids the excess and defect ionic clouds which modify the state of polarization of the EDL depend on the semiaxis dimensions. In spite of this, given the linearity of the problem, it is possible to consider separately the situations of the particle aligned with its symmetry axis along the field direction and perpendicular to it, distinguishing two typical values of the diffusion length,  $L_{D,\parallel}$  and  $L_{D,\perp}$  respectively. The ionic cloud size is similar to the characteristic dimension of the particle in the field direction. The characteristic relaxation time can be approximated by [70]:

$$\tau_{\alpha,i} \simeq \frac{L_{D,i}^2}{2D_{\text{eff}}} \quad (2.32)$$

Figure 2.5 shows a schematic representation of the  $\alpha$  polarization for prolate and oblate spheroids, aligned parallel and perpendicular to the electric field. As observed, for the elongated geometry,  $L_{D,\parallel} \simeq a$  and  $L_{D,\perp} \simeq b$ . On the other hand, for oblate spheroids, two similar characteristic times can be expected for either orientation, since the ions cannot find a diffusion path along the minor axis, and  $L_{D,\parallel} \simeq L_{D,\perp} \simeq b$  [70]. Although a discussion of the contribution to the dipolar coefficient is not presented, the same arguments as in the case of spheres hold for the decrease of  $C$  as compared to the MWO polarization. More detailed information can be found elsewhere [70].

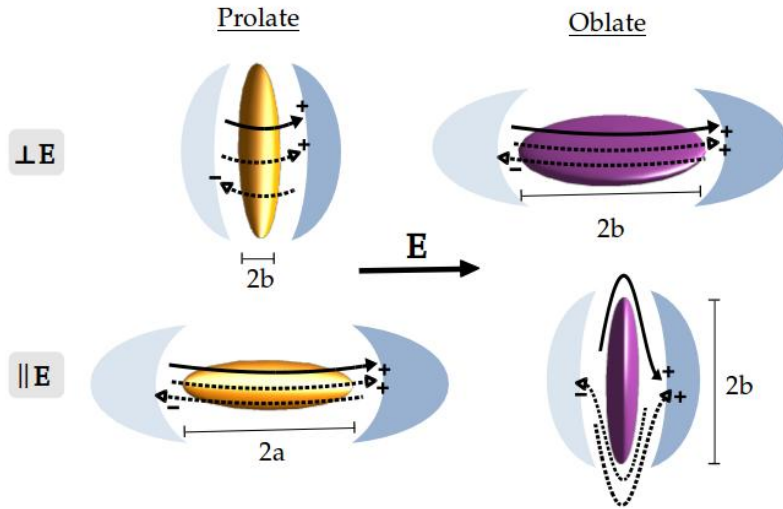


**FIGURE 2.5:** Representation of the diffusive (dashed arrows) and electromigrational (solid arrows) flows of the ions inside the EDL for a prolate and an oblate particle, in the cases of orientation of the symmetry axis parallel and perpendicular to the external field.

### 2.2.4. Extension to non-homogeneous particles

Up to this point, particles in suspension have been considered homogeneous. In this section, we analyse the extension of the **MWO polarization** theory for a **non-homogeneous particle** composed by a core and a charged dielectric shell, both with spheroidal geometries. Schematic representations of a prolate and an oblate particle with these characteristics are shown in Figure 2.6.

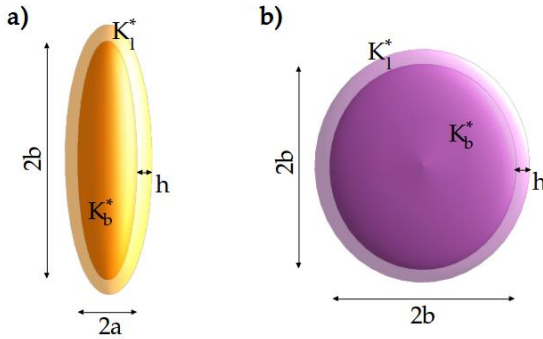


**FIGURE 2.6:** Representation of particles formed by a core and a cover, both with spheroidal shape, in the case of a) prolate and b) oblate geometries.

In this situation, Equations 2.28-2.31 still hold, but the calculation of the complex conductivity of the particle is not well-defined, since the spheroid is not homogeneous. In order to make use of these expressions we use the Maxwell mixture formula, which allows the replacement of this system by an equivalent homogeneous particle with complex conductivity  $K_{p,i}^*$  along its main axes [61]. In our case, we have a spheroidal core with bulk conductivity  $K_b$  and symmetry and transverse semi-axes  $a$  and  $b$  respectively, covered by a dielectric layer of complex conductivity  $K_l^*$  and thickness  $h$ . The semi-axes of the equivalent homogeneous particle are  $a+h$  and  $b+h$ . In these conditions, the Maxwell mixture formula can be written as [61, 71]:

$$\frac{1}{3} \frac{K_{p,i}^* - K_l^*}{K_l^* + (K_{p,i}^* - K_l^*)L_i'} = \frac{\gamma}{3} \frac{K_b^* - K_l^*}{K_l^* + (K_b^* - K_l^*)L_i'} \quad (2.33)$$

where  $L_i$  and  $L_i'$  are the depolarization factors of the core and the equivalent

lent particle along the  $i$  direction and

$$\gamma = \frac{ab^2}{(a+h)(b+h)^2} \quad (2.34)$$

From Equation 2.33, the conductivity of the equivalent particle along its symmetry and transverse axes can be obtained as

$$K_{p,i}^* = K_l \frac{(K_b^* - K_l^*)(L'_i + \gamma - \gamma L_i) + K_l^*}{(K_b^* - K_l^*)(L'_i - \gamma L_i) + K_l^*} \quad (2.35)$$

and the theory developed for homogeneous particles can be used in this special case.

## 2.3. Polarization of metallic particles

### 2.3.1. Induced EDL of metallic spherical particles

Up to this point in our description, it has been considered that modifications of the equilibrium structure of the EDL because of the application of external electric fields can be considered as perturbations. As mentioned, in general this is a very good approximation for charged particles under the usual applied voltages. Nevertheless, if particles are barely charged and highly polarisable, this consideration is no longer valid, and induced-charge electrokinetic phenomena must be taken into account [72]. This is the case for metallic particles, which normally present a small surface charge and large induced dipoles. In this situation, the EDL structure in equilibrium is very weak, as represented in Figure 2.7a. However, upon application of an electric field, the induced charge accumulation inside the particle will attract ions in solution, with different sign on each side (Figure 2.7b). Hence, while at equilibrium the EDL is almost non-existing, under the application of an electric field two double layers are induced, one on each side of the particle [72, 73]. As a consequence, the analysis of the polarization of metallic particles must be carried out separately.

For the theoretical approach, the induced double layers are modelled as capacitors [72, 74], with capacitance per surface unit  $C_{\text{EDL}} = \frac{Q}{S\varphi_S}$ , where  $Q$  is the accumulated charge,  $S$  the particle surface and  $\varphi_S$  the value of the potential on the particle surface. Moreover, in the case of thin EDLs and within the Debye-Hückel approximation:

$$C_{\text{EDL}} = \epsilon_0 \epsilon_m \kappa \quad (2.36)$$

The accumulated electric charge is due only to the electric current coming from the electrolyte, and hence it can be calculated from the ion current density  $\mathbf{J}$  reaching the particle surface, as:

$$\mathbf{J} = K_m \mathbf{E}_{\perp S} \rightarrow Q = C_{\text{EDL}} S \varphi_S = K_m S \int E_{\perp S} dt = \frac{K_m S}{i\omega} E_{\perp S} \quad (2.37)$$

where  $\mathbf{E} = E_0 e^{i\omega t}$  and  $E_{\perp S}$  denotes the component of the electric field

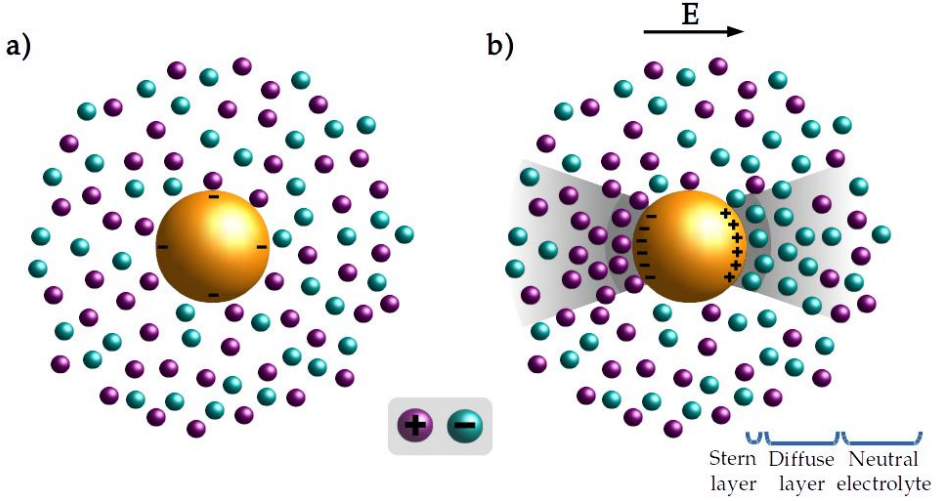


**FIGURE 2.7:** Representation of the EDL structure of a metallic spherical particle with very low negative charge a) at equilibrium and b) under the application of an external electric field.

perpendicular to the particle surface. Therefore, the following condition is fulfilled [74]:

$$\mathbf{E}_{\perp S}|_S = \nabla\varphi \cdot \hat{\mathbf{n}}|_S = \frac{i\omega\mathcal{C}_{\text{EDL}}}{K_m}\varphi_S \quad (2.38)$$

being  $\hat{\mathbf{n}}$  the unit surface vector. The potential far from the particle is taken as 0 with no loss of generality.

For a spherical particle of radius  $a$ , using Equations 2.8 and 2.10, the electric potential on the particle surface can be written as:

$$\varphi_S = aE_0 \cos\theta[C - 1] \quad (2.39)$$

and the components of the electric field on the particle surface are given by:

$$\begin{aligned} E_{\perp S} &= -\left.\frac{d\varphi}{dr}\right|_S = E_0 \cos\theta[1 + 2C] \\ E_{\parallel S} &= -\left.\frac{1}{r}\frac{d\varphi}{d\theta}\right|_S = -E_0 \sin\theta[C - 1] \end{aligned} \quad (2.40)$$

Taking into account these expressions, and applying condition 2.38, it can be shown that  $1 + 2C = i\omega a\mathcal{C}_{\text{EDL}}[1 - C]/K_m$ , and hence

$$\text{Re}[C] = \frac{(\omega/\omega_{\text{EDL}})^2 - 2}{(\omega/\omega_{\text{EDL}})^2 + 4} \quad \omega_{\text{EDL}} = \frac{K_m}{a\mathcal{C}_{\text{EDL}}} \quad (2.41)$$

In this manner, the spectral dependence of the dipolar coefficient of metallic particles, shown in Figure 2.8, is obtained. Taking the high and low frequency limits on Equations 2.40 and 2.41, it can be observed that:

$$\begin{aligned} C &= -\frac{1}{2} & E_{\perp S} &= 0 & \omega &\rightarrow 0 \\ C &= 1 & E_{\parallel S} &= 0 & \omega &\rightarrow \infty \end{aligned} \quad (2.42)$$

This behaviour can be physically explained in the following manner [74, 75]: When the electric field is applied, the metallic particle reaches perfect polarization ( $C = 1$ ) almost instantaneously. Hence, the field lines enter the particle perpendicular to its surface ( $E_{\parallel S}=0$ ) and an electric dipole is induced on the system. This situation is presented in Figure 2.8. In contrast, for field frequencies below  $\omega_{\text{EDL}}$ , ions in solution have enough time to accumulate in the proximities of the particle charge and screen its effect. In other words, the charging of the capacitors can be established between two field inversions. In this situation, also shown in Figure 2.8, the dipole induced on the particle and the one arising from ion redistribution counteract each other and no system polarization is observed. Thus, the system behaves as an insulator and the field lines are parallel to the particle surface ( $E_{\perp S}=0$ ). The dipole coefficient goes to  $-1/2$ , a situation described by Equation 2.14 with  $K_p \ll K_m$  (the conductivity of the medium is effectively much larger than that of the particle).

### 2.3.2. Asymptotic analysis for elongated geometries

For non-spherical particles, the solution of Poisson equation and the application of condition 2.38 are not straight-forward. For this reason, an asymptotic analysis is carried out for the case of extremely elongated geometries. This approach is based on the consideration that, without loss of generality, the applied electric field gives rise to a charge distribution

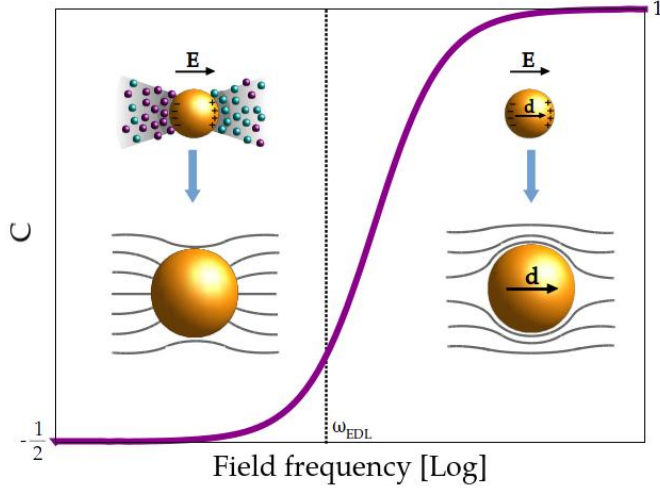


**FIGURE 2.8:** Dipolar coefficient spectrum of a spherical metallic particle in an electrolyte solution. The simplified structure of the charges and the field lines around the particle are also shown.

on the suspended particles, which in turn is responsible for the induced dipole [74]. Let us consider a needle-shaped particle, with its major axis placed along the  $x$  direction and its center situated on the origin. The major and minor axis lengths are  $2a$  and  $2b$  respectively, with  $b \ll a$ . For this geometry, the induced charge distribution  $\lambda(x)$  can be considered unidimensional, and caused by the component of the field parallel to the particle axis,  $E_{\parallel}$ . The total potential consists of the term corresponding to the external field and the perturbation due to the induced charge distribution. Thus [74, 76],

$$\varphi(x, \rho) = -E_{\parallel}x + \frac{1}{4\pi\epsilon_0\epsilon_m} \int_{-a}^a \frac{\lambda(x')}{\sqrt{(x-x')^2 + \rho^2}} dx' \quad (2.43)$$

where  $\rho$  is the distance to the needle's major axis.

For very thin cylinders, the linear charge distribution varies over distances of the order of  $a \gg b$ . Thus, in the proximities of the particle surface ( $\rho \approx b \ll a$ ),  $\lambda(x)$  can be taken out of the integral as a reasonable approximation [74]. The remaining integral expression can also be

approximated as:

$$\int_{-a}^a \frac{dx'}{\sqrt{(x-x')^2 + \rho^2}} = \int_{x-a}^{x+a} \frac{dt}{\sqrt{t^2 + \rho^2}} \approx \ln \frac{a + \sqrt{a^2 + \rho^2}}{-a + \sqrt{a^2 + \rho^2}} \approx 2 \ln \frac{2a}{\rho} \quad (2.44)$$

and, hence, the potential and the potential gradient in the proximities of the particle surface are given by the equations:

$$\begin{aligned} \varphi(x, \rho) &= -E_{\parallel} x + \frac{\lambda(x)}{2\pi\epsilon_0\epsilon_m} \ln \frac{2a}{\rho} \\ |\nabla\varphi \cdot \hat{\mathbf{n}}| &= \frac{\partial\varphi(x, \rho)}{\partial\rho} \approx -\frac{\lambda(x)}{2\pi\epsilon_0\epsilon_m\rho} \end{aligned} \quad (2.45)$$

which can be evaluated on the particle surface simply by substituting  $\rho = b$ . Next, introducing these expressions into condition 2.38, we get:

$$\lambda(x) = 2\pi\epsilon_0\epsilon_mE_{\parallel}x \frac{i\omega/\omega_{\text{EDL}}}{1 + i\omega/\omega_{\text{EDL}} \ln \frac{2a}{b}} \quad \omega_{\text{EDL}} = \frac{K_m}{b\mathcal{C}_{\text{EDL}}} \quad (2.46)$$

from which the real part of the parallel electric polarizability can be calculated as:

$$\text{Re}[\alpha_{\parallel}^e] = \frac{1}{E_{\parallel S}} \text{Re} \left[ \int_{-a}^a x\lambda(x)dx \right] = \frac{4\pi a^3\epsilon_0\epsilon_m}{3} \frac{\omega^2/\omega_{\text{EDL}}^2 \ln \frac{2a}{b}}{1 + \omega^2/\omega_{\text{EDL}}^2 \ln^2 \frac{2a}{b}} \quad (2.47)$$

Finally, we obtain that the behaviour of the polarization of very elongated metallic particles along their major axis is qualitatively similar to that of the spherical case: For low frequencies, there is no overall polarization because of ion redistribution. For frequencies of the order of  $\omega_{\text{EDL}}$ , ions can no longer follow the field oscillations and the polarization grows until it reaches the maximum value,  $\frac{4\pi a^3\epsilon_0\epsilon_m}{3 \ln(2a/b)}$ .

To estimate the particle polarizability along the minor axis, the following approach is followed in [74]: For an infinitely long needle placed along the  $x$  axis, the potential originated by a field perpendicular to it, along the  $z$  axis, is independent of the  $x$  coordinate. Hence, we take a planar disk (the

cross section of the cylinder) and solve the two-dimensional Laplace equation in cylindrical coordinates [74]. The general solution for the potential reads:

$$\varphi(\rho, \theta) = \sum_{n=1}^{\infty} \left( C_n \rho^n + \frac{D_n}{\rho^n} \right) (A_n \cos \theta + B_n \sin \theta) \quad (2.48)$$

where  $A_n$ ,  $B_n$ ,  $C_n$  and  $D_n$  are constants. Far from the particle, the electric potential is only due to the external field, and hence the condition  $\varphi = -Ez = -E\rho \cos \theta$  must be imposed at long distances ( $\rho \rightarrow \infty$ ). As a consequence:

$$\varphi(\rho, \theta) = -E_{\perp} \rho \cos \theta + \frac{d_l}{2\pi\epsilon_0\epsilon_m\rho} \cos \theta \quad (2.49)$$

where  $d_l = \frac{\alpha_{\perp}^e E_{\perp}}{2a} = 2\pi\epsilon_0\epsilon_m D_1$  is the dipole moment per unit length. Now we can apply the boundary condition given by Equation 2.38 on the particle surface ( $\rho = b$ ), to get:

$$\text{Re}[\alpha_{\perp}^e] = 4\pi ab^2\epsilon_0\epsilon_m \frac{\omega^2/\omega_{\text{EDL}}^2 - 1}{\omega^2/\omega_{\text{EDL}}^2 + 1} \quad (2.50)$$

Thus, the qualitative behaviour of the polarization of the metallic particle along its short axis is similar to that along its major axis. However, the maximum value of the electric polarizability along the two directions differ by a factor  $3 \ln(2a/b) \frac{b^2}{a^2}$ , almost zero in the case of very elongated geometries [74]. Therefore, for needle-shaped particles,  $\alpha_{\perp}^e$  can be neglected as compared to  $\alpha_{\parallel}^e$ .

## 2.4. Non-spherical particle electro-orientation

### 2.4.1. Electric torque and electro-orientation

As explained in previous sections, the polarization of non-spherical particles is in general anisotropic, and  $\tilde{\alpha}^e$  is a tensor. For axially symmetric particles, using its symmetry axis as the reference frame, only two tensor

components are independent and non-zero. Therefore, a scalar polarizability anisotropy  $\Delta\alpha^e$  can be defined as:

$$\Delta\alpha^e = \alpha_{\parallel p}^e - \alpha_{\perp p}^e \quad (2.51)$$

where  $\alpha_{\parallel p}^e$  and  $\alpha_{\perp p}^e$  are the electric polarizability along the directions parallel and perpendicular to the symmetry axis. Normally, polarization along the major axis is larger than along the minor axis, and therefore  $\Delta\alpha^e$  is expected to be positive (negative) for prolate (oblate) particles [77]. Due to this anisotropy in the electric polarizability, the external electric field and the total dipole moment that it induces are not parallel, as made evident by Equation 2.23. As a consequence, an electric torque  $\tau^e$  appears on the particle and forces it to rotate until the dipole and the electric field are aligned [49, 78]. This phenomenon is known as **electro-orientation**, and competes with rotational diffusion, which tends to randomise particle orientation. A schematic representation of the situation just described is shown in Figure 2.9.

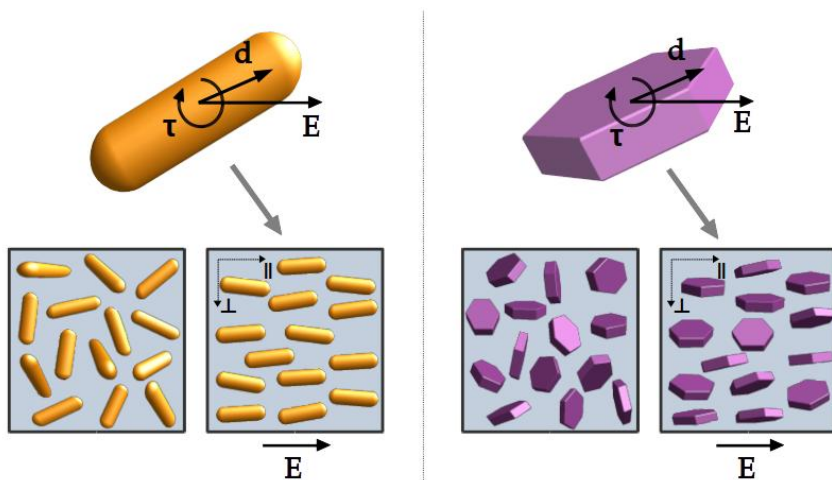


**FIGURE 2.9:** Representation of electro-orientation of non-spherical particles under an external electric field for an elongated and a planar geometry.

The electric torque exerted by an external field  $\mathbf{E}$  on an induced dipole  $\mathbf{d}$  can be obtained as  $\boldsymbol{\tau}^e = \mathbf{d} \times \mathbf{E} = (\tilde{\alpha}^e \cdot \mathbf{E}) \times \mathbf{E}$ . Thus, in the case of

axially-symmetric particles under an alternating field, the average torque reads [49]:

$$\tau_{\text{DC}}^e = -\frac{1}{2}\Delta\alpha^e E_0^2 \sin\theta \cos\theta \hat{e}_\theta \quad (2.52)$$

where Equation 2.25 was considered. It is worth mentioning that even if multipolar terms of the electric potential are considered, they do not contribute to the electric torque, as shown in [49]. Hence, the dipolar approximation taken in the potential does not have an effect on the electro-orientation description.

In general, besides  $\tau^e$ , a hydrodynamic torque  $\tau^H$  may also contribute to particle orientation. This hydrodynamic effect is caused by viscous forces exerted by the fluid on the particle surface. Given the complexity of this problem, calculations of this contribution are not available even for spherical geometries, and simplifications are normally used to shed some light on the possible hydrodynamic effects on particle electro-orientation [49]. For instance, in the case of centro-symmetric and moderately-charged particles with thin double layers, it has been shown by means of symmetry arguments that  $\tau^H = 0$  [79]. This result may be reasonably extended for highly-charged particles considering that the expressions for the velocity, pressure and electric fields depend on odd powers of the external field [49], this giving a zero average value over a field cycle. Thus, the hydrodynamic term of the torque is normally not taken into account.

Nonetheless, in some situations the hydrodynamic contribution can be non-negligible, as in the case of barely-charged metallic particles subjected to low-frequency fields [74], detailed later in the text. Moreover, for concentrated suspensions, particle orientation is also strongly affected by the hydrodynamic torque, and its consideration is fundamental to understand anomalous effects as those observed in bimodal systems [1, 80] and poly-disperse suspensions [78]. Nevertheless, taking into account these exceptions, in general the total torque can be approximated by the electric contribution described in Equation 2.52.

When non-spherical particles in suspension are subjected to very high electric fields, perfect orientation can be achieved. However, for moderate

potentials, there is a balance between electric orientation and thermal agitation. In this case, the state of orientation of the system is characterized by the non-polar orientational order parameter [81, 82]:

$$S_{\text{DC}} \equiv \int_0^\pi P_2(\cos \theta) f_{\text{DC}}(\theta) \sin \theta d\theta \quad (2.53)$$

where  $P_2$  is the second Legendre polynomial and  $f_{\text{DC}}(\theta)$  the normalised orientational distribution function of the sample. The subscript DC indicates that the magnitudes are time-averaged. From this definition, it is straightforward to obtain  $S_{\text{DC}} = 0$  for random orientation (uniform  $f_{\text{DC}}(\theta)$ ). The angular distribution is proportional to the Boltzmann factor [81]:

$$f_{\text{DC}}(\theta) = F \exp\left(\frac{-W_{\text{DC}}(\theta)}{k_B T}\right) \quad (2.54)$$

being  $F$  a normalisation constant and  $W_{\text{DC}}(\theta)$  the stationary orientation potential energy, which in turn can be obtained from the torque exerted on the particles as [43, 82]:

$$W_{\text{DC}}(\theta) = - \int_0^\theta \tau_{\text{DC}} \cdot \hat{e}_\theta d\theta \quad (2.55)$$

For an oscillating electric field, neglecting the hydrodynamic contributions to the dipole, Equations 2.52 and 2.55 lead to:

$$W_{\text{DC}}(\theta) = -\frac{1}{4} \Delta \alpha^e E_0^2 \cos^2 \theta + k \quad (2.56)$$

being  $k$  an integration constant. The same final result for  $S_{\text{DC}}$  can be found by analysing the forces acting on the particles rather than their potential energy [49], which can be a more suitable description when dissipative effects are present, or by solving the Smoluchowski equation [83].

OJO: Revisar lo ultimo.

#### 2.4.2. Main features of stationary electro-orientation

The dependence of the orientational order parameter with the **electric field amplitude** is given in general by Equations 2.53-2.56. In the case of

elongated and planar axially-symmetric particles, explicit expressions of  $S_{DC}$ , represented in Figure 2.10, are available [81, 84]. Hereunder, two limiting cases, indicated in the same figure, are analysed in more detail: Kerr's regime for weak fields and saturation of the orientation for high fields.

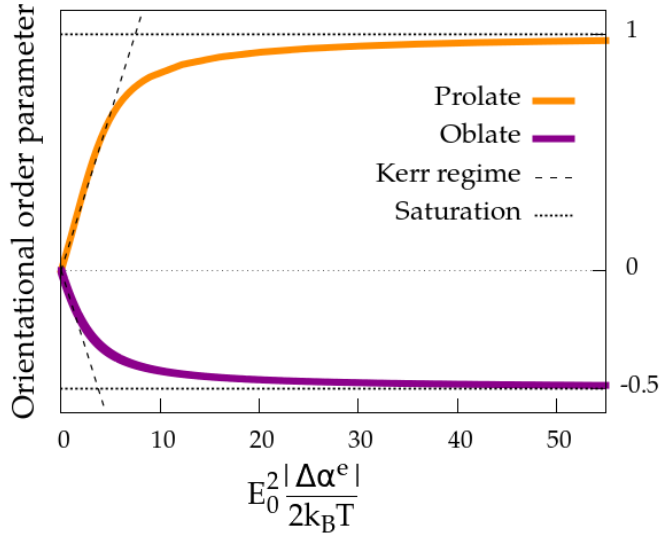


FIGURE 2.10: Order parameter as a function of the field amplitude for prolate and oblate axially-symmetric particles.

In the first case, for low-enough fields ( $W_{DC} \ll k_B T$ ), the time-averaged orientation distribution function can be approximated by:

$$f_{DC}(\theta) \approx F \left( 1 - \frac{W_{DC}}{k_B T} \right) \quad F \approx \frac{1}{2} \quad (2.57)$$

where the normalisation constant was obtained from the condition  $\int_0^\pi f_{DC}(\theta) \sin \theta d\theta = 1$  with  $f_{DC}(\theta) \approx F$ . Introducing this expression in Equation 2.53 and using Equation 2.56, the stationary order parameter for low fields reads [81, 84]:

$$S_{DC} = \frac{\Delta\alpha^e E_0^2}{30k_B T} \quad \Delta\alpha^e E_0^2 \ll k_B T \quad (2.58)$$

a quadratic dependence known as **Kerr's law**.

On the other hand, for very high fields, almost all particles are fully oriented with the external field and **saturation of the electro-orientation** is achieved. In this situation, no field dependence is observed. From the definition of  $S_{\text{DC}}$  (Equation 2.53), it is straight-forward to obtain that, for prolate particles, for which the symmetry and major axes coincide,  $S_{\text{DC}} = 1$  [81]. In contrast, oblate particles orient with their symmetry (minor) axis perpendicular to the external field, and hence  $S_{\text{DC}} = -1/2$  in the saturation regime [84].

As previously explained, the torque that orients non-spherical particles under an external electric field is due to their polarizability anisotropy, and hence, in general,  $S_{\text{DC}}$  is expected to strongly depend on  $\Delta\alpha^e$ . In the Kerr regime, in fact, electro-orientation is proportional to this quantity, as expressed by Equation 2.58. Thus,  $S_{\text{DC}}$  shows the same **frequency dependence** as  $\Delta\alpha^e$ . As previously shown, electric polarizability exhibits a rich spectral behaviour, governed by the relaxation of polarization mechanisms.  $\Delta\alpha^e$  presents an even more complex frequency dependence, since it is affected by both  $\alpha_{\parallel p}^e$  and  $\alpha_{\perp p}^e$  [49]. Figure 2.11 shows the spectrum of  $\alpha_{\parallel p}^e$ ,  $\alpha_{\perp p}^e$  and  $\Delta\alpha^e \propto S_{\text{DC}}$  for an oblate dielectric particle with specific properties in the Kerr regime. It must be noted that this example is not representative of all oblate spheroids because of the strong dependence of  $\Delta\alpha^e(\omega)$  on the electric and geometrical properties of the suspended particles. In the opposite limiting case, in the saturation regime, all particles are fully oriented and no spectral dependence is observed in  $S_{\text{DC}}$  if the saturation condition is maintained for all frequencies.

### 2.4.3. Orientation due to ICEO flows

Up to this point, we have focused on the orientation of non-spherical particles due to the dipole induced on them by the action of an external electric field since, using symmetry arguments, the hydrodynamic torque was found to be negligible under reasonable assumptions. Nevertheless, this is not the case of barely charged metallic particles, for which the asymmetric ion accumulation provokes charge migration and the subsequent dragging of liquid [41, 72–74, 85, 86]. This effect is called induced charge electro-

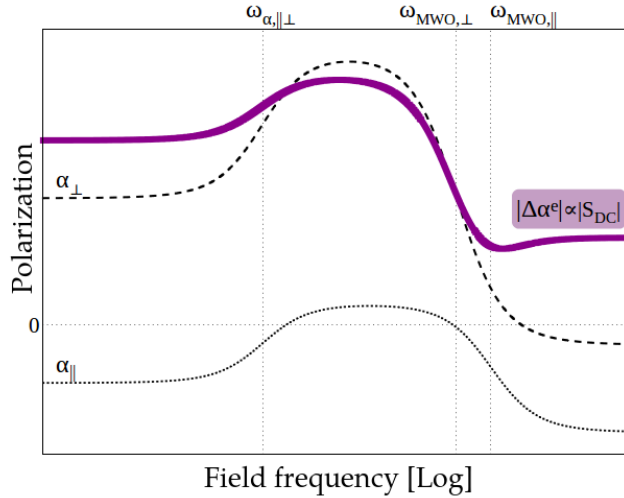


**FIGURE 2.11:** Polarizability spectrum of the oblate particles with specific properties. The polarizability along the symmetry and transverse axes and absolute value of the polarizability anisotropy are displayed.

osmosis (ICEO), and effectively orients non-spherical metallic particles at low field frequencies.

The ICEO phenomenon is represented schematically in Figure 8.8a in the case of a spherical particle subjected to a low field frequency, for which the induced double layers are formed. Here, it can be observed that the electric field component tangential to the particle surface exerts a force on the ions in the induced EDLs, which in turn gives rise to the movement of the fluid with respect to the particle [75]. The case of elongated geometries is exemplified in Figure 8.8b. The component of the electric field parallel to the major axis is responsible for charge separation inside the elongated particle, which gives rise to the formation of the induced EDLs if the field frequency is sufficiently low. The ions in these double layers are affected by both components of the electric field, but here we focus on the effect of  $E_{\perp}$ , which moves negative ions to the left and positive ions to the right, dragging liquid in the same directions. This gives rise to an effective rotation of the particle which tends to orient its major axis along the external field [74].

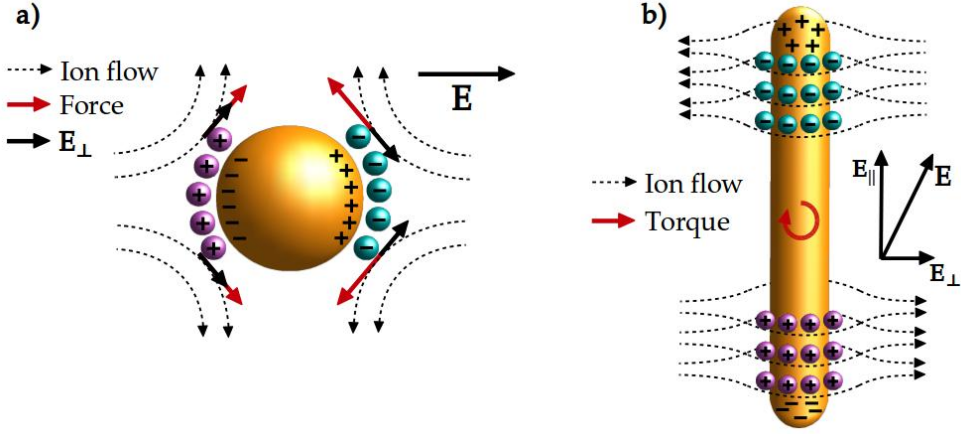


FIGURE 2.12: Schematic representation of the ICEO flows for the case of a) a spherical particle and b) a very elongated particle.

The hydrodynamic torque caused by the ICEO flows in the case of very elongated geometries is given by [74]:

$$\tau^H = \gamma \dot{\theta} = \frac{8\pi a^3 \epsilon_m E_0^2}{3f(\lambda)} \frac{\sin \theta \cos \theta}{1 + (\omega/\omega_{DL})^2} \quad (2.59)$$

where  $\dot{\theta}$  is the angular velocity of the particles,  $\gamma$  the friction coefficient,  $\lambda = \log(2a/b)$  and  $f(\lambda) = \lambda - 1.14 - 0.2/\lambda - 16/\lambda^2$ . This expression is analogous to Equation 2.52, and from it, the contribution of the viscous torque to electro-orientation can be obtained. In the case of weak fields, the order parameter can be approximated by:

$$S_{DC} = \frac{4\pi a^3 \epsilon_m E_0^2}{45f(\lambda)k_B T} \frac{1}{1 + (\omega/\omega_{DL})^2} \quad (2.60)$$

According to this expression, for high-frequency fields there is no hydrodynamic contribution to electro-orientation, an expected feature since ions cannot redistribute between two field inversions. For low frequencies, on the other hand, the electric contribution is null, according to Equation 2.47, but there is a non-zero viscous torque responsible for slight particle orientation along the electric field direction. This response is also proportional to  $E_0^2$ , and hence Kerr's law is fulfilled also for this orientation mechanism.

#### 2.4.4. AC component of electro-orientation

The previous section was devoted to the analysis of the stationary electro-orientation of non-spherical particles in suspension. However, for alternating fields, a time-dependent contribution to the orientation can also be present [83]. This AC component can be easily understood in the following manner: For low frequencies, rotational diffusion has enough time to randomise particle orientation between two field inversions. On the other hand, for high values of the field frequencies, the particles can no longer follow the field oscillations and no AC birefringence component is observed. Thus,

$$S = S_{\text{DC}} + S_{\text{AC}} \sin(2\omega t - \delta) \quad (2.61)$$

where  $S_{\text{AC}}$  and  $\delta$  are, respectively, the amplitude and retardation of the AC contribution to electro-orientation. In this expression, it can be observed that the AC component oscillates with twice the frequency of the applied field, a consequence of the quadratic dependence of orientation with the field amplitude [83, 87]. This can be easily explained if it is taken into account that each time the alternating field passes through zero, twice a cycle, the particles slightly randomise their orientation, and the order parameter passes by a minimum.

The value of  $S_{\text{DC}}$  has been obtained in a previous section by energetic arguments. In order to study the AC component, in contrast, the diffusion equation must be solved. Under a uniform electric field, this equation reads [83]:

$$\nabla^2 f(t, \theta) - \frac{d(t)E(t)}{k_B T} \frac{1}{\sin \theta} \frac{\partial}{\partial \theta} [\sin \theta f(t, \theta)] = \frac{1}{\Theta} \frac{\partial f(t, \theta)}{\partial t} \quad (2.62)$$

where  $\Theta$  is the rotational diffusion coefficient of the particles and  $d$  and  $E$  the modulus of the induced dipole and the electric field. In the case of an alternating field of frequency  $\omega$ , this equation leads to the following expressions for the AC component of the order parameter [83]:

$$S_{AC} = S_{DC,0} \frac{\omega/(3\Theta)}{1 + [\omega/(3\Theta)]^2} \quad (2.63)$$
$$\delta = \arctan[\omega/(3\Theta)]$$

where  $S_{DC,0}$  is the low-frequency limiting value of  $S_{DC}$ . Thus, as expected, the amplitude of the AC component of electro-orientation tends to zero for high frequency fields, and the behaviour is related only to particle rotational diffusion.

## 2.5. Non-spherical particle electro-optics

In the absence of external fields, non-spherical particles in suspension are randomly oriented and hence, the dispersions are isotropic. However, when an electric field is applied, particle electro-orientation gives rise to an anisotropy of the physical properties of the system at a macroscopic scale. The electro-optical effects are those related to the changes in the optical properties of colloidal suspensions by the application of electric fields [42, 88]. Here, two electro-optical phenomena related to electro-orientation are analysed: linear dichroism (LD) and electric birefringence (EB).

### 2.5.1. Linear dichroism

In general, the absorbance of a material is defined as  $A = \log(I_0/I)$ , where  $I_0$  and  $I$  are the incoming and transmitted light intensities. For non-spherical particles, this quantity is not isotropic, since they are more absorbent along their major dimension [43, 89]. As a consequence, when particles in suspension are oriented with an external electric field, an anisotropy in the macroscopic absorption coefficient of the sample, or linear dichroism  $\Delta A$ , appears. In general, LD is defined as:

$$\Delta A = A_{\parallel} - A_{\perp} \quad (2.64)$$

where  $A_{\parallel(\perp)}$  is the absorbance of the samples for linearly polarised light with polarization plane parallel (perpendicular) to the electric field. For normal orientation, the major axis of the particles is placed along the field direction and hence  $\Delta A$  is positive for elongated particles and negative for oblate geometries. Equation 2.64 can be rewritten in the following manner:

$$\Delta A = \Delta A_{\parallel} - \Delta A_{\perp} \quad \Delta A_{\parallel(\perp)} \equiv A_{\parallel(\perp)} - A_0 \quad (2.65)$$

In this expression,  $A_0$  is the absorbance of the sample for random orientation, this is, in the absence of external field. For the case of axially symmetric particles, and neglecting the possible contribution of the solvent, it reads:

$$A_0 = \frac{A_{\parallel p} + 2A_{\perp p}}{3} \quad (2.66)$$

where  $\parallel_p$  and  $\perp_p$  indicate the directions parallel and perpendicular to the symmetry axis of the particles. For normal orientation, the direction  $\parallel_p$  corresponds to  $\parallel$  in the case of prolate geometries and to  $\perp$  for oblate particles. Taking these considerations into account, Equations 2.65 and 2.66 lead to the relations:

$$\Delta A_{\parallel} = \begin{cases} 2/3\Delta A \\ 1/3\Delta A \end{cases} \quad \Delta A_{\perp} = \begin{cases} -1/3\Delta A & \text{for prolate particles} \\ -2/3\Delta A & \text{for oblate particles} \end{cases} \quad (2.67)$$

The macroscopic linear dichroism of the dispersions is related to the optical properties of the colloidal particles and their degree of orientation, as [43, 90]:

$$\Delta A = \phi \Delta A_p S \quad (2.68)$$

OJO: No tengo acceso al libro, pero digo yo que vendra, no??

where  $\phi$  is the volume fraction of the sample and  $\Delta A_p > 0$  the dichroism of a single particle, defined as the difference in light absorbance along its major and minor axes.

### 2.5.2. Electric birefringence

As explained in previous sections, when an electric field is applied to a colloidal suspension, it gives rise to particle polarization. When the frequency of the applied field is in the visible spectrum, the term optical polarizability,  $\alpha^o$ , is used [49]. The electric field of a light beam traversing a suspension will provoke this type of polarization which, in the case of non-spherical geometries, is anisotropic. For axially-symmetric particles, the optical polarizability anisotropy,  $\Delta\alpha^o$ , can be defined analogously to  $\Delta\alpha^e$  in Equation 11.6, and the same sign discussion can be applied to this case.

For particles with a characteristic size much smaller than the wavelength of the incident light, the Rayleigh approximation can be used. In this case, the bulk refractive index,  $n_p$ , is homogeneous, and an expression of  $\Delta\alpha^o$  can be obtained taking into account Equation 2.28 [50]:

$$\Delta\alpha^o = V_p\epsilon_0\epsilon_m \left( \frac{n_p^2 - n_m^2}{n_m^2 + (n_p^2 - n_m^2)L_1} - \frac{n_p^2 - n_m^2}{n_m^2 + (n_p^2 - n_m^2)L_2} \right) \quad (2.69)$$

being  $n_m$  the refractive index of the medium, and  $L_1$  and  $L_2$  the depolarization factors along the major and minor axes of the particles respectively.

Because of this anisotropy in the optical polarization, the effective refractive index of non-spherical particles is different along their longitudinal and traversal directions. As a consequence, when the particles are oriented by the action of an external electric field, a macroscopic anisotropy in the refractive index of the suspension, or electric birefringence (EB), arises [42, 43]. This birefringence  $\Delta n$  is defined as:

$$\Delta n = n_{\parallel} - n_{\perp} \quad (2.70)$$

where again  $\parallel$  and  $\perp$  indicate the directions parallel and perpendicular to the applied field. The macroscopic electric birefringence is related to the microscopic optical properties of the particles as [42]:

$$\Delta n = \frac{\Delta\alpha^o\phi}{2n_m\epsilon_0V_p} S \quad (2.71)$$

As observed, the sign of  $\Delta n$  is determined by  $S$  and  $\Delta\alpha^o$ , two quantities that are expected to exhibit the same sign (positive for prolate particles, negative for oblate geometries). Hence  $\Delta n$  is generally positive, a situation corresponding to particles with a higher electric and optical polarizability along their major axes. Nevertheless, negative birefringence can be observed experimentally. This effect can be due either to an anomalous sign of  $\Delta\alpha^o$  [89] or to an anomalous orientation of the particles, with their minor axes along the field direction [50, 78].

### 2.5.3. Main features of EB and LD

In the first place, according to Equations 2.68 and 2.71, both the electric birefringence and the linear dichroism are proportional to the particle volume fraction of the suspensions. This is the case for dilute samples, for which particle interactions can be neglected, a feature that was assumed in the theoretical approach. In the case of concentrated systems, models exist for the electrokinetic response of suspensions of spherical particles under certain conditions [91, 92], which have been partially extended to elongated geometries [28, 29].

However, little is known about the effect of particle interactions on the electro-orientation of the system. In fact, at high concentrations, particle alignment occurs spontaneously due to steric repulsion [93], giving rise to the formation of liquid crystal phases. The problem can be even more complex if it is taken into account that particles are charged, and hence there exists an electric interaction whose range is limited only by the size of the EDL. Moreover, even for dilute suspensions, particle interactions have been found to play an important role in some cases for very low field frequencies, in which the relative motion among the particles leads to strong dependences on the concentration [78, 80]. Here, we restrict ourselves to the dilute regime, and the independent particle assumption is implicitly used along the text unless indicated otherwise.

Electric birefringence and linear dichroism are proportional to the orientational order parameter (Equations 2.68 and 2.71), and hence the analysis developed for  $S$  may be used to study the main features of  $\Delta A$  and  $\Delta n$ . In this manner, Equation 2.61 is translated into:

$$\begin{aligned}\Delta A &= \Delta A_{\text{DC}} + \Delta A_{\text{AC}} \sin(2\omega t + \delta) \\ \Delta n &= \Delta n_{\text{DC}} + \Delta n_{\text{AC}} \sin(2\omega t + \delta)\end{aligned}\tag{2.72}$$

where  $\Delta A_{\text{DC(AC)}}$  and  $\Delta n_{\text{DC(AC)}}$  are given by Equations 2.68 and 2.71 using the DC (AC) component of the orientational order parameter,  $S_{\text{DC(AC)}}$ . Most works focus their attention on the DC component, which is normally referred to simply as linear dichroism  $\Delta A$  and electric birefringence  $\Delta n$ . Hereafter, we follow this nomenclature and specify the subscript only for

the AC component.

The dependence of LD and EB on the electric field is determined by Equations 2.53-2.55. Hence, the observation of the Kerr regime and saturation are expected at low and high fields respectively. The saturation values are:

$$\Delta A_{sat} = \begin{cases} \phi \Delta A_p \\ -\frac{1}{2} \phi \Delta A_p \end{cases} \quad \Delta n_{sat} = \begin{cases} \frac{\Delta \alpha^o \phi}{2n_s \epsilon_0 V_p} & \text{for prolate particles} \\ -\frac{1}{2} \frac{\Delta \alpha^o \phi}{2n_s \epsilon_0 V_p} & \text{for oblate particles} \end{cases} \quad (2.73)$$

whereas in the Kerr regime:

$$\Delta A = \Delta A_{sat} \frac{\Delta \alpha^e E_0^2}{30k_B T} \quad \Delta n = \Delta n_{sat} \frac{\Delta \alpha^e E_0^2}{30k_B T} \quad (2.74)$$

In the case of electric birefringence, it is usual to work with the Kerr constant, a magnitude independent of  $E_0$  at low fields, defined as:

$$K = \frac{\Delta n}{\lambda_0 E_0^2 / 2} = \phi \frac{\Delta \alpha^o \Delta \alpha^e}{30k_B T \lambda_0 n_s \epsilon_0 V_p} \quad (2.75)$$

where  $\lambda_0$  is the wavelength of the incident light. The frequency dependence of EB and LD are determined by the spectral behaviour of  $S_{DC}$ , which was discussed in a previous section.

#### 2.5.4. Dynamics of EB and LD

The electro-orientation of non-spherical particles and the subsequent randomisation process upon removal of the electric field provoke, respectively, the rise and the decay of the linear dichroism and the electric birefringence. These processes are not instantaneous, but rather present a complex dynamic behaviour that is analysed in this section. Henceforth, the discussion for EB is expounded; its extrapolation to the case of LD is straight-forward.

The randomisation process is due only to thermal agitation, and causes the decay of the birefringence in a finite time after the field is removed. The EB decay is expected to be in the form of a single exponential function for

monodisperse samples; for the more realistic case of polydisperse suspensions, in contrast, it must be computed as a superposition of independent exponential processes with characteristic time  $\tau_i$  [47, 94]:

$$\Delta n(t) = \Delta n_0 \sum_i A_i \exp(-t/\tau_i) \quad \tau_i = \frac{1}{6\Theta_i} \quad (2.76)$$

being  $\Delta n_0$  the value of the electric birefringence just before the field is turned off,  $\Theta_i$  the rotational diffusion coefficient of each particle and  $A_i$  coefficients which measure the contribution of each process to the decay. In the case of electric birefringence, this contribution is proportional to particle volume. This can be deduced from Equation 2.75, taking into account that  $\Delta\alpha^o$  and  $\Delta\alpha^e$  are proportional to  $V_p$ .

To obtain an explicit expression for the shape of the birefringence decay of polydisperse suspensions, we assume a continuous particle size distribution  $P(m)$ , and calculate the EB as [45, 46]:

$$\Delta n(t) = \Delta n_0 \int P(m) A(m) e^{-t/\tau(m)} \quad (2.77)$$

where  $m$  is the characteristic dimension of each particle, and  $A(m)$  and  $\tau(m)$  are analogous to  $A_i$  and  $\tau_i$  in the discrete case. We will further assume a size distribution in the shape  $P(m) \propto e^{-Cm^p}$ , where  $C$  is a constant and  $p$  a positive number. From this expression, using the saddle-point approximation and neglecting logarithmic corrections at very short times, it can be shown that  $\Delta n(t)$  presents the shape of a stretched exponential function [45, 46]:

$$\Delta n = \Delta n_0 e^{-(t/\tau)^\alpha} \quad (2.78)$$

where  $\alpha$  is a polydispersity factor, ranging from 0 to 1 (monodisperse case), and  $\tau$  is a characteristic decay time, which can be related to the average rotational diffusion coefficient of the particles as  $\Theta = 1/(6\tau)$ .

The rise of electric birefringence is more complicated than the decay, since it is affected by both rotational diffusion and the action of the external field. For this reason, the general case is not analysed; instead two limiting cases, weak and high fields, are considered:

- In the first place, when the electric fields are weak, the EB rise is dominated by diffusive processes, and it is symmetric to the decay, formerly explained. Thus [95],

$$\Delta n(t) = \Delta n_{st} \left[ 1 - e^{-(t/\tau)^\alpha} \right] \quad (2.79)$$

where  $\Delta n_{st}$  is the stationary value of the birefringence, and  $\tau$  and  $\alpha$  present the same value as in the case of the decay.

- On the other hand, for high values of the applied field, diffusion is negligible as compared to the electric driving force. In this situation, for a single particle, we may equate the torque to the rotational friction force to obtain the angular velocity  $\dot{\theta}$  of the particle [96]:

$$\boldsymbol{\tau}^e = \mathbf{d} \times \mathbf{E} = \zeta_R \dot{\boldsymbol{\theta}} \quad \rightarrow \quad \dot{\theta} = \frac{\Delta \alpha^e E}{4 \zeta_R} \sin \theta \cos \theta \quad (2.80)$$

being  $\zeta_R = k_B T / \Theta$  the friction coefficient. In this expression,  $\Delta \alpha^e$  and  $\zeta_R$  are proportional to particle volume, and hence  $\dot{\theta}$  is independent of the particle size. As a consequence, the rise of the birefringence is expected to be in the form of a single exponential function even for polydisperse suspensions [89, 96]. In this manner:

$$\Delta n = \Delta n_{st} \left[ 1 - e^{-t/\tau_r} \right] \quad (2.81)$$

where  $\tau_r$  is a characteristic rise time, whose inverse is expected to depend linearly on the square of the field amplitude, both in the low and high field ranges [81, 87], according to the expression:

$$\frac{1}{\Delta n_{st}} \frac{d(\Delta n(t))}{dt} = \frac{1}{\tau_r} = \frac{2}{5} \frac{\Delta \alpha^e E_0^2}{k_B T} \Theta \quad (2.82)$$

Figure 2.13 shows an example of the rise and decay dynamics of EB under different conditions. Here, it can be observed that the decay is independent of the frequency and amplitude of the applied field, as it depends only on particle diffusion (Equation 2.78). In the case of low fields, the rise of the EB, given by Equation 2.79, is symmetric with respect to the decay. On the

other hand, for high fields, the rise of the birefringence is given by Equations 2.81 and 2.82. The AC oscillations only appear at low frequencies, as deduced from Equation 2.63.

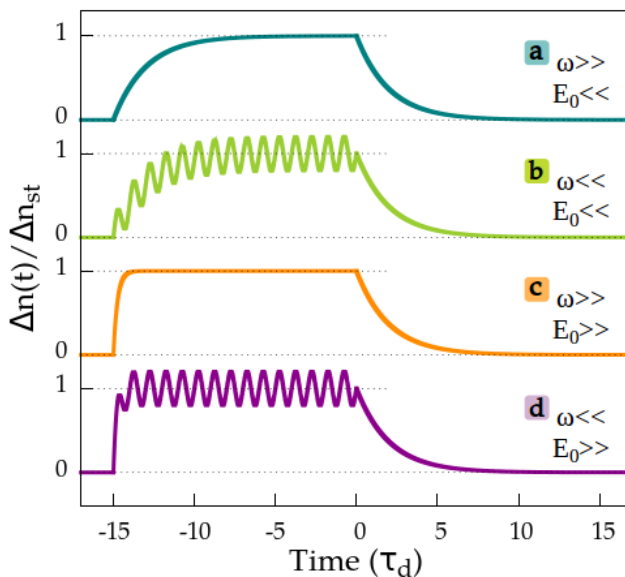


**FIGURE 2.13:** Birefringence rise and decay of a polydisperse sample under 4 different conditions. The time is given in units of  $\tau_d$ . The decay is a stretched exponential function with  $\alpha = 0.5$ . In a) and b),  $W_{DC} \ll k_B T$ , and hence the rise and the decay are symmetrical. In c) and d), on the other hand, the rise is in the shape of a single exponential function with  $\tau_r = \tau_d/4$ . In a) and c),  $\omega \gg 3\Theta$  and, as a consequence, the AC component of the birefringence is not observed. In b) and d), in contrast, the birefringence oscillates with twice the frequency of the applied field ( $\omega = \pi/\tau_d$ ,  $\Delta n_{AC} = 0.2\Delta n_{st}$ ).

# 3

## MATERIALS AND METHODS



## 3.1. General information

In this section we present the information regarding the methodology and the materials used during the present work. Most of the experimental determinations have been carried out at a laboratory of the Applied Physics Department of the University of Granada, referred to as UGR laboratory. Additionally, some experimental work was developed during a short-term stay at Queen Mary London University (QMLU). As general information, the water used in the cleaning of the materials, the synthesis and sample preparation was deionized and filtered by a membrane of 0.2  $\mu\text{m}$  (Milli-Q Academic, Millipore, France). The chemical products have analytical quality and were purchased from Sigma-Aldrich (USA). The measurements of the absorption spectra (6705 UV/Vis spectrophotometer, Jenway, UK), zeta potential (Malvern Zeta Sizer Nano-ZS, Malvern Instruments, UK), dynamic light scattering (same instrument) and depolarised dynamic light scattering (3D-DLS System, LS Instruments, Switzerland) were carried out with commercial devices available in the UGR laboratory. The environmental scanning electron microscope pictures were obtained in the *Centro Andaluz de Nanomedicina y Biotecnología*, Málaga. The rest of the microscopy determinations were carried out with the instruments of the *Centro de Instrumentación Científica* of the University of Granada.

## 3.2. Materials

### 3.2.1. Sodium montmorillonite

Montmorillonite is a laminar clay derived from pyrophyllite, a mineral composed of sheets consisting of two tetrahedral layers of silica and an intermediate octahedral layer of alumina[97, 98]. In montmorillonite, certain atoms of this structure are replaced by others with lower positive valence. This isomorphic substitution provokes a lack of positive charge in every layer, which favours the adsorption of cations on the surface. In the presence of water, the compensating cations can be easily exchanged by others available in the solution, known as exchangeable cations. These can pen-

strate the structure, and therefore are located both on the particle surface and in between the layers. Moreover, the water molecules also enter the laminar structure, which strongly increases the basal distance of the clay, an effect known as swelling. In aqueous suspension, this material can expand its volume by a factor 10-15 [97, 99].

The surfaces and the edges of sodium montmorillonite particles present different charging mechanisms:

- As mentioned, the surface charge is caused by imperfections of the crystalline structure due to the isomorphous substitution of atoms in the lattice. This negative charge is constant and independent of pH and salt concentration.
- On the other hand, the edge charge is due to the interruption of the silica and alumina layers, and the subsequent adsorption of potential-determining ions on the broken bonds [98]. The main charging mechanism is the exposure of  $Al^{3+}$  ions [98, 100]. This gives rise to a strongly pH-dependent charge, which becomes more positive for low pH values and decreases for more acid pHs, getting to reserve its sign. Different works have shown that the edge charge is positive for pH lower than 7 [101, 102].

Figure 3.1 shows a schematic representation of the mentioned structure in an acidic medium. The layers of the material are negatively charged. In aqueous suspension, the water molecules and the exchangeable ions ( $Na^+$  in the case of sodium montmorillonite) penetrate in between the sheets and cause the swelling of the material. On the edges of the particles, the  $H^+$  ions are absorbed, furnishing a pH-dependent charge.

In order to control the species present in the montmorillonite suspensions, it is convenient to substitute the cations in between the layers by those of the added electrolyte, so that all exchangeable ions are of the same kind. In this manner, sodium montmorillonite (NaMt) was obtained from bentonite (Serrata de Níjar, Spain) by a process of homoionization [103], consisting of successively rinsing the clay with a 1 M sodium chloride solution; surplus ions were removed by repeated cycles of centrifugation and redispersion in deionized water. The resulting gel was dried and put aside

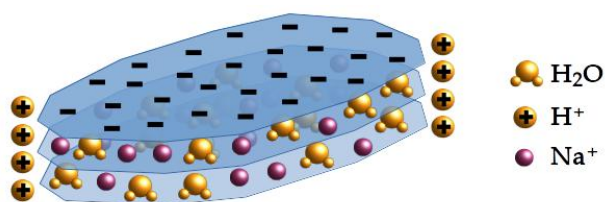


**FIGURE 3.1:** Schematic representation of a sodium montmorillonite particle in an acidic medium.

for sample preparation. The NaMt samples were sonicated for 5 minutes prior to measurements being taken.

The sodium montmorillonite particles were observed by environmental scanning electron microscopy. This technique allows us to maintain a certain level of humidity in the chamber (around 20% in our case), avoiding particle aggregation. As a result, individual NaMt particles can be distinguished. As shown in Figure 3.2, NaMt particles are planar and irregular, and the sample is very polydisperse. The average diameter is  $1.2 \pm 0.3 \mu\text{m}$ , where the error indicates the standard deviation of the distribution by number. These pictures do not allow the determination of the particle thickness. The individual layers are only intuitively appreciated at the broken edges of the particle (Figure 3.2b).

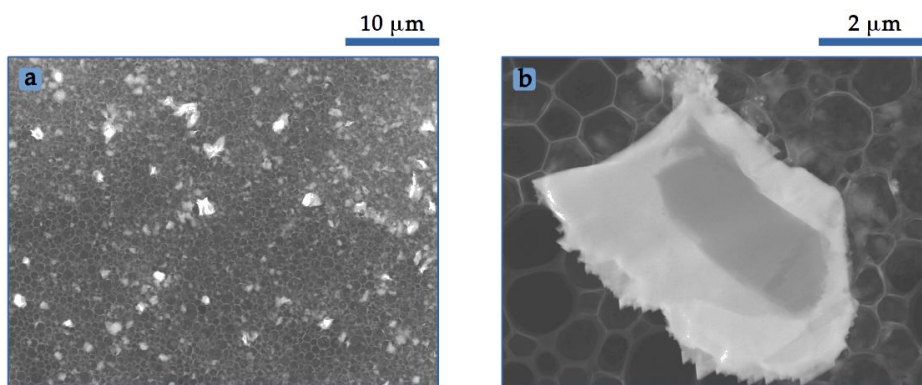


**FIGURE 3.2:** a) Environmental scanning electron microscopy picture of the sodium montmorillonite sample. b) Detail of a single particle.

### 3.2.2. Gold nanorods

The gold nanorods (AuNRs) used in this work were synthesised in the UGR laboratory following the  $\text{Ag}^+$ -mediated seeded growth method [104], in which the anisotropic growth is achieved by a capping layer of cetyltrimethylammonium bromide (CTAB). At the end of the synthesis procedure, the CTAB forms a 3.3 nm compact bilayer that covers the rods completely. Gold nanorods present a very low negative charge, insufficient to achieve stability of the suspensions. Instead, it is the  $\text{CTA}^+$  chains attached to the gold surface which provide a large net positive charge that prevents particle aggregation [? ]. Hence, the CTAB layer is essential for the stability of aqueous suspensions of AuNRs. Figure 3.3 shows a schematic representation of the structure of a CTAB-stabilised gold nanorod. These particles have a zeta potential of 50 mV. When the CTAB is removed by centrifugation, the zeta potential goes to small negative values, and the particles aggregate.

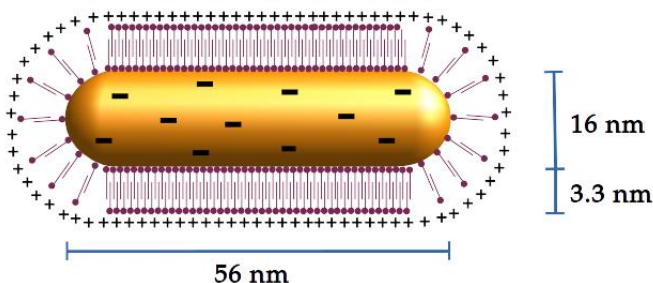


FIGURE 3.3: Schematic representation of a gold nanorod (orange) stabilised by a compact CTAB layer (purple).

To synthesise the gold nanorods, a seed solution and a growth solution were prepared and mixed as follows [105]:

- The seed solution was obtained by adding 25  $\mu\text{L}$  of 50 mM  $\text{HAuCl}_4$  and 300  $\mu\text{L}$  of 10 mM  $\text{NaBH}_4$  to 4.7 mL of a 100 mM CTAB solution.
- For the growth solution, 190  $\mu\text{L}$  of 37%  $\text{HCl}$ , 120  $\mu\text{L}$  of 10 mM  $\text{AgNO}_3$ , 100  $\mu\text{L}$  of 50 mM  $\text{HAuCl}_4$  and 100  $\mu\text{L}$  of 100 mM ascorbic acid were added to 10 mL of a 0.1 M CTAB solution.

- Lastly, 24  $\mu\text{L}$  of the seed solution were added to the growth solution and the mixture was stored overnight at 30°C.

A transmission electron microscope (TEM) picture of the resulting particles is displayed in Figure 3.4, where it can be observed that the sample is quite monodisperse and the shape of the rods is regular. From the measurement of 70 particles, an average length of  $56\pm 9$  nm, a mean diameter of  $16\pm 4$  nm and an average aspect ratio  $3.7\pm 0.8$  were obtained.

Because of their metallic nature and elongated shape, AuNRs display two plasmon resonances, due to the oscillation of electrons along the transverse and longitudinal axes [105]. Thus, AuNR suspensions exhibit beautiful colors, which depend strongly on the rod size and shape. In Figure 3.5, the optical absorption spectrum of a 9.8 mg/L suspension of the synthesised AuNRs is shown. Here, two absorption peaks, corresponding to the two characteristic dimensions of the rods, are clearly observed. The transverse mode is situated at a wavelength of 520 nm, and the longitudinal mode at 850 nm. The resulting suspension color, purplish red, is shown in the same image.

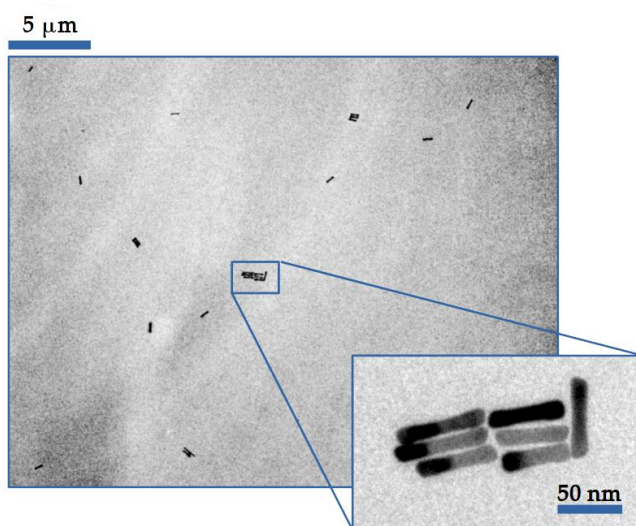
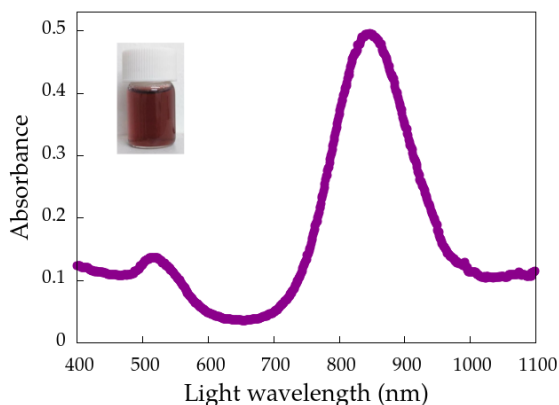


FIGURE 3.4: High-resolution TEM picture of the AuNR sample.



**FIGURE 3.5:** Absorption spectrum of a 9.8 mg/L gold nanorod suspension. The inset shows the color of a 98 mg/L AuNR suspension.

The concentration of the suspension resulting from the synthesis was estimated from the amount of gold precursor. The obtained value, 98 mg/L, yields an extinction coefficient at the longitudinal plasmon peak of  $6.6 \cdot 10^9 \text{ Lmol}^{-1}\text{cm}^{-1}$ , which is in very good agreement to measured values for rods with a similar effective radius,  $4.5\text{-}6.5 \cdot 10^9 \text{ Lmol}^{-1}\text{cm}^{-1}$  [106]. For the experiments that required higher particle concentrations, the solutions were concentrated by two centrifugation cycles (15000 rpm, 5 min) up to 1400 mg/L.

### 3.2.3. Silver Nanowires

The silver nanowires (AgNWs) used in this work were obtained commercially from PlasmaChem, Germany. Figure 3.6 shows TEM pictures of these particles at two different zoom-scales. Here, it can be observed that the particles are highly elongated, and the sample presents significant polydispersity. From the measurement of 480 wires, we determined a mean particle length of  $3.0 \pm 2.3 \mu\text{m}$  and an average diameter of  $121 \pm 17 \text{ nm}$ . Furthermore, in the zoom-in microscope picture, it can be observed that the AgNWs seem to present a coating with a thickness of a few nanometers. The composition of this layer was analysed by X-ray photoelectron spec-

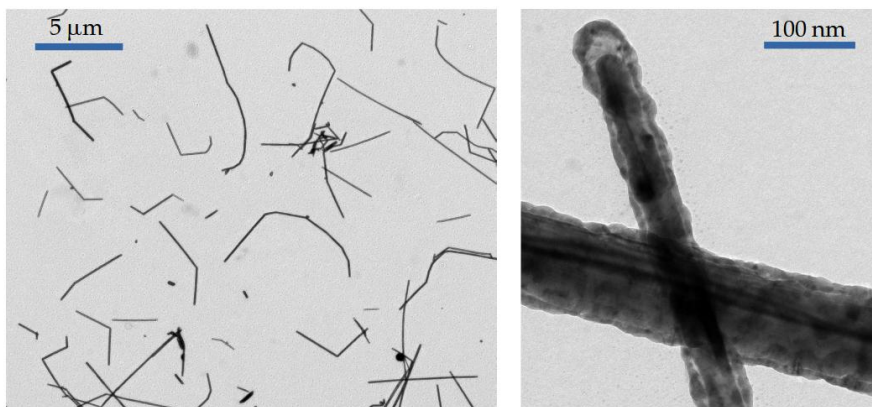


FIGURE 3.6: TEM pictures of the AgNWs at two different zoom scales.

trospectroscopy (XPS), which shows the presence of silver and oxygen. The XPS peaks corresponding to these two elements are shown in Figure 3.7. These results suggest that the particle surface is at least partially oxidised.

As determined by electrophoretic mobility measurements, the silver nanowires present a small negative charge, probably due to the capping agents used in the synthesis reaction. The zeta potential value ranges from -20 to -40 mV, depending on the ion content. The particles could be easily dispersed in water with the help of a sonicator, and the suspensions remained stable for hours. The absorption spectrum of the wires is presented in Figure 3.8, where a peak at around 400 nm is observed. This may be attributed to the transversal surface plasmon resonance of the wires [107].

#### 3.2.4. Carbon Nanotubes

Carbon nanotubes consist of rolled-up graphene sheets, typically with a length in the micro-scale and a diameter of a few nanometers [108]. The orientation of the rolled graphene layers strongly affects the microscopic properties of the tubes, such as electronic transport [109, 110]. In fact, because of the different possible atomic structures, statistically one third of the carbon nanotubes are metallic and two thirds, semiconducting [111]. Figure 3.9a shows a schematic representation of a graphene layer, where

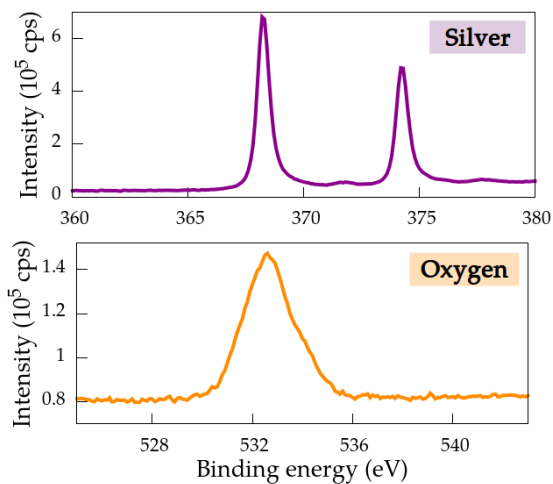


FIGURE 3.7: XPS peaks corresponding to silver and oxygen.

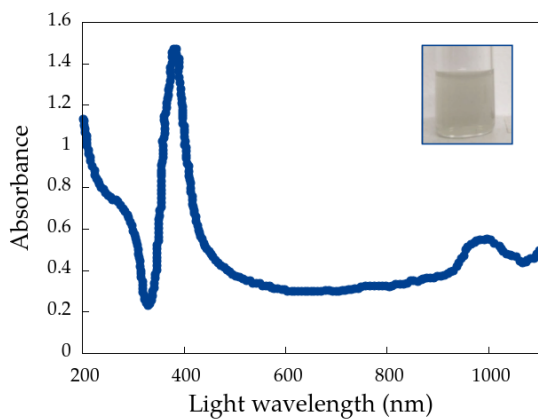
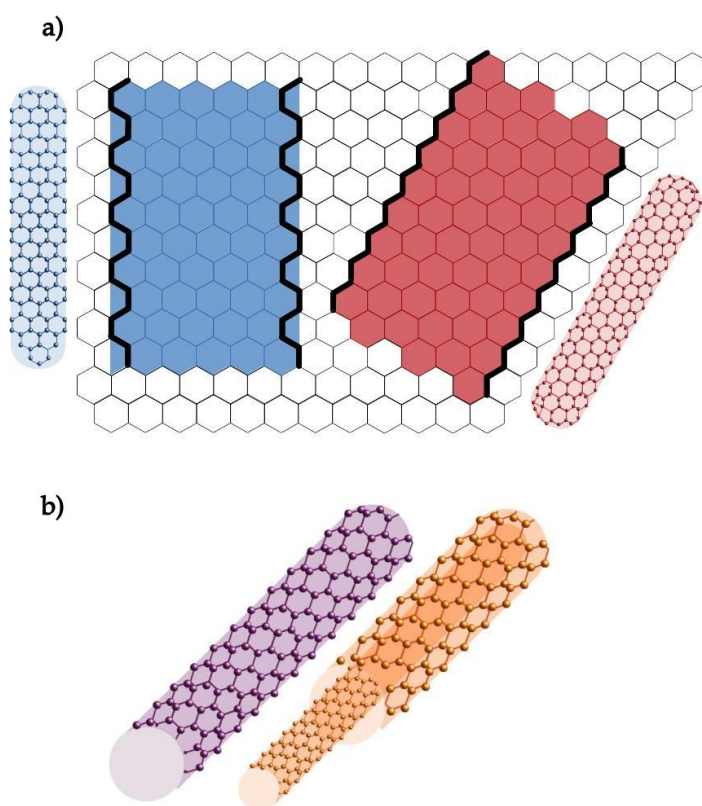


FIGURE 3.8: Absorption spectrum of a 100 mg/L sample of AgNWs in aqueous suspension. The inset is a colour picture of the sample.

two possibilities for the geometry of the carbon nanotubes, one metallic and one semiconducting, are indicated. Moreover, carbon nanotubes can be formed by multiple coaxial graphene layers, which further complicates the analysis of their characteristics. In this work, we use single-walled carbon nanotubes (SWNTs) and double-walled carbon nanotubes (DWNTs), whose simplified structure is shown in Figure 3.9b. For DWNTs, it must be taken into account that all particles with at least one conducting layer,  $5/9$  of the total, are metallic [112].



**FIGURE 3.9:** Schematic representations of carbon nanotubes. a) Two possibilities for the formation of carbon nanotubes from a graphene layer. The black lines indicate the atoms that coincide after the sheet is rolled. The blue and red configurations correspond to a semiconducting and a metallic tube respectively. b) Structure of a metallic SWNT (purple) and DWNT (orange).

The single- and double-walled carbon nanotubes used in the present work, synthesised by the arch-discharge method, were obtained commercially from Carbolex and US Research Nanomaterials respectively. The SWNTs were subjected to a process of soxhletting for 12 hours using toluene, in order to remove amorphous carbon. The resulting sample contains 90% SWNTs and 10% encapsulated catalyst (nickel). The DWNT sample was used with commercial purity, 60%, since the main impurities, single- and multi-walled carbon nanotubes, cannot be removed by this process. In both cases, the particles were dispersed in 1,2-dichloroethane with the help of an ultrasonic probe.

Figures 3.10 and 3.11 display TEM pictures of the SWNT and DWNT samples. Although the manufacturers report a value of the individual tube diameter of 1.4 nm and 1-3 nm, in the microscope image it can be observed that particles are bundled, with a mean bundle width of 12 nm and 9 nm respectively. The average lengths are 500 nm and 600 nm, and the standard deviation is 400 nm in both cases.

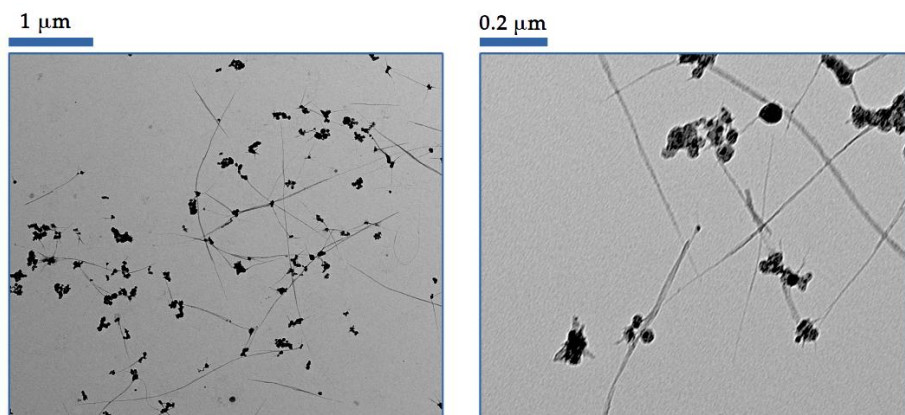


FIGURE 3.10: TEM pictures of the SWNTs.

### 3.2.5. Graphene oxide flakes

Graphene is an allotrope of carbon consisting of a single layer of atoms arranged in a hexagonal lattice [113]. When the sheet is decorated at

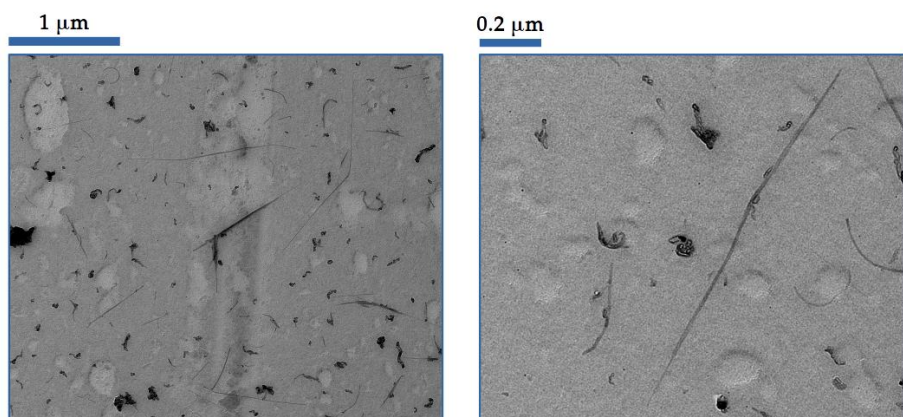
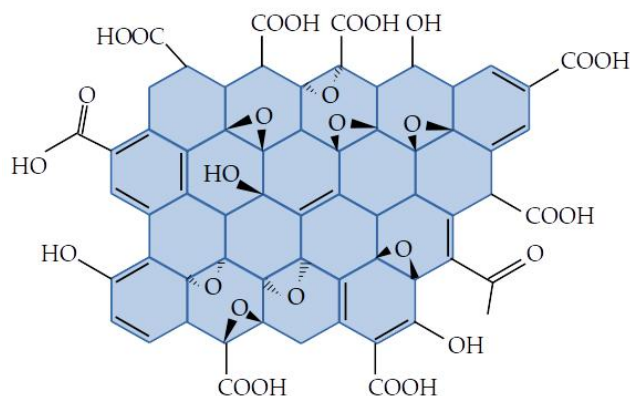


FIGURE 3.11: TEM pictures of the DWNTs.

some degree with oxygen containing groups, mainly hydroxyl and epoxy groups on the surface and carbonyl and carboxyl groups at the edges [114], the material is referred to as graphene oxide (GO). The degree of oxidation strongly affects the properties of the GO flakes, such as electric conductivity, optical absorbance or hydrophobicity [115, 116]. For instance, while graphene is a good conductor, for GO a transition from metallic to semiconducting and insulating behaviour can be observed as oxidation increases [117]. This occurs because of the presence of  $sp^3$  hybridised carbon atoms due to the functional groups, which perturb the pure  $sp^2$  hybridisation of graphene.

The exact atomic structure of GO is still uncertain, and depends on several factors. Furthermore, recently it has been reported that the functional groups are distributed aperiodically, and that typically there are bare graphene areas combined with heavily functionalised regions [118]. In spite of this, a schematic model of a sheet of graphene oxide, showing possible oxygen-containing functionalities, is shown in Figure 3.12.

The graphene oxide flakes used in this work, purchased from Graphe-nea (Spain), were obtained by chemical processing of bulk graphite. According to the manufacturer, the particles are formed by a monolayer in a high percentage (>95%). From a scanning electron microscope image of



**FIGURE 3.12:** Schematic representation of a possible atomic structure of a GO flake.

the flakes, shown in Figure 3.13, a mean major axis length of  $2.5 \pm 2.2 \mu\text{m}$  was obtained. The C:O ratio of the particles was determined by XPS measurements, which provide a value of 2.1. The XPS peaks corresponding to carbon and oxygen are shown in Figure 3.14. Thanks to the functional groups present on the GO surface, the particles could be easily dispersed in water with the help of a sonicator. The GO platelets present a small negative charge, with a zeta potential of around  $-30 \text{ mV}$ .

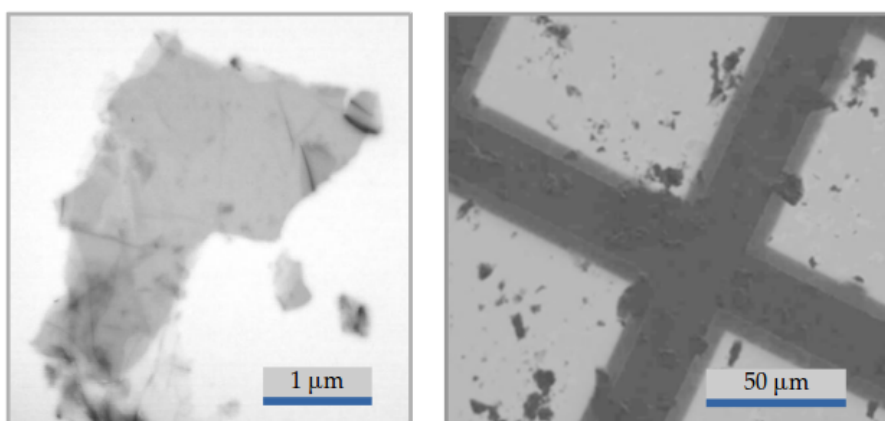


**FIGURE 3.13:** High resolution scanning electron microscopy pictures of the graphene oxide flakes.

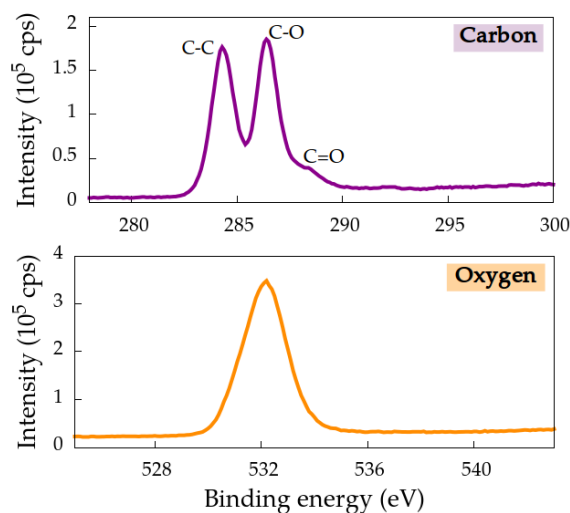


FIGURE 3.14: XPS peaks corresponding to carbon and oxygen.

### 3.2.6. Other particles

An overview of additional materials used in this work is given below. In all cases, the particles could be easily dispersed in water with the help of a sonicator, and the suspensions were stable for hours.

**Goethite needles:** Goethite is the mineral form of iron(III) oxide-hydroxide,  $\alpha\text{-Fe}^{3+}\text{O}(\text{OH})$ . The goethite needles used in this work were purchased from Sigma Aldrich (USA), and observed by TEM (Figure 3.15a). As shown, the particles are irregular and very elongated, and the sample is highly poly-disperse. An average length value of  $410\pm 190$  nm and mean aspect ratio of  $12\pm 6$  were obtained from the measurement of 80 particles.

**PTFE rods:** Polytetrafluoroethylene (PTFE) particles were obtained from Ausimont (Italy), and kindly provided by Drs. Bellini and Mantegazza (University Milano-Bicocca, Italy). Figure 3.15b displays a microscope image of the sample, where the regular rod shape can be appreciated. From the observation of 300 particles, the average length ( $480\pm 100$  nm), diameter ( $240\pm 50$  nm) and aspect ratio ( $2.0\pm 0.5$ ) were obtained.

**Gibbsite platelets:** Gibbsite,  $\text{Al}(\text{OH})_3$ , is one of the mineral forms of alu-

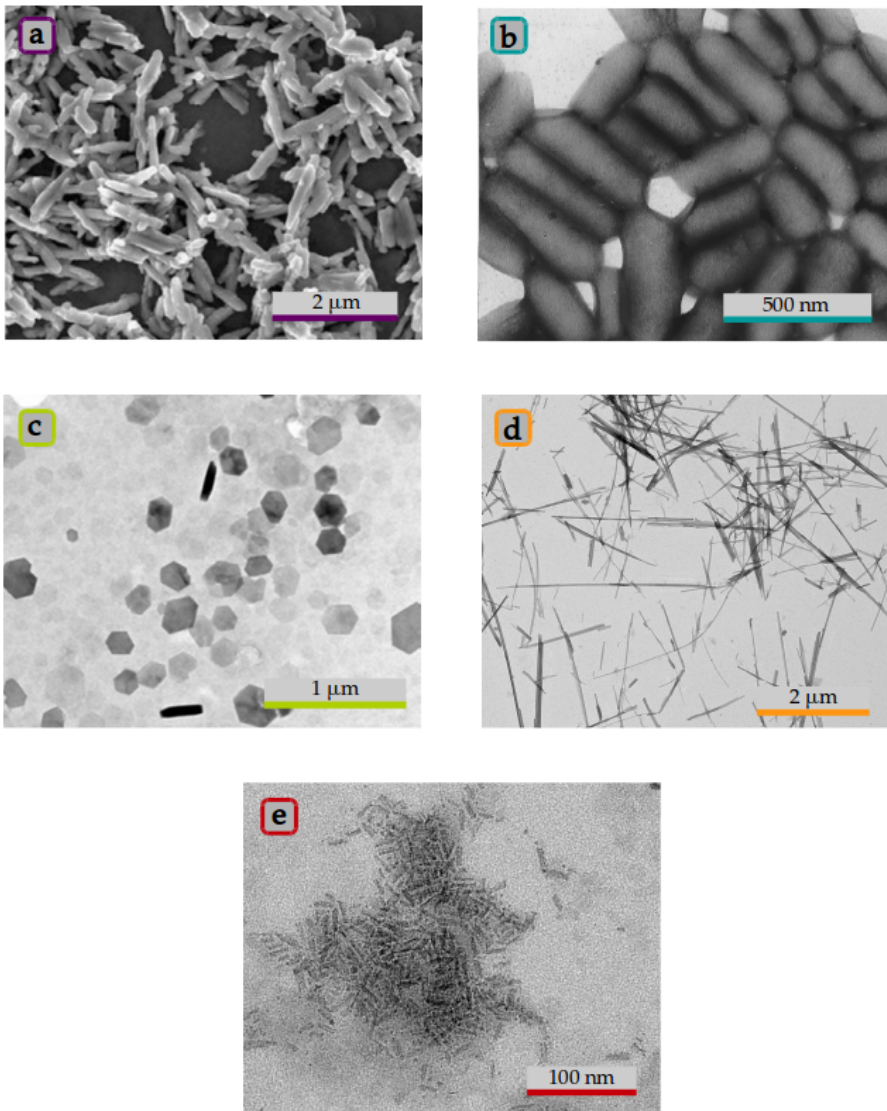


**FIGURE 3.15:** TEM pictures of a) goethite needles, b) PTFE rods, c) gibbsite platelets, d) sepiolite particles and e) laponite nanodisks.

minium hydroxide. The gibbsite platelets used in this work, synthesised by the procedure detailed in [119], were kindly provided by Drs. Bellini

and Mantegazza. As observed in the microscope picture (Figure 3.15c), the particles are planar, with a quite regular hexagonal shape. From 140 particles, a volume-averaged length of  $250\pm 60$  nm was obtained. Gibbsite platelets are very slim, with a reported aspect ratio of 13 [50].

**Sepiolite needles:** Elongated particles of sepiolite, a clay mineral, were purchased from Sigma Aldrich and used for comparison measurements. In the TEM picture shown in Figure 3.15d, it can be observed that the particles are needle-shaped, and the sample is extremely polydisperse. The average length is  $600\pm 500$  nm.

**Laponite nanodisks:** Laponite<sup>®</sup>-RD nanodisks were obtained from BYK (Germany) and used for supplementary measurements. A TEM picture of these synthetic clay particles, provided by Dr. Ramos (University of Jaén, Spain), is shown in Figure 3.15e. Although particle distinction is not straight-forward because of their very small size, it can be appreciated that the sample is very monodisperse, with a particle size in the nanoscale.

**LUDOX spheres:** LUDOX<sup>®</sup> AS-30 colloidal silica particles were purchased from Sigma-Aldrich. The particles are spherical and negatively charged, and have a diameter of 30 nm. The sample can be considered monodisperse.

## 3.3. Methods

### 3.3.1. Electro-optical determinations

Electric birefringence and linear dichroism measurements were performed with a home-made device based on the measurement of the change in light transmission through an optical setup containing the samples, when these are subjected to external electric fields. The optical setup is different for EB and LD measurements, but the main characteristics of the experiments are similar in both cases. The samples are placed in a quartz cell (Starna Scientific, UK) of 1 cm path length, shown in Figure 3.16. In general, plastics, especially when they are subjected to the stress necessary to build the cell, are birefringent, what would introduce a parasitic contribution in the measurements. For this reason, quartz was chosen as a suitable material to

minimise the stress birefringence. The cell was thermostated at 15°C using a water circuit. The samples are subjected to an external uniform electric field via vertical planar stainless steel electrodes with a 1 mm separation (Figure 3.16) immersed in it.

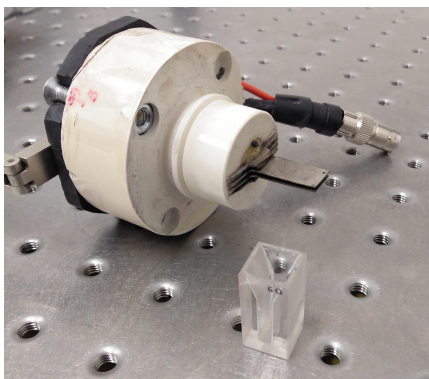


**FIGURE 3.16:** Detail of the electrodes and quartz cell used in the experiments.

Sinusoidal electric field pulses in a frequency range of 10 Hz-50 MHz are sent to the electrodes from a commercial generator (Tektronix AFG 3101, USA). When needed, low frequency (Piezo Systems Inc. EPA-104, USA) and high frequency (AR Modular RF KMA2020, USA) amplifiers are used. The application of the field in the form of pulses instead of a continuous signal serves a double purpose: It prevents the overheating of the sample and allows the observation of the dynamic response of the system. The pulse duration is adjusted for each sample, and varies from some milliseconds to several seconds. High-quality HP wires were used, which present a good behaviour in the wide spectral and field strength ranges used in this work. A He-Ne laser beam (Laser Products 05-LHP-151, USA) traverses the optical setups for the determination of EB and LD, which include the sample. All the optical plates were purchased from Edmund Optics, UK. The transmitted intensity is collected by a photodiode (Edmund Optics, UK) connected to a digital oscilloscope (Tektronix TDS 2012C, USA). The data acquisition and analysis are computer controlled. Figure 3.17 shows a complete picture of the experimental setup, where the mentioned elements can be distinguished.

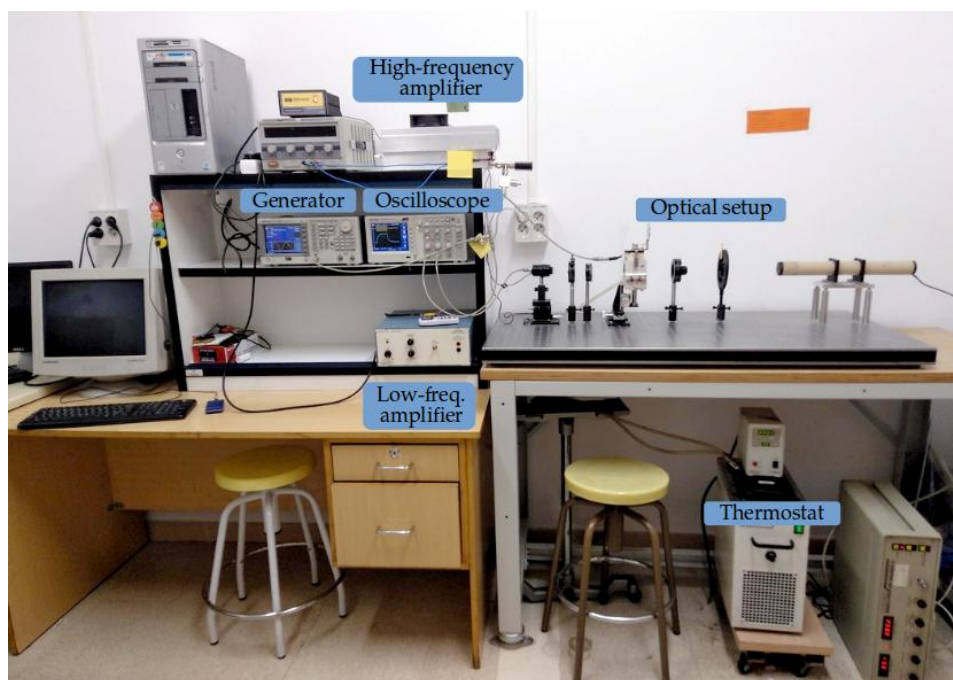


FIGURE 3.17: Picture of the experimental setup for electro-optical measurements. The main elements are indicated on the image.

In the QMLU laboratory, a similar device for the determination of LD and EB was used. In this case, the samples were placed in a 3 cm long Teflon cell with glass walls. The electrodes have a separation of 2 mm. The room temperature was kept at  $20 \pm 0.2^\circ\text{C}$ . The electric field was supplied by a function generator (Thurlby Thandor Instruments model TG5011, UK) in a frequency range of 100 Hz-10 kHz, and was amplified using a commercial voltage amplifier (Trek 609E-6, USA). The silicon junction photodiode and all the optical plates were purchased from Thorlabs, USA.

### Linear dichroism

The linear dichroism measurements are based on the changes in light transmission caused by the orientation of the particles due to their higher absorbance along the major axis. The optical setup consists of *i*) a polar-

izer parallel to the electric field and *ii*) the suspension. Figure 3.18 shows a schematic representation of this setup and a picture of the ensemble.

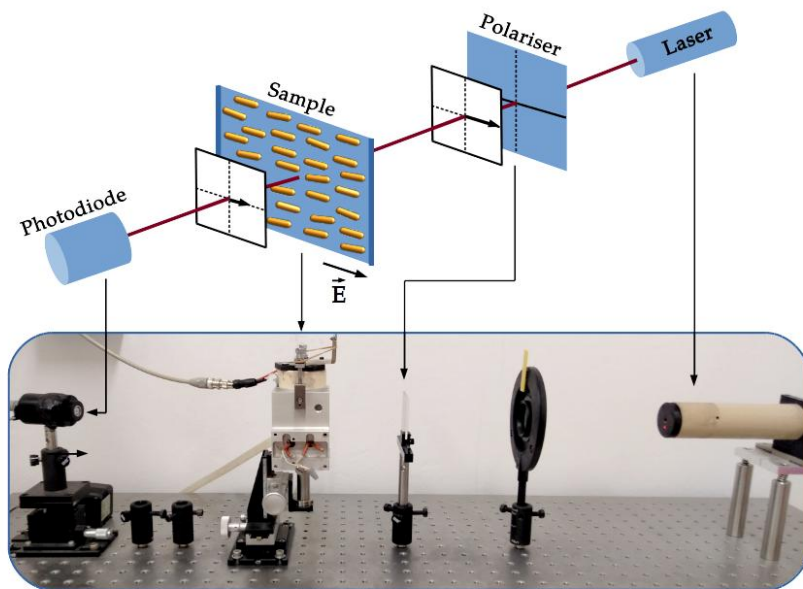


**FIGURE 3.18:** Optical setup for the determination of linear dichroism. The elements of the schematic representation can be identified in the picture.

In the case of elongated particles, the normal orientation is with the symmetry axis along the direction of the field, and therefore parallel to the light polarization. In this case, the light intensity  $I(t)$  transmitted by this setup is related to the parallel dichroism of the sample as  $\Delta A_{\parallel} = \log_{10} I_0/I(t)$ , where  $I_0$  is the light intensity transmitted when no electric field is applied to the suspension. Taking into account Equation 2.67, the total dichroism can be obtained via the equation [89]

$$\Delta A = \frac{3}{2} \log_{10} \frac{I_0}{I(t)} \quad (3.1)$$

On the other hand, oblate particles align with their symmetry axis perpendicular to the electric field, and hence to the polarization plane of the incident light. Thus,  $\Delta A_{\perp} = \log_{10} I_0/I(t)$  and:

$$\Delta A = -3 \log_{10} \frac{I_0}{I(t)} \quad (3.2)$$

### Electric birefringence

When a linearly polarised light beam travels through a suspension of particles oriented with an external electric field, a retardation  $\delta$  appears between the components parallel and perpendicular to the orientation axis, due to the different speeds of propagation in these directions [43]. Hence, the light beam exits the system elliptically polarised. The resulting retardation is directly related to the birefringence of the medium as:

$$\delta = \frac{2\pi l}{\lambda_0} \Delta n \quad (3.3)$$

where  $l$  is the path length. The optical setup for the measurement of EB is based on this effect. It consists of *i*) a polarizer at  $45^\circ$  to the electric field, *ii*) the suspension, *iii*) a quarter-wave plate whose fast axis is placed parallel to the polarizer axis and *iv*) an analyser at  $90^\circ - \alpha$  to the initial polarization. The angle  $\alpha$  is small, normally with a value of  $\pm 3^\circ$ . Figure 3.19 shows a schematic representation of this setup and a picture of the ensemble.

Because of the complexity of this optical system, the calculations of the transmitted intensity were carried out by Jones calculus, modelling the birefringent sample as an element which introduces a retardation  $\delta$ . A complete description of the calculations can be found in Reference [120]. Taking into account Equation 3.3, the birefringence of the sample can be obtained as

$$\Delta n(t) = \frac{\lambda}{\pi l} \left[ \arcsin \left( \sqrt{\frac{I(t)}{I_0}} \sin \alpha \right) - \alpha \right] \quad (3.4)$$

This setup for the experimental determination of EB presents several advantages over other options. In the first place, the choice of a configuration with non-crossed polarisers allows to minimise the effect of light transmission through crossed non-ideal polarisers. Moreover, the measurements are based on the ratio  $I/I_0$ , which is convenient, since the photodiode gives

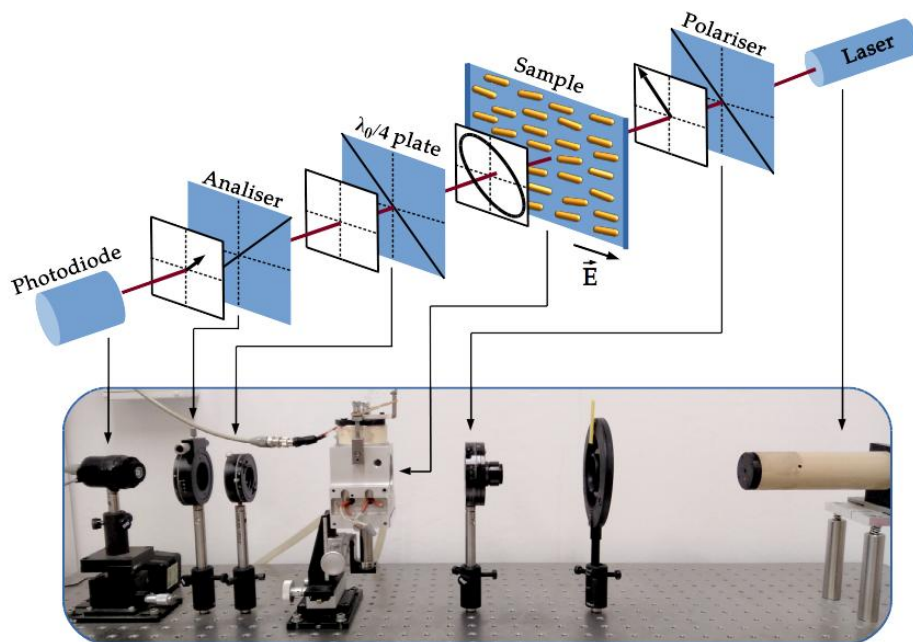


FIGURE 3.19: Optical setup for the determination of electric birefringence. The elements of the schematic representation can be identified in the picture.

a signal proportional to  $I$ , but not its actual value. In addition, this configuration allows the determination of the sign of the birefringence, unlike others which do not include a quarter-wave plate. This setup also enables the correction of the stress birefringence introduced by the cell, provided that it is sufficiently small, by a simple procedure described in detail in Reference [120]: When assembling the optical setup, in the first place,  $\alpha$  is set to zero and the analyser is slightly rotated until the minimum transmitted intensity is found. After this,  $\alpha$  is set to its final value. With this protocol, the stress birefringence is counteracted.

OJO: Dice Angel que explique por que el fotodiodo no da la intensidad, pero no se a que se refiere.

Furthermore, linear dichroism can also affect the experimental determination of electric birefringence. Thus, when light polarised at  $45^\circ$  to the orientation of the particles traverses the sample, not only a retardation ap-

pears between the two components, but also does a difference in the absorption between the two main directions occur, affecting the transmitted intensity. If the absorption of the particles is significant, this effect can alter the birefringence measurements. Our experimental setup enables the correction of such effect, given that LD is previously measured. For this purpose, Equation 3.4 must be modified in the following manner [89, 121]:

$$\Delta n(t) = \frac{\lambda}{\pi L} \left( \arcsin \left( \sqrt{\frac{\frac{I(t)}{I_0} \sin^2 \alpha - \zeta(\Delta A)}{\Omega(\Delta A)}} \right) - \alpha \right) \quad (3.5)$$

$$\zeta(\Delta A) = 1/4 \cdot 10^{-2\Delta A/3} + 1/4 \cdot 10^{\Delta A/3} - 1/2 \cdot 10^{-\Delta A/6}$$

$$\Omega(\Delta A) = 10^{-\Delta A/6}$$



# 4

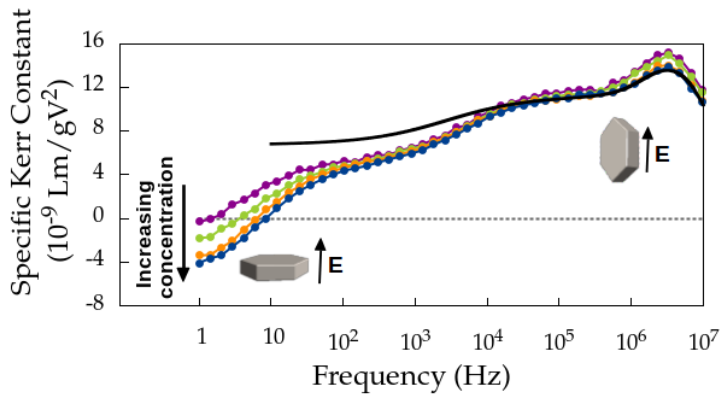
## ELECTRIC BIREFRINGENCE SPECTROSCOPY OF MONTMORILLONITE PARTICLES



## Electric Birefringence Spectroscopy of Montmorillonite Particles

P. Arenas-Guerrero, G. R. Iglesias, A. V. Delgado, M. L. Jiménez (2016). *Soft matter*, 12(22), 4923-4931.

Electric birefringence (EB) of suspensions of anisotropic particles can be considered an electrokinetic phenomenon in a wide sense, as both liquid motions and polarization of the electrical double layer (EDL) of the particles participate in the process of particle orientation under the applied field. The EB spectrum can be exploited for obtaining information on the dimensions, average value and anisotropy of the surface conductivity of the particles, and concentration and Maxwell-Wagner polarization of the EDLs. It is thus a highly informative technique, applicable to non-spherical particles. In this paper, we investigate the birefringent response of plate-like montmorillonite particles as a function of the frequency and amplitude of the applied AC electric field, for different compositions (pH, ionic strength, particle concentration) of the suspensions. The transient electric birefringence (i.e., the decay of the refractive index anisotropy with time when the field is switched off) is used for estimating the average dimensions of the particle axes, by modeling it as an oblate spheroid. The obtained values are very similar to those deduced from electron microscopy determinations. The frequency spectra show a very distinct behaviour at low (on the order of a few Hz) and high (up to several MHz) frequencies: the  $\alpha$  and Maxwell-Wagner-O'Konski relaxations, characteristic of EDLs, are detected at frequencies above 10 kHz, and they can be well explained using electrokinetic models for the polarization of EDLs. At low frequencies, in contrast, the birefringence changes to negative, an anomalous response meaning that the particles tend to orient with their symmetry axis parallel to the field. This anomaly is weaker at basic pHs, high ionic strengths and low concentrations. The results can be explained by considering the polydispersity of real samples: the fastest particles redistribute around the slowest ones, inducing a hydrodynamic torque opposite to that of the field, in close similarity with results previously described for mixtures of anisometric particles with small amounts of spherical nanoparticles.



## 4.1. Introduction

The optical properties of suspensions of non-spherical colloidal particles can be modified by the application of an electric field [42, 49, 88]. One of these electro-optical effects is the electric birefringence (EB), that is, the anisotropy of the refractive index of the suspension caused by the electrically induced orientation of the particles. The analysis of EB has been proposed as a suitable technique for the characterization of non-spherical particles [1, 42, 43, 49, 88, 122], as it is susceptible to provide much useful information not only about the optical, electrical and geometrical properties of the particles in suspension but also about the electrokinetic phenomena taking place at their interfaces. For instance, Transient Electric Birefringence (TEB), the study of the dynamic response of the system, is utilized to examine the size distribution of the particles in the sample [45, 48–50, 87]. Electric Birefringence Spectroscopy (EBS), the analysis of the behaviour of the birefringence as a function of the frequency of the applied field, albeit yet incomplete, can provide exhaustive information about the different polarization mechanisms of the nanoparticles and their electric double layers (EDLs) [1, 25, 26, 49, 122, 123].

However, although the foundations of the electric birefringence have been long-established, the process is hitherto not understood on the whole and cannot yet be considered as a widespread characterization technique [26, 80, 124, 125]. Thus, microscopic models relating the nanoparticle properties to their macroscopic birefringent response are to date not completely satisfactory [1, 25, 26, 45]. For instance, only simplified geometries are considered; the effect of the polydispersity of the sample and the presence of interparticle interactions are taken into account partially if at all; the effect of the hydrodynamic torque is normally neglected [25] and the contribution of a heterogeneous charge distribution is still an open question [25, 55, 126]. Consequently, further research of the topic is needed, not only from an applied point of view, but also at a fundamental level.

Similar to other laminar materials, sodium montmorillonite (NaMt) is a good candidate for the analysis of EB, since these clay particles are known to possess a non-homogeneous and pH-dependent charge [97, 103, 127,

128]. Moreover, it has been found that suspensions of sodium montmorillonite and other similar clays exhibit a negative (anomalous) birefringence [84, 124, 129], sparking interest in the phenomenon. The mentioned anomaly consists in the tendency of the particles to orient under some conditions with their major axis perpendicular to the external field, instead of parallel, as in "normal" EB. In dilute suspensions, negative birefringence has been recently reported for a variety of materials [50, 80, 125, 130, 131], and in most cases it cannot be explained theoretically inside a classical framework.

With this motivation, in this article we will focus our attention on the study of the birefringence phenomenology of sodium montmorillonite suspensions. Firstly, TEB experiments are performed together with electron microscopy determinations in order to estimate the size distribution of the sample. Thereupon, an extensive examination of the spectral response of this material is carried out in order to study the electrical properties of the particles and the origin of the anomalous response.

## 4.2. Theory

### 4.2.1. Electro-orientation of non-spherical particles.

When an electric field  $E$  is applied to a colloidal suspension, an electric dipole is induced on the particles [52, 66, 67]. If these are not spherical, their electric polarizability is anisotropic [25, 70, 122, 123], and for axially symmetric particles, this anisotropy can be expressed by the scalar quantity  $\Delta\alpha^e = \alpha_b^e - \alpha_a^e$ , being  $\alpha_b^e$  ( $\alpha_a^e$ ) the electric polarizability along their major (minor) axis,  $b$  and  $a$ , respectively. In general, this quantity is different from zero, and hence, the total dipole moment induced by an applied field is not parallel to the latter. As a consequence, it appears an electric torque that tends to orient the particle with its major axis parallel to the external field.

In addition, most non-spherical nanoparticles exhibit anisotropic optical polarizability  $\Delta\alpha^o = \alpha_b^o - \alpha_a^o$ , due to their shape and/or their anisotropic crystal structure. Normally, when the particles are suspended in an elec-

trolyte solution, their orientation is random and the system is optically isotropic on a macroscopic scale. However, upon application of an external electric field, particles orient, giving rise to an anisotropy in the refractive index of the suspension known as birefringence and given by [42]

$$\Delta n = \frac{\Delta\alpha^o\phi\langle P_2(\cos\theta)\rangle}{2n_s\epsilon_0V_p} \quad (4.1)$$

where  $\phi$  is the volume fraction of dispersed particles,  $n_s$  the refractive index of the suspending solution,  $\epsilon_0$  the vacuum permittivity and  $V_p$  the particle volume.  $\langle P_2(\cos\theta)\rangle$  is the average value of the second Legendre polynomial of the orientational distribution, which is a measure of the degree of alignment of the particles with the external electric field.

In this contribution we restrict ourselves to diluted suspensions of particles with no intrinsic dipole moment and we work in the low field range, where expansions in power series of  $E$  are usable. In these conditions, and neglecting the viscous forces (which is a good approximation for high frequency fields [26]) an explicit expression of  $\Delta n$  is available [122]

$$\Delta n = \frac{\Delta\alpha^o\Delta\alpha^e\phi E_0^2}{30n_s k_B T V_p} \quad (4.2)$$

Here  $k_B$  is the Boltzmann constant,  $T$  the temperature and  $E_0$  the field amplitude. The quadratic dependence of the birefringence on  $E_0$  is known as Kerr's law and allows us to define the Kerr constant, a magnitude independent of the field strength, as

$$K = \frac{\Delta n}{\lambda E_0^2} \quad (4.3)$$

where  $\lambda$  is the wavelength of the incident light beam.

#### 4.2.2. Transient Electric Birefringence (TEB).

Upon removal of the external electric field, rotational diffusion due to thermal agitation will randomize the orientation of the nanoparticles in a finite time. The subsequent decay of the birefringence is expected to

be in the form of a simple exponential for monodisperse samples; for the more realistic case of polydisperse samples, however, the relaxation of the birefringence must be computed as a superposition of independent exponential processes. In this manner, under reasonable assumptions, it can be shown that  $\Delta n(t)$  presents the shape of a stretched exponential function [45]

$$\Delta n(t) = \Delta n_0 \exp [-(t/\tau)^\alpha] \quad (4.4)$$

where  $\tau$  is a characteristic decay time and  $\alpha$  a polydispersity factor. These two parameters provide an average rotational diffusion coefficient  $\Theta$  for the particles in suspension by the relation [45]

$$\Theta = \frac{\alpha}{6\tau\Gamma(1/\alpha)} \quad (4.5)$$

where  $\Gamma$  is the Euler gamma function.

This coefficient depends on the third power of the particle size, and therefore its measurement can provide a good estimation of the size distribution of the sample. The diffusion coefficient is related solely to the particle's size and shape, and analytical expressions are available for simple geometries. In this work we have modelled our particles as oblate ellipsoids of major axis  $b$  and aspect ratio  $\rho = b/a$ . In this case,  $\Theta$  can be written as [132]

$$\Theta = \frac{3k_B T}{16\pi\eta a^3} \left[ \frac{(2 - \rho^2)(1 - \rho^2)^{-1/2} \arctan(\sqrt{\rho^2 - 1}) - 1}{1 - \rho^4} \right] \quad (4.6)$$

being  $\eta$  the viscosity of the suspending medium. Making use of eqns (4.5) and (4.6), an estimation of the average particle size can be calculated from TEB measurements.

### 4.2.3. Electric Birefringence Spectroscopy (EBS).

When the electric field applied to the suspension is alternating,  $\Delta n$  can be separated into two spectral components: a time-independent DC component or steady-state birefringence and an AC component oscillating with twice the frequency  $\nu$  of the field

$$\Delta n = \Delta n_{DC}(\nu) + \Delta n_{AC}(\nu) \sin(4\pi\nu t) \quad (4.7)$$

The spectral behaviour of  $\Delta n_{DC}$  and of  $\Delta n_{AC}$  furnish information about different properties of the particles in the suspension. On the one hand, the amplitude of the AC oscillations decreases with  $\nu$ , becoming negligible at a certain value of the frequency of the applied field. Such value gives an idea of the characteristic time at which the particles can no longer follow the field oscillations, and therefore provides an estimation of the particle size.

On the other hand, the spectral behaviour of the DC term is related to the relaxations of the particle's dipole, and hence a thorough analysis of the  $\Delta n_{DC}$  spectrum is very useful for the characterization of the electrical properties of the nanoparticles in suspension. Because the AC component averages to zero over time, the DC Kerr constant can be defined as

$$K(\nu) = \frac{2\langle\Delta n(\nu)\rangle}{\lambda E_0^2} \quad (4.8)$$

Normally, two relaxations can be observed in the DC birefringence spectrum of colloidal suspensions, namely, the  $\alpha$  and the Maxwell-Wagner-O'Konski (MWO) relaxations. The  $\alpha$  relaxation is related to the concentration polarization, which is in turn produced by the different transport numbers of coions and counterions in the double layer [67]. The characteristic frequency for the  $\alpha$  relaxation can be estimated as  $\nu_\alpha \sim D/R^2$ , being  $D$  the diffusion coefficient of the ions in solution and  $R$  the characteristic diffusion length, of the order of the particle size. If the frequency of the field is larger than  $\nu_\alpha$  the concentration polarization mechanism cannot be established and therefore can no longer contribute to the formation of the electric dipole. In this case, the dipole is determined by the MWO polarization mechanism. For spherical and insulating particles, it has been demonstrated [66] that MWO electric polarizability is the same as that of a conductive particle with an effective conductivity of  $K^{\text{eff}} = 2K^\sigma/R$ , being  $K^\sigma$  the surface conductivity. This is normally the case of colloidal particles, where the excess of conduction in the EDL can be simulated as a surface conductivity. If particles are not spherical, the effective conduc-

tivity is different for the two axes,  $K_{b,a}$  [25], being the relation between them a geometrical factor in the case of homogeneous charge. For the case of non-homogeneously charged particles this relation is not geometrically determined [49]. This polarization relaxes at a characteristic frequency,  $\nu_{MWO}$ , determined by the particle and medium conductivities and permittivities [66]. When  $\nu > \nu_{MWO}$ , the free charges in the EDL of the particle cannot successfully redistribute anymore and only the molecular polarization contributes to the dipole formation.

### 4.3. Materials and Methods

#### 4.3.1. Materials

NaMt was obtained from bentonite (Serrata de Níjar, Spain) by a process of homoionization [103] consisting in successive rinses of the clay with a 1 M sodium chloride solution; surplus ions were removed by repeated cycles of centrifugation and redispersion in deionized water (Milli-Q Academic, Millipore, France). The resulting NaMt gel was dried and put aside for sample preparation.

Sodium montmorillonite is a laminar clay with negative charge on the faces and a pH dependent charge on the edges [97, 103], whose isoelectric point is located at pH 7, a value close to the natural pH of the NaMt suspensions (6.8). The average dimensions of the particles were firstly determined by environmental scanning electron microscopy (ESEM, FEI Quanta 250 SEM, The Netherlands). This technique allows us to maintain a certain level of humidity (around 20 % in our case) in the chamber, avoiding particle aggregation. As a result, individual particles can be distinguished, as shown in Fig. 4.1a. From this image, the histogram in Fig. 4.1b is obtained and the average length (by volume) of the major axis of the particles is estimated as  $1.7 \pm 0.6 \mu\text{m}$ . In addition, in Fig. 4.1a we can see that the particles are planar, and hence, we can approximate their shape by oblate spheroids.

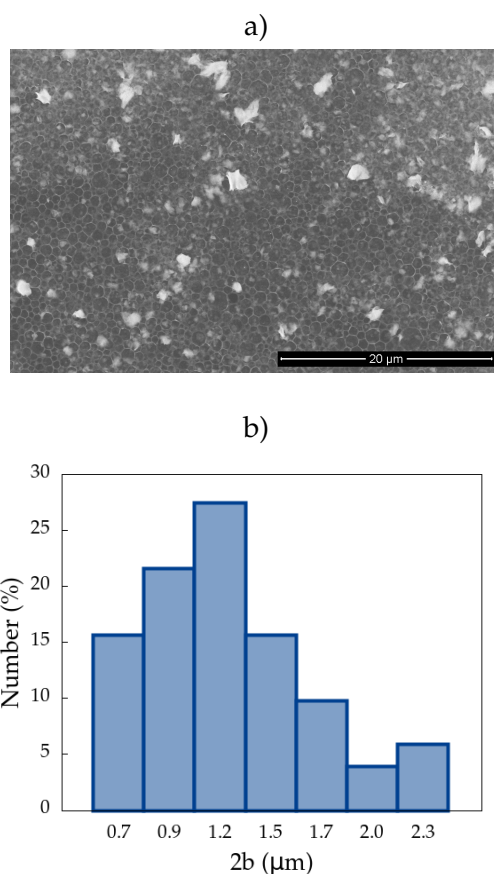


**FIGURE 4.1:** Geometrical characterization of the clay particles. a) ESEM picture of a NaMt sample; b) histogram of the largest axis lengths obtained from a).

### 4.3.2. Methods

The electric birefringence of the suspensions is obtained via the analysis of the polarization of light after passing through the samples [43, 133]. In the experimental setup, a He-Ne laser beam traverses *i)* a polarizer at  $45^\circ$  to the electric field, *ii)* the suspension, *iii)* a quarter-wave plate whose fast axis is placed parallel to the polarizer axis and *iv)* an analyser at  $90^\circ - \alpha$  to the initial polarization. All the optical elements were purchased from Edmund Optics, UK.

The sample is placed in an optically neutral quartz cell of 1 cm path length

(Starna Scientific, UK), thermostated at  $15.0 \pm 0.2^\circ\text{C}$ , and subjected to an external uniform electric field via vertical planar stainless steel electrodes immersed in it and separated 1 mm. Sinusoidal electric field pulses (duration of 5 s) in a frequency range of 1 Hz-10 MHz are sent to the electrodes from a commercial generator (Tektronix AFG 3101, USA). The light intensity transmitted through the optical setup is collected by a photodiode (Edmund Optics T59-142, UK) connected to a digital oscilloscope (Tektronix TDS 2012C, USA). The data acquisition and analysis are computer controlled. The light intensity  $I$  reaching the photodiode at time  $t$  is directly related to the birefringence of the sample,  $\Delta n(t)$ , by [120]

$$\Delta n(t) = \frac{\lambda}{\pi l} \left[ \arcsin \left( \sqrt{\frac{I(t)}{I_0}} \sin \alpha \right) - \alpha \right] \quad (4.9)$$

where  $I_0$  is the intensity transmitted by the setup when no electric field is applied and  $l$  is the path length. In order to determine the steady-state birefringence, the plateau region of 1 or 2 pulses is averaged over time. The stress birefringence introduced by the cell is subtracted as indicated elsewhere [120].

## 4.4. Results and Discussion

### 4.4.1. General features

In Fig. 4.2 the birefringent response of a sample of NaMt subjected to electric field pulses is shown. As can be observed, the shape of the transient behavior of the DC component is independent of the frequency of the applied field. Systematic measurements do not show any dependence on the particle concentration, ionic strength, pH of the sample, field strength, and pulse duration. On the other hand, the AC oscillations can only be observed for the 1 Hz data, being negligible for other presented frequencies. This can be seen in a more detailed way in Fig. 4.3a, where the amplitude of the AC oscillations as a function of the frequency of the applied field is presented. The oscillations decay strongly with  $\nu$ , becoming negligible at a frequency of about 100 Hz. This behavior indicates that for times shorter

than 0.01 s the particles are not able to follow the field oscillations, which is expected for micron-sized particles.

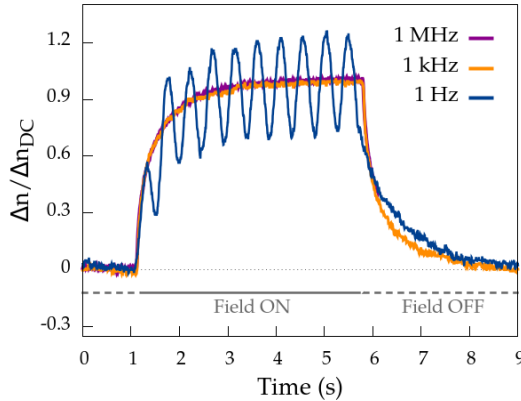


**FIGURE 4.2:** Birefringent response (relative to the stationary DC value) of EB measurements of a sample of NaMt 1 g/L and 0.3 mM NaCl when subjected to field pulses of different frequencies, 5 seconds of duration and a field amplitude of 10 V/mm .

A more precise estimation of the particle's size can be achieved from TEB measurements. In Fig. 4.3b, the obtained decay of the birefringence after the field is turned off is presented together with a fit of the data via a stretched exponential function (eq 4.4). From the obtained values of  $\tau$  and  $\alpha$  ( $374 \pm 2$  ms and  $0.593 \pm 0.002$ , respectively), making use of eqns (4.5) and (4.6), and assuming  $\rho = 3$ , we obtain a diameter of  $1.9 \mu\text{m}$  for these particles. This value is very similar to the one obtained via ESEM pictures, differing from it by no more than 20%, a deviation comparable to that found for other planar particles [50]. These results show that, even though our sample is polydisperse, this method is adequate for the estimation of the particle size.

In our experiments, Kerr's law is satisfied in every case for  $E_0 < 11$  V/mm. At larger fields, deviation from this law due to saturation of the birefringence is observed, in agreement with the data reported elsewhere [128] where it was found that linearity with  $E_0^2$  is lost above 20 V/mm for similar clays. Hereafter all experiments are performed with an electric field of 10 V/mm and hence, the Kerr constant can be properly used.

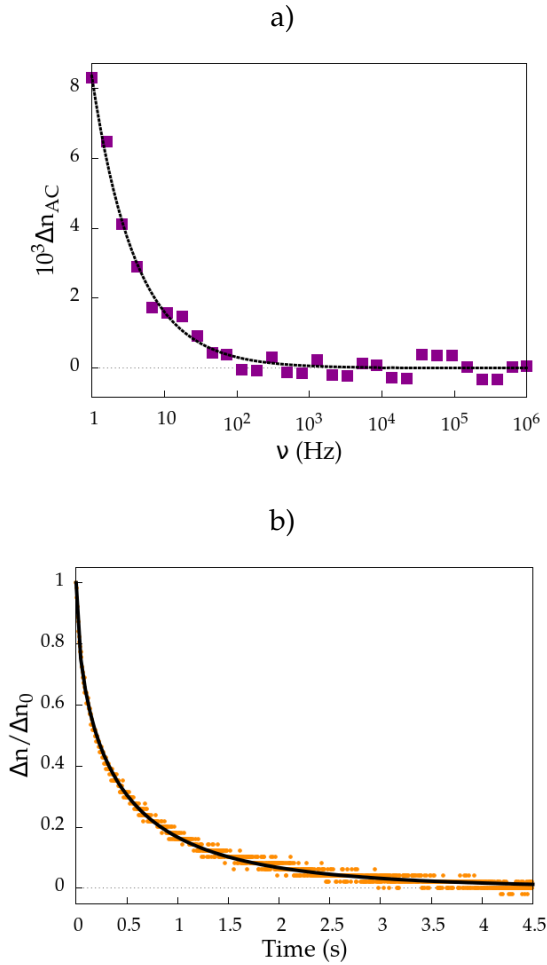


**FIGURE 4.3:** EB measurements of a sample of NaMt 1 g/L and 0.3 mM NaCl; the field amplitude is 10 V/mm. a) Spectrum of the AC component of the birefringence. The dashed line is a guide to the eye. b) Birefringent response (relative to the stationary DC value) of the sample when subjected to field pulses of different frequencies and 5 seconds of duration.

Fig. 4.4a shows a typical birefringence spectrum of NaMt. The spectrum exhibits a complex structure with different dispersion processes occurring at all explored frequencies. As already pointed, if only the electric torque promoted by the external field is taken into account, the Kerr constant is proportional to the polarizability anisotropy (see ec. 4.2), and hence, the

dispersion in Fig. 4.4a is a manifestation of the different electrokinetic phenomena that contribute to the induced polarization. The electrokinetic expectations are depicted in Fig. 4.4b for oblate spheroids with a radius of 800 nm and an aspect ratio of 3, suspended in 0.3 mM NaCl solution. In these and subsequent calculations, the models used are those in [25, 122]. Two cases are presented: particles that exhibit a homogeneous charge distribution (for which  $K_a/K_b = 0.27$ ), and particles presenting a strong charge anisotropy ( $K_a/K_b = 0.008$ ). The observed spectra can be understood considering the frequency dependences of the mechanisms responsible for the polarization along the minor ( $\alpha_a^e$ ) and major ( $\alpha_b^e$ ) axes of the particle. Both polarizabilities increase in the kHz range at similar frequencies, but the rise is more significant for  $\alpha_b^e$  due to the larger characteristic size in this direction, and the balance between  $\alpha_a^e$  and  $\alpha_b^e$  produces an increase in  $\Delta\alpha_e$ . The increase in polarizabilities is associated to the disappearance of concentration polarization (ions cannot move a distance of the order of  $R$  between two field inversions), which diminishes the polarizability when it is present. On the other hand, around 10 MHz, both polarizabilities decrease sharply, being again the amplitude of the relaxation larger for  $\alpha_b^e$ , and at frequencies highly dependent on the particle conductivity. In the case of non-homogeneous charge distribution, this conductivity, and, hence, the characteristic frequency differs for the two polarizations, and can be distinguished in the spectrum of  $\Delta\alpha_e$  in this frequency range: an increase due to the MWO relaxation associated to  $\alpha_a^e$  is followed by a larger decrease associated to  $\alpha_b^e$ . The decay of  $\alpha_{a,b}^e$  is due to the progressive disappearance of the dipole associated to the mismatch of particle/medium conductivities. The most relevant difference between the spectra calculated for homogeneous and non-homogeneous charge distributions is the presence of the hump before the MWO decay in the latter case, whereas the homogeneous case presents a dip after the MWO decay.

The features of the electrokinetic predictions in Fig. 4.4b are in line with the experimental results of Fig. 4.4a. In the kHz range there exists an increase of the Kerr constant which corresponds to the  $\alpha$  relaxation. This increase occurs at a frequency comparable to that expected from electrokinetic calculations, although the amplitude of the jump is larger than pre-

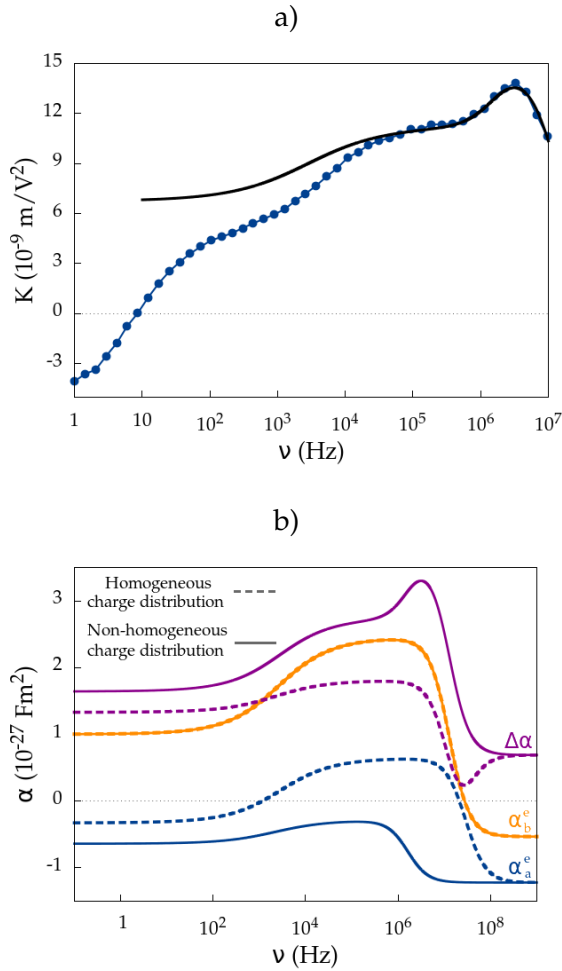


**FIGURE 4.4:** a) Kerr constant of NaMt suspensions (1 g/L particles, 0.3 mM NaCl) as a function of the frequency of the applied field. The points are the experimental data and the line is the electrokinetic prediction. Field strength 10 V/mm. Electrokinetic predictions for the electric polarizability along the major ( $\alpha_b^e$ ) and minor ( $\alpha_a^e$ ) axes of the particles and for the electric polarizability anisotropy ( $\Delta\alpha^e$ ). Two cases are analysed: homogeneous ( $K_a/K_b = 0.27$ ) and heterogeneous ( $K_a/K_b = 0.008$ ) charge distribution. The particles are oblate spheroids with major semiaxis  $b = 800$  nm and aspect ratio  $b/a = 3$ . Dispersion medium: 0.3 mM NaCl

dicted. This can be understood, since in the kHz range the hydrodynamic torque, not taken into account in the theoretical calculations, can play an

important role on the orientation of the particles [26]. In the MHz range, the hump and final decay in this spectrum is well reproduced by the electrokinetic model. According to the model, this hump indicates that NaMt particles have an heterogeneous charge distribution. In the Hz range the birefringence presents a negative value, indicating a switch in the axis of alignment of the particles that is not predicted by classical electrokinetics, in line with findings by other authors working with sodium montmorillonite and other similar clays [84, 124, 125, 129, 131]. Note that the negative values correspond to an anomalous orientation of the particle, with its axis of symmetry along the electric field. The characteristic frequency of this process ( $\nu_c$ ) is located at around 7 Hz.

Some features of the spectrum are similar to those presented by other planar particles like gibbsite in Ref. [50], although the Kerr constant values and the MWO relaxation frequency are much higher in the present work because of the larger particle size and surface conductivity. For example, at 1 MHz, the value of the electrical polarizability is  $\alpha_a^e = -5.49 \times 10^{-28} \text{ Fm}^2$  along the symmetry axis and  $\alpha_b^e = 2.41 \times 10^{-27} \text{ Fm}^2$  along the particle surface. In this case, the polarizability anisotropy per unit volume,  $\Delta\alpha^e/V_p = 3.7 \times 10^{-9} \text{ F/m}$ , is comparable to values obtained elsewhere [124, 128] for similar materials.

From the experimental birefringence spectrum much information about the properties of the particles in suspension can be obtained. First, we determined the value of their optical anisotropy,  $\Delta\alpha^o = 4.3 \times 10^{-33} \text{ Fm}^2$ . This value corresponds to particles with a lower refractive index than the one of NaMt ( $n = 1.5$ ) due to the swelling of this material [97]: sodium montmorillonite particles absorb water, which lowers their refractive index, thus reducing the magnitude of the Kerr constant. From the value of  $\Delta\alpha^o$  we can calculate the refractive index of the swollen particles, and hence estimate their water content. The obtained value of the volume fraction, 88% of water, is in agreement with the values found elsewhere [97, 99] (90-93%) for the osmotic swelling of sodium montmorillonite.

From the electrokinetic predictions we can also obtain information about the geometrical properties of the particles in suspension. Note that the degree of swelling does not only affect the refractive index but also the aspect

ratio of the hydrated particles, in the same proportion. In fact, from the experimental results we obtain an aspect ratio  $\rho = 3.3$  for the swollen particles. Given the water content, this corresponds to an aspect ratio of 30 for the dry particles, a reasonable value for these particles. The obtained value of the major axis length is  $1.6 \mu\text{m}$ , in good agreement with the average size obtained from both ESEM and TEB determinations.

#### 4.4.2. Effects of pH and ionic strength

The birefringent response of sodium montmorillonite is modified substantially when the pH of the sample is changed, as can be clearly observed in Fig. 4.5. This is an intriguing result, since the pH alters only the edge charge, which is much smaller than the surface charge. Note that these results cannot be caused by structure formation, since TEB experiments confirm that the transient behaviour is not altered by edge charge variation. Therefore it can be suggested that indeed the charge distribution plays an important role on particle electro-orientation. The effect of the pH on the birefringence spectrum can be introduced in the electrokinetic predictions via the modification of the conductivity along the particle symmetry axis. The agreement between the experimental data and the theoretical predictions is very good for frequencies above  $10^4$  Hz, where the MWO dispersion is the predominant contribution. As it can be seen in Table 4.1, the pH modifies the particle's conductivity anisotropy, the more so at more acid pHs, when the edges are charged positively in contrast with the negatively charged faces. However the experimental values are always far from the case of homogeneously charged particles, for which  $K_{\parallel}/K_{\perp}=0.27$ . The conductivity values  $K^{\sigma}$  are rather large, probably a manifestation of the presence of the Stern layer conductivity [52, 134, 135]. This comes from the motion of ions (not liquid) in the stagnant layer, that is, the volume comprised between the solid boundary of the particle and its slip or electrokinetic plane, which roughly corresponds to the beginning of the diffuse part of the EDL. This agrees with the estimations of  $K^{\sigma}$  of montmorillonite particles of the same origin as those used in this work, obtained using DC conductivity data [136]. These authors found  $K^{\sigma} = 6 \times 10^{-8}$  S, comparable to our present data. Concerning the values of effective particle

conductivity  $K^{\text{eff}}$ , our results yield  $K^{\text{eff}} = 0.05 \text{ S/m}$ , almost identical to those reported in Ref. [136], as expected from the similarities between the samples. The values of surface conductivity shown in Table 4.1 are however larger than those reported by other authors in layered materials. For example, Dozov et al. [128] calculated  $K^\sigma = 0.5 \times 10^{-8} \text{ S}$  for beilitedite particles. However, this corresponds to a larger value for  $K^{\text{eff}}$  (15 S/m in their case), that is, to highly conductive particles.

**TABLE 4.1:** Values of the surface conductivity and charge anisotropy obtained from the fit of the electrokinetic expressions to the experimental data. The pH dependence is analysed at 0.3 mM NaCl. The ionic strength dependence is studied at pH 7

pH	$K^\sigma (10^{-8} \text{ S})$	$K_a/K_b$
5	4.4	0.003
7	4.0	0.008
9	3.7	0.009
NaCl (mM)	$K^\sigma (10^{-8} \text{ S})$	$K_a/K_b$
0.1	4.1	0.008
0.3	4.0	0.008
0.6	3.9	0.008
1	3.5	0.008

In Fig. 4.6 the EB spectra for different values of the NaCl concentration are shown. The same features as in the previous figures are observed, and a similar analysis provides the surface conductivities shown in Table 4.1. The relation  $K_a/K_b$  does not change appreciably, which is coherent with the fact that neither the edge nor the face charges are modified by changes in the ionic strength.

#### 4.4.3. Low-frequency anomalous birefringence

As mentioned, it is remarkable that in the low frequency range there exists a reversal of the birefringence for all values of the pH and the ionic strength (Figs. 4.5a and 4.6a). Such an effect has been previously reported for a number of materials [50, 80, 84, 124, 125, 129–131], always for DC or slowly oscillating fields, and cannot be explained by classical electrokinetic theories.

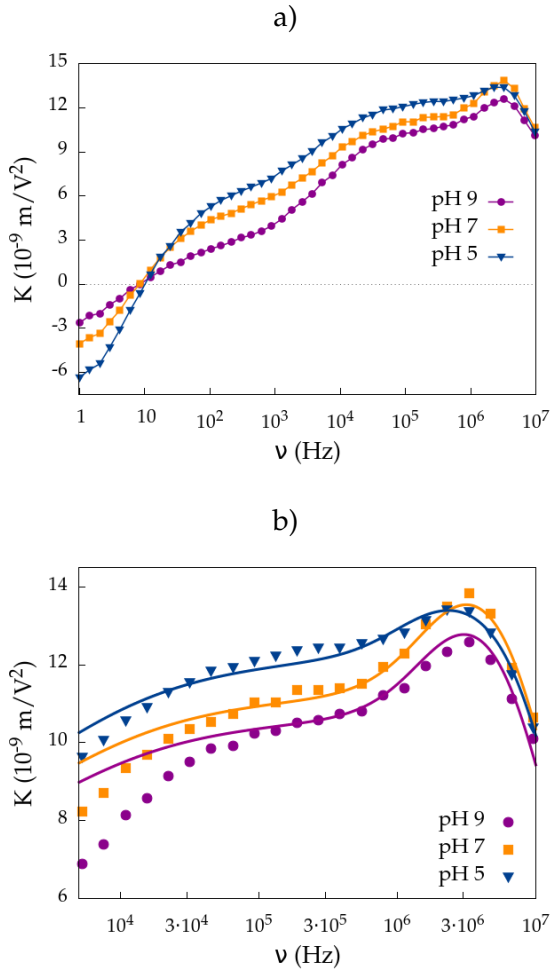


**FIGURE 4.5:** Kerr constant spectra of NaMt suspensions (1 g/L and 0.3 mM NaCl) for the indicated pH values. a) Complete frequency range; b) detail of the high frequency region. The points are the experimental data and the lines correspond to the predictions of the electrokinetic model [25].

The features of the anomalous effect for sodium montmorillonite samples can be summarized as follows. First, in Fig. 4.2 we observe that the dynamic behaviour is the same in the negative and positive birefringence regions, with Kerr’s law being always fulfilled. The negative effect is larger for more acidic values of the pH (Fig. 4.5a), when the edge and face charges

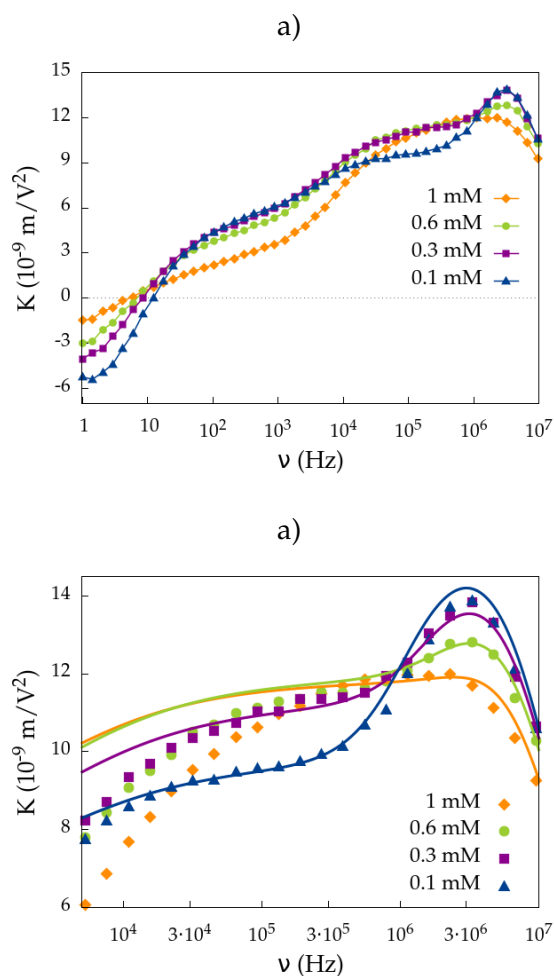


**FIGURE 4.6:** EB spectra of samples of sodium montmorillonite (1 g/L, pH 7) with different values of the ionic strength: a) Complete frequency range, b) zoom in the high frequency range. The points are the experimental data and the lines correspond to the predictions of the electrokinetic model [25].

exhibit opposite signs. Regarding the ionic strength dependence, in Fig. 4.6a it can be seen that the anomalous birefringence is more pronounced for smaller values of the salt concentration.

A first hypothesis for the explanation of the negative effect could be the formation of structures. This can be ruled out since such phenomenon

would lead to a change in the dynamic behaviour in the low frequency range, which is not detected. However, long range particle interactions are still plausible. In order to explore this possibility, we studied the EB spectrum as a function of particle concentration  $C$ . The results are shown in Fig. 4.7a, where it can be observed that in the kHz and MHz ranges all curves collapse to the same values, indicating that the Kerr constant is proportional to the particle concentration. We can thus consider that the system is dilute and particle interactions can be neglected in the high frequency range. On the other hand, in the Hz range  $K/C$  depends strongly on the particle concentration. These results lead to the conclusion that the negative torque is caused by long-range particle interactions and rule out an explanation based on a single particle phenomenon. In Fig. 4.7b, the spectrum of the logarithmic derivative of the normalized Kerr constant ( $\frac{1}{C} \frac{dK}{d \log \nu}$ ) is presented. Here, it can be observed that the shape of the curve is independent of the particle concentration. Thus, even though a larger value of the concentration yields a more pronounced negative effect, the characteristic frequency of the process does not depend on the volume fraction.

The negative birefringence can have either an electric or hydrodynamic origin. In the former approach, the existence of a permanent [84, 129] or saturable [124, 130] induced dipole moment for these particles has been proposed as possible explanation for this effect. However, a theory based only on the existence of a dipole of electric origin perpendicular to the particle surface cannot account for the concentration dependence found in Fig. 4.7a. Moreover, the fulfillment of Kerr's law is not compatible with the existence of a saturable induced dipole moment.

In order to explain this concentration dependence, a particle-concentration induced mechanism that gives rise to an overall perpendicular dipole moment was proposed in [125] to account for the anomalous orientation of laponite and hectorite. There it was argued that, for high concentrations, the overlapping of the EDLs of the edges of adjacent particles diminishes the polarization along the particle surface, leaving unperturbed the perpendicular component. At some point, the latter can reach larger values, leading to a preferred perpendicular orientation. Nevertheless, if this is the case, the effect should occur whatever the frequency of the applied field, in

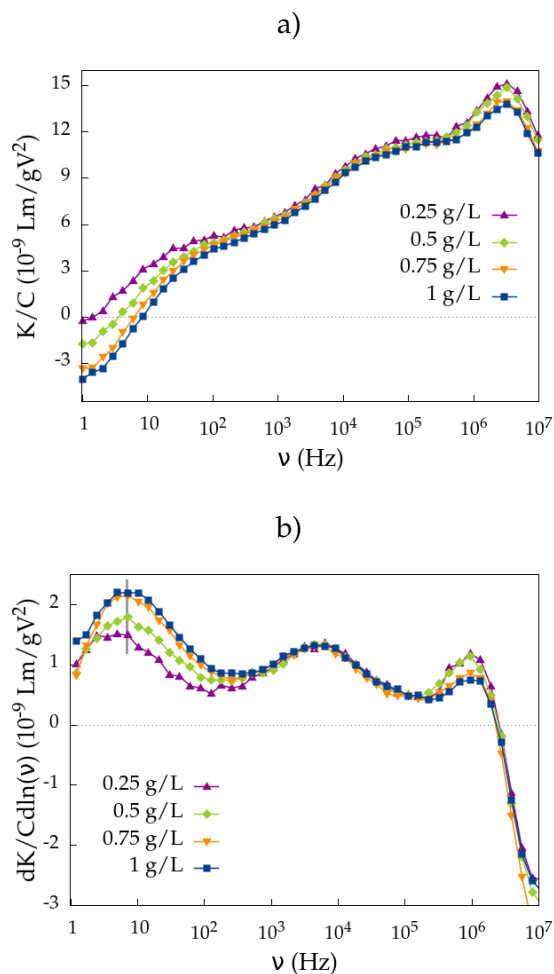


**FIGURE 4.7:** a) Birefringence spectra of samples with 0.3 mM NaCl and different concentrations of NaMt. The birefringence is normalized to the particle concentration  $C$ . b) Spectrum of the logarithmic derivative of  $K/C$ . The characteristic frequency of the anomalous behaviour ( $\nu_c = 7$  Hz) is indicated in grey.

contrast to our results. In fact, in the MHz range the Kerr constant does not depend on the particle concentration, ruling out the EDL overlapping as a possible explanation for our system. In addition, since the EDL is very thin in our case (around 20 nm), particles would need to be very close for this effect to occur. Hence, some dependence of the dynamics of the system

with the particle concentration would be expected, but this has not been found.

The anomalous orientation has also been observed in bidisperse systems of non spherical particles (or primary particles, PPs) and smaller (secondary) nanoparticles (SPs) of different composition [50, 80]. This effect is enhanced when the SP concentration increases, whereas smaller SPs tend to produce this action for a wider frequency range. The anomalous torque experienced by the primary particles is subsequently confirmed in these cases through measurements of the turbidity of the samples for incident laser light polarized either parallel or perpendicular to the electric field [137]. The explanation for the negative  $K$  values was based on the assumption that in the low frequency range the SPs distribute themselves asymmetrically around the PPs exerting a hydrodynamic torque that forces them to orient with their minor axis along the electric field. Similarly to normal hydrodynamic torques or electrical ones, the existence of the anomalous torque should not affect the randomization time. Also, this effect should occur at low frequency, where an asymmetric particle distribution, driven by their different electrophoretic velocities, is possible.

Such a possibility is in fact theoretically confirmed in [26], where the author shows that when ions accumulate asymmetrically around a particle, they can provoke a hydrodynamic torque opposite to the electric one, producing an anomalous orientation at low enough frequencies. In the case of bidisperse systems there are not slow ions, but the mechanism described in [26] is still valid: the SPs migrate at different velocity than PPs and hence, they move asymmetrically around the particle provoking the anomalous orientation.

The anomalous effect in [80] has several similarities with our experimental results. Particularly, in our case, the role of SPs can be played by the smaller size range in the polydisperse sample, thus explaining the negative effect and the low frequency range at which it occurs. This explanation is coherent with the absence of any effect on the relaxation time, as shown in Fig. 4.2 and with the enhancement of the anomalous effect with the particle concentration, displayed in Fig. 4.7a. In contrast, the characteristic frequency at which it occurs depends only on the particles velocity, and is

therefore independent of the concentration, in line with results in Fig. 4.7b. The pH dependence is also coherent with this picture: for acid pHs, the negatively charged faces of the smaller particles will be more strongly attracted to the positive edges of the larger ones, enhancing the anomalous orientation. In addition, increasing the ionic strength will reduce their attraction by the larger electrostatic screening. This explains the smaller significance of the anomaly for higher NaCl concentrations (Fig. 4.6).

## 4.5. Conclusions

The analysis described of the birefringence of sodium montmorillonite suspensions demonstrates the positive prospects of this technique and the amount of information that it can provide on such complex systems. The frequency spectra of the birefringence permits the observation of well known relaxations of the ionic clouds in EDLs, namely,  $\alpha$  and Maxwell-Wagner. The use of classical electrokinetic theories further enables a quantitative analysis from which the surface conductivity and its anisotropy (associated to the face-edge inhomogeneous charge distribution) can be obtained. Interestingly, the low frequency range of the birefringence spectra shows anomalous negative values, that is, a tendency of the particles to orient with their faces perpendicular to the applied field, instead of parallel. Such effect is minimized at basic pHs (all surfaces are negatively charged), high ionic strengths (electrostatic screening) and low concentrations. Comparison with previous data on bimodal suspensions suggest that this behavior is the result of an additional torque induced by the interaction between the smallest particles of the size distribution of the clay and the largest ones. Such interaction necessarily occurs at low frequencies, where particle accumulation, driven by their difference velocities, is possible.

## Acknowledgements

Financial support of this investigation by Junta de Andalucía, Spain (grant no. PE2012-FQM0694), MINECO, Spain (project no. FIS2013-47666-C3-

1-R), Feder Funds (EU) and MINECO, Ramón y Cajal Programme (RYC-2014-16901) is gratefully acknowledged. One of the authors (P.A.) thanks MEC, Spain for her FPU grant. We also thank Professor F. Mantegazza for his help with the experimental technique.

# 5

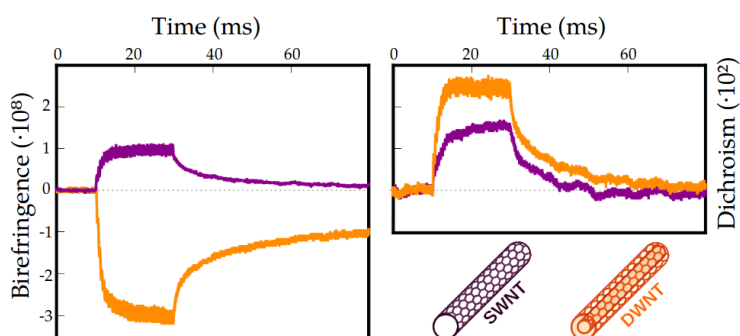
## ELECTRIC BIREFRINGENCE OF CARBON NANOTUBES: SINGLE- VS DOUBLE-WALLED



## Electric Birefringence of Carbon Nanotubes: Single- vs Double-Walled

P. Arenas-Guerrero, M. L. Jiménez, K. Scott,  
K. J. Donovan (2018). *Carbon*, 126, 77-84.

When subjected to an external electric field, carbon nanotubes in suspension are polarized and forced to rotate due to the consequent electric torque. The analysis of this electro-orientation is interesting not only at a fundamental level, but also because of the many applications that require the alignment of these particles. Moreover, the study of the interaction of the tubes with an electric field is a highly informative technique, able to provide much information on their microscopic properties. In order to monitor the orientation of the particles, in this work we measured the macroscopic optical anisotropy of the suspension, or electric birefringence, that emerges when the tubes are oriented by the field. Two types of particle were studied: single-walled and double-walled carbon nanotubes. The electric, optical and geometrical properties of the suspended tubes were analysed via the field dependence of the electric birefringence over a wide range. Remarkably, it was found that, whilst SWNTs show a positive signal, DWNTs exhibit a negative birefringence caused by an anomalous optical anisotropy of unknown origin.





## 5.1. Introduction

Carbon nanotubes consist of rolled-up graphene sheets with a diameter in the nanoscale but a micron-sized length. Because of their extreme aspect ratio, they can be considered as the nearly one dimensional form of fullerenes. They were discovered in 1991 [108], and since then they have generated much interest both because of their unique physical properties [109, 110, 138, 139] and their potential applications [109, 138–141] in electronics, nanomaterials or nanomedicine.

Much work has been carried out on the characterization of carbon nanotubes, regarding their thermal, geometrical, mechanical, chemical or electronic properties [109, 138, 139, 142–144]. Furthermore, many works focus on the optical properties of carbon nanotubes and other carbon-based nanoparticles, and their potential applications [142, 145–148].

Special attention has been paid to the morphology of the tubes [109, 110], which directly affects their microscopic properties. For instance, electronic transport is highly affected by the atomic structure, and depending on the orientation of the rolled graphene layers, the tubes can be either metallic or semiconducting [111]. Furthermore, carbon nanotubes can be made of a single graphene sheet, or by several of them structured coaxially. In the latter case, the interplay of the different layers can also play an important role in the microscopic properties of the tube [112, 149].

Moreover, the current understanding of the interaction of carbon nanotubes with external electric fields is basic not only at the fundamental level, but also from the applied point of view. Thus, many applications require the controlled deposition and orientation of these particles [150–153]. For instance patterns of aligned tubes have been used as DNA or protein sensors [13, 154], microscopy nanoprobe [14], structures for field emission displays [155] and photodetectors [15]. The use of electric fields has proven a simple and efficient method for the controlled orientation of these particles [22, 150], but is not yet a widespread technique. Furthermore, the separation of the metallic and semiconducting nanotubes, essential for applications in nanoelectronics, may be tackled via dielectrophoresis [19, 156]. Although some effort has been carried out to understand the orientation

of carbon nanotubes in electric fields [22, 96, 157–159], further work is still needed for achievement of its full potential.

With this motivation, in this work we monitored the orientation of single- and double-walled carbon nanotubes in non-aqueous suspension under the application of an external electric field, via the measurement of the electric birefringence (EB) and the linear dichroism (LD). The thorough study of the birefringent phenomenology provides information about the electric, optical and geometrical properties of the tubes [78, 96].

Non-spherical particles present anisotropic microscopic properties, in particular an anisotropic polarizability [25, 49] which, for intrinsically homogeneous materials, is determined solely by the particle geometry. In the case of elongated, axially symmetric particles, this polarizability anisotropy can be written as  $\Delta\alpha = \alpha_L - \alpha_d$ , where L(d) refers to the major(minor) axis of the particle.

Hence, when an electric field is applied to a suspension of non-spherical particles, the dipole induced on them [25, 49] is generally not parallel to the electric field, due to the electrical polarizability anisotropy at the field frequency,  $\Delta\alpha^\omega$ . This generates a torque that forces the particles to orient until the dipole is aligned with the field direction, normally with their major axis parallel to it. This phenomenon, known as electro-orientation, competes with the rotational diffusion of the particles, which tends to randomize their orientation.

The electro-orientation of the particles under the application of an electric field gives rise to an optical anisotropy of the suspension at a macroscopic level. In this work we analysed the electric birefringence  $\Delta n$ , and the linear dichroism  $\Delta A$ .

The electric birefringence is the anisotropy induced on the refractive index of the suspension due to the electro-orientation of the particles, and it can be written as [42]

$$\Delta n = \frac{\Delta\alpha^\omega \phi \langle P_2(\cos \theta) \rangle}{2n_s \epsilon_0 V_p} \quad (5.1)$$

where  $\phi$  is the volume fraction of the particles,  $n_s$  the refractive index of the suspending solution,  $\epsilon_0$  the vacuum permittivity and  $V_p$  the particle

volume.  $\Delta\alpha^o$  is the polarizability anisotropy of the particles at optical frequencies,  $\theta$  the angle between the particle symmetry axis and the electric field and  $\langle P_2(\cos\theta) \rangle$  the average value of the second Legendre polynomial of the orientation distribution, a measure of the degree of alignment of the particles with the external electric field. For large enough fields, when the particles are fully oriented,  $\langle P_2(\cos\theta) \rangle = 1$  and the birefringence tends to the saturation value

$$\Delta n_{\text{sat}} = \frac{\Delta n(E \rightarrow \infty)}{\phi} = \frac{\Delta\alpha^o}{2n_s\epsilon_0 V_p} \quad (5.2)$$

For low fields, however,  $\langle P_2(\cos\theta) \rangle$  decreases due to the effect of rotational diffusion. When expansions in power series of  $E_0$  are usable, it can be shown that the average of the Legendre polynomial, and therefore the EB, is proportional to the second power of the field strength, a dependence known as Kerr's law. Thus, the Kerr constant, a magnitude independent of the field strength, can be defined as

$$K = \frac{\Delta n}{\lambda E_0^2/2} \quad (5.3)$$

where  $E_0$  is the field amplitude and  $\lambda$  the light wavelength.

Because of this proportionality, when a sinusoidal electric field of frequency  $\nu$  is applied to the suspension, the birefringence presents both a DC and an AC component [49], the latter oscillating with twice the frequency of the applied field

$$\Delta n = \Delta n_{\text{DC}} + \Delta n_{\text{AC}} \sin(2\nu t) \quad (5.4)$$

Unless indicated otherwise, the birefringence refers to the DC component. The AC component averages to zero over time and therefore the value of  $\Delta n_{\text{DC}}$  can be easily obtained from the experimental signal.

In this contribution we restrict ourselves to diluted suspensions of particles with no intrinsic dipole moment. Furthermore, the viscous torque is neglected, a good approximation in the case of uncharged rods [49]. In these conditions, an explicit expression of the Kerr constant is available in the low-field range [122]

$$K = \frac{\Delta\alpha^o \Delta\alpha^e \phi}{30n_s \epsilon_0 k_B T V_p \lambda} \quad (5.5)$$

where  $k_B$  is the Boltzmann constant,  $T$  the temperature and  $\Delta\alpha^e$  the electric polarizability at field frequencies.

After the application of an electric field the induced birefringence grows and reaches a stationary value in a finite time. As mentioned, the build-up process of the electric birefringence presents in general both a diffusive and an electric contribution. However, for large-enough fields, the former can be neglected.

In these conditions, it was found that the angular velocity of orientation of the particles does not depend on their size, but only on the applied field and the viscosity of the medium [96]. Hence, the polydispersity of the sample is not relevant for the build-up process, which, as a result, is in the shape of a single-exponential function

$$\Delta n(t) = \Delta n_{st}(1 - e^{-t/\tau_r}) \quad (5.6)$$

Here  $\Delta n_{st}$  is the stationary value of the birefringence and  $\tau_r$  the characteristic rise time. The inverse of  $\tau_r$  is expected to depend linearly on the square of the field amplitude, both in the low field [87] and high field [81] ranges, according to the expression ( $\Theta$  is the rotational diffusion coefficient of the particles):

$$\left. \frac{d(\Delta n / \Delta n_{st})}{dt} \right|_{t \rightarrow 0} = \frac{1}{\tau_r} = \frac{2\Delta\alpha^e E_0^2}{5k_B T} \frac{\Theta}{2} \quad (5.7)$$

Upon removal of the external electric field, rotational diffusion due to thermal agitation will randomize the orientation of the particles in a finite time. The rotational diffusion coefficient is strongly size-dependent, and, for the case of long cylinders ( $\rho > 2$ ), can be written as [160]

$$\Theta = \frac{3k_B T}{\pi \eta L^3} [\ln \rho + C_r] = \frac{F_\Theta}{L^3} \quad (5.8)$$

$$C_r = -0.662 + 0.917/\rho - 0.050\rho^2$$

where  $\eta$  is the viscosity of the suspending medium and  $\rho = L/d$  the aspect ratio of the particles. As a result, the decay of the birefringence is highly affected by the particle size and by the sample polydispersity. The decay of the birefringence is expected to be a superposition of individual exponential processes. Under reasonable assumptions, such superposition yields a decay in the form of a stretched exponential function [45, 46]

$$\Delta n(t) = \Delta n_0 \exp \left[ - \left( \frac{t}{\tau_d} \right)^\alpha \right] \quad (5.9)$$

where  $\Delta n_0$  is the initial value of the birefringence,  $\tau_d$  a characteristic decay time and  $\alpha$  a polydispersity factor. From these parameters, an average diffusion coefficient can be calculated as

$$\Theta = \frac{\alpha}{6\tau\Gamma(\alpha^{-1})} \quad (5.10)$$

Thus, from the analysis of the birefringence decay, the diffusion coefficient can be obtained. From it, the length of the particles can be calculated using Eq. 5.8. This procedure, referred to as stretched exponential method, has been used in many works for size determination from birefringence measurements [50, 78, 161]. Since the birefringent signal is proportional to  $V_p$ , the average size provided by this technique is weighted by volume.

The electro-orientation of non-spherical particles also gives rise to an anisotropy in the light absorption of the sample. The linear dichroism is defined as the difference between the absorption  $A$  in the directions parallel and perpendicular to the applied electric field

$$\Delta A = A_{\parallel} - A_{\perp} = \Delta A_{\parallel} - \Delta A_{\perp} \quad (5.11)$$

where  $\Delta A_{\parallel(\perp)} = A_{\parallel(\perp)} - A_0$  and  $A_0$  is the absorption when no electric field is applied to the suspension.

For normal orientation, the major axis of the particles, more absorbent, is in the parallel direction. Therefore  $A_{\parallel} > A_{\perp}$  and  $\Delta A$  is positive. Only when the particles orient anomalously, with their minor axis along the field direction, is a negative LD expected. Since the linear dichroism is proportional to the orientation of the particles in the sample, the same general

features of EB (frequency and field strength dependences, effect of the concentration, transient behaviour, ...) are expected in the case of LD.

## 5.2. Experimental

### 5.2.1. Materials

In this work we have analysed the electro-optic behaviour of two different types of particles: single-walled carbon nanotubes (SWNTs) and double-walled carbon nanotubes (DWNTs), obtained commercially from Carbolex and US Research Nanomaterials respectively. In all experiments, the particles were dispersed in 1,2-dichloroethane with the help of an ultrasonic probe. It has been checked that the electro-optic response of the solvent is negligible under the applied fields. The suspensions are stable over periods of several days, but were sonicated for 20 minutes prior to measurements being taken in every case.

The tubes were synthesized by the arch discharge method. The SWNTs were purified by soxhletting for 12 hours using toluene. This process removes amorphous carbon, much more soluble than SWNTs. Acetone was used to remove toluene from the sample, which was then dried. Approximately 12-15% of the original sample is left after this procedure, of which it was found that approximately 90% are SWNTs, the other 10% encapsulated catalyst (nickel). However, as the impurities do not have large electric dipoles (either permanent or induced), and they are isotropic and small in size, they do not affect the anisotropy measurements; they only contribute to isotropic absorption, but not to birefringence. This was experimentally tested for the present work. For the DWNTs, the main impurities are single- and multi-walled carbon nanotubes, which cannot be removed by this method. Thus, the sample was used at the commercial purity, 60%.

According to the manufacturers, the SWNTs and DWNTs present an individual diameter of 1.4 nm and 1-3 nm respectively. Electron transmission microscopy images of the tubes are shown in Figure 5.1, where it can be observed that the samples are very polydisperse and that the particles are bundled in both cases. The presence of the catalyst nanoparticles can be ap-

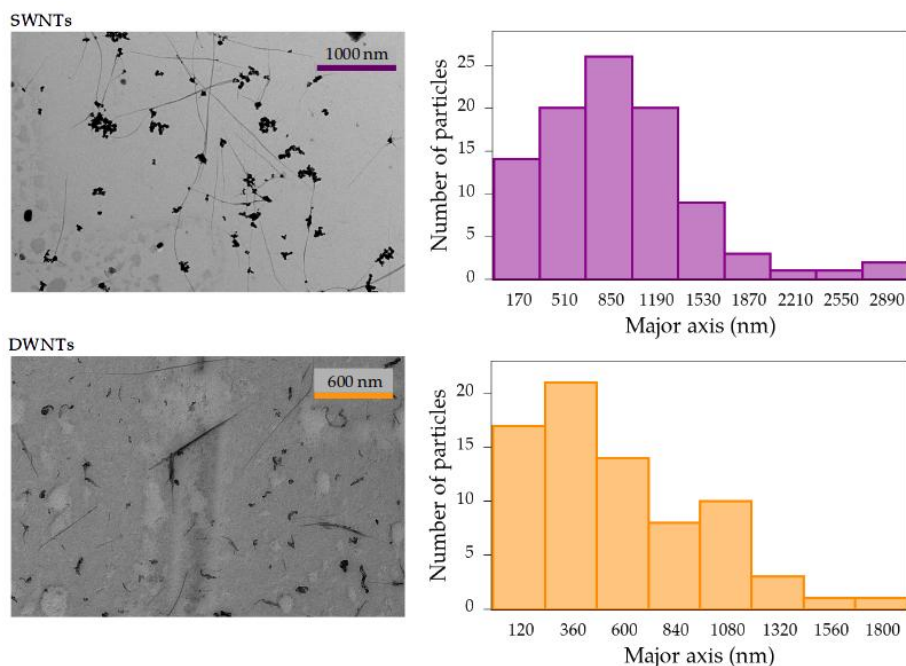


**FIGURE 5.1:** Electron Transmission Microscopy images of the SWNTs and the DWNTs along with the size distribution obtained from them.

preciated. For the SWNTs (DWNTs), the mean bundle diameter obtained from the microscopy images is 12 nm (9 nm) and the mean bundle length is  $900 \pm 570$  nm ( $550 \pm 390$  nm), where the error is the standard deviation of the distributions. The information on the particle length is presented in Table 5.1.

For calculations carried out in this work, the density of the nanotubes is needed. For the SWNTs, we used the value found via gradient sedimentation measurements for the density of bundled SWNTs, 1.87 g/L [162]. In the case of the DWNTs, the density, 2.1 g/L, is provided by the manufacturer. The values of the density (1.26 g/L), the refractive index ( $n_s=1.44$ ), the viscosity ( $\eta_s = 0.84$  cP) and the dielectric constant ( $\epsilon_s=10.5$ ) of the 1,2-dichloroethane were also used.

### 5.2.2. Methods

The standard methods for the determination of the electric birefringence and the linear dichroism are based on the measurement of the change in the light transmission through an optical setup containing the samples [42, 43, 120]. In this work, a 7 mW, 500:1 polarised, low noise He-Ne laser beam ( $\lambda = 633$  nm) is used (JDS Uniphase model 1137p, UK). The samples are placed in a Teflon cell of 3 cm path length, which is kept at 20°C, and they are subjected to an external electric field in the form of short sinusoidal pulses supplied by a function generator (Thurlby Thandor Instruments model TG5011, UK) in a frequency range of 100 Hz-10 kHz. The external field is amplified using a commercial voltage amplifier (Trek 609E-6, US). The light intensity is collected by a silicon junction photodiode (Thorlabs PDA36, USA). All the optical plates were purchased from Thorlabs.

For the LD measurement, the optical setup consists of i) a polarizer parallel to the electric field and ii) the suspension. The light intensity  $I$  transmitted by this setup is related to the parallel dichroism of the sample as  $\Delta A_{\parallel} = \log_{10} \frac{I_0}{I(t)}$ , where  $I_0$  is the light intensity transmitted when no electric field is applied to the suspension. Taking into account that, due to symmetry,  $\Delta A_{\parallel} = -2\Delta A_{\perp}$ , the total dichroism can be obtained via the equation [163]

$$\Delta A(t) = \frac{3}{2} \log_{10} \frac{I_0}{I(t)} \quad (5.12)$$

In the case of EB, the optical setup consists of i) a polarizer at 45° to the external electric field, ii) the suspension, iii) a quarter-wave plate whose fast axis is placed parallel to the polarizer axis and iv) an analyzer at 90°- $\alpha$  to the initial polarization. The offset  $\alpha$  allows the sign of EB to be determined as well as the magnitude. The light intensity  $I$  transmitted by this setup is related to the birefringence of the sample via the expression

$$\Delta n(t) = \frac{\lambda}{\pi L} \left( \arcsin \left( \sqrt{\frac{I(t)}{I_0}} \sin \alpha \right) - \alpha \right) \quad (5.13)$$

where  $L$  is the path length.

A complete description of this setup can be found in [120]. Other methods have been proposed that substitute the quarter-wave plate by a photoelastic modulator, which changes the polarization of the incident light [164]. The sensitivity of  $\Delta n$  is somewhat smaller than in our case, but the technique can be used with much shorter optical path lengths. On the other hand, our setup allows the correction of the stress birefringence of the cell walls with a simple procedure, described in [120].

Moreover, when the absorption of the sample is not negligible, the changes in the transmitted intensity caused by LD can affect the experimental determination of EB. Our experimental setup enables the correction of such effect, given that LD is previously measured. For this purpose, Eq. 5.13 must be modified [121]

$$\Delta n(t) = \frac{\lambda}{\pi L} \left( \arcsin \left( \sqrt{\frac{\frac{I(t)}{I_0} \sin^2 \alpha - \zeta(\Delta A)}{\Omega(\Delta A)}} \right) - \alpha \right) \quad (5.14)$$

$$\zeta(\Delta A) = 1/4 \cdot 10^{-2\Delta A/3} + 1/4 \cdot 10^{\Delta A/3} - 1/2 \cdot 10^{-\Delta A/6}$$

$$\Omega(\Delta A) = 10^{-\Delta A/6}$$

Lastly, for future calculations, it is also necessary to obtain the absorptivity of the carbon nanotubes. For this purpose, we used a commercial spectrophotometer (6705 UV/Vis spectrophotometer, Jenway, UK) to measure the transmission of red light through the nanotube suspensions. From these data, the extinction coefficient  $k$  was experimentally estimated both for the SWNTs ( $k = 0.79$ ) and the DWNTs ( $k = 1.58$ ).

## 5.3. Results and discussion

### 5.3.1. Sign of the electric birefringence and the linear dichroism

Experimental birefringent signals of the SWNT and DWNT suspensions subjected to an electric pulse of 20 ms are shown in Figure 5.2a. The most remarkable feature of these measurements is that the SWNTs and DWNTs exhibit a positive and negative birefringence respectively. The anomalous

(negative) birefringence of the DWNTs has been observed for all the studied range of frequencies, field amplitudes and particle concentrations.

Negative birefringence has been reported for a variety of materials under different conditions [78, 80, 125], and is normally associated with an anomalous orientation of the particles where their major axis aligns perpendicular to the direction of the electric field. In order to check whether this explanation applies in the case of the carbon nanotubes, the linear dichroism of both samples under the same conditions was also measured.

As can be observed in Figure 5.2b, both SWNTs and DWNTs present a positive dichroism, corresponding to a normal orientation of the particles parallel to the field. Thus, the negative birefringence of the DWNTs is not caused by an anomalous orientation and hence, according to Equation 5.5, the optical polarizability anisotropy of the DWNTs must exhibit a negative value.

### 5.3.2. Effect of the field frequency and the particle concentration

The frequency dependence of the EB of a SWNT suspension is shown in Figure 5.3. Here, it can be observed that the AC oscillations decay strongly with the field frequency, and become negligible at about 10 kHz. This behaviour indicates that for times shorter than 0.1 ms, the particles are not able to follow the field oscillations, which is expected for micron-sized particles.

On the other hand, for frequencies above 500 Hz, the DC component of the birefringence is independent of the frequency of the applied field. This behaviour was expected, since there are no frequency-dependent polarization mechanisms in the non-aqueous media in this range. The same features have been found for the linear dichroism and for the case of the DWNTs. It can be noticed, however, that the value of the birefringence at 100 Hz is lower than the rest. For these slowly varying fields, the particles can travel a long distance between two field inversions, and they can migrate to the electrodes and deposit on them. To avoid such effects, a frequency of 1 kHz was chosen for the measurements.

The concentration dependence of the EB of the samples has also been

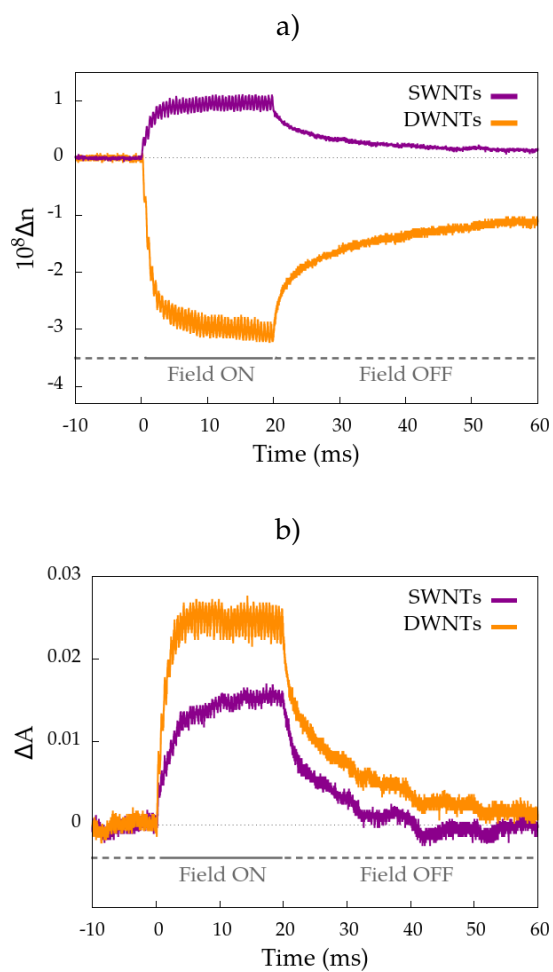


**FIGURE 5.2:** Electro-optic response of suspensions of SWNTs and DWNTs  $10^{-4}$  wt% when subjected to sinusoidal field pulses of 1 kHz, 20 ms of duration and a field amplitude of 250 V/mm. a) Electric birefringence. b) Linear dichroism.

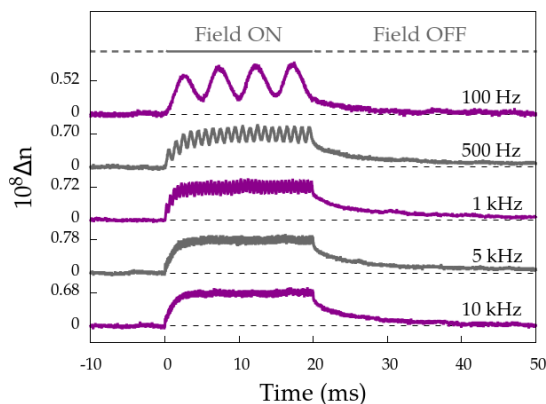


**FIGURE 5.3:** Transient birefringent response of a SWNT suspension  $10^{-4}$  wt% when subjected to sinusoidal field pulses of 20 ms of duration, a field amplitude of 250 V/mm and different frequencies.

analysed. The suspensions used in this work have a particle concentration of  $10^{-4}$  wt%, which, taking into account the average dimensions of the tubes and their low density, corresponds approximately to 1 particle/ $100 \mu\text{m}^3$ . Hence, the measurements have been carried out in the dilute regime, and no particle interactions are expected to affect the measurements. This is confirmed by the linear dependence of the birefringence with the particle concentration that can be observed in Figure 9.4. Thus, particle interactions like the ones in [112] do not have an effect on the electro-optical behaviour of the samples.

### 5.3.3. Transient behaviour of the birefringence

The transient behaviour of the EB of the samples also provides information about the particles in suspension. Figure 5.5a shows the normalized birefringent response of the SWNTs and the DWNTs as a function of time, in the same experimental conditions, when subjected to an electric pulse of 20 ms. Interestingly, it can be observed that both types of nanotubes undergo almost the same orientation process (rise of the birefringence), whilst the randomization process (decay of the birefringence) is different for each kind of particle. Moreover, similarly to what was found elsewhere [96], the

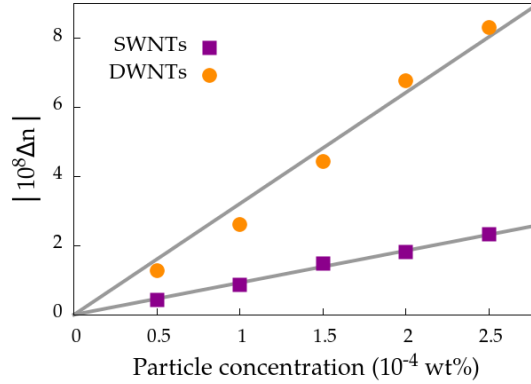


**FIGURE 5.4:** Stationary electric birefringence (in absolute value) of SWNT and DWNT suspensions of different concentrations. The field strength is 250 V/mm and the field frequency 1 kHz.

rise of the EB can be fitted to a single exponential function.

This shape of the rise suggests that the build-up process does not depend on the particle size and, therefore, the diffusive contributions to the build-up process must be negligible in comparison to the electric contributions. In these conditions, the inverse of the characteristic time of the single-exponential build-up process is expected to depend linearly on the square of the field amplitude. Using Equations 5.7, 5.8 and 5.16, this dependence can be written as

$$\frac{1}{\tau} = \frac{\epsilon_0 \epsilon_s E_0^2}{10 \eta_s} \left( \frac{\ln \rho + Cr^\perp}{\ln 2\rho - 1} \right) \left( 1 + \frac{4/3 - \ln 2}{\ln 2\rho - 1} \right) \quad (5.15)$$

As can be observed, the  $L^3$  contributions of  $\Delta\alpha^e$  and  $\Theta$  cancel out, and the expected slope depends only on properties of the solvent and slowly varying logarithmic functions of the aspect ratio. Since  $\rho$  is very similar for both the SWNTs and the DWNTs, the expected value of the slope is almost identical for both types of particles, thus explaining their similar build-up process. As can be observed in Figure 5.5b, proportionality is found in all the field range. The experimental values of the slope,  $g = (2.20 \pm 0.02) \cdot 10^{-8} \text{ m}^2/\text{sV}^2$  and  $g = (2.18 \pm 0.02) \cdot 10^{-8} \text{ m}^2/\text{sV}^2$ , differ from the theoretical ones

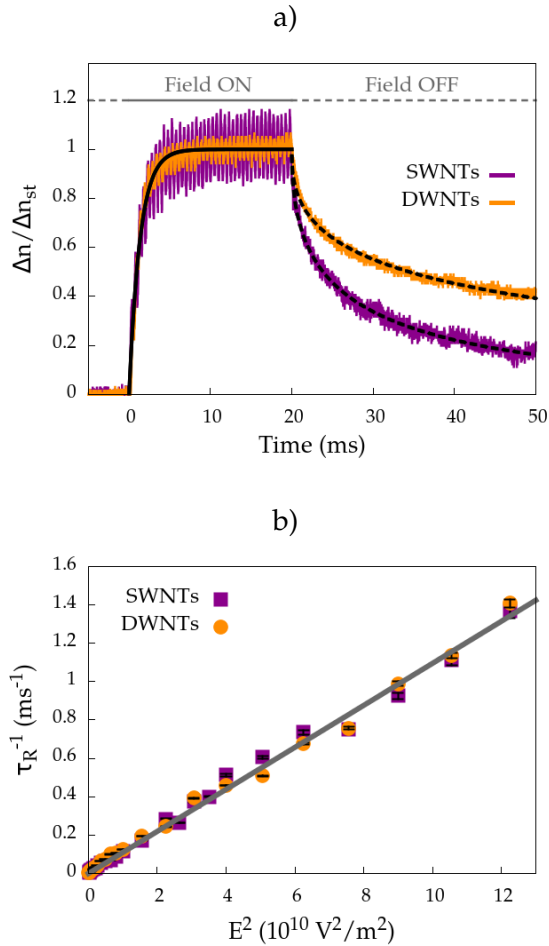


**FIGURE 5.5:** a) Transient electric birefringence (normalised to the stationary value) of the samples of carbon nanotubes  $10^{-4}$  wt% when subjected to field pulses of a duration of 20 ms, a field amplitude of 250 V/mm and a frequency of 1 kHz. The solid line is a fit of the build-up to a single exponential function. The dashed line is a fit of the decay to a stretched exponential function. b) Inverse of the rise time as a function of the square of the field amplitude for the samples in a). The line is a fit of the data to a linear function.

only by 2% and 5% respectively.

On the other hand, the decay of the birefringence is strongly dependent on the particle size, and therefore the decays of the SWNT and DWNT samples are very different. Since carbon nanotubes are entangled, the dynamics of the decay are related to the morphology of the particle bundles. In both cases, the decays can be fitted to a stretched exponential function, as it is shown in figure 5.5.

From the fitting parameters of the SWNTs ( $\alpha=0.545\pm0.002$ ,  $\tau_r=6.95\pm0.03$  ms) and the DWNTs ( $\alpha=0.3166\pm0.0006$ ,  $\tau_r=33.4\pm0.1$  ms), the length of the tubes was estimated using equations 5.10 and 5.8 and assuming the bundle width found via microscopy. The results are shown in Table 5.1. As previously mentioned, the average lengths provided by this method are weighted by volume.

The value of the particle length obtained with this method for the SWNTs, 1100 nm, is very similar to the volume-averaged length obtained from microscopy measurements, 1270 nm, within a 15% difference. However, in the case of the DWNTs, the length obtained with the stretched exponential method, 2400 nm, is much larger than the volume-averaged mean length provided by microscopy measurements, 860 nm. This indicates that, when in suspension, the DWNTs are more bundled than when the particles are dried.

**TABLE 5.1:** Experimental values of the particle length found by microscopy measurements (averaged and volume averaged), by the analysis of the birefringence decay via the stretched exponential method and by the analysis of the electrical polarizability anisotropy. For the microscopy measurements, the error is obtained from the standard deviation of the distribution.

Method	SWNTs	DWNTs
Microscopy (averaged)	900 ± 570 nm	580 ± 40 nm
Electrical polarizability anisotropy	1080 ± 200 nm	1630 ± 100 nm
Microscopy (volume averaged)	1270 ± 660 nm	860 ± 430 nm
Stretched exponential method	1100 nm	2400 nm

### 5.3.4. Effect of the field strength

The effect of the field strength on EB has been studied in depth since, as discussed previously, it can provide useful information about the electric properties of the particles in suspension. Figures 9.5a and 9.5b show the experimental birefringence as a function of  $E_0^2$  for the carbon nanotubes. The data presented on these graphs have been corrected to remove the effect of LD in the birefringence experiment. Although the dichroism cannot be reliably measured at very high fields, as the experiment is very sensitive to small changes in the sample, it was possible to determine LD until saturation was achieved, and use this saturation value for the correction at larger fields.

On the graphs, it can be observed that, as expected, Kerr's law is satisfied at low fields, although there exists some intercept that could be caused by small misalignments or by a not fully corrected stress birefringence introduced by the cell. For high fields, saturation of the birefringence is achieved. This behaviour is similar to the one observed for other carbon-based particles [112]. However, since in our case the suspension is non-aqueous, the only contribution to polarization is that of the particles, unlike in [112], where additional polarization mechanisms associated to the particle charge are present. For this reason, the magnitude of  $\Delta n$  in Figure 9.5a is not as large and saturation is achieved at larger fields.

Table 7.1 shows the experimental values of the Kerr constant  $K$ , the saturation birefringence  $\Delta n_{\text{sat}}$  and the field at which saturation is achieved  $E_{\text{sat}}$  both for the SWNTs and the DWNTs. The values of the electric and optical polarizability anisotropies, also presented in Table 7.1, were calculated from  $K$  and  $\Delta n_{\text{sat}}$ , using Equations 5.2 and 5.5.

It has been shown elsewhere that the contribution to electric polarizability is much higher for the metallic tubes than for the semiconducting ones [158]. In the case of the SWNTs, the conducting tubes correspond to 1/3 of the total concentration. For the DWNTs, all particles with at least one conducting layer, 5/9 of the total, behave as metallic [112]. The polarizability anisotropy of a metallic cylinder of length  $L$  and a very large aspect ratio  $\rho$  in a medium with a static dielectric constant  $\epsilon_s$  can be written as [63]

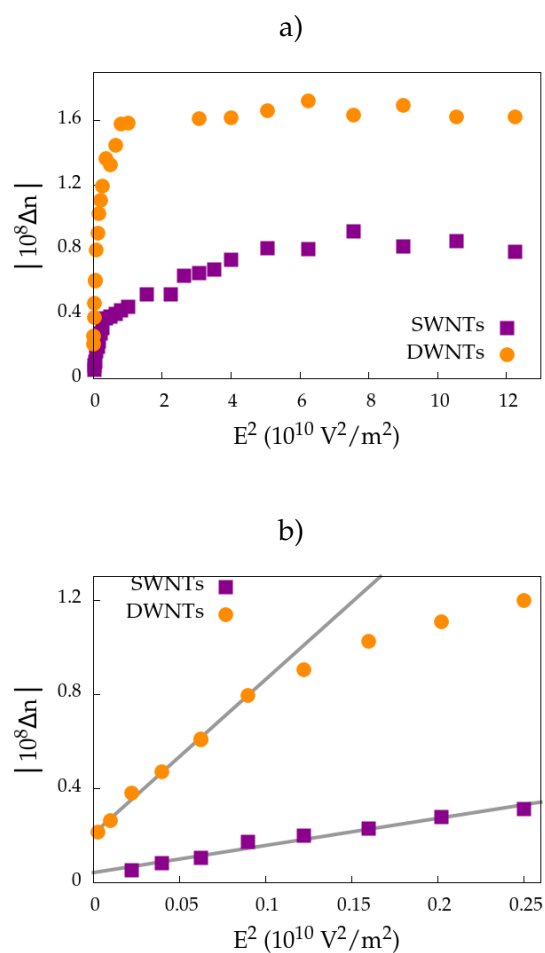


**FIGURE 5.6:** Electric birefringence of the samples as a function of the amplitude of the applied field. The particle concentration is  $10^{-4}$  wt% and the field frequency 1 kHz. a) Full range. b) Zoom in the low-field range. The points are the experimental data and the line is the fit to Kerr's law.

**TABLE 5.2:** Experimental values found from the measurements in Figure 9.5: Kerr constant, saturation value of the birefringence, saturation field, electrical and optical polarizability anisotropies and refractive index of the SWNTs and DWNTs.

	SWNTs	DWNTs
$K$ ( $10^{-12}$ m/V <sup>2</sup> )	$3.6 \pm 0.2$	$-20.5 \pm 0.7$
$\Delta n_{\text{sat}}$	$0.041 \pm 0.007$	$-0.074 \pm 0.004$
$E_{\text{sat}}$ (V/mm)	$200 \pm 20$	$100 \pm 20$
$\Delta\alpha^e$ ( $10^{-30}$ Fm <sup>2</sup> )	$16.9 \pm 3.1$	$48.7 \pm 3.3$
$\Delta\alpha^o$ ( $10^{-34}$ Fm <sup>2</sup> )	$1.09 \pm 0.18$	$-2.18 \pm 0.13$
$n_p$	$2.6 \pm 0.1$	$\approx 2.2$

$$\Delta\alpha^e \approx \alpha_L^e = \frac{4\pi\epsilon_0\epsilon_s L^3}{24(\ln 2\rho - 1)} \left( 1 + \frac{4/3 - \ln 2}{\ln 2\rho - 1} \right) \quad (5.16)$$

With this equation, the length of the nanotubes can be estimated from the experimental value of  $\Delta\alpha^e$ . The results are presented in Table 5.1 and, in the case of SWNTs, are in perfect agreement with the length values obtained from the stretched exponential determination, differing only by 2%. The result is also very similar to the one found from microscopy measurements, within a 15% difference. These results confirm that the electro-optical response is due mainly to the metallic tubes.

In the case of the DWNTs, the obtained length is larger than the result obtained by microscopy, which suggests that the DWNTs are more bundled or aggregated when suspended. This supports the previous results obtained via the stretched exponential method, which provided a much larger mean length than the volume-averaged length provided by microscopy. However, it is not possible to directly compare the results provided by the stretched exponential method and by the determination of the electrical polarizability anisotropy, since the former is averaged by volume while the second is not.

As previously mentioned, carbon nanotubes are entangled, which can af-

fect their band structure and therefore their electric properties. Indeed, it has been shown elsewhere that bundling enhances the metallic nature of the tubes [165]. However, a larger conductivity does not modify the strength of the electric dipole, but only the characteristic frequency at which it relaxes. This frequency is orders of magnitude higher than that of our experiments, so changes in it do not affect our EB results.

The optical polarizability anisotropy of non-spherical particles is directly related to their complex refractive index,  $n_p^* = n_p + ik$ . In the case of highly elongated rods, this dependence can be written as [25]

$$\Delta\alpha^o = \frac{\epsilon_0 V_p}{4\pi} \text{Re} \left[ \frac{(n_p^{*2} - n_s^2)^2}{n_p^{*2} + n_s^2} \right] \quad (5.17)$$

This expression is valid only for a homogeneous refractive index, which is expected in the case of the honeycomb structure of graphene. According to Eq. 5.17, if the complex part of the refractive index is known, the real part can be obtained from the experimental value of the optical polarizability anisotropy. As already mentioned, the value of  $k$  for the SWNTs and DWNTs was determined with a spectrophotometer. The values of  $n_p$  obtained in this manner are presented in Table 7.1.

For the SWNTs, the obtained refractive index, 2.6, is within a 5% difference with the one found for graphene in [166], 2.73, and very similar to the values given in [167]. The major contribution to the error is due to the uncertainty in the purity of the sample, which is estimated to range between 85% and 95%. Despite this rather large uncertainty in the concentration, the error in  $\Delta\alpha^o$  is quite small (<4%). Therefore, this is a suitable method to obtain the refractive index of suspended particles.

In the case of the DWNTs, the larger absorption of the particles explains the negative sign of the optical polarizability anisotropy. It is, to our knowledge, the first time that a negative birefringence associated with the absorbance of the particles has been reported. The obtained value of the refractive index of the DWNTs cannot be considered accurate because of the uncertainty in the concentration of the suspension due to the moderate sample purity.

## 5.4. Conclusion

The study of the electric birefringence of suspensions of carbon nanotubes allowed the real-time monitoring of their alignment with an external electric field, and the extraction of much information on the microscopic properties of the suspended tubes. The analysis of the field dependence of the birefringence permitted the calculation of the polarizability anisotropy both at the frequency of the applied field and at optical frequencies for the SWNTs and DWNTs. From this information, the average length of the SWNTs and their refractive index were obtained. The results are in excellent agreement with the ones found in other works using different techniques. Furthermore, it was possible to prove that the metallic tubes, and not the semiconducting ones, control the electro-optical response of the system.

Interestingly, it was found that DWNTs exhibit a negative birefringence, in contrast to the positive signal found for SWNTs. Electric dichroism experiments allowed the conclusion that the negative sign of the birefringence is not due to an anomalous orientation, but rather to a negative optical polarizability anisotropy. This anomalous feature could be explained taking into account the absorptivity of the DWNTs.

## Acknowledgements

Financial support for this investigation by Junta de Andalucía, Spain (grant No. PE2012-FQM0694), MICINN, Spain (project No. FIS2013-47666-C3-1-R), is gratefully acknowledged. One of the authors (P. A.) thanks MEC, Spain for her FPU grant and University of Granada, Spain, for her mobility grant.

# 6

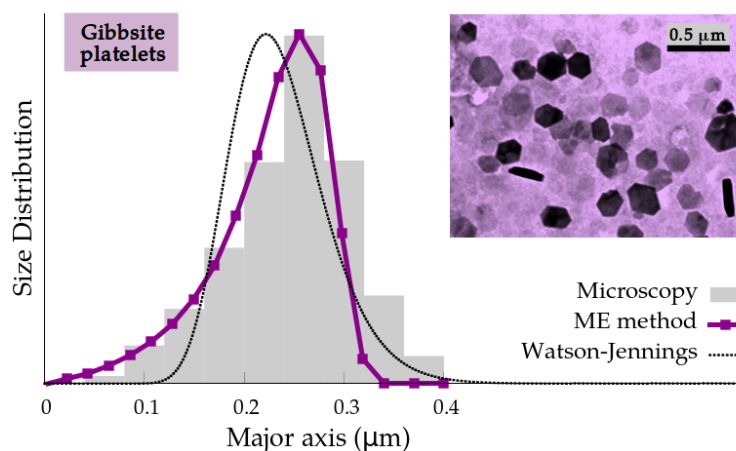
## DETERMINATION OF THE SIZE DISTRIBUTION OF NON-SPHERICAL NANOPARTICLES BY ELECTRIC BIREFRINGENCE-BASED METHODS



## Determination of the Size Distribution of Non-Spherical Nanoparticles by Electric Birefringence-Based Methods

P. Arenas-Guerrero, A. V. Delgado, K. J. Donovan, K. Scott, T. Bellini, F. Mantegazza, M. L. Jiménez (2018). *Scientific Reports*, 8(1), 9502.

The in situ determination of the size distribution of dispersed non-spherical nanoparticles is an essential characterization tool for the investigation and use of colloidal suspensions. In this work, we test a size characterization method based on the measurement of the transient behaviour of the birefringence induced in the dispersions by pulsed electric fields. The specific shape of such relaxations depends on the distribution of the rotational diffusion coefficient of the suspended particles. We analyse the measured transient birefringence with three approaches: the stretched-exponential, Watson-Jennings, and multi-exponential methods. These are applied to six different types of rod-like and planar particles: PTFE rods, goethite needles, single- and double-walled carbon nanotubes, sodium montmorillonite particles and gibbsite platelets. The results are compared to electron microscopy and dynamic light scattering measurements. The methods here considered provide good or excellent results in all cases, proving that the analysis of the transient birefringence is a powerful tool to obtain complete size distributions of non-spherical particles in suspension.





## 6.1. Introduction

Non-spherical micro and nanoparticles have gained a growing interest because of the number of applications associated specifically to shape (drug delivery, nanosensors, electrorheology, printed electronics, photodetectors, ... [15, 168–171]) as well as their possible use as models with well defined aspect ratios. Progress in size characterization techniques for these particles is thus essential both for further development of these applications and for general progress in nanoparticle synthesis [172–174]. While historically most efforts in size characterization have been directed towards spherical geometries [175], recent works have specifically targeted the size characterization of non-spherical particles.

Thus, techniques such as micro-flow imaging, asymmetrical flow field fractionation, dynamic light scattering (DLS), focused beam reflectance measurements or centrifugal separation analysis have been applied to particles with different shapes, although there are still many limitations [176–180]. Very promising results have been achieved with the analysis of the optical absorption spectra of two-dimensional materials like MoS<sub>2</sub> [181]. For more general non-spherical geometries, the study of the electric birefringence of dispersed particles has proven a useful tool for size characterization [182].

### 6.1.1. DLS for size characterization of non-spherical particles

Dynamic light scattering is an in situ size characterization technique for nanoparticles in suspension based on the measurement of their translational diffusion coefficient, related to the length  $L$  of their major axis as

$$D = \frac{k_B T}{3\pi\eta L} F_D \quad (6.1)$$

where  $\eta$  is the viscosity of the solvent,  $k_B$  the Boltzmann constant and  $T$  the temperature of the sample.  $F_D$  is a geometrical coefficient depending on the shape, but not the size, of the particles. For spheres,  $F_D = 1$ . Expressions of  $F_D$  for the geometries used in this work can be found in the Supporting Information.

DLS is the most used tool for the size characterization of spherical particles, commercial equipments being available and widespread. In many cases, these commercial devices, prepared for spheres, are used for the size characterization of non-spherical particles in suspension [177, 183–189]. However, it has been shown that, for these geometries, the contribution of rotational diffusion, not taken into account, can have important effects on the DLS determinations [190, 191], and hence alternative approaches must be proposed.

In recent years, an effort is being made to develop depolarised dynamic light scattering as a suitable tool for the characterization of non-spherical particles [178, 192–197]. Nevertheless, this technique still faces experimental challenges and cannot yet be considered as a widespread method [198]. Moreover, the results are still limited to average dimensions of the particles and can hardly provide complete size distributions.

### **6.1.2. Electric birefringence-based methods for size characterization**

Electric birefringence (EB) is the macroscopic optical anisotropy that emerges in a suspension of non-spherical particles when they are oriented by the application of an external electric field. Upon removal of the field, thermal agitation randomises the orientation of the particles and the birefringence of the sample decays. This randomisation process, controlled by rotational diffusion and strongly size-dependent, can be monitored via the measurement of the birefringence decay and, in this manner, information on the size distribution of the suspended particles can be extracted.

The use of birefringence-based methods for particle size characterization presents several advantages. First of all, this technique analyses the particles directly in suspension, so they do not need to be dried out or placed near a surface. This avoids the corruption of the sample and the modification of the state of aggregation. Secondly, a very wide range of sizes, including the nano and microscale, can be studied with the same method. In this technique, it is not necessary to know the concentration of the sample, as long as it can be ensured that particle interactions do not modify the

rotational diffusion of the single particle.

EB-based methods measure the rotational diffusion coefficient  $\Theta$  of the particles, which depends on size as

$$\Theta = \frac{3k_B T}{\pi\eta L^3} F_\Theta \quad (6.2)$$

where  $F_\Theta$  is a shape factor, with a value of 1/3 in the case of spheres. Expressions of  $F_\Theta$  for the geometries used in this work can be found in the Supporting Information. Note that the dependence of rotational diffusion on particle size is much stronger than that of translational diffusion. Therefore, EB measurements are more sensitive to size than DLS experiments. Moreover, the EB measurements are not affected by translational diffusion, which simplifies the data analysis as compared to DLS, affected by both rotational and translational diffusion.

With this motivation, in this work we analyse the suitability of three different birefringence-based approaches for particle size determination: the stretched exponential (SE) [45, 199], multi-exponential (ME) [47] and Watson-Jennings (WJ) [48] methods. From the analysis of a single birefringence decay, the former enables the determination of the average particle dimensions, and the latter two can provide a complete size distribution of the particles in the sample. It is worthy to note that the ME method was proposed elsewhere [47], but it has not been experimentally tested for colloidal particles.

These methods are applied to suspensions of four different types of elongated particles, namely teflon rods, goethite needles, and single- and double-walled carbon nanotubes, and two types of planar particles, sodium montmorillonite particles and gibbsite platelets. The obtained results are compared amongst the three methods and to size distributions obtained from electron microscopy (EM) and DLS measurements.

Recall that when a suspension of non-spherical particles is subjected to an external electric field, this will induce an anisotropic distribution of particle orientations because of the torque of the field on the induced and/or permanent dipoles of the particles and their electrical double layers. As a consequence, an optical anisotropy arises at the macroscopic scale, this

is, the refractive index of the suspension along the direction parallel to the electric field ( $n_{\parallel}$ ) is different to that along the perpendicular direction ( $n_{\perp}$ ). The difference  $\Delta n = n_{\parallel} - n_{\perp}$  is the electric birefringence of the system.

When the field is turned off, the particles randomise their orientation due to rotational diffusion. The three EB-based methods mentioned for size characterization measure the diffusion coefficient  $\Theta$  of the particles analysing this transient behaviour of electric birefringence upon removal of the electric field. They can be summarised as follows (more detailed information is provided in the Supplementary Information file):

**SE Method.** The decay of the electric birefringence of a polydisperse sample is expected to be, under reasonable assumptions, in the form of a stretched exponential function [45, 199]

$$\Delta n(t) = \Delta n_0 \exp \left[ - \left( \frac{t}{\tau} \right)^{\alpha} \right] \quad (6.3)$$

where  $\Delta n_0$  is the initial value of the birefringence,  $\alpha$  a polydispersity factor and  $\tau$  a characteristic decay time, which can be related to the average rotational diffusion coefficient of the particles as  $\Theta = \frac{1}{6\tau}$ .

As previously mentioned, the diffusion coefficient is strongly dependent on the particle size (Equation 6.2), expressions being available for simplified geometries (presented in the Supporting Information). Thus, from the obtained value of  $\Theta$ , the average dimensions of the particles can be estimated. Note that, since the birefringent signal is proportional to the particle volume, the average values provided by this method are volume-weighted.

**WJ method.** The Watson-Jennings method [48] assumes that the length distribution of the sample has the shape of a log-normal function

$$P(L) = \frac{1}{L\sigma(2\pi)^{1/2}} \exp \left\{ \frac{-[\ln(L/L_M)]^2}{2\sigma^2} \right\} \quad (6.4)$$

where  $L_M$  is the median and  $\sigma$  the breadth parameter of the distribution. For highly oriented systems, these parameters are directly related to the

initial logarithmic derivative,  $D_{\text{WJ}}$ , and the area under the curve,  $I_{\text{WJ}}$ , of the normalised birefringence decay, as

$$D_{\text{WJ}} = \frac{d}{dt} \left( \ln \frac{\Delta n(t)}{\Delta n_0} \right)_{t \rightarrow 0} = -\frac{6L_{\text{M}}^3}{F\Theta} e^{15\sigma^2/2} \quad (6.5)$$

$$I_{\text{WJ}} = \int_0^\infty \frac{\Delta n}{\Delta n_0} dt = \frac{e^{9\sigma^2}}{D_{\text{WJ}}} \quad (6.6)$$

In this manner,  $L_{\text{M}}$  and  $\sigma$ , and hence the size distribution of the sample, can be obtained from a single birefringence decay measurement.

**ME method.** The multi-exponential method [47] assumes that the birefringence decay can be built as a superposition of single exponential decay processes, each corresponding to a fraction of a well-defined size, as

$$\frac{\Delta n(t)}{\Delta n_0} = \sum_{i=1}^N C_i e^{-t/\tau_i} \quad (6.7)$$

The coefficients  $C_i$  weight the contribution of each population to the overall signal, which in the case of birefringence is proportional to the particle volume. Thus, these coefficients provide a volume distribution of the particle dimensions in the sample. The characteristic decay time for each population is determined from the respective rotational diffusion coefficient with the expression  $\tau_i = 1/6\Theta_i$ , where  $\Theta_i$  can be calculated if the geometry of the particle is known. The values of  $t$  and  $\Delta n$  are obtained from the measured EB decay. The equation system 6.7 is solved to obtain the  $C_i$ .

In contrast with the WJ method, no specific form is assumed for the distribution. Moreover, unlike the SE method, this technique provides a complete size distribution of the particles in suspension. In order to minimize the contribution of experimental noise, the birefringence decay data must be smoothed in some manner. In this work, we have chosen to use the fitting to a stretched-exponential function for the application of the ME Method. Furthermore, it must be noted that a reasonable length range must be found to carry out the calculations. For this purpose, we used the size estimation provided by the SE method.

## 6.2. Methods

We have selected particles both in the micro and nanoscale, with different shapes, including elongated and planar geometries. Goethite and teflon (PTFE) rods were purchased from Sigma Aldrich (Spain) and Ausimont (Italy) respectively. Single- and double-walled carbon nanotubes were acquired from Carbolex (USA) and US Research Nanomaterials (USA). As planar particles we studied gibbsite platelets, synthesised following the procedure described elsewhere [119], and sodium montmorillonite (NaMt) particles, obtained from bentonite (Serrata de Níjar, Spain) by a process of homoionisation to the Na-form [103]. Briefly, this consisted in rinsing the sample with a 1 M sodium chloride solution, and redispersing in deionised water (Milli-Q Academic Millipore, France). All samples were prepared by simple dispersion of the particles in the solvent with the help of a sonicator.

The electric birefringence data presented in this work have been measured in different laboratories using the standard device, based on the measurement of the changes in light transmission through an optical setup containing the suspension, which is subjected to electric field pulses [78]. The DLS measurements have been performed with a commercial apparatus (Zetasizer, Malvern Instruments (UK)) which provides the diameter distribution of the particles assuming they are spherical. In order to obtain the major length of the non-spherical particles, we recalculate the measured translational diffusion coefficient using the expression for spheres and then obtain  $L$  from equation 6.1.

Note that, in order to apply DLS and the three EB-based methods, expressions for the translational and rotational diffusion coefficients of the particles are needed. For this purpose, here we assume that they can be approximated either by short rods, long rods, thin disks or oblate spheroids and use equations 6.1 and 6.2, and the expressions of  $F_D$  presented in the supporting information, where  $\rho$  is the aspect ratio, this is, the quotient between the major and minor axis of the particles.

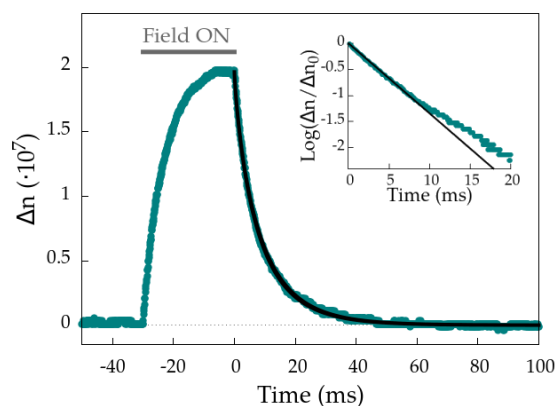


**FIGURE 6.1:** Birefringence signal of the goethite sample subjected to an electric field pulse of 30 ms. The points are the experimental data, and the black line a fitting of the decay to a stretched exponential function. In the inset, the data for short times (points) are presented in logarithmic scale, along with a linear fitting (black line), to show the linear dependence.

## 6.3. Results

Figure 6.1 shows the birefringence signal of the goethite sample. Here, it can be observed that, when the electric field is turned on, the birefringence grows and reaches a stationary value. When the field is turned off, the birefringence decays to zero following a stretched exponential function. In this figure, we also present this decay in logarithmic scale for short times, in order to calculate the initial logarithmic derivative required for the WJ method (Eq. 6.5). The birefringence decay of all the studied suspensions can be consulted in the Supporting Information of this contribution. The results found for the six samples with the SE, ME and WJ methods are presented and discussed below, together with the electron microscopy and DLS measurements.

### 6.3.1. Goethite needles

The electric birefringence of goethite particles, purchased from Sigma Aldrich (USA), was analysed in aqueous suspension, at 10 mg/L. The sample was subjected to electric field pulses of 5 V/mm and 100 kHz. These

and subsequent experiments with aqueous suspensions were carried out at 15°C, to minimise heating effects and solvent evaporation. Figure 6.2a shows a transmission electron microscopy image of these particles, from which the volume-averaged length (0.64  $\mu\text{m}$ ) and mean aspect ratio ( $\rho=12.3$ ) have been obtained. For calculations, we used the expression of the diffusion coefficients of short rods and the microscopy value of  $\rho$ . The assumption of constant aspect ratio is not expected to produce a significant effect on the results, since the *rho*-dependence of  $\Theta$  through  $F(\Theta)$  is very smooth, as compared to the  $L^{-3}$  dependence. In fact, when contrasted with the assumption of constant diameter, both obtained distributions are comparable, although the constant aspect ratio approximation yields better results (Fig. S2 of the Supplementary Information).

The length distributions provided by the ME and WJ methods, together with the one obtained from EM, are shown in Fig. 6.2b. The values of the mean length and standard deviation of all methods, including DLS, can be consulted in Table 6.1. All presented distributions and averages are in volume.

The SE method ( $\tau=7.96$  ms and  $\alpha=0.836$ ) furnishes a mean length of 0.67  $\mu\text{m}$ , within a 5% difference of the microscopy value, and coinciding with the average length provided by the ME method. As shown in Fig. 6.2b, the ME method yields excellent results, as the obtained distribution is almost identical to the one found from EM. The WJ method also gives satisfactory results, with a mean length of 0.68  $\mu\text{m}$ . However, the WJ distribution is narrower than the EM results and its maximum is slightly shifted to the left.

In Table 6.1, the discrepancy of the DLS measurement with EM and the SE, ME and WJ methods is evident. The distribution obtained by DLS is wider and strongly shifted to larger lengths than all other results.

### 6.3.2. PTFE rods

The elongated PTFE particles were purchased from Ausimont (Italy). In the experiments, an electric field of 40 V/mm and 100 kHz was applied to a 0.1% v/v PTFE aqueous suspension. Fig. 6.3a shows a transmission

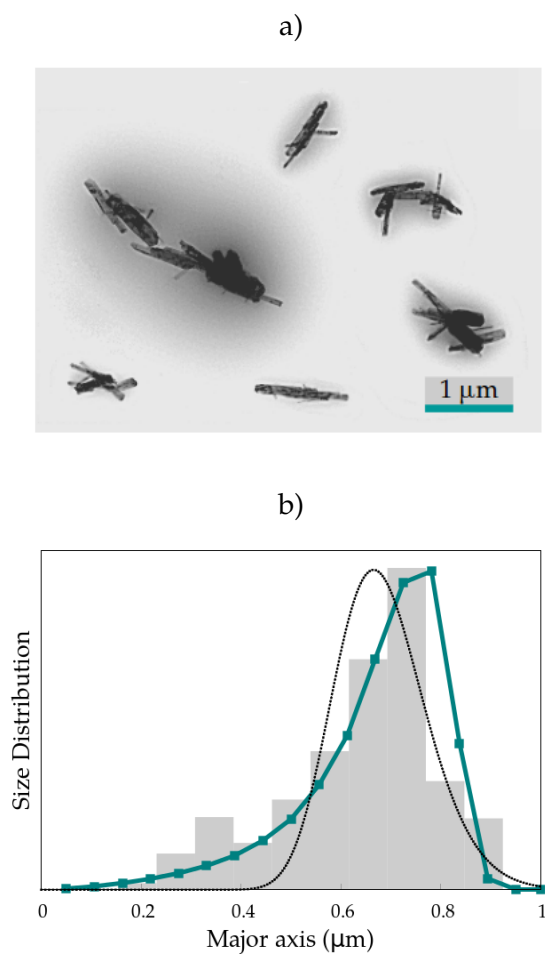


**FIGURE 6.2:** a) Electron microscope image of the goethite particles. b) Volume size distribution obtained via the ME method (colored squares and line) and WJ method (dotted black line), compared with the distribution determined from electron microscopy (grey bars).

**TABLE 6.1:** Volume-averaged length of the major axis of the particles (and standard deviation of the distribution when available) obtained via EM and DLS measurements and with the SE, ME and WJ methods.

	Goethite	PTFE
SE method	0.67 $\mu\text{m}$	0.50 $\mu\text{m}$
ME Method	0.67 $\mu\text{m}$ (21%)	0.49 $\mu\text{m}$ (31%)
WJ method	0.68 $\mu\text{m}$ (14%)	0.46 $\mu\text{m}$ (23%)
Microscopy	0.64 $\mu\text{m}$ (24%)	0.50 $\mu\text{m}$ (22%)
DLS	0.99 $\mu\text{m}$ (38%)	0.24 $\mu\text{m}$ (45%)
	SWNTs	DWNTs
SE method	0.88 $\mu\text{m}$	1.61 $\mu\text{m}$
ME method	0.89 $\mu\text{m}$ (53%)	1.69 $\mu\text{m}$ (98%)
WJ method	0.94 $\mu\text{m}$ (28%)	1.60 $\mu\text{m}$ (57%)
Microscopy	0.89 $\mu\text{m}$ (62%)	0.86 $\mu\text{m}$ (50%)
DLS	0.58 $\mu\text{m}$ (45%)	1.10 $\mu\text{m}$ (27%)
	Gibbsite	NaMt
SE method	0.23 $\mu\text{m}$	1.74 $\mu\text{m}$
ME method	0.23 $\mu\text{m}$ (25%)	1.73 $\mu\text{m}$ (42%)
WJ method	0.24 $\mu\text{m}$ (20%)	1.61 $\mu\text{m}$ (33%)
Microscopy	0.25 $\mu\text{m}$ (25%)	1.62 $\mu\text{m}$ (43%)
DLS	0.18 $\mu\text{m}$ (37%)	0.42 $\mu\text{m}$ (35%)

electron microscope image of the PTFE rods, where it can be observed that they present a significant polydispersity. From this picture, values for the volume-averaged length ( $0.50 \mu\text{m}$ ) and mean aspect ratio ( $\rho = 2.0$ ) were obtained. Again, we modelled the particles as short rods and assumed the microscopy value of  $\rho$ , the same approximation as in the case of goethite.

The results obtained by all methods are presented in Fig. 6.3b and Table 6.1. The SE method ( $\tau=12.00$  ms and  $\alpha=0.721$ ) provides a mean length of  $0.50 \mu\text{m}$ , which is in perfect agreement with both the EM and the ME results. As shown in Fig. 6.3b, the size distribution found by the ME method is very similar to the microscopy one for lengths over  $0.40 \mu\text{m}$ . However, this method predicts the presence of small particles that were not identified in the image, which results in a slightly broader distribution. Note that the PTFE particles present an aspect ratio of 2, which is in the limit of the application range of the expressions used for the diffusion coefficient of short rods. Hence, the deviations could be related to the geometrical approximation. In spite of this, the difference in the average length is only 3%. The WJ method gives very good results, with a size distribution that is very similar to the EM one, but slightly shifted to the left, which results in a value of the mean length 8% lower than expected.

In the DLS measurement of the PTFE sample, two peaks were observed. The one corresponding to shorter lengths is spurious, due to the rotational diffusion effect on the DLS measurement, as already reported elsewhere [191] for suspensions of gold nanorods. This peak was not taken into account for the calculation of the average length and standard deviation presented in Table 6.1. Despite this consideration, the obtained mean length is smaller by 50% than measured by EM and the EB-based methods, and the distribution is notably wider.

### 6.3.3. Single-walled carbon nanotubes

Single-walled carbon nanotubes (SWNTs) were suspended in 1,2-dichloroethane with a volume fraction of  $10^{-4}\%$ . The carbon nanotubes required a very high field,  $250 \text{ V/mm}$ , to be oriented. The field frequency was 1 kHz and the measurement temperature  $20^\circ \text{C}$ .

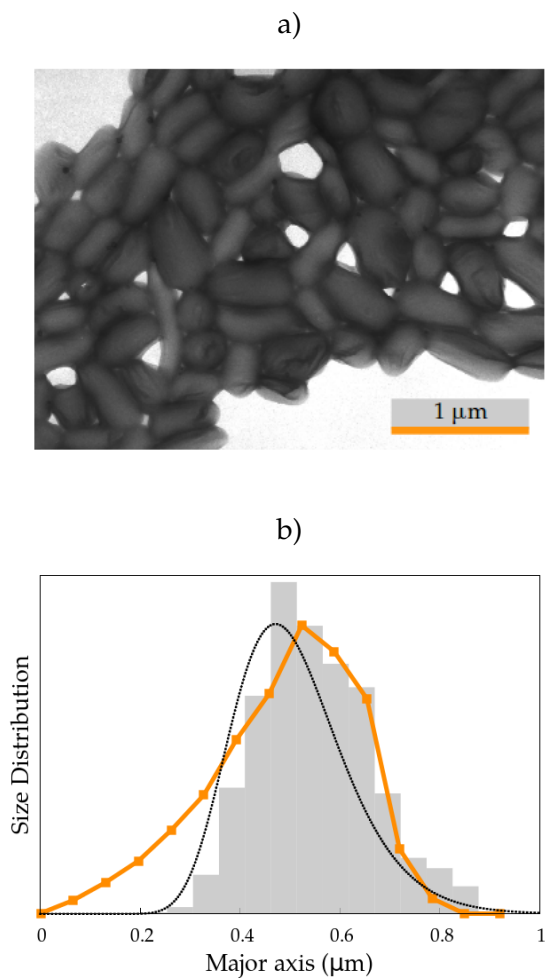


**FIGURE 6.3:** Same as Fig. 6.2 but for the PTFE rods.

A transmission electron microscope image of the SWNTs can be found in Fig. 6.4a, where it can be observed that the particles appear bundled, with a mean bundle width of 12 nm. From 300 particles, an average length value of  $0.98 \mu\text{m}$  was obtained. The polydispersity in length is quite important, whilst the width is more uniform. Naked-eye distinction of the bundles in the picture is not straightforward, but an effort has been made to look at the image at different zooms to account for all present lengths. In calculations, we used the expression of the diffusion coefficients of long rods and assumed a constant particle diameter of 12 nm. All results are presented in Table 6.1 and Fig. 6.4b.

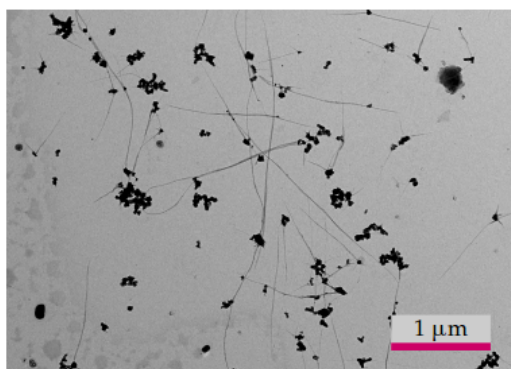
The birefringence decay fits perfectly to a stretched exponential function ( $\tau=6.95 \text{ ms}$ ,  $\alpha=0.545$ ), and the SE method furnishes a value for the volume-averaged length very similar to that found from EM, with less than a 1% difference. The ME method also provides excellent results, giving a size distribution very similar to the one found from microscopy determinations, the more so taking into account the poor particle distinction in the picture. The WJ method calculates a mean length reasonably similar to the EM result, within a 5% difference, but the distribution is notably different, as it is clear from the comparison of their standard deviations.

The results obtained by the EM and the EB-based methods are also compatible with the mean length value of  $1.08 \pm 0.20 \mu\text{m}$  found elsewhere [89] for a similar sample via the measurement of the electrical polarizability anisotropy of the conducting tubes. On the other hand, the results found by DLS deviate strongly from all other methods, being the given mean length 35% smaller than, for example, the EM value.

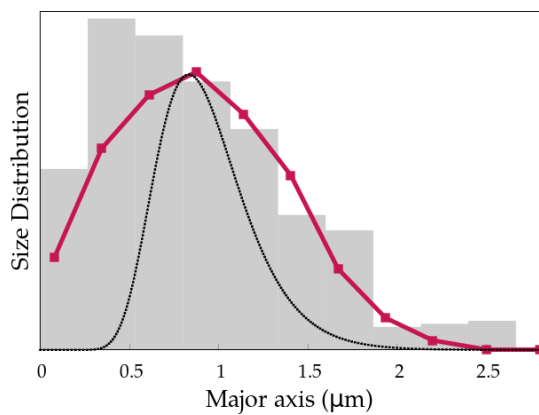
#### 6.3.4. Double-walled carbon nanotubes

The birefringence of double-walled carbon nanotubes (DWNTs) was determined in the same experimental conditions as the SWNT sample. A transmission electron microscope image of these particles (Fig. 6.5a) shows that they are also bundled, with a bundle width of 9 nm. From 75 tubes, a mean length of  $0.86 \mu\text{m}$  was obtained. Again, the particles are not easily distinguished. For the calculations, we use a constant width of 9 nm and

a)



b)

**FIGURE 6.4:** Same as Fig. 6.2 but for the SWNT suspension.

the diffusion coefficient of long rods.

The birefringence decay of this suspension is quite slow and could be fitted by a stretched exponential function with fitting parameters  $\tau=33.4$  ms and  $\alpha=0.3166$ , indicating a very polydisperse sample. The results are presented in the usual way in Table 6.1 and Fig. 6.5b, where it can be observed that the volume-averaged particle length provided by the three EB-based methods, around  $1.63 \mu\text{m}$ , is quite different from that obtained via EM.

These findings are in line with the results reported elsewhere [89], where the length of the bundles in a similar sample was obtained from the experimental determination of their electrical polarizability. The obtained mean length,  $1.63 \pm 0.10 \mu\text{m}$ , is identical to the value found by our methods. These results suggest that, when in suspension, the DWNTs are more entangled than observed by EM. This is one of the advantages of the birefringence-based methods over the use of microscopy techniques, since particles are analysed directly in suspension and do not need to be dried out.

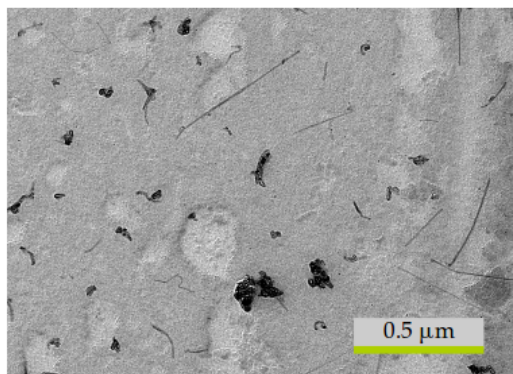
In the DLS measurement of the DWNTs, a spurious peak was found and removed for the calculations. In spite of this, again, the measured value of the mean length is notably smaller than that found by the EB-based methods (Table 6.1).

### 6.3.5. Gibbsite platelets

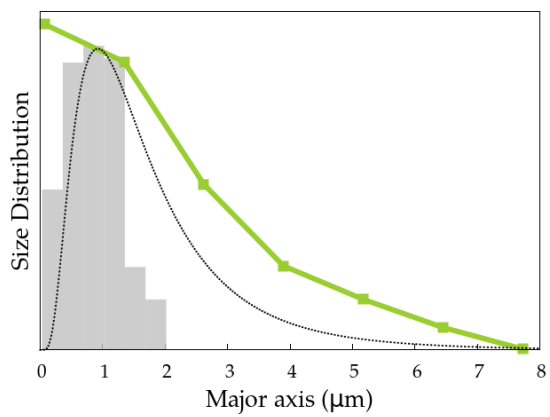
We also considered the birefringence decay of gibbsite platelets, studied in aqueous suspension with a particle concentration of 0.1% v/v and 0.1 mM potassium chloride, under a 30 V/mm electric field of 100 kHz. In the transmission electron microscope image of the sample (Fig. 6.6a) the platelets can be easily told apart. From this picture, a volume-averaged length of  $0.25 \mu\text{m}$  was obtained. Since the particles are very slim, the thin disk approximation was used for the calculations. The results are presented as before in Table 6.1 and Fig. 6.6b.

The decay of the birefringence can be suitably fitted to a stretched exponential function ( $\tau=8.7$  ms,  $\alpha=0.501$ ). The SE method provides a mean diameter of  $0.23 \mu\text{m}$ , very similar to the microscopy value and identical to the ME result. The size distribution obtained by the ME method is in very

a)



b)

**FIGURE 6.5:** Same as Fig. 6.2 but for the DWNT sample.

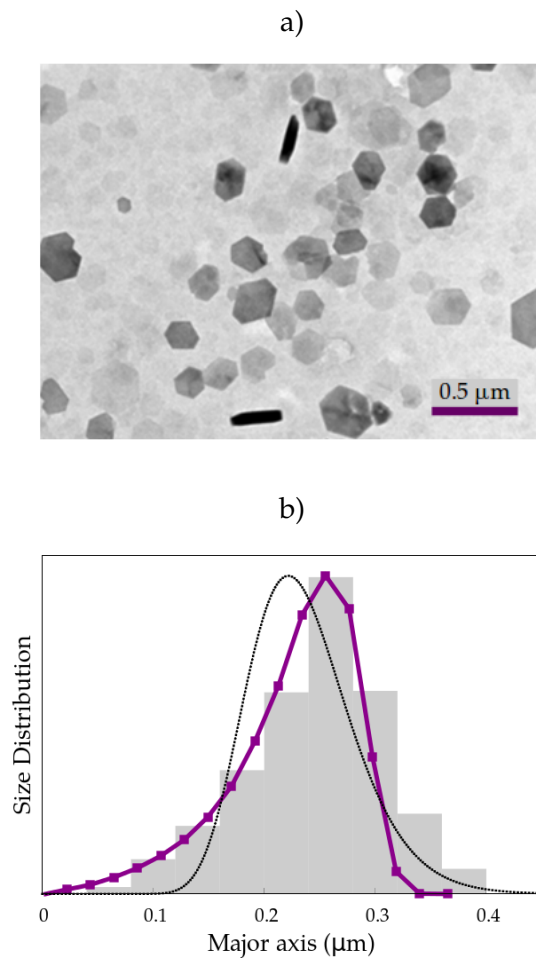


FIGURE 6.6: Same as Fig. 6.2 but for the gibbsite platelets.

good agreement with the EM determinations, although there is a slight underestimation of the presence of particles over  $0.3 \mu\text{m}$  that accounts for the 8% difference in the mean length values.

In the case of the WJ method, although the obtained average length and standard deviation are similar to the ones given by the other techniques, the distribution is somewhat different, with the peak slightly shifted to shorter sizes. This could be due to the log-normal distribution assumed in this procedure, that does not seem to account for the distribution found by EM.

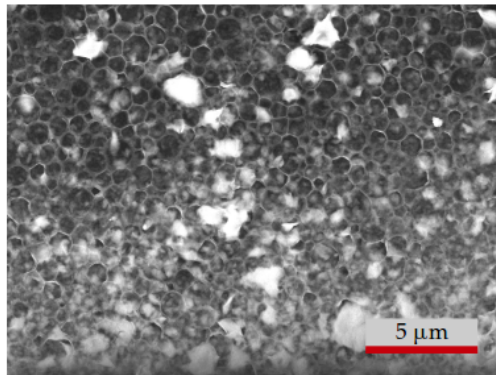
As for the DLS results, once more, the obtained size distribution is considerably wider and strongly shifted to short lengths as compared to both EM determinations and the SE, ME and WJ results.

### 6.3.6. Montmorillonite particles

Finally, we analysed the electric birefringence of NaMt particles dispersed in a 0.3 mM sodium chloride solution, with a concentration of 1 g/L. An oscillating electric field of 10 V/mm and a frequency of 1 MHz was applied. An environmental scanning electron microscope picture of the sample is shown in Fig. 6.7a, where it can be seen that distinction of the particles is quite difficult. From 320 particles, a value of  $1.65 \mu\text{m}$  for the average diameter was obtained. For the calculations, the geometry was modelled by oblate spheroids with a constant aspect ratio of 3.3 [78], an approximation already discussed in the goethite case. The results are presented in Table 6.1 and Fig. 6.7b.

The birefringence decay fits perfectly to a stretched exponential function ( $\tau=375 \text{ ms}$ ,  $\alpha=0.594$ ), and provides a volume-averaged length of  $1.74 \mu\text{m}$ . This is within 8% of the microscopy value and very similar to the ME result. The latter fails to account for the size distribution found via EM, as it overestimates the presence of long particles. This could be attributed to the approximations used for these particles, which are very irregular and planar, but were approximated by spheroids. In spite of this, both distributions are reasonably similar, with the same standard deviation and a mean length differing only by 7%. The WJ method provides very good results,

a)



b)

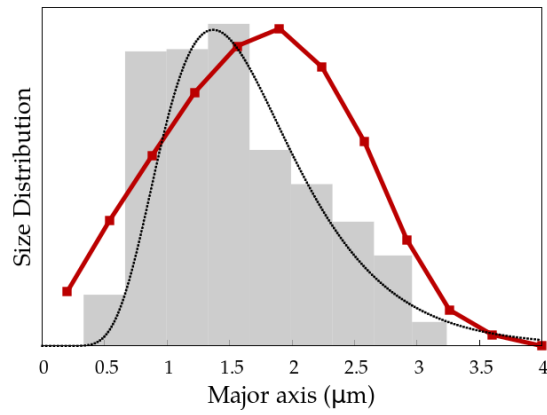


**FIGURE 6.7:** Same as Fig. 6.2 but for the NaMt sample.

giving the same value of the mean length as EM and a good shape of the size distribution, although the standard deviation is smaller than measured by microscopy.

For the sodium montmorillonite particles, a spurious peak was found in the DLS measurements and removed for the calculations. The mean length found by this technique is again notably smaller than predicted by all other methods.

## 6.4. Discussion

In this work, we have compared the performance of three birefringence-based characterization techniques, namely the stretched-exponential, Watson-Jennings and multi-exponential methods, with electron microscopy and DLS measurements. Differently from the other two EB-based approaches, the SE method enables determining only the average size, which we find to match the one obtained by the ME method. This is expected, since the two approaches share common assumptions. The value determined from SE allows a first estimate of the size, which is useful to choose the range of work of the ME method.

The ME method furnishes a complete size distribution of the sample, and the results are excellent in most cases. Thus, for the goethite needles, the SWNTs and the gibbsite platelets, the obtained distributions are in perfect agreement with the microscopy results. For the DWNTs, the ME method gives a length identical to the one found by other techniques [89] and also by the WJ method, which suggests that these particles are more bundled in suspension than when prepared for microscopy measurements.

For the PTFE and NaMt particles, there are slight differences between the ME and the EM results, but they are not large (below 8%) and can be attributed to the approximations employed such as a constant aspect ratio or the simplified geometry for the rotational diffusion coefficient. Therefore, these differences may be tackled by an improvement of the models. Moreover, distinction of the particles in the microscope pictures is sometimes non-straightforward, as in the case of the SWNTs, which could also

account for slight deviations between the results.

The WJ method, in addition to the already mentioned approximations, assumes a fixed shape for the size distribution of the sample, which could be responsible for the larger deviations with respect to the microscopy results that are observed in almost all cases as compared to the ME method. For instance, for the SWNTs, where the sample deviates strongly from the log-normal length distribution, the WJ results differ substantially from the ones obtained by both EM and the ME method.

In our results, it can be observed that the peak of the distributions obtained by the WJ method is systematically shifted to the left as compared with the other procedures. This can be understood taking into account that the log-normal function must go quickly to zero for short lengths, underestimating the presence of small particles, which leads to a shifted maximum. Furthermore, the determination of the initial logarithmic derivative, needed for the WJ calculations, is in some cases non-straightforward, since it is sometimes unclear where the linear behaviour is lost. In spite of this, the results of the WJ method are very satisfactory.

In general, it can be remarked that, except for the DWNTs for the explained reasons, deviations between the mean length obtained by EM and the EB-based methods are in all cases smaller than 8%. This is an excellent result taking into account the very different nature, characteristic sizes and geometries of the selected particles.

On the other hand, the DLS results present strong deviations with respect to the average length found by microscopy, no less than 28% in all cases and up to 74%. Although no systematic behaviour can be confirmed, the DLS distributions present normally a shorter mean length than that found by EM and the SE, ME and WJ methods, which can be attributed to the contribution of rotational diffusion, interpreted as a faster translational diffusion, and hence a smaller size, by the commercial setup. In addition, DLS typically predicts wider standard deviations, a well known feature, analysed elsewhere for elongated geometries [191]. These findings show that the use of commercial DLS setups provides a rough estimation of the characteristic size of non-spherical particles, but not a complete and accurate description of the sample. Nevertheless, these measurements have proven

useful, for example, for the characterization of two-dimensional particles, for which a good correlation can be found between the hydrodynamic radii and the dimensions obtained by EM [177].

In conclusion, the results obtained in this work show that the analysis of transient electric birefringence is a powerful tool for the determination of the size distribution in polydisperse suspensions of non-spherical particles. The multi-exponential method was found to be the most suitable technique for the analysis of the birefringent decay, providing excellent results, although the Watson-Jennings method performance is also very satisfactory.

## Supplementary information

### Translational and rotational diffusion coefficients of non-spherical particles

The rotational and translational diffusion coefficients of suspended particles,  $D$  and  $\Theta$  respectively, can be calculated as indicated in Equations 1 and 2 of the main text, where  $F_D$  and  $F_\Theta$  are geometrical factors depending only on the particle shape. In this work, we used the expressions of  $D$  and  $\Theta$  for several simplified geometries, namely, short rods [160], long rods [200], thin disks [48] and oblate spheroids [132]. The expressions of  $F_D$  and  $F_\Theta$  corresponding to these particle shapes are presented in Table 6.2.

### Experimental birefringence decay curves

The normalised birefringence decays of all the suspensions studied in this work are shown in Fig. 6.8, where it can be observed that the data are suitably fitted by stretched exponential functions in all cases. In this figure, we also show the decays in logarithmic scale for short times, in order to calculate the initial logarithmic derivative required for the WJ method.

**TABLE 6.2:** Expressions of the coefficients  $F_D$  and  $F_\Theta$  in equations 6.1 and 6.2 for the simplified geometries used in this work.

Short rods	$F_D = \log \rho + 0.312 + 0.565/\rho - 0.1/\rho^2$ $F_\Theta = \log \rho - 0.662 + 0.918/\rho + 0.05/\rho^2$
Long rods	$F_D = \log \rho + 0.312 + 0.565/\rho - 0.1/\rho^2$ $F_\Theta = \log \rho - 0.2/(\log 2\rho) - 16/(\log 2\rho)^2$ $+ 63/(\log 2\rho)^3 - 62/(\log 2\rho)^4$
Thin disks	$F_D = \pi/2 \quad F_\Theta = \pi/4$
Oblate spheroids	$F_D = \rho \arctan(\sqrt{\rho^2 - 1})/\sqrt{\rho^2 - 1}$ $F_\Theta = \rho^3((2 - \rho^2)G_\Theta - 1)/(2 - 2\rho^4)$ $G_\Theta = \arctan(\sqrt{\rho^2 - 1})/\sqrt{\rho^2 - 1}$

## Data analysis

The birefringence decay of a monodisperse sample is known to be in the form of a single-exponential function, with characteristic time  $\tau_m$ :

$$\Delta n(t) = \Delta n_0 \exp[-t/\tau_m] \quad (6.8)$$

For a polydisperse system, the overall signal is a superposition of these independent exponential processes, and the contribution of every population must be taken into account. In this manner, the birefringence signal can be expressed as

$$\Delta n(t) = \Delta n_0 \int P(L)S(L) \exp[-t/\tau(L)]dL \quad (6.9)$$

where  $\tau(L)$  is the decay time for a particle with characteristic dimension  $L$ ,  $P(L)$  is the size distribution of the sample and  $S(L)$  measures the con-

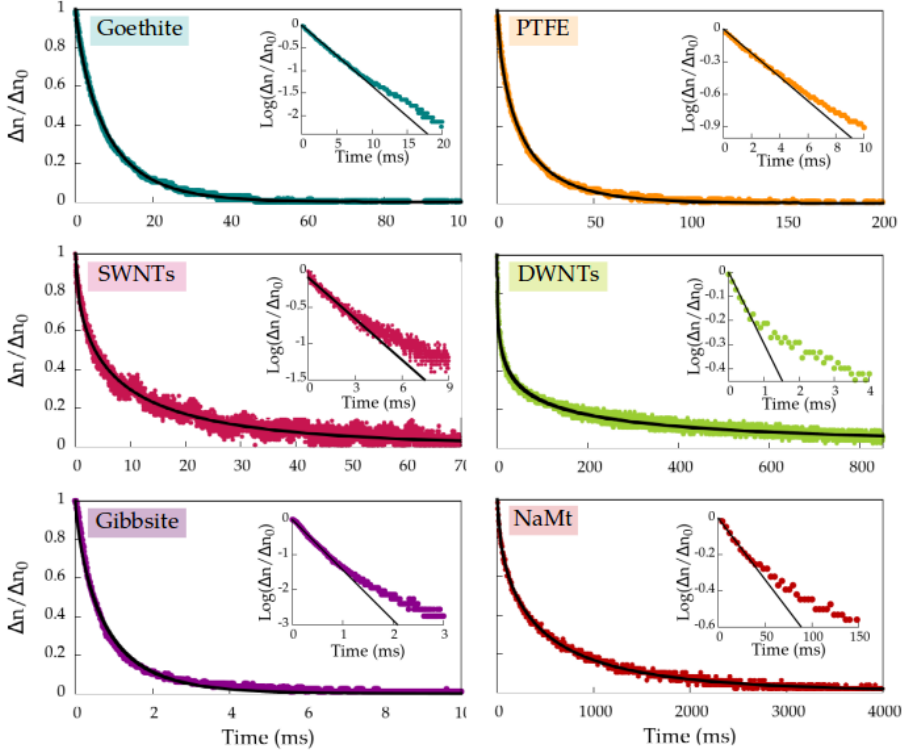


**FIGURE 6.8:** Normalized birefringence decays of the studied suspensions. The points are the experimental data, and the black lines fittings to stretched exponential functions. In the insets, the data for short times (points) are presented in logarithmic scale, along with a linear fitting (black line), to show the linear dependence.

tribution of each independent process to the total birefringence signal. It is further assumed that  $P(L) \propto \exp(-AL^p)$ ,  $S(L) \propto L^r$  and  $\tau(L) \propto L^q$ , where  $A$  is a constant and  $p$ ,  $q$  and  $r$  positive integers. As a result, it has been demonstrated that [45, 46]

$$\Delta n(t) \propto t^\gamma \exp[-t/\tau_m] \quad (6.10)$$

where the contribution of the  $t^\gamma$  factor is only significant at very short times, and is neglected to obtain equation 3 of the main text. A non-linear fitting of the birefringence decay data to this stretched-exponential function yields the parameters  $\alpha$  and  $\tau$ , and from the latter the rotational diffu-

sion coefficient is obtained.

A more realistic shape for the size distribution is typically the log-normal function (equation 4 of the main text). Assuming this distribution and calculating the average of the rotational diffusion coefficient of the particles and its inverse, it is possible to relate the distribution parameters,  $L_M$  and  $\sigma$  to the initial logarithmic derivative and the area under the curve of the normalised birefringence decay. Details of the derivation of equations 5 and 6 of the main text can be found in the original reference [48]. The area under the curve,  $I_{WJ}$ , is calculated numerically, whereas the initial derivative,  $D_{WJ}$  is obtained from a linear fitting of the short-time decay data, as shown in Figure 6.8.

In the multi-exponential method, no assumption is made for the shape of the size distribution of the sample. Instead, a superposition analogous to that made in equation 6.9 is used in the discrete form, as indicated in equation 7 of the manuscript. For the data analysis, the experimental results are previously fitted to a stretched-exponential function, in order to smooth the time dependence. Then, this function is sampled, and  $M=10.000$  pairs of  $t_j, \Delta n(t_j)$  are taken. Later,  $N$  size intervals, typically around 10, are chosen. The covered size range must be reasonable, and can be estimated from the SE result. Finally, a linear equation system is obtained, which can be expressed in matrix form as:

$$\begin{pmatrix} \Delta n(t_1) \\ \Delta n(t_2) \\ \dots \\ \Delta n(t_M) \end{pmatrix} = \begin{pmatrix} e^{-t_1/\tau_1} & e^{-t_1/\tau_2} & \dots & e^{-t_1/\tau_N} \\ e^{-t_2/\tau_1} & e^{-t_2/\tau_2} & \dots & e^{-t_2/\tau_N} \\ \dots & \dots & \dots & \dots \\ e^{-t_M/\tau_M} & e^{-t_M/\tau_2} & \dots & e^{-t_M/\tau_N} \end{pmatrix} \begin{pmatrix} C_1 \\ C_2 \\ \dots \\ C_N \end{pmatrix} \quad (6.11)$$

Here, the only unknowns are the  $C_i$ , obtained numerically by solving the matrix equation with Matlab<sup>®</sup>.

### Effect of the constant aspect ratio approximation

For goethite needles, PTFE rods and NaMt particles, the aspect ratio is assumed to be constant in order to carry out the required calculations. As

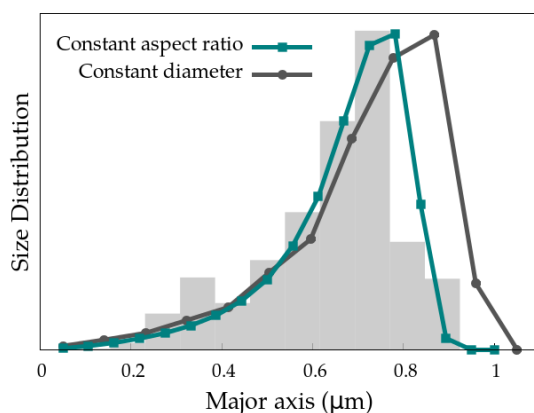


**FIGURE 6.9:** Comparison of the size distributions obtained by the ME method for the goethite sample, assuming a constant aspect ratio and a constant particle width. The microscopy result (grey bars) is also shown.

discussed in the main text, this approximation is not expected to have a strong effect on the final results, due to the smooth dependence of the rotational diffusion on  $\rho$ , as compared to the major axis length. As an example, Figure 6.9 shows the size distribution of the goethite sample obtained by the ME method using the constant aspect ratio and the constant particle diameter assumptions. The differences are not very pronounced, indicating that the chosen approximation is not critical. Nevertheless, it is clear that the constant  $\rho$  assumption yields better results, since it is more reasonable for this system.

# 7

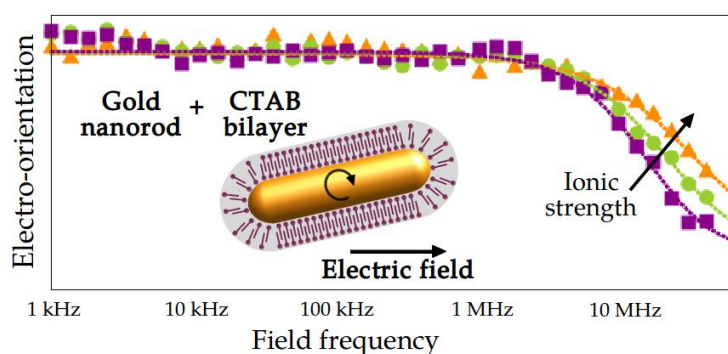
## ELECTRIC BIREFRINGENCE OF GOLD NANORODS: EFFECT OF SURFACTANT COATING



## Electric Birefringence of Gold Nanorods: Effect of Surfactant Coating

P. Arenas-Guerrero, S. Ahualli, A. V. Delgado,  
M. L. Jiménez. Submitted to **Soft matter**.

The optical and electrical properties of gold nanorods, together with the possibility to control their orientation, have proven crucial for their use in applications such as metamaterials, nanoelectronics, molecular devices or particle traps. Due to the synthesis procedure, these particles present a complex structure, with a metallic core surrounded by a CTAB soft layer that prevents particle aggregation. When the rods are immersed in liquid media, their orientation can be controlled by electric fields and monitored by electro-optical techniques. We demonstrate that both the charged CTAB layer and the conducting core affect electro-orientation. An interpretation in light of a soft particle polarization model is provided: below 1 MHz, ions in the surfactant layer produce a large dipole accountable for the response of the system. With this model, we obtain the charge density of the CTAB coating and the conductivity of the metallic core, which is of the same order as values found for similar particles. The results are contrasted with electrophoresis data, providing information about the charge on the particle-solution interface. We also study the transient orientation behaviour, and demonstrate that the presence of CTAB micelles in the medium slows down the dynamics of the system.





## 7.1. Introduction

In recent years, gold nanorods (AuNRs) have sparked a strong interest because of their unusual physical properties and their electronic, optical and biomedical applications, enhanced by their non-spherical shape [201–205]. Moreover, the possibility to control the orientation of these particles has opened new possibilities of applications ranging from nanoelectronics to particle traps [10, 11, 206, 207]. For this reason, the manipulation of gold nanorods in suspension via the application of electric fields is rapidly gaining importance [74, 208, 209].

Nevertheless, although many steps have been taken towards the synthesis of highly monodisperse elongated gold nanoparticles and their optical and geometrical characterization, few works target the study of their interaction with external electric fields [210–213]. In fact, the fundamental electrokinetic properties of metallic particles in aqueous suspension have received far less attention than those of insulating ones. Furthermore, in the few works related to this topic, particles are made of an homogeneous conducting material [73, 74, 214, 215]. However, gold nanorods are normally covered by a soft capping layer, necessary to prevent particle aggregation. While the chemical and geometrical properties of this shell have been extensively studied [216–220], little attention has been paid to the effect that its presence may exert on the electrical properties of the conducting rods.

As it is well known, electric birefringence (EB) is an electro-optical phenomenon associated to the orientation of non-spherical particles in suspension under the application of external electric fields, and it has been demonstrated as a powerful tool for their geometrical, electric and optical characterization. In particular, the birefringence spectrum (that is, the frequency dependence of the EB signal) is strongly related to the polarization mechanisms of the particles, and hence provides vital information on their interaction with electric fields [1, 25, 26, 49, 78, 123]. Therefore, the analysis of the experimental birefringence phenomenology of gold nanorods can provide useful information for further understanding of these particles and progress in their applications.

With this motivation, in this contribution we present an extensive inves-

tigation of the EB of gold nanorods in aqueous suspension, together with flow birefringence, electron transmission microscopy and depolarised dynamic light scattering measurements as complementary experiments.

## 7.2. Experimental section

### 7.2.1. Materials

Gold nanorods were synthesised by the  $\text{Ag}^+$ -mediated seeded growth method [104]. The seed solution was obtained adding 25  $\mu\text{L}$  of 50 mM  $\text{HAuCl}_4$  and 300  $\mu\text{L}$  of 10 mM  $\text{NaBH}_4$  to 4.7 mL of a 100 mM CTAB solution. For the growth solution, 190  $\mu\text{L}$  of 37% HCl, 120  $\mu\text{L}$  of 10 mM  $\text{AgNO}_3$ , 100  $\mu\text{L}$  of 50 mM  $\text{HAuCl}_4$  and 100  $\mu\text{L}$  of 100 mM ascorbic acid were added to 10 mL of a 0.1 M CTAB solution. Lastly, 24  $\mu\text{L}$  of the seed solution were added to the growth solution and the mixture was stored overnight at 30°C. As mentioned, the AuNRs synthesised in this manner are stabilised by a 3.3 nm compact bilayer of CTAB that covers the rods completely [218].

Fig. 7.1a shows a transmission electron microscope image of the AuNRs together with a length histogram obtained from 70 particles. The rods present an average length of  $L=56\pm 9$  nm and a mean diameter of  $d=16\pm 4$  nm. In Fig. 7.1b, the optical absorption spectrum of a 9.8 mg/L suspension of AuNRs, obtained with a 6705 UV-VIS spectrophotometer (Jenway, UK), is shown. Here, two absorption peaks due to the plasmon resonance, corresponding to the two characteristic dimensions of the rods, are clearly observed.

From the amount of gold precursor, a particle concentration of 98 mg/L was calculated for the suspension resulting from the synthesis. This estimation is reasonable, since the extinction coefficient obtained from the absorption measurements at the plasmon peak,  $6.6 \cdot 10^9 \text{ L mol}^{-1} \text{ cm}^{-1}$ , is in good agreement with measured values of  $4.5 - 6.5 \cdot 10^9 \text{ L mol}^{-1} \text{ cm}^{-1}$  for rods with an effective radius of 13-15 nm [106], similar to that of our particles. In electric birefringence measurements, the used samples are diluted down to 90% from the initial suspension and the particle concentration is

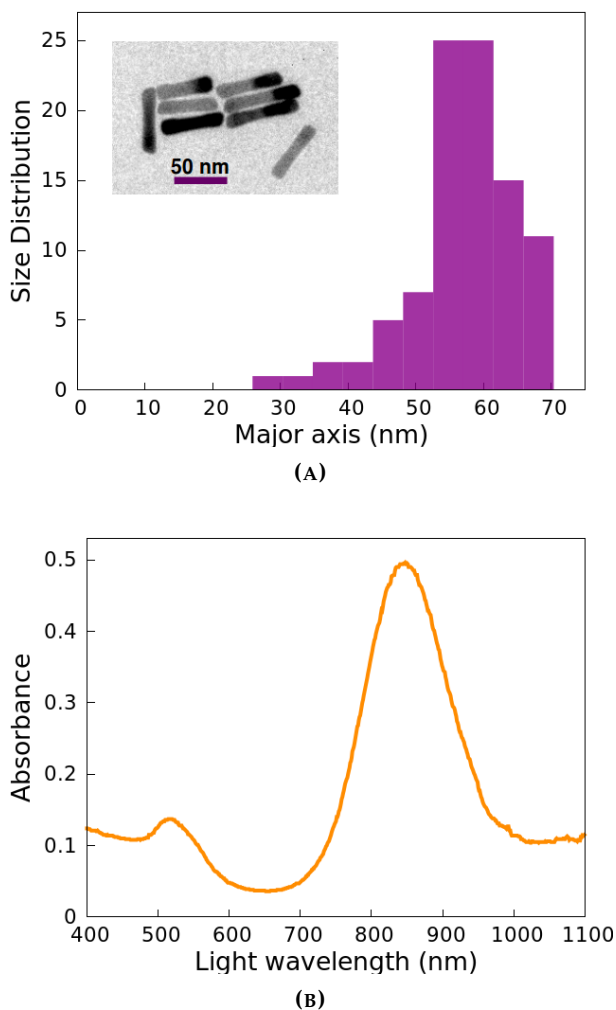


**FIGURE 7.1:** a) Length histogram of the AuNR sample obtained by TEM pictures. The inset shows one of the microscope images. b) Absorption spectrum of a 9.8 mg/L gold nanorod suspension.

88 mg/L. For flow birefringence and depolarised dynamic light scattering experiments, the solutions had to be concentrated by two centrifugation cycles (15000 rpm, 5 min) up to 1400 mg/L.

For comparison purposes, sepiolite rods purchased from Sigma Aldrich (USA) and laponite<sup>®</sup>-RD platelets obtained from BYK (Germany) were

also used.

### 7.2.2. Methods

The experimental setup for the determination of electric birefringence is based on the measurement of the changes in the transmitted light intensity of a He-Ne laser beam that traverses *i*) a polariser at  $45^\circ$  to the electric field, *ii*) the suspension, *iii*) a quarter-wave plate whose fast axis is placed parallel to the polariser axis and *iv*) an analyser at  $90^\circ - \alpha$  to the initial polarization [43, 78]. All the optical plates were purchased from Edmund Optics, UK.

The sample is placed in a quartz cell of 1 cm path length (Starna Scientific, UK), and is thermostated at  $15.0 \pm 0.2^\circ\text{C}$ . With the help of a commercial generator (Tektronix AFG 3101, USA) and low frequency (Piezo Systems Inc. EPA-104, USA) and high frequency (AR Modular RF KMA2020, USA) amplifiers, 2 ms long sinusoidal electric field pulses in a frequency range of 1 kHz-10 MHz are sent to stainless steel electrodes immersed in the sample. The light intensity transmitted through the optical setup is collected by a photodiode (Edmund Optics, UK) connected to a digital oscilloscope (Tektronix TDS 2012C, USA). The transmitted light intensity  $I$  at time  $t$  is directly related to the birefringence of the sample,  $\Delta n(t)$ , by [78]

$$\Delta n(t) = \frac{\lambda}{\pi l} \left[ \arcsin \left( \sqrt{\frac{I(t)}{I_0}} \sin \alpha \right) - \alpha \right] \quad (7.1)$$

where  $I_0$  is the intensity transmitted by the setup when no electric field is applied and  $l$  is the path length. A value of  $-3^\circ$  was chosen for  $\alpha$ . The stress birefringence of the cell is corrected as indicated elsewhere [120]. The effect of linear dichroism on the EB measurements, obtained following the procedure detailed in another work [89], is less than 1% in all cases.

An estimation of the surface charge of gold nanorods was obtained by measuring the electrophoretic mobility of the (CTAB-coated) particles as a function of ionic strength with a Malvern Zetasizer NanoZS (Malvern Instruments, UK). The same instrument was used to control particle aggregation via the determination of the hydrodynamic diameter.

Depolarised dynamic light scattering measurements were performed with a commercial setup (3D-DLS System, LS Instruments, Switzerland), with which the autocorrelation function  $g_2(t) - 1$  was measured in the vertical-vertical (vv) and vertical-horizontal (vh) configurations. The results can be related to the diffusion coefficients of the rods according to the expressions [221]

$$\begin{aligned} g_2^{vv}(t) - 1 &= \beta e^{-2D_t q^2 t} [A + (1 - A)e^{-6\Theta t}]^2 \\ g_2^{vh}(t) - 1 &= \beta' e^{-(2D_t q^2 + 12\Theta)t} \end{aligned} \quad (7.2)$$

where  $D_t$  is the translational diffusion coefficient of the particles and  $q = 1.9 \cdot 10^7 \text{ m}^{-1}$  the light scattering vector. The parameter  $A$  is related to the polarizability of the rods along their main directions, and  $\beta$  and  $\beta'$  are correction factors.

## 7.3. Results and discussion

### 7.3.1. General features of the electric birefringence of AuNRs

Electric birefringence,  $\Delta n$ , is the macroscopic anisotropy that arises in the refractive index of a colloidal suspension of non-spherical particles when these are oriented by an external electric field.  $\Delta n$  is defined as  $n_{\parallel} - n_{\perp}$ , that is, the difference of the refractive index of the suspension along the directions parallel and perpendicular to the field. For particles with no intrinsic dipole moment, and neglecting the possible contribution of viscous forces, the electric birefringence for low applied fields can be calculated as [122]

$$\Delta n = \frac{\Delta\alpha^o \Delta\alpha^e \phi E_0^2}{2n_s \epsilon_0 V_p 30k_B T} \quad (7.3)$$

where  $E_0$  is the field amplitude,  $\phi$  the volume fraction of the suspended particles,  $n_s$  the refractive index of the solution,  $\epsilon_0$  the vacuum permittivity,  $V_p$  the particle volume and  $\Delta\alpha^{e(o)}$  the polarizability anisotropy at the field (light) frequency.

Fig. 7.2 shows complete birefringence measurements of the AuNRs in suspension at different field frequencies. Here it can be observed that, when the field is turned on, the absolute value of the birefringence grows in a finite time and reaches a stationary value. When the field is turned off, the particles randomise their orientation and the birefringence decays to zero. Moreover, it can be observed that for low frequencies, the birefringence oscillates with twice the frequency of the applied electric field. This AC component of the birefringence, referred to as  $\Delta n_{AC}$ , is due to the partial randomisation of the system between two field inversions for sufficiently slow alternating fields.

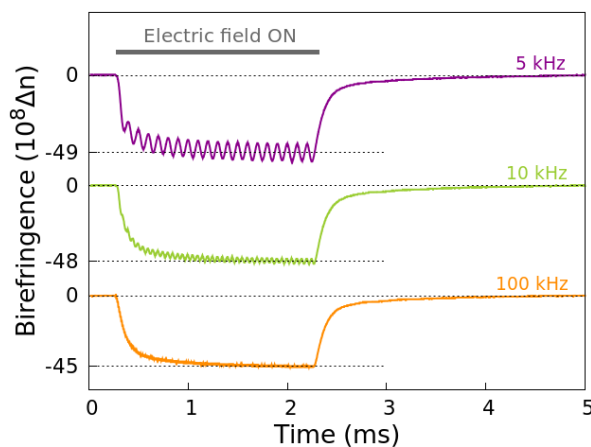


**FIGURE 7.2:** Electric birefringence signal of the AuNRs subjected 150 V/mm electric field pulses of 2 ms duration, at different field frequencies. The sample has a particle concentration of 85 mg/L and 0.1 mM KCl.

The first noticeable feature is that gold nanorods exhibit negative birefringence for all the studied frequencies. According to Eq. 7.3, this can be due to a negative value of either the electric or the optical polarizability anisotropy. In the first case, the particle orients anomalously, with its major axis perpendicular to the direction of the applied field. This has been observed, for instance, for polydisperse samples and bidisperse suspensions at low field frequencies. In these systems, the anomalous orientation was caused by the accumulation of the smallest particles around the largest ones [78, 80, 125]. In the second case, the particle orients normally,

with its major axis along the field direction, but  $\Delta\alpha^o$  is negative. This behaviour has been observed for suspensions of double-walled carbon nanotubes [89].

In order to explore these two possibilities for the gold nanorods, flow birefringence measurements were performed. This method is based on the fact that non-spherical particles in suspension can also be oriented parallel to a narrow channel by the effect of a flow velocity gradient [222, 223]. The birefringence arising in this case is known as flow birefringence, and its sign is determined solely by the optical polarizability anisotropy  $\Delta\alpha^o$  of the suspended particles.

The results are presented in Fig. 7.3, where it can be observed that AuNRs exhibit negative flow birefringence, unlike sepiolite needles. In flow birefringence experiments, the orientation of the particles, parallel to the channel, is determined by their geometry, and hence it is similar for sepiolite and gold rods. Therefore, the negative sign in the case of AuNRs can only be due to a negative optical anisotropy of these particles. Note that the observed oscillations in these measurements are due to flow jumps because of the pump.

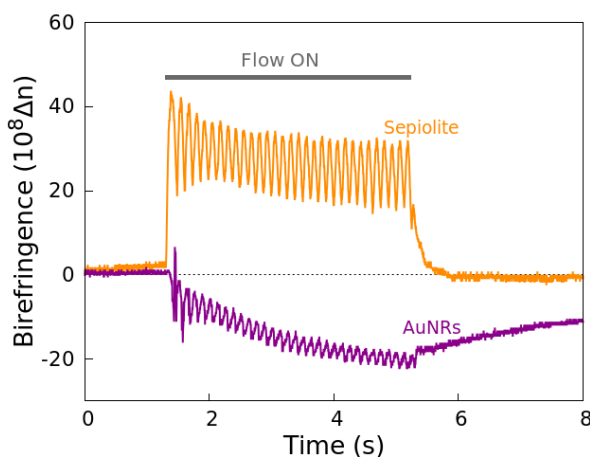


**FIGURE 7.3:** Flow birefringence measurements of a 1400 mg/L sample of AuNRs and a 1 g/L aqueous suspension of sepiolite particles. The 0.2 mL/s flow is maintained for 4 seconds through a channel of 1 mm<sup>2</sup> section.

The optical polarizability anisotropy is related to both the mismatch between the optical properties of the AuNRs and the medium, and the elongated geometry of the particles. It can be calculated as

$$\Delta\alpha^o = V_p\epsilon_0\text{Re} \left[ \frac{(A_L - A_d)(n_p^2 - n_s^2)^2}{((1 - A_L)n_s^2 + A_L n_p^2)} \right] \quad (7.4)$$

where  $A_{L/d}$  are the depolarization factors of rods [63] and  $n_p$  is the refractive index of the particle, which is assumed to be uniform. Since gold is highly absorbent, the AuNRs present a complex refractive index, which for a light wavelength of 633 nm has been measured to be  $n_p = 0.143 + 3.610i$  [224]. This yields a value for the optical polarizability anisotropy of  $\Delta\alpha^o = -1.4 \cdot 10^{-33} \text{ Fm}^2$ . Thus, the negative sign of the electric and flow birefringence of gold nanorods can be successfully explained in terms of their absorbance, as was also the case for double-walled carbon nanotubes studied elsewhere [89].

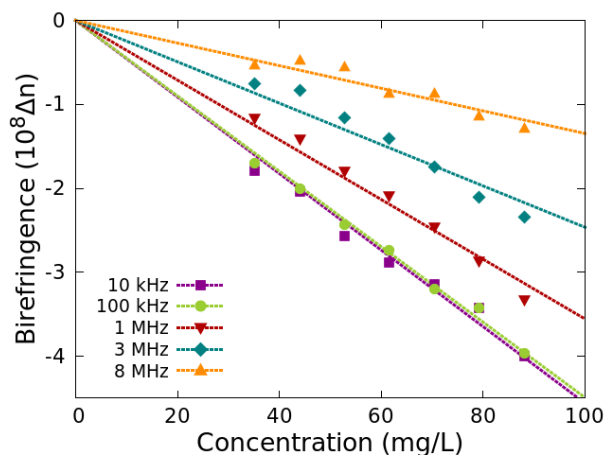
Fig. 7.4a shows that the electric birefringence is proportional to particle concentration in the studied range, and hence it can be assured that we find ourselves in the dilute regime, where particle interactions can be neglected. In Fig. 7.4b, it can be observed that the birefringence is also proportional to the square of the field amplitude, and therefore Kerr's law (Eq. 7.3) is satisfied in the field range used in this work. Then, the Kerr constant  $K$  can be defined as

$$K = \frac{2\Delta n}{\lambda E_0^2} \quad (7.5)$$

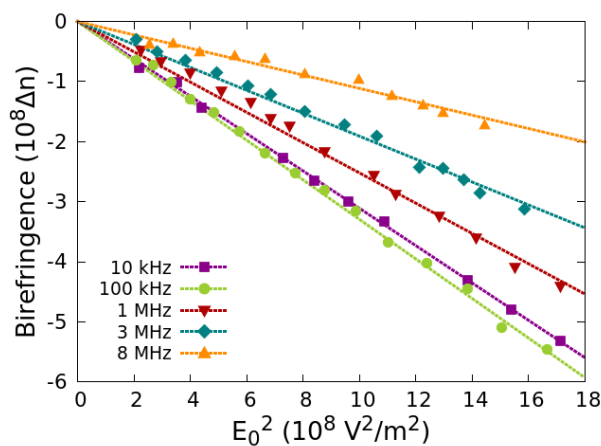
being  $\lambda = 633 \text{ nm}$  the wavelength of the incident light in vacuum.

### 7.3.2. Birefringence spectrum

Fig. 7.5 shows the Kerr constant of the AuNRs as a function of the frequency of the applied field, for different values of the ionic strength. Here, it can be observed that the birefringence spectrum is flat and independent of the salt content for frequencies up to 1 MHz. On the other hand, for higher values of  $\nu$ , the absolute value of the birefringence decays strongly



(A)



(B)

**FIGURE 7.4:** Electric birefringence of the AuNRs as a function of a) particle concentration and b) square of the field amplitude, for different frequencies of the applied field. The points are the experimental data and the lines fittings to linear functions. In a) the field strength is 37 V/mm, and in b) particle concentration is 88 mg/L.

and some increase of  $K$  with ionic strength is observed. From the Kerr constant, using Eqs. 7.3 and 7.5 and the calculated value of  $\Delta\alpha^o$ , the electrical polarizability anisotropy (right axis in Fig. 7.5) was also obtained.

The polarizability anisotropy of colloidal particles is strongly frequency-

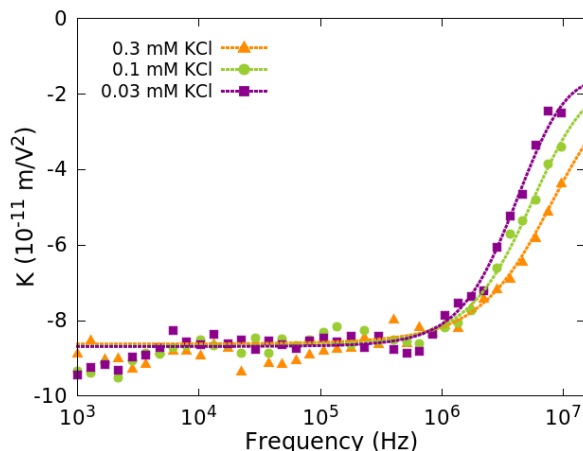


**FIGURE 7.5:** Kerr constant as a function of the frequency of the applied field, for a sample of gold nanorods at 88 mg/L and three different values of the ionic strength. The points are the experimental data and the lines fittings to the used model.

dependent, due to the relaxation of the polarization mechanisms involved in the dipole formation, which in general depend on the properties of both the particles and their electric double layers. For metallic particles with zero or very low charge, there is no electric double layer in the absence of field. In this situation, it has been shown that, for high-frequency fields, the dipole is that of a perfectly polarizable particle immersed in a dielectric. On the other hand, for low frequencies, the ions in the dispersing medium are attracted by the displaced charges of the metal, and form an induced double layer that screens the particle electric dipole, lowering the absolute value of the birefringence [74, 75].

These theoretical expectations for barely-charged conducting particles have been experimentally confirmed in the case of silver nanowires [74]. Nevertheless, for the AuNRs, the opposite behaviour is observed. Hence, in order to explain the experimental birefringence spectra, the system must be analysed in all its complexity, and the effect of the CTAB covering the AuNRs must be taken into account. This layer provides a surface charge that gives rise to the formation of an electrical double layer. In this situation, the dominant mechanism is the Maxwell-Wagner-O’Konski polarization, due to the mismatch of conductivities between the bulk solution

and the particle plus its electrical double layer. The electrical polarizability anisotropy can then be written as [25]

$$\Delta\alpha_{\text{MW}}^e = \frac{\epsilon_0\epsilon_s V_p}{3} \text{Re} \left[ \frac{K_p^L - K_s}{K_s + (K_p^L - K_s)A_L} - \frac{K_p^d - K_s}{K_s + (K_p^d - K_e)A_d} \right] \quad (7.6)$$

being  $\epsilon_s$  the relative permittivity of the medium and  $K_s = \sigma_s + i2\pi\nu\epsilon_s\epsilon_0$  its complex conductivity. Here,  $\epsilon_s$  is that of water and  $\sigma_s$  can be obtained from ion concentration. The presence of the CTAB layer is also taken into account in the calculation of the complex conductivity of the particle,  $K_p^{L/d}$ , modelling it as a metallic rod surrounded by a homogeneous charged shell of constant width.

For that purpose, we make use of the Maxwell mixture formula [225], which allows the replacement of this system by an equivalent homogeneous particle with complex conductivity  $K_p^{L/d}$  along its major/minor axis respectively. In our case, we have a spheroidal metallic particle with complex conductivity  $K_i$  and dimensions  $L$  and  $d$ , covered by a dielectric layer of complex conductivity  $K_l$  and thickness  $h$ . The equivalent homogeneous particle has dimensions  $L + 2h$  and  $d + 2h$ . In these conditions, and from the Maxwell mixture formula, the conductivity of the equivalent particle along its major/minor axis can be obtained as [61, 71]

$$K_p^{L/d} = K_l \frac{(K_i - K_l)(A'_{L/d} + \gamma - \gamma A_{L/d}) + K_l}{(K_i - K_l)(A'_{L/d} - \gamma A_{L/d}) + K_l} \quad (7.7)$$

where  $A'_{L/d}$  are the depolarization factors of the equivalent particle and  $\gamma = \frac{Ld^2}{(L+2h)(d+2h)^2}$ .

As above described, the AuNRs are modelled as prolate spheroids 56 nm long and 16 nm wide, with a 3.3 nm thick soft layer of CTAB [218]. Although experimental values in a range 2.5-4 nm have been found for this thickness [216–219], it has been checked that the selection of values within this range has negligible influence on the results. The values of the conductivities of both the particle core and the layer determine the absolute value of the birefringence at low frequencies. The intrinsic conductivity

of the gold cores,  $\sigma_i$ , is taken from published values for gold nano-objects, which range from  $3.5$  to  $440 \cdot 10^5$  S/m depending on the particle geometry and synthesis route [226? –232]. Only the values in the low side of this range, below  $10 \cdot 10^5$  S/m, fit our experimental data. This can be understood, since our particles are much shorter than those used in determining the range referred to above, and conductivity has been shown to be lower for shorter wires [232]. A value of  $8 \cdot 10^5$  S/m was chosen as the most suitable, although variations inside the mentioned range do not affect the results substantially.

Therefore, the conductivity inside the CTAB layer,  $\sigma_l$ , is left as the only adjustable parameter, and Fig. 7.5 shows that the fitting achieved is very acceptable. The fitted values of  $\sigma_l$  depend slightly on ionic strength, yielding  $0.15$ ,  $0.19$  and  $0.26$  S/m for  $0.03$  mM,  $0.1$  mM and  $0.3$  mM KCl concentration respectively. From these values, the charge density of the CTAB layer, assuming electroneutrality, can be obtained. The results are shown in Table 7.1.

The electrophoretic behaviour of particles consisting in a core surrounded by a soft layer has been widely studied in literature [233? ? ?]. In particular, it has been shown that the core and shell charges determine this response. For AuNRs, the electrophoretic mobility is inside a range of  $4.0$ - $4.4 \cdot 10^{-8}$  m<sup>2</sup>/Vs for all measured ionic strengths, a value that can be justified by the presence of mobile counterionic charge inside the CTAB layer. A model elaborated by Ahualli et al. [233] was used for calculating the surface conductivity of the layer, using its volume charge density as adjustable parameter. Since the theory is defined for spheres, the experimental mobility  $u_e$  was compared to a calculation for randomly oriented spheroids, modelled as

$$u_e = \frac{2}{3}u_e(d) + \frac{1}{3}u_e(L) \quad (7.8)$$

where  $u_e(d)$  and  $u_e(L)$  are the electrophoretic mobilities of soft spheres with core diameter  $d$  and  $L$  respectively. We consider that the CTAB shell is a  $3.3$  nm thick neutral layer, in which the CTAB charges are balanced by counterions that preserve electroneutrality. From the best-fit value, we can

calculate the charge density of the layer, to be compared with that obtained from EB measurements

The values obtained in this manner are also shown in Table 7.1, where it can be observed that both EB and electrophoresis results are in reasonable agreement, considering the approximations made in the calculations. The numerical differences are below 20%, and in both cases the same tendency is observed: the charge density increases slightly with ionic strength. This increment is compatible with the fact that, in most cases, the coating thickness decreases with salt concentration, since the interchain electrostatic repulsion is better screened the larger the ionic strength [77], and this produces, for a fixed total charge, an increase of the charge density.

**TABLE 7.1:** Charge density of the CTAB layer ( $\text{MC}/\text{m}^3$ ) obtained from electric birefringence experiments and electrophoretic mobility determinations, for three different values of the ionic strength.

KCl Conc. (mM)	0.03	0.1	0.3
Electric Bir.	1.9	2.4	3.3
Electroph. Mob.	1.8	2.6	2.8

### 7.3.3. Effect of CTAB micelles on AuNR rotational diffusion

Electric birefringence has been extensively used as a technique for the characterization of rotational diffusion of suspended nanoparticles and, from that, excellent results have been obtained for the determination of particle dimensions [45, 46, 78? ]. In order to study the diffusion coefficient of the AuNRs from electric birefringence measurements, two approaches are available. The first one consists in the analysis of the decay of the birefringence after the electric field is turned off. This decay is shown in Fig. 7.6a, and could be fitted by a single exponential function, which indicates a high monodispersity of the sample. From the decay time,  $\tau=107.6\pm 0.3 \mu\text{s}$ , the rotational diffusion coefficient of the particles can be obtained as  $\Theta = 1/6\tau=1550\pm 5 \text{ s}^{-1}$ . Since the birefringence is proportional to particle volume, the value of  $\Theta$  obtained in this manner is volume-averaged.

The second approach consists in the analysis of the frequency dependence of the AC component of the birefringence,  $\Delta n_{AC}$ , also related to particle diffusion. For low frequencies, particles have enough time to randomise their orientation between two field inversions. However, for high values of the field frequencies, the rods can no longer follow the field oscillations and no AC contribution is observed. For a rod with no permanent dipole moment,  $\Delta n_{AC}$  can be written as [83]

$$\Delta n_{AC} = \frac{\Delta n(\nu \rightarrow 0)}{\sqrt{1 + \left(\frac{2\pi\nu}{3\Theta}\right)^2}} \quad (7.9)$$

where  $\Delta n(\nu \rightarrow 0)$  is the low frequency limit of the DC component of the birefringence and  $\Theta$  is volume-averaged if the sample presents polydispersity. Fig. 7.6b shows the AC birefringence spectrum of the AuNRs, together with a fitting to Eq. 7.9, which provides a value of  $1500 \pm 40 \text{ s}^{-1}$  for  $\Theta$ . Thus, the results obtained by the two methods are very similar.

Nevertheless, these results are quite different from the value of  $\Theta$  that can be obtained from the particle dimensions, making use of the expression for the diffusion coefficient of short rods [200]

$$\Theta = \frac{3k_B T (\log \rho + C_r)}{\pi \eta L^3} \quad (7.10)$$

where  $\eta$  is the viscosity of the suspending solution,  $\rho = L/d$  the aspect ratio of the particles, and  $C_r = -0.662 + 0.917/\rho - 0.050/\rho^2$ . For a particle with volume-averaged length 59 nm and width 18 nm, covered by a 3.3 nm layer, the theoretical value of the rotational diffusion coefficient is  $7750 \text{ s}^{-1}$ . Depolarised dynamic light scattering measurements were also performed for the AuNRs, and from them, a value of the rotational diffusion coefficient of  $\Theta = 8075 \pm 3 \text{ s}^{-1}$  was obtained using Eq. 7.2. This result is within a 5% difference of the theoretical value. Comparable results are found in the literature for similar AuNRs [221].

The difference between the values of  $\Theta$  obtained from EB and from light scattering measurements suggests that the application of a strong electric field gives rise to a mechanism that slows down the rotational diffusion of the rods up to a factor 5. We propose that this mechanism is related to the

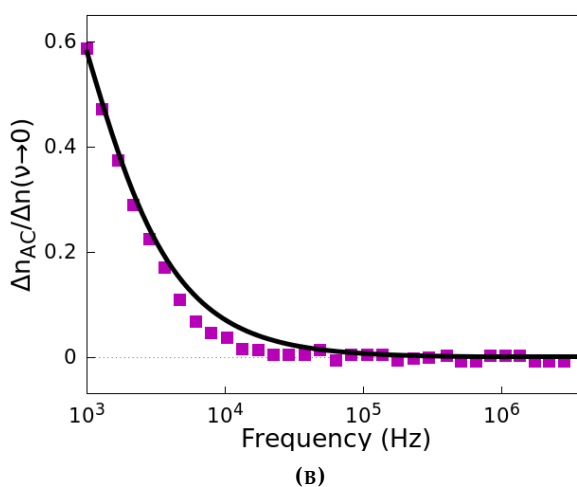
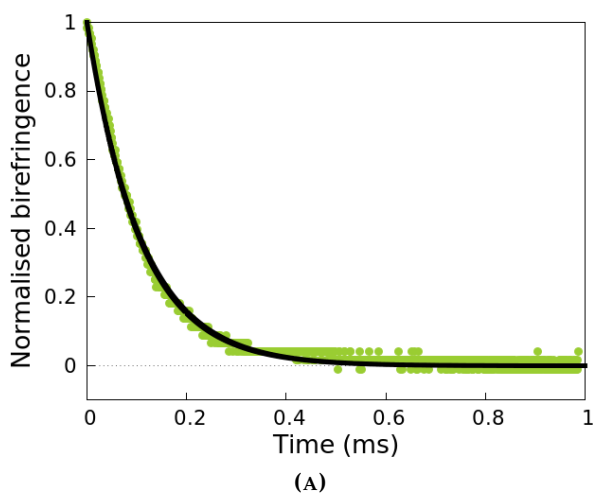


**FIGURE 7.6:** a) Decay of the electric birefringence of the AuNRs after the field is turned off. The birefringence is normalised to the initial value. b) Spectrum of the oscillating component of the electric birefringence normalised to the low-frequency value of the DC component. In both cases, the points are the experimental data and the lines, fittings to the theory.

presence of CTAB micelles. It can be expected that the AuNR suspensions are bidisperse, formed by gold nanorods as primary particles and CTAB micelles, with a 5-6 nm diameter [234], as secondary particles. In this type

of systems, it has been shown that electric fields induce an accumulation of secondary particles around the primary ones [50, 78, 80]. Since rotational diffusion strongly decreases with particle size, this accumulation can affect the value of  $\Theta$ , thus explaining qualitatively the observed phenomenology.

In order to test this hypothesis, CTAB micelles can be removed by dialysing the system with deionised water. Nevertheless, lowering the CTAB amount below the critical micelle concentration provokes the detachment of the CTAB bilayer from the gold surface and the subsequent aggregation of the particles, a fact confirmed by dynamic light scattering measurements. For this reason, we tested the hypothesis with a different, more stable system: the electric birefringence of laponite<sup>®</sup>-RD particles, with a very fast response, was measured in the presence and absence of CTAB micelles. The obtained results are shown in Fig. 7.7. In this case, the decays were fitted by stretched exponential functions [45]

$$\Delta n(t) = \Delta n_0 \exp[-(t/\tau)^\alpha] \quad (7.11)$$

since polydispersity is more significant. The fitting parameters are  $\tau = 827 \mu\text{s}$ ,  $\alpha = 0.538$  and  $\tau = 339 \mu\text{s}$ ,  $\alpha = 0.552$  respectively. Hence, the presence of CTAB slows down the rotational diffusion of the laponite platelets by a factor 2.4. In this manner, the effect of the micelles on the diffusion dynamics of small particles is shown, qualitatively justifying the AuNR results.

## 7.4. Conclusions

The electric birefringence of gold nanorods in aqueous suspension presents a rich phenomenology that provides information on their microscopic properties, including electrical, optical and diffusional. It has been experimentally observed that AuNRs exhibit negative electric birefringence. Flow birefringence measurements allowed us to show that this feature is not explained by an anomalous orientation but rather by the strong optical absorbance of gold, which results in a negative optical polarizability anisotropy of the rod.

It has also been shown that the birefringence spectra of gold nanorods

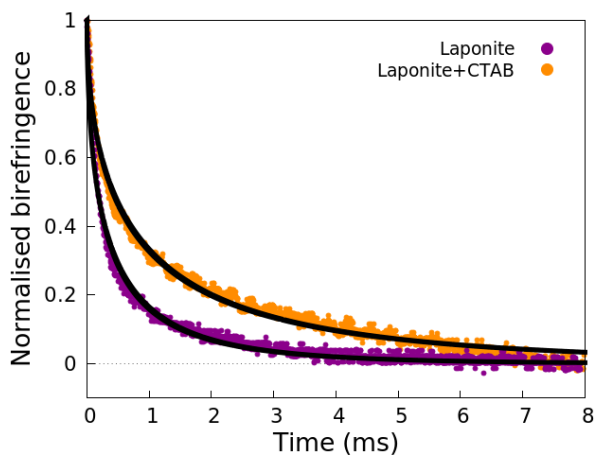


**FIGURE 7.7:** Birefringence signal of two laponite samples a particle concentration of ??? and 0.1 mM KCl. One of the samples is in the presence of 1.5 mM CTAB. The field strength is 60 V/mm.

cannot be explained considering only the polarization of a barely-charged metallic particle immersed in an electrolyte solution. Instead, the CTAB bilayer that stabilises the rods plays a crucial role on their electric properties and determines the spectral birefringence behaviour. From the experimental measurements, the electric conductivity of the gold rods,  $8 \cdot 10^5$  S/m, could be obtained. Moreover, the charge density of the surfactant layer as a function of the ionic strength could be determined. The results are in good agreement with the values found by a soft-particle model that provides the charge density inside the CTAB layer from the experimental determination of the electrophoretic mobility.

Furthermore, the analysis of the AC birefringence spectra and the transient electric birefringence shows that the rotational diffusion of gold nanorods is slower than expected from their geometry. Nevertheless, depolarised dynamic light scattering measurements of the AuNR sample in the absence of field provide a value of the rotational diffusion coefficient in good agreement with the theory. This suggests that it is the application of the electric field that induces a mechanism that slows down the rotational diffusion of these particles. Here, we propose that this field-induced mechanism consists in the accumulation of the CTAB micelles, present in the suspension,

around the gold nanorods. Measurements of the transient electric birefringence of laponite platelets in the presence and absence of CTAB micelles support this hypothesis.

In conclusion, the complete analysis of the electric birefringence of gold nanorods has allowed the determination of optical, electrical and diffusion properties of these particles in aqueous suspension. The presence of CTAB, needed for the stability of the samples, strongly affects the electric properties of the gold rods, a feature that is specially relevant for the potential applications in which the interaction of AuNRs with electric fields plays an important role.

# 8

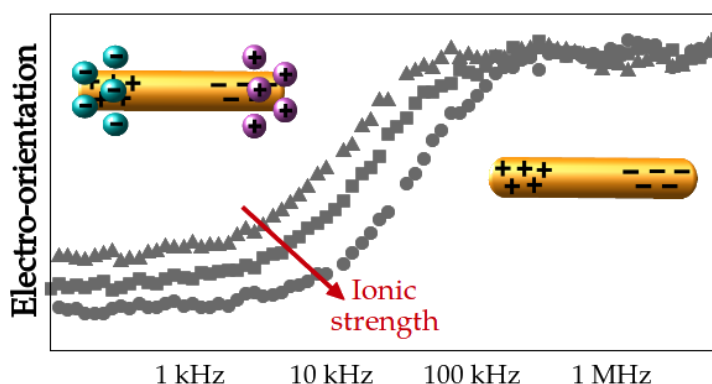
## ELECTRO-ORIENTATION OF SILVER NANOWIRES IN ALTERNATING FIELDS



## Electro-Orientation of Silver Nanowires in Alternating Fields

P. Arenas-Guerrero, A. Ramos, A. V. Delgado,  
M. L. Jiménez. Submitted to **Langmuir**.

In this work we analyse the orientation of silver nanowires immersed in aqueous solutions, under the effect of alternating electric fields in a broad frequency range, covering from a few Hz to several MHz. The degree of orientation is experimentally determined by electro-optical techniques, which present the advantage of measuring multiple particles at the same time. In the electro-orientation spectrum, we observe a frequency dispersion in the kHz range, and provide a theoretical explanation for this behaviour: at high frequencies, charge separation in the nanoparticles leads to a large induced dipole, responsible for strong orientation. On the other hand, at low frequencies, redistribution of the ions in solution gives rise to an induced double layer that screens the dipolar fields and, as a consequence, the degree of orientation decreases. Moreover, we measure the transient response when the electric field is switched off, from which the size distribution of the polydisperse sample is obtained. The results match those given by electron microscopy determinations.





## 8.1. Introduction

In the last decade, interest in the investigation of noble metal nanoparticles has rapidly increased due to their unique conductive, optical and mechanical properties [235]. For example, thanks to the existence of the surface plasmon resonance, applications of these particles have been found in enhanced Raman spectroscopy, photothermal therapy, or as optical sensors. In these techniques, the particle shape often plays an important role, and the performance can be improved in many cases by the use of elongated geometries [236]. For instance, it has been shown that high-aspect-ratio metal nanostructures, such as Au and Ag nanorods/nanowires, can be used to transport optical signals over distances of several micrometers [237, 238]. Moreover, the antibacterial activity of silver nanoparticles, which has become an issue of intense research [239], is also highly influenced by particle shape [6].

In many applications of metallic non-spherical particles, promoting and/or controlling their orientation is an important goal. For instance, thin films of silver nanowires can be used as conductive transparent electrodes in different optical devices [12, 240]. The structure of the wires inside these films can provide nanoscale control of the transmission, manipulation and switching of optical signals. Other examples are the reported particle assemblies with negative refractive index [241, 242] or the finding that electromagnetic energy can be coherently guided in devices with size below the diffraction limit, due to near-field coupling of neighbour particles [243, 244].

However, despite their potential, controlling the orientation and understanding the properties of metallic nanowires are still open issues. In this context, a system to monitor such orientation is no less important. While direct observation of the particles is an intuitive option, it presents some limitations. For instance, only large particles can be measured, and for these, viscous interactions with the cell cannot be ruled out [245]. Furthermore, the orientation cannot be accurately determined, and measuring a statistically significant number of particles is normally time-consuming. In contrast, electro-optical methods are suitable for the study of nanosized

particles, and allow the observation of the degree of orientation of a large number at once. For these reasons, in this work we use electric birefringence, an electro-optical method based on the determination of the refractive index anisotropy induced in a suspension of non-spherical particles by an external electric field.

During the last years, this technique has been successfully applied to a number of non-spherical particles [49, 78, 145, 211, 246–248], although only a few works are devoted to a physical understanding of the observed phenomena [25, 26, 122]. It is well known that the electric torque that causes the orientation is due to the dipole induced on the nanoparticle by the external electric field. However, while this effect has been extensively studied in the case of non-conducting charged particles, only a few works deal with the electric response of conducting but weakly charged non-spherical particles, as those here treated. In these contributions, for instance, it has been shown that induced electro-osmosis [72, 86] can play an important role in the orientation of metallic particles under slowly oscillating electric fields [38, 74, 249].

In this work we provide a study of the electro-orientation of silver nanowires in aqueous suspension, in the presence of alternating electric fields. From the electric birefringence phenomenology, the orientation mechanisms are analysed and optical, electrical and geometrical properties of the particles are obtained.

## 8.2. Experimental Section

Silver nanowires (AgNWs) were purchased from PlasmaChem, Germany. Figure 8.1 shows a transmission electron microscope (TEM) picture of these particles, where it can be observed that they are highly elongated and poly-disperse, with a mean length of  $3.0 \pm 2.3 \mu\text{m}$  and an average diameter of  $121 \pm 17 \text{ nm}$  (the errors indicate the standard deviations of the length and diameter distributions by number).

The electric birefringence (EB) was determined with a home-made experimental device described elsewhere.[43, 78] Briefly, a linearly polarised

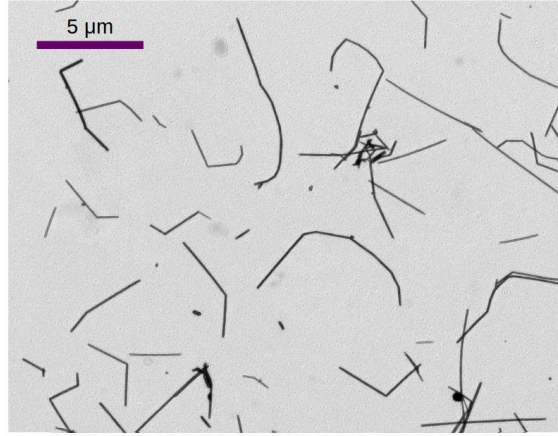


**FIGURE 8.1:** TEM picture of the AgNWs.

He-Ne laser beam passes through the suspension. After crossing the sample, it traverses a quarter wave plate and another polariser, which is nearly crossed with the former (at  $90^\circ - \alpha$ , being  $\alpha = -3^\circ$ ). All the optical plates were purchased from Edmund Optics, UK. After sonicating, the sample is placed in a quartz Kerr cell and thermostated at  $15^\circ\text{C}$ . A pair of electrodes with 1 mm separation and oriented at  $45^\circ$  with respect to the incident beam polarisation direction are immersed in the sample. The sinusoidal electric fields are obtained with a signal generator (Tektronix AFG 3101, USA) in a frequency range of 100 Hz-10 MHz. The light intensity transmitted by this setup is collected by a photodiode (Edmund Optics, UK) connected to a digital oscilloscope (Tektronix TDS 2012C, USA). The transmitted light intensity  $I$  at time  $t$  is directly related to the birefringence of the sample,  $\Delta n(t)$ , as [78]

$$\Delta n(t) = \frac{\lambda}{\pi l} \left[ \sin^{-1} \left( \sqrt{\frac{I(t)}{I_0}} \sin \alpha \right) - \alpha \right] \quad (8.1)$$

where  $\lambda = 632 \text{ nm}$  is the wavelength of the incident beam,  $l = 1 \text{ cm}$  the path length inside the Kerr cell, and  $I_0$  the transmitted intensity in the absence of electric field. The value of  $I_0$  does not change significantly during the time of the experiment, indicating that sedimentation is negligible.

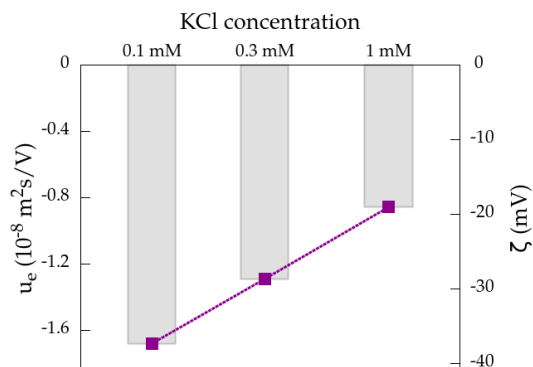


FIGURE 8.2: Electrophoretic mobility (left axis) and zeta potential (right axis) of the AgNWs as a function of the ionic strength.

## 8.3. Results and Discussion

### 8.3.1. Characterisation of the wires

The electrophoretic mobility  $u_e$  of the AgNWs was determined by dynamic light scattering (Malvern Zetasizer NanoZS, Malvern Instruments, UK). From these measurements, the zeta potential  $\zeta$  of the wires was calculated modelling them as infinitely long cylinders and making use of the Ohshima model [250]. The results for different values of the electrolyte concentration are shown in Figure 8.2, where it can be observed that the particles present some negative electric charge, which can be attributed to the capping agents used to terminate the reaction during the synthesis, necessary for the stability of the suspension. The decrease of the zeta potential with the ionic strength is a consequence of the contraction of the Debye layer.

Figure 9.2a displays a zoom-in TEM picture of the wires, where it can be observed that they seem to present a coating with a thickness of approximately 10 nm (and up to 40 nm on the wire tip). In order to analyse the composition of this layer, X-ray photoelectron spectroscopy (XPS) measurements were carried out. This technique indicates the presence of oxygen, in a ratio of approximately 3:2 with respect to silver. The XPS

peaks corresponding to these two elements are shown in Figure 9.2b. These results suggest that the particle surface is at least partially oxidised.

### 8.3.2. General features of the EB of silver nanowires

When an electric field is applied to a suspension of non-spherical nanoparticles, they tend to orient along the field direction, and the suspension becomes optically anisotropic. For axially symmetric particles, the electric birefringence  $\Delta n = n_{\parallel} - n_{\perp}$  is defined as the difference between the refractive index of the suspension along the directions parallel and perpendicular to the electric field. In general, this quantity is given by

$$\Delta n = \Delta n_{\max} S \quad (8.2)$$

where  $S$  is the orientational order parameter of the suspension, which for elongated geometries ranges from 0 (random orientation) to 1 (total alignment). The saturation birefringence,  $\Delta n_{\max}$ , reads:

$$\Delta n_{\max} = \frac{N \Delta \alpha^{\circ}}{2n_s \varepsilon_0} \quad (8.3)$$

being  $N$  the particle concentration by number,  $n_s$  the refractive index of the solvent and  $\varepsilon_0$  the vacuum permittivity.  $\Delta \alpha^{\circ}$  is the optical polarisability anisotropy of the particles, defined as  $\Delta \alpha^{\circ} = \alpha_a^{\circ} - \alpha_b^{\circ}$ , where  $a$  and  $b$  indicate the directions parallel and perpendicular to the major axis, respectively.

Figure 8.4a shows the EB of a silver nanowire suspension as a function of time, for different frequencies of the applied electric field. Here, it can be observed that when the field is turned on the EB signal grows and reaches a stationary value. When the field is turned off, the birefringence decays to zero. AgNWs exhibit negative birefringence in the whole explored frequency range, a feature that has been already observed for other conducting materials [89]. In those cases, the effect was due to a negative value of  $\Delta \alpha^{\circ}$ , caused by the strong optical absorbance of the metallic particles [89]. However, the negative sign can also be due to an anomalous orientation of the AgNWs, with their major axis perpendicular to the field

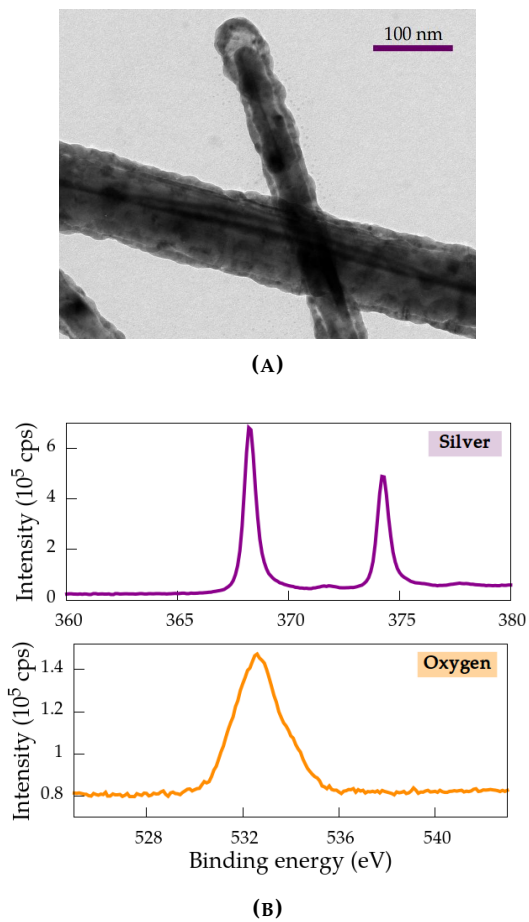


**FIGURE 8.3:** a) Zoom-in TEM picture of the AgNWs. b) XPS peaks corresponding to silver and oxygen.

direction, resulting in a negative value of  $S$ , and hence of the birefringence (Equation 8.2). This has been observed for polydisperse suspensions and bidisperse systems at low field frequencies [78, 80].

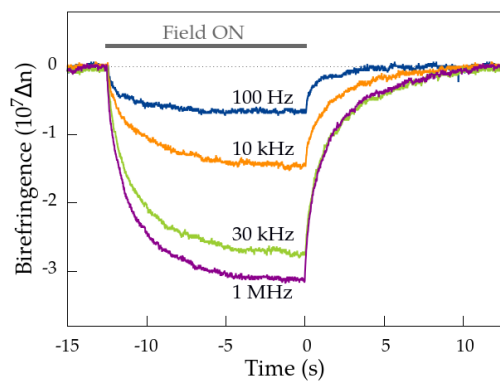
In order to discriminate between both possibilities, we performed flow birefringence experiments. When rigid rods flow through a thin capillary, the velocity gradient produces an orientation of the particles with their major axis parallel to the channel, independently of their nature. This gives rise to an induced birefringence, whose sign is determined solely by  $\Delta\alpha^o$ . In our experiments, we substituted the cell and vertical electrodes of the EB setup by an horizontal channel with a cross section  $1 \times 1 \text{ mm}^2$ , and we pumped the suspension at a flow rate of  $0.2 \text{ mL/s}$ , which means a shear rate of approximately  $300 \text{ s}^{-1}$ . The results for AgNWs are shown in Figure 8.4b, together with measurements of sepiolite needles (Sigma Aldrich, USA), for the sake of comparison. The data indicate that, unlike the case of sepiolite particles, silver nanowires present a negative optical polarisability anisotropy, responsible for the negative sign of the electric birefringence.

For very elongated particles, a theoretical value of the polarisability anisotropy at optical frequencies can be obtained from the refractive index of the medium,  $n_m$ , and the particle,  $n_p$ , as:

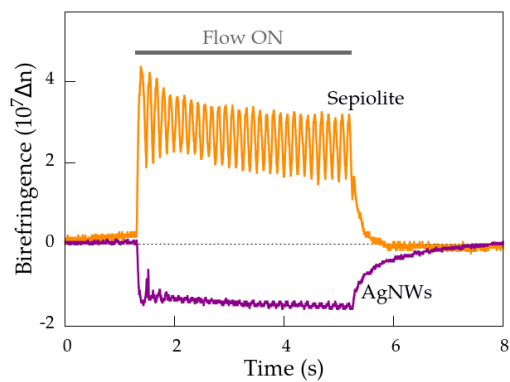
$$\Delta\alpha^o = V_p \varepsilon_0 \text{Re} \left[ \frac{(n_p^2 - n_m^2)^2}{n_p^2 + n_m^2} \right] \quad (8.4)$$

where  $V_p$  is the particle volume. Using the bibliography value of  $n_p$  [224] and the particle dimensions obtained by microscopy, a theoretical value of  $\Delta\alpha^o = -4.9 \cdot 10^{-30} \text{ Fm}^2$  was found for the AgNWs. Thus, the negative sign of the optical polarisability anisotropy is a consequence of particle absorbance.

It is worth mentioning that, given the length of the AgNWs, one may expect some interaction among them. This would be reflected in a slowing down of the transient decay, or equivalently a larger hydrodynamic size, for more concentrated samples, which is not observed. Furthermore, Figure 8.5a shows that birefringence is proportional to particle concentration, which further rules out any particle interactions. Figure 8.5b shows that the EB is also proportional to the square of the field amplitude,  $E_0$ , a quadratic



(A)



(B)

**FIGURE 8.4:** a) Electric birefringence of a 100 mg/L AgNW suspension in 0.03 mM KCl as a function of time. The electric field pulses have an amplitude of 2 V/mm, a duration of 12.5 s and the indicated frequencies. b) Flow birefringence of suspensions of AgNWs at 200 mg/L and sepiolite needles at 2 g/L, as a function of time.

dependence known as Kerr's law, which is fulfilled for sufficiently weak fields.

### 8.3.3. Electric birefringence dynamics

In Figure 8.6a, the electric birefringence signal as a function of time is presented normalised by the stationary value,  $\Delta n_{st}$ , to make evident that the dynamics of the process is independent of the field frequency. The decay of the birefringence after the field is turned off is due to thermal agitation, and hence it is related only to the rotational diffusion coefficient  $\Theta$  of the wires. Due to the strong dependence of  $\Theta$  with the particle dimensions, the analysis of the birefringence decay has been long used to determine the size of non-spherical particles in suspension [45, 77, 78, 94, 96, 246, 248].

For polydisperse samples, the birefringence decay can be obtained as a superposition of independent single-exponential processes, as [47, 94]

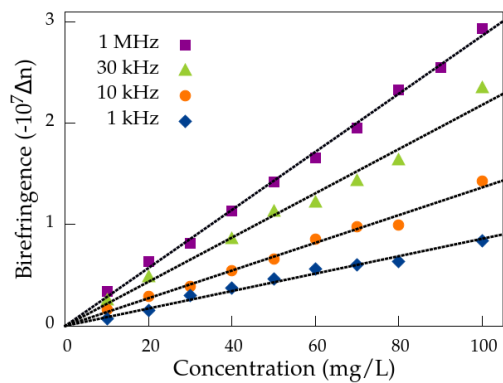
$$\Delta n(t) = \Delta n_{st} \sum_{i=1}^N C_i e^{-t/\tau_i} \quad (8.5)$$

where  $\tau_i = 1/6\Theta_i$  the characteristic rotation time of particles of a well-defined size, and  $C_i$  are coefficients which measure the contribution of each population to the overall signal. Since electric birefringence is proportional to the particle volume, the  $C_i$ 's provide a size distribution in volume of the polydisperse suspension. The rotational diffusion coefficient of each population can be calculated from the wire dimensions, with the expressions [200]:

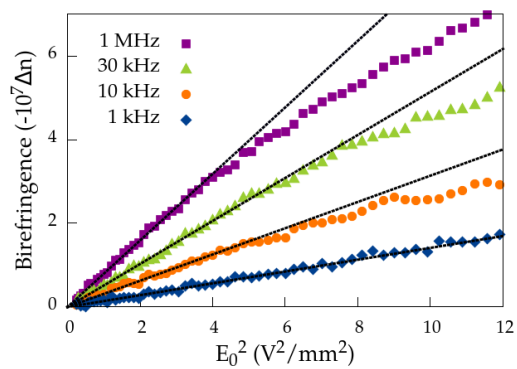
$$\Theta_i = \frac{3k_B T}{\pi\eta(2a_i)^3} F(r_i) \quad (8.6)$$

$$F(r_i) = \log r_i - 0.2/\log 2r_i - 16/(\log 2r_i)^2$$

being  $k_B$  the Boltzmann constant,  $T$  the temperature of the suspension,  $a_i$  the major semiaxis of the particles in population  $i$ ,  $r_i = a_i/b$  their aspect ratio and  $\eta$  the solvent viscosity. The particle radius  $b$  is considered constant for all populations.

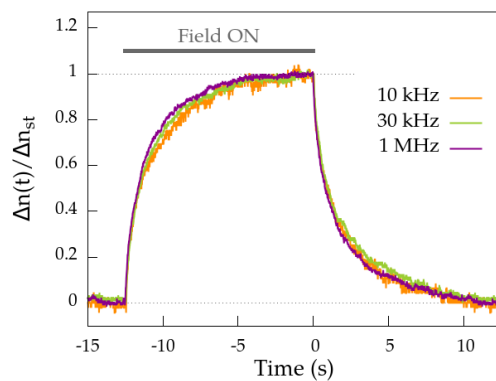


(A)

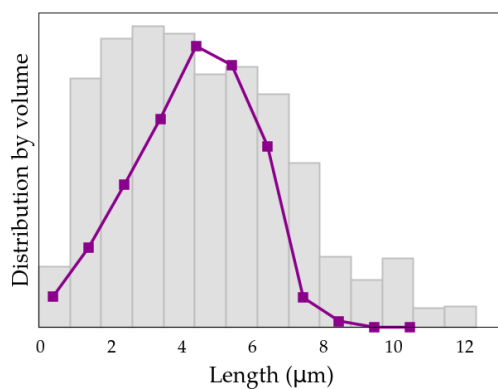


(B)

**FIGURE 8.5:** Electric birefringence of a silver nanowire suspension at 0.03 mM KCl a) as a function of particle concentration and b) as a function of the square of the field amplitude, for the indicated field frequencies. In a)  $E_0$  is 2 V/mm and in b) the particle concentration is 100 mg/L.



(A)



(B)

**FIGURE 8.6:** a) Normalised birefringence of the AgNWs in 0.03 mM KCl solution, as a function of time. b) Length distribution by volume of the AgNW sample as obtained from microscopy pictures (bars) and from the multi-exponential method (line).

In this manner, the length distribution of the AgNW sample, shown in Figure 8.6b, was obtained from the analysis of the birefringence decay.[47, 94] The results are compared to electron microscopy determinations, with a very good agreement, indicating that particles are well dispersed in the solution. The volume-averaged wire length obtained from the birefringence decay is  $4.3 \pm 1.7 \mu\text{m}$ , within a 10% difference of the microscopy value,  $4.5 \pm 2.9 \mu\text{m}$ . Nevertheless, it can be observed that the EB-obtained distribution is slightly narrower, which can be associated to the difficulties of size determination from the microscope pictures in such a long particle system.

### 8.3.4. Electric birefringence spectra

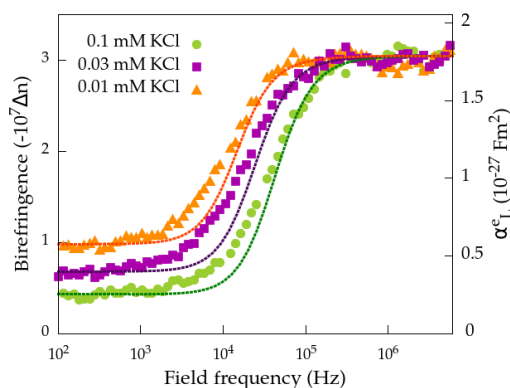
In Figure 8.7a we show the electric birefringence spectra of AgNWs, measured inside the Kerr regime, at three different values of the salt concentration. With the aid of Equation 8.2, the orientational order parameter  $S$  can be experimentally determined. Two contributions are expected to the electro-orientation. On one hand, the external electric field induces an electric dipole that produces an orientation  $S_1$  given by:

$$S_1 = \frac{\Delta\alpha^e(\nu)E_0^2}{30k_B T} \quad (8.7)$$

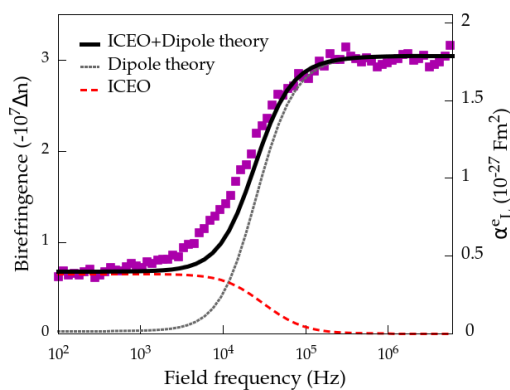
where  $\Delta\alpha^e = \alpha_a^e - \alpha_b^e$  the anisotropy of the electrical polarisability of the particles at a given field frequency  $\nu$ .

The polarisation of low-charged conducting particles has been studied elsewhere [74, 85], modelling them as ideally polarisable, a reasonable assumption for moderate potentials. Following this approach, it was shown that two mechanisms contribute to polarisation: The fastest one is the large dipole generated by electron migration inside the particles, opposite to the field. The slowest mechanism is related to the subsequent redistribution of ions in the electrolyte solution, which accumulate near the region of the particle with opposite charge.

In the case of very elongated particles, it can be demonstrated that  $\alpha_b^e \sim \frac{1}{r^2} \log(r)\alpha_a^e \ll \alpha_a^e$  [74]. Hence,  $\Delta\alpha^e \approx \alpha_a^e$ . Moreover, it can be further



(A)



(B)

**FIGURE 8.7:** a) Electric birefringence of AgNW samples with the indicated salt concentrations, as a function of the field frequency. The field strength is 2 V/mm and the particle concentration 100 mg/L. The points are the experimental data and the dotted lines fittings to the model for conducting wires. b) Same as a) but only for 0.03 mM KCl (points), with the electric (dotted grey line) and viscous (dashed red line) contributions given by the model, presented separately. The solid black line is the sum of the two effects.

assumed that the charge separation induced by the external field is given by a one-dimensional charge density. In this situation, it has been shown that the electrical polarisability anisotropy of infinitely elongated metallic particles can be expressed as [74]:

$$\Delta\alpha^e(\nu) = \frac{4\pi a^3 \varepsilon_m}{3} \frac{1}{\log r} \frac{\nu^2/\nu_{\text{DL}}^2}{1 + \nu^2/\nu_{\text{DL}}^2} \quad \nu_{\text{DL}} = \frac{\sigma_m}{2\pi b \log r C_{\text{DL}}} \quad (8.8)$$

being  $\varepsilon_m$  and  $\sigma_m$  the medium permittivity and conductivity, and  $C_{\text{DL}}$  the double layer capacitance. According to this expression, there is a dispersion in the electro-orientation spectrum with a characteristic frequency  $\nu_{\text{DL}}$ , which can be understood as follows: at low frequencies, the induced ion accumulation screens the particle dipole, and particle polarisation (and hence electro-orientation) is small. At high frequencies, ions do not have time to redistribute and there is no induced charge in the liquid. Thus, the strong polarisation of the metallic particle gives rise to an increase in the orientation degree. In our case, the calculation of the electric dipole is carried out numerically by solving Laplace equation with the boundary conditions of the problem, and taking into account the axial symmetry of the particles (see details in Reference[74]). However, the essential features of this phenomenon are captured by Equation 8.8.

In addition to the electric contribution, the existence of a hydrodynamic torque must be taken into account. Thus, the countercharge in the particle proximities migrates under the effect of the external electric field, dragging electro-osmotic fluxes. While for centrosymmetric charged particles this flux does not produce a net torque [49], in the case of barely charged metallic particles, the induced ion accumulation at low frequencies is asymmetrical, and the charges migrate around the particle, also dragging liquid with them [41, 72–74, 85, 86]. This effect is called induced charge electro-osmosis (ICEO), and is schematically represented in Figure 8.8.

Here, it can be observed that the component of the electric field parallel to the particle's major axis is responsible for charge separation inside the metallic wire, which gives rise to ion accumulation if the field frequency is sufficiently low. The ions in these induced double layers are affected by both components of the electric field, but here we focus on the effect

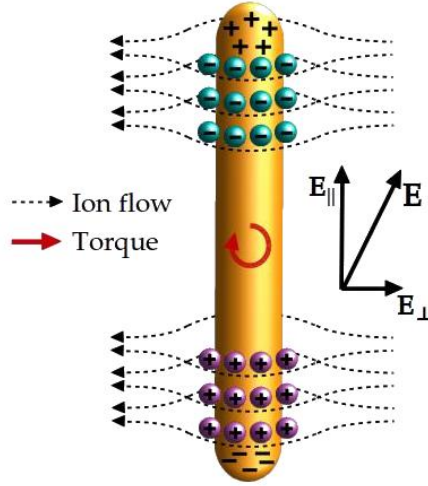


FIGURE 8.8: Schematic representation of the ICEO flows for a very elongated particle.

of  $E_{\perp}$ , which moves the negative ions to the left and the positive ions to the right, dragging liquid in the respective directions. This gives rise to an effective rotation of the particle, which tends to orient its major axis along the external field. The contribution of the ICEO flows to the order parameter of the suspension for weak fields is, in the limit of infinitely long cylinders [74]:

$$S_2 = \frac{4\pi a^3 \varepsilon_m E_0^2}{45 f(\lambda) k_B T [1 + (\nu/\nu_{DL})^2]} \quad (8.9)$$

where  $\lambda = \log(2a/b)$  and  $f(\lambda) = \lambda - 1.14 - 0.2/\lambda - 16/\lambda^2$ . As observed, this quantity is non-zero only at low frequencies, when ions have time to redistribute along distances of the order of the particle length. In this situation, the viscous torque slightly orients the particles along the field direction. In Equation 8.9, it can be observed that the response is also proportional to the square of the field amplitude, and hence Kerr's law is preserved. As in the case of  $S_1$ , more accurate results can be found by a numerical calculation of the hydrodynamic contribution, as was done by Arcenegui et al.[74]. Again, Equation 8.9 can help to better understand the frequency behaviour of this contribution.

In different works, it has been found that the theoretical value of the ICEO fluid velocity is up to an order of magnitude higher than measured experimentally [36, 74, 251]. The cause of such difference is still unclear, although several possibilities have been suggested, such as the effect of the dielectric coating, ion adsorption and/or surface roughness [74]. To include this fact in the data fitting, the slip velocity is multiplied by a correction factor  $0 < \Lambda < 1$ . Finally, the birefringence can be calculated as:

$$\Delta n = \Delta n_{max} (S_1 + \bar{S}_2) \quad (8.10)$$

being  $\bar{S}_2$  the modification of  $S_2$  when the correction factor  $\Lambda$  is taken into account.

The experimental data in Figure 8.7a are fitted to the previously detailed model for metallic particle polarisation. The adjustable parameters are the double layer capacitance, the  $\Lambda$  factor and the saturation birefringence. From the high-frequency value of  $\Delta n$ , and taking into account that  $\bar{S}_2 = 0$  in this frequency limit,  $\Delta n_{max}$  can be obtained from Equations 9.4 and 8.10 after numerically calculating of  $\Delta\alpha^e$ . The low-frequency limit of the birefringence, together with Equation 8.10 and the value of  $\Delta n_{max}$ , allow us to obtain  $\bar{S}_2$ , and hence  $\Lambda$ . Finally, from the characteristic frequency of the dispersion,  $C_{DL}$  can be determined. In Figure 8.7b, the contributions of the electrical and viscous torque to the overall signal are presented separately.

The value of the double layer capacitance obtained from the fittings is  $C_{DL} = (1.4 \pm 0.1)\varepsilon_m\kappa^{-1}$ , corresponding to 1.4 times the Debye-Hückel capacitance, a reasonable result. Note that for nanowires of  $3 \mu\text{m}$  length, an electric field  $E_0 = 2 \text{ V/mm}$  produces a voltage drop of  $\varphi \approx 6 \text{ mV}$  along the particle, and hence  $e\varphi/k_B T \approx 0.2$ . For this value, some deviations can be expected from the linearized Debye-Hückel model. The  $\Lambda$  correction factors for the suspensions with 0.1, 0.03 and 0.01 mM KCl are, respectively, 0.08, 0.13 and 0.19. These values are similar to those obtained elsewhere [36, 252]. Moreover, our results show a tendency of  $\Lambda$  to increase for lower ionic strengths, as also observed in other works [36, 253, 254].

The birefringence saturation value obtained from the fittings of the spectra is  $\Delta n_{max} = -52 \cdot 10^{-7}$ , which, according to Equation 8.3 corresponds

to an optical polarisability anisotropy of  $\Delta\alpha^o = -2.8 \cdot 10^{-31} \text{ F/m}^2$ . This value is 18 times smaller than the theoretical prediction for very elongated wires and the optical constants of silver. Similar differences have been found, for instance, for gibbsite platelets [50] or sodium montmorillonite particles [78]. In these works, the mismatch was attributed respectively to an intrinsic anisotropy of the material, due to its crystalline structure, and to clay swelling. In our case, we suggest that the effect may be related to the oxidation of the wire surface. In fact, as derived from TEM and XPS determinations, the AgNWs seem to be coated by an oxide layer of several nanometers. The optical properties of oxidised silver films were studied elsewhere [255], and values of the complex refractive index of  $n = (2.0 \pm 0.3) + (0.8 \pm 0.5)i$  were reported for high oxidation. These values are compatible with our experimental optical polarisability anisotropy.

## 8.4. Summary and Conclusions

In this work, the complete electric birefringence phenomenology of suspensions of silver nanowires was studied. Under all experimental conditions, we found a negative response, a feature also observed for other conducting materials and that could be attributed to particle absorbance. The analysis of the transient EB behaviour provided the size distribution of the wires in suspension, in good agreement with that obtained from electron microscopy determinations.

Moreover, the spectral electro-orientation behaviour of the AgNWs was analysed in a wide frequency range, for different values of the ionic strength. For high frequency fields, electro-orientation is due only to the electric polarisation of the metallic particles. At low frequencies, on the other hand, the orientation decays to a small value associated to the appearance of an induced double layer, which screens the particle dipole. However, this low-frequency limit is non-zero due to the contribution of electro-osmotic fluxes, which produce a viscous torque also orienting the particles along the field direction. The results could be suitably fitted by a theoretical model, which allowed the calculation of the capacitance of the electrical double layer and the slip velocity. The latter is an order of magnitude lower

than expected, as observed for other similar systems.

In this manner, EB experiments allowed the analysis of the different polarisation mechanisms of AgNWs in aqueous suspension, an important step towards applications in which these particles are oriented or, in general, interact with external electric fields. Moreover, information can be obtained on the optical and geometrical properties of the silver needles, proving the characterisation potential of the electro-optical techniques.

# 9

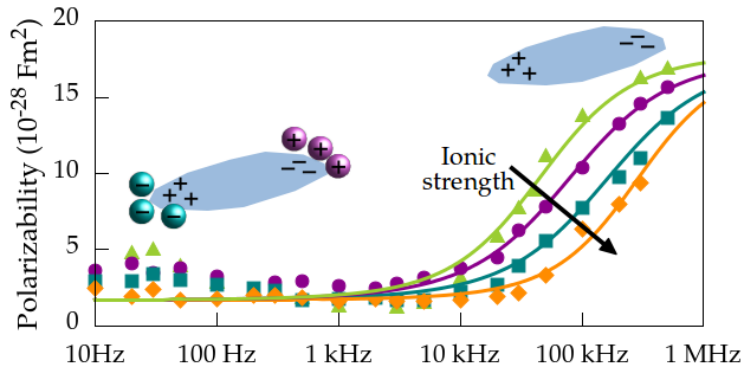
## ANALYSIS OF THE ELECTRO-OPTICAL RESPONSE OF GRAPHENE OXIDE DISPERSIONS UNDER ALTERNATING FIELDS



## Analysis of the Electro-Optical Response of Graphene Oxide Dispersions under Alternating Fields

P. Arenas-Guerrero, A. V. Delgado, M. L. Jiménez. Submitted to **Carbon**.

Recently, graphene oxide (GO) has attracted much attention because of its many potential applications, such as the fabrication of transparent electrodes or drug delivery, in addition to its use as a precursor for large-scale production of graphene flakes. However, the interaction of this material with electric fields is yet poorly understood, and only recently the orientation of GO particles with an electric field was achieved. In this work, we analyse the electro-orientation of GO flakes in aqueous suspension in the absence of interparticle interactions, under different experimental conditions. From the measurement of linear dichroism, the electrical polarizability of the GO flakes as a function of the field frequency was calculated. The results show a pronounced relaxation process in the kHz range that leads to a large high-frequency polarizability. This phenomenology is explained as follows: For high-frequency fields, the polarizability is that of conducting particles immersed in a dielectric; for frequencies below the kHz range, in contrast, ions in solution redistribute and screen the induced dipole. Hence, the use of high-frequency electric fields strongly enhances GO electro-orientation. Furthermore, from the linear dichroism measurements, the particle absorption coefficient and the sample size distribution could be obtained.



## 9.1. Introduction

Graphene oxide (GO) consists of a single layer of graphene, oxidised in different degrees with oxygen-containing functional groups, which strongly affect the electric and mechanical properties of the material [115, 256]. While GO has been mainly studied as a precursor for large-scale graphene fabrication by reduction processes [257], in the recent years, it is gathering much interest because of their potential use in applications like photocatalysis, drug delivery, separation membranes, transparent conductive films or optical devices [11, 117, 258–261]. Among other suitable properties, GO particles are dispersible in polar solvents and easily functionalised [258]. Moreover, their mechanical and electric properties can be tuned by modifying the degree of oxidation, providing high versatility [262–264].

Controlled orientation of the GO flakes, essential for many of these applications, is being targeted by different methods, such as spray deposition, vacuum filtration, the Langmuir-Blodgett technique or magnetic orientation [265–268]. In particular, the use of electric fields, widespread for many materials, presents difficulties in the case of graphene oxide [269]. Thus, only recently, high-frequency AC electric fields have been successfully used to orient weakly-interacting GO platelets in suspension [145, 270–272]. Hence, much work is still needed to understand the behaviour of GO flakes under the effect of electric fields, necessary for future implementation in applications.

In this work, we analyse the orientation ordering of diluted suspensions of GO particles under the application of oscillating electric fields, as a function of the field frequency and amplitude. Experimentally, this electro-orientation is monitored via the analysis of the macroscopic linear dichroism that arises in the suspension when the particles are oriented by the external field.

## 9.2. Theoretical background

Under the application of an external electric field, non-spherical particles in suspension tend to orient with their major axis parallel to the field di-

rection, and the absorbance  $A$  of the sample becomes anisotropic [89]. To quantify this effect, the linear dichroism (LD) is defined as

$$\Delta A = A_{\perp} - A_{\parallel} \quad (9.1)$$

where  $A_{\perp(\parallel)}$  is the absorption of the sample along the direction perpendicular (parallel) to the applied field. The absorbance anisotropy is proportional to the state of orientation of the system, characterised by an order parameter  $S$ . In this manner [84]

$$\Delta A = \Delta A_{\text{sat}} S \quad (9.2)$$

where  $\Delta A_{\text{sat}}$  is the saturation value of linear dichroism, directly related to the absorbance properties of the suspended particles and the sample concentration.

For oblate particles, the order parameter can be obtained as a function of the field strength as [84]:

$$S = \frac{3}{4\gamma} \left[ 1 - \frac{2\sqrt{\gamma}e^{-\gamma}}{\int_{-\sqrt{\gamma}}^{\sqrt{\gamma}} e^{-x^2} dx} \right] - \frac{1}{2} \quad \gamma = \frac{\Delta\alpha^e E_0^2}{4k_B T} \quad (9.3)$$

being  $E_0$  the field amplitude,  $k_B$  the Boltzmann constant and  $T$  the suspension temperature.  $\Delta\alpha^e = |\alpha_d^e - \alpha_L^e|$  is the electrical polarizability anisotropy of the particles, where  $\alpha_d^e$  ( $\alpha_L^e$ ) is the polarizability along their minor ( $d$ ) and major ( $L$ ) axis respectively. For oblate shapes,  $S$ , and hence also  $\Delta A$ , are negative for normal orientation. The low-field limit of the former expression provides a quadratic dependence of the order parameter with  $E_0$ , known as Kerr's law:

$$S = -\frac{\Delta\alpha^e E_0^2}{30k_B T} \quad (9.4)$$

For very high fields, on the other hand, saturation of the dichroism is achieved. In the case of axially-symmetric planar particles, perfect alignment along the major axis, perpendicular to the symmetry axis, gives a value of  $-1/2$  for the order parameter, and  $\Delta A = -1/2\Delta A_{\text{sat}}$  (Equation 9.3).

After the application of the electric field, the orientation of the system is not immediate, but rather the dichroism grows and reaches the stationary value  $\Delta A_\infty$  in a characteristic rise time, which in general depends on the field strength [81, 95]. Upon removal of the electric field, the particles randomise their orientation due to rotational diffusion, and the dichroism decays to zero.

Rotational diffusion is strongly size-dependent, and hence the analysis of the dichroism decay can provide information on the dimensions of the suspended particles [45, 94]. For this purpose, here we use the multi-exponential method [47, 94], which assumes that, for a polydisperse sample, the LD decay can be built as a superposition of single exponential decay processes, corresponding to fractions of a well-defined size. Each process has a characteristic decay time  $\tau_{di} = 1/6\Theta_i$ , where  $\Theta_i$  is the rotational diffusion coefficient of the population  $i$ , which can be obtained from the particle dimensions. The relative contribution of each process is weighted by a coefficient  $C_i$ . In this manner:

$$\frac{\Delta A(t)}{\Delta A_0} = \sum C_i e^{-t/\tau_{di}} \quad (9.5)$$

where  $\Delta A_0$  is the initial value of the dichroism. Since LD depends on the particle volume, the coefficients  $C_i$  are proportional to the volume fraction of particles with size  $i$  of the polydisperse sample. Thus, if the decay of the dichroism is measured, Equation 9.5 can be solved to obtain a volume size distribution of the particles in suspension.

### 9.3. Experimental section

Graphene oxide particles were purchased from Graphenea, Spain, and dispersed in aqueous suspension with the help of a sonicator. A microscope image of these particles is shown in Figure 9.1, where it can be observed that the sample is very polydisperse. From the measurement of 150 particles, an average major axis length of  $2.5 \pm 2.2 \mu\text{m}$  was obtained for the graphene flakes, where the error represents the standard deviation of the distribution.

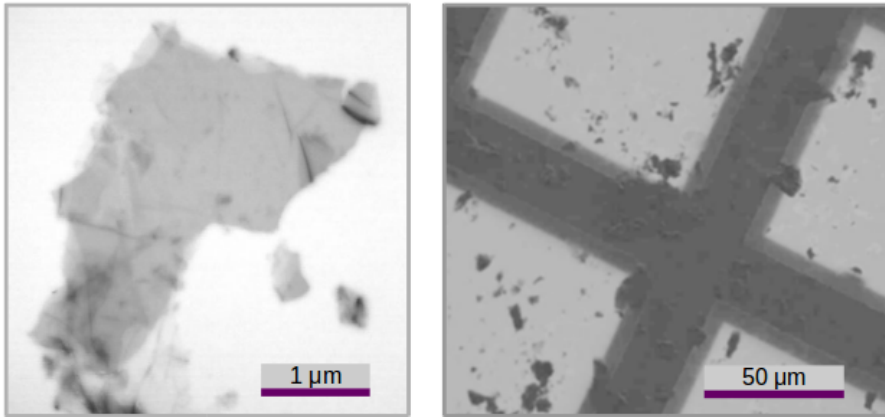


**FIGURE 9.1:** Transmission electron microscopy pictures of the graphene oxide particles at two different zoom scales.

The GO platelets present a small negative charge, being the zeta-potential of the particles around  $-30$  mV (Malvern Zeta Sizer Nano-ZS, Malvern Instruments, UK). In order to determine the oxygen content of the particles, XPS measurements were performed on the GO sample. Figure 9.2 shows the peaks corresponding to carbon and oxygen, from which a mass content of 39% of oxygen is obtained. This corresponds to a mild oxidation, as compared to other samples which contain up to 60% oxygen [273]. The conductivity of the GO flakes with this composition is around  $1$  S/m [273].

For the electric dichroism measurements, the sample is placed in a quartz cell of  $1$  cm path length and subjected to AC electric field pulses with the help of a function generator (Tektronix AFG 3101, USA) and a field amplifier (Piezo Systems Inc. EPA-104, USA). The pulse duration must be adjusted with the field amplitude to avoid heating effects. The frequency range is  $10$  Hz- $500$  kHz, and the sample temperature  $15^\circ\text{C}$ .

A He-Ne laser beam linearly polarised parallel to the field direction is passed through the sample and collected by a photodiode (Edmund Optics, UK), whose signal is recorded by a digital oscilloscope (Tektronix TDS 2012C, USA). The dichroism of the sample can be obtained from the light intensity  $I$  transmitted by this setup as [89]

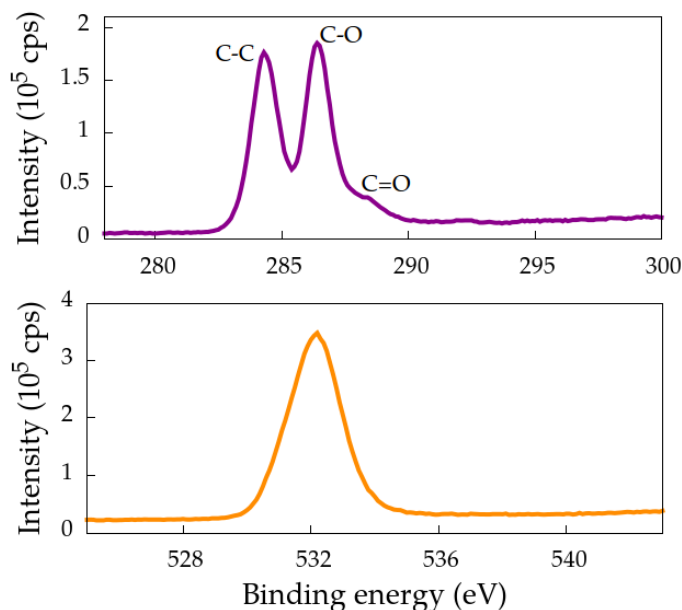


FIGURE 9.2: XPS peaks corresponding to carbon (top) and oxygen (bottom).

$$\Delta A = \frac{3}{2} \log_{10} \frac{I_0}{I(t)} \quad (9.6)$$

being  $I_0$  the transmitted intensity in the absence of applied field.

## 9.4. Results and discussion

### 9.4.1. General features

Figure 9.3 shows a complete linear dichroism signal of a graphene oxide dispersion. Here, it can be observed that LD is negative, as expected for planar particles. Therefore, we can conclude that the orientation of the GO layers is normal, with their major axis along the field direction. When the field is turned on, the dichroism signal grows in a short time, which depends on the value of the field strength, and reaches a stationary value. When the field is turned off, the dichroism decays during several seconds.

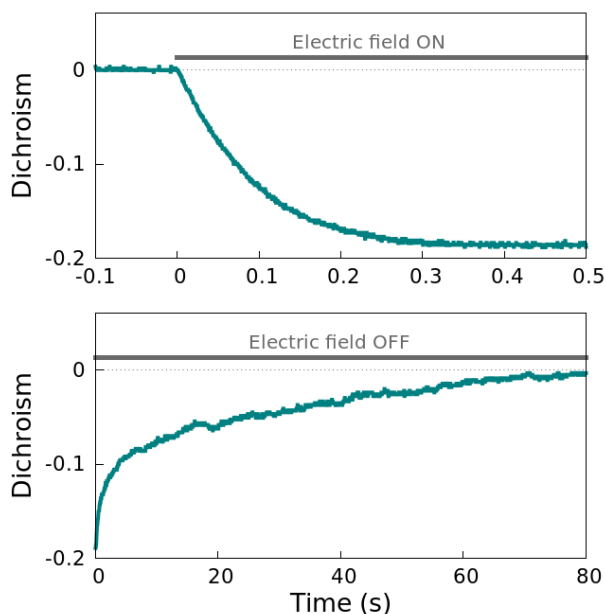
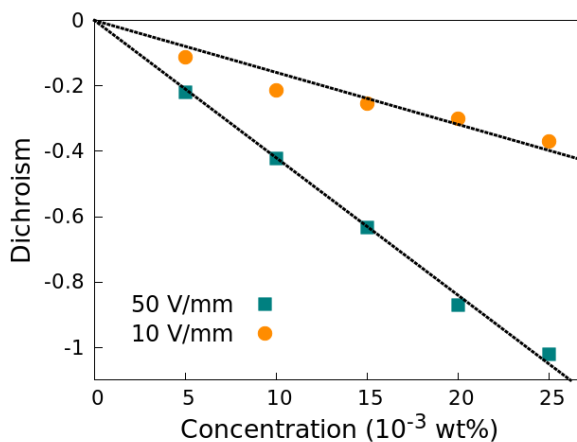


**FIGURE 9.3:** Linear dichroism measurements of a 50 mg/L aqueous suspension of GO, with 0.3 mM KCl. The field strength is 50 V/mm and the frequency 10 kHz.

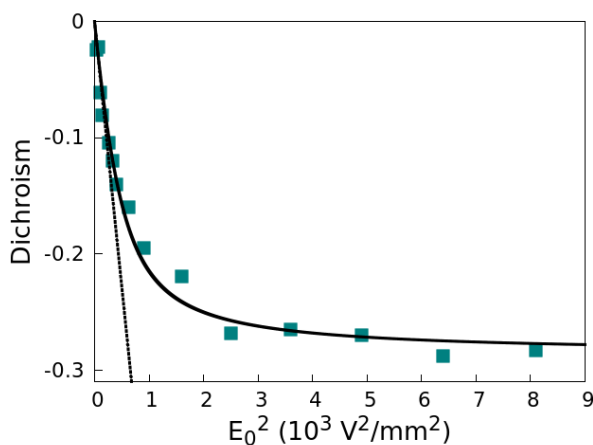
In the first place, in order to check that we find ourselves in the dilute regime, we measured  $\Delta A$  as a function of particle concentration. The results are displayed in Figure 9.4, where it can be observed that proportionality is found in the studied range, and hence particle interactions can be neglected. This is specially relevant, since it has been shown that concentrated GO suspensions can exhibit insensitivity to electric fields [270].

Figure 9.5 shows the linear dichroism of the GO flakes as a function of the field strength, together with a fitting to theory. Here, it can be observed that the field dependence of  $\Delta A$  is well-described by Equation 9.3, with fitting parameters  $\Delta A_{\text{sat}} = 0.57 \pm 0.10$  and  $\gamma/E_0^2 = (6.0 \pm 0.5) \cdot 10^{-9} \text{ m}^2/\text{V}^2$ . Deviations from Kerr's behaviour begin at a field strength of around 20 V/mm, and saturation is achieved at approximately 50 V/mm.

In the case of oblate-like geometries, the dichroism of the sample for saturating fields can be expressed as:



**FIGURE 9.4:** Linear dichroism of the GO platelets as a function of particle concentration, under a 10 kHz electric field of 10 V/mm and 50 V/mm. The salt concentration is 0.3 mM KCl.



**FIGURE 9.5:** Linear dichroism of a dispersion of GO particles at 50 mg/L and 0.3 mM KCl as a function of the square of the field strength. The field frequency is 10 kHz. The points are the experimental data, and the solid line a fitting to Equation 9.3. The dashed line indicates the low-field linear behaviour (Equation 9.4)

$$\Delta A = -\frac{1}{2}\Delta A_{\text{sat}} = cl \frac{\alpha_L^{\text{abs}} + \alpha_d^{\text{abs}}}{2} - cl\alpha_L^{\text{abs}} \approx -\frac{1}{2}cl\alpha_L^{\text{abs}} \quad (9.7)$$

where  $\alpha_L^{\text{abs}}$  and  $\alpha_d^{\text{abs}}$  are the absorption coefficients of the particles along the major ( $L$ ) and minor ( $d$ ) axes,  $c$  is the sample concentration and  $l$  the path length. In this expression, the Lambert-Beer law ( $A = \alpha^{\text{abs}}cl$ ) and the approximation  $\alpha_d^{\text{abs}} \ll \alpha_L^{\text{abs}}$  were used. In this manner,

$$\alpha_L^{\text{abs}} \approx \frac{\Delta A_{\text{sat}}}{cl} \quad (9.8)$$

From this expression, using the experimental saturation value of LD, an absorption coefficient of  $\alpha_L^{\text{abs}} = 1140 \pm 20 \text{ mLmg}^{-1}\text{m}^{-1}$  was found for the GO flakes along their major axis, for a light wavelength of 633 nm. Again, for oblate particles, the absorbance for random orientation is  $\alpha = \frac{2\alpha_L^{\text{abs}} + \alpha_d^{\text{abs}}}{3} \approx \frac{2}{3}\alpha_L^{\text{abs}} = 760 \pm 10 \text{ mLmg}^{-1}\text{m}^{-1}$ . This value is smaller than those measured for graphene, which range 1390-6600  $\text{mLmg}^{-1}\text{m}^{-1}$  at 660 nm [274–278]. This is compatible with a mildly oxidised GO sample, since absorbance decreases with the degree of oxidation [279].

Furthermore, according to Equation 9.3, the value of the electric polarizability anisotropy can be obtained from the experimental value of  $\gamma/E_0^2$ . For planar particles like ours, it can be considered that  $\Delta\alpha^e \approx \alpha_L^e$ , since  $\alpha_L^e \gg \alpha_d^e$ . With this approach, a value of  $\alpha_L^e = (9.5 \pm 0.8) \cdot 10^{-29} \text{ F/m}^2$  was found for the polarizability of the GO particles along their major axis for a field frequency of 10 kHz. The polarizability of the GO flakes in a wide frequency range is obtained and discussed later in the text.

#### 9.4.2. Decay of the birefringence and size determination

Figure 9.6 displays the decrease of the dichroism of the GO flakes as a function of time after the electric field is turned off. Here, it can be observed that this decay is independent of the field strength, as expected since the randomisation process is related only to the morphology of the particles. The experimental data were analysed by the multi-exponential method in order to obtain a major length distribution of the polydisperse sample. For this purpose, the particles were modelled as infinitely thin disks, with rotational diffusion coefficient [48]

$$\Theta = \frac{3k_B T}{4\eta L^3} \quad (9.9)$$

being  $\eta$  the solvent viscosity and  $L$  the particle diameter.

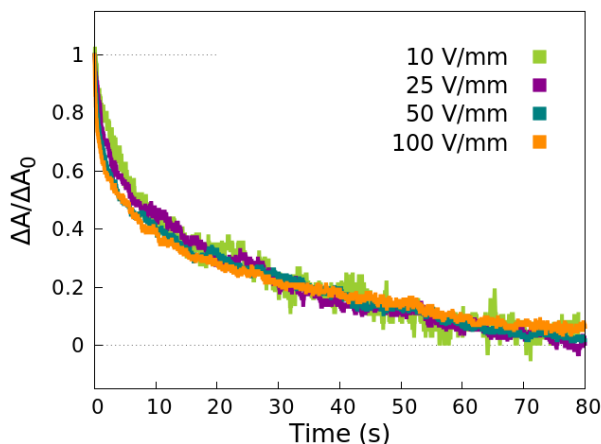


**FIGURE 9.6:** Decay of the linear dichroism of a dispersion of GO particles at 50 mg/L and 0.3 mM KCl after the application of a 10 kHz electric field of the indicated amplitude.  $\Delta A$  is normalised to the initial value.

The obtained results are presented in Figure 9.7, together with those given by microscopy determinations. In this graph, it can be observed that the distributions are in very reasonable agreement, considering the used approximations and the poor particle distinction in the microscope pictures. The volume-averaged diameters are, respectively,  $5.8 \pm 3.2 \mu\text{m}$  and  $6.3 \pm 2.9 \mu\text{m}$ , where the errors correspond to the standard deviations. Thus, the difference between the mean length values is below 8%, and the widths of the distributions are also very similar.

### 9.4.3. Rise of the birefringence

Figure 9.8a shows the rise of linear dichroism as a function of time after the field is switched on, for different values of the field strength. Here, it can be observed that, unlike the decay, the build-up dynamics is strongly dependent on the field amplitude. In the high-field limit, where rotational

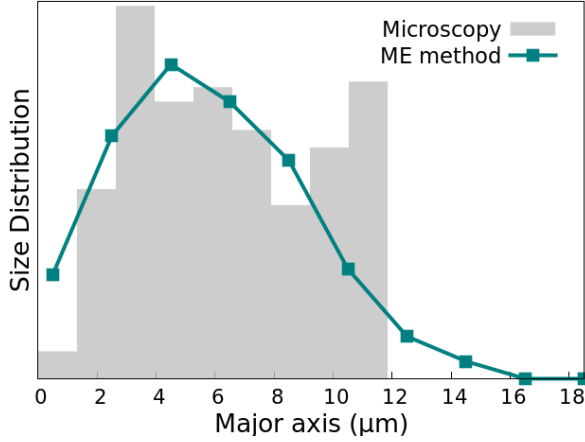


**FIGURE 9.7:** Volume-weighted length distribution of the GO particles, as obtained from microscopy determinations and using the multi-exponential (ME) method for the analysis of the dichroism decay.

diffusion can be neglected as compared to the effect of the external field, the rise of LD as a function of time can be described as [95]

$$\frac{\Delta A}{\Delta A_{\infty}} = -2S = 1 - \frac{3e^{t/\tau_r}}{e^{t/\tau_r} - 1} \left[ 1 + \frac{1}{\sqrt{e^{t/\tau_r} - 1}} \left( \arctan \frac{1}{\sqrt{e^{t/\tau_r} - 1}} - \frac{\pi}{2} \right) \right]$$

$$\frac{1}{\tau_r} = -\frac{\Theta \Delta \alpha^e}{k_B T} E_0^2$$
(9.10)

where  $\Delta A_{\infty}$  is the stationary linear dichroism, which at saturating fields has a value of  $-\Delta A_{\text{sat}}/2$ .

In this expression, it must be pointed out that the  $L^3$  dependence of  $\Theta$  and  $\Delta \alpha^e$  cancel out, and hence the particle size (and therefore the polydispersity) does not play a role on the dichroism rise. This explains the excellent agreement between the experimental data of our polydisperse GO sample and Equation 9.10, obtained in principle for monodisperse suspensions. As observed in Figure 9.8b, the fitting parameter  $\tau_r$  is inversely proportional to the square of the field amplitude for all studied fields, as expected.

From the value of  $\gamma/E_0^2 = (6.0 \pm 0.5) \cdot 10^{-9} \text{ m}^2/\text{V}^2$  obtained in a previous

section, and the slope in Figure 9.8b,  $b = -\Theta\Delta\alpha^e/k_B T = (-12.9 \pm 0.1) \cdot 10^{-9} \text{ m}^2/\text{sV}^2$ , the rotational diffusion coefficient of the GO flakes can be calculated as  $\Theta = \frac{b}{\gamma/E_0^2}$ . The obtained value,  $\Theta = 0.54 \pm 0.05 \text{ s}^{-1}$ , corresponds to particles with an average diameter of  $1.70 \pm 0.16 \text{ }\mu\text{m}$ , within a 35% difference of the number-averaged mean length obtained by microscopy determinations. These results are in reasonable agreement taking into account the high polydispersity and the irregular particle shape.

#### 9.4.4. Spectral behaviour

The polarization of colloidal particles under alternating electric fields is strongly dependent on the field frequency,  $\nu$ . Normally, in order to obtain the polarizability anisotropy spectrum from LD measurements, electro-orientation is measured at low fields, since in this situation  $S$  is directly related to  $\Delta\alpha^e(\nu)$ , according to Equation 9.4. However, this expression is only valid inside Kerr's regime, which is difficult to maintain for the GO suspensions, since they achieve saturation at relatively low fields. For this reason, the frequency dependence of  $\Delta\alpha^e$  was obtained by a different approach, based on the analysis of the LD build-up.

According to Equation 9.10, for arbitrary values of the field strength,  $\alpha_L^e \approx \Delta\alpha^e$  can be calculated from  $\tau_r$ , if the rotational diffusion coefficient of the particles is known. Here, we use the value of  $\Theta$  obtained in a previous section. In this manner, the spectrum of  $\alpha_L^e$  can be obtained by measuring the rise dynamics for different values of the field frequency. The results for GO suspensions with different ionic strengths are shown in Figure 9.9a, where it can be observed that, for frequencies below 10 kHz,  $\alpha_L^e$  is very low, and it grows quickly for higher frequencies.

In all cases, the polarizability spectrum could be fitted by a Cole-Cole type relaxation function

$$\alpha_L^e = \text{Re} \left[ \alpha_{L\infty}^e + \frac{\alpha_{L0}^e - \alpha_{L\infty}^e}{1 + (i\nu/\nu_c)^{1-\xi}} \right] \quad (9.11)$$

with  $\xi = 0.25 \pm 0.03$ , indicating the significant sample polydispersity. The high- and low-frequency limiting values of the polarizability,  $\alpha_{L\infty}^e = (0.5 \pm$

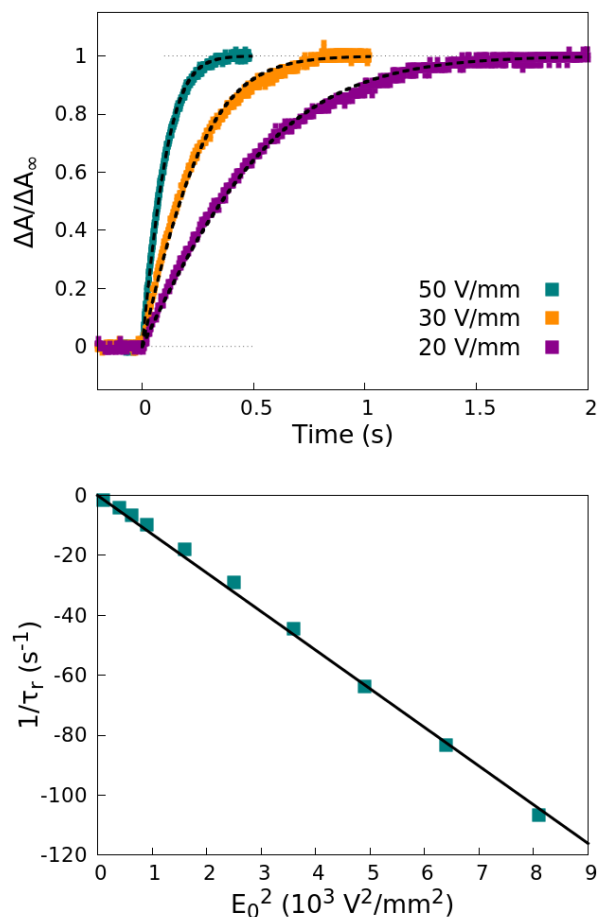


**FIGURE 9.8:** Rise dynamics of the the dichroism of a dispersion of GO particles at 50 mg/L and 0.3 mM KCl. The field frequency is 10 kHz. a) Normalised rise of LD for different field amplitudes. The dashed black lines are fittings to Equation 9.10. b)  $1/\tau_r$  as a function of the square of the field amplitude. The black line is a linear fitting.

$0.2) \cdot 10^{-28} \text{ Fm}^2$  and  $\alpha_{L0}^e = (5.3 \pm 0.5) \cdot 10^{-28} \text{ Fm}^2$  respectively, are independent of ion concentration. The characteristic relaxation frequency  $\nu_c$ , in contrast, grows with increasing ionic strength, as clearly observed in Figure 9.9b.

The fact that the fitting of the data does not show any dependence of  $\alpha_{L\infty}^e$  on ion concentration can be understood taking into account that the maxi-

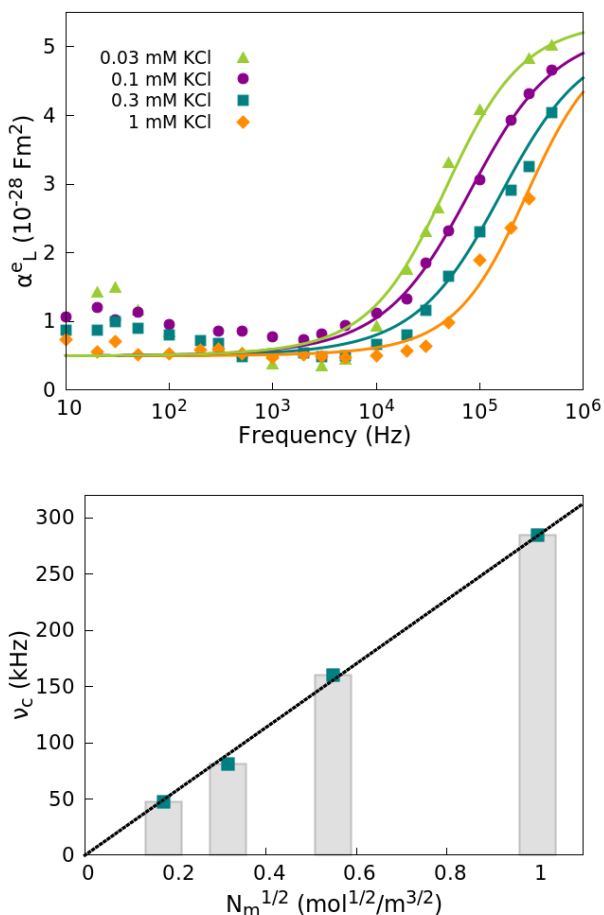


**FIGURE 9.9:** a) Polarizability spectra of four samples of GO flakes at 50 mg/L, with different values of the ionic strength. The points are the experimental data and the solid lines fittings to Cole-Cole relaxation functions. b) Relaxation frequency as a function of ion concentration.

medium conductivity is  $10^{-2} \text{ S/m}$ , a value much lower than the estimated particle conductivity ( $1 \text{ S/m}$ ). In fact, the value of the polarizability in the high-frequency range corresponds to that of a perfectly conducting particle with diameter  $L = 1.03 \pm 0.05 \mu\text{m}$ , a reasonable result, according to the expression [123]:

$$\alpha_L^e = 2L^3 \epsilon_m / 3 \quad (9.12)$$

For frequencies below the kHz range, the electrical polarizability decreases by an order of magnitude. This spectrum shape has been also observed for other conducting particles with low charge, namely silver nanowires [74]. In this case, these features can be explained as follows: For high-frequency fields, the particle polarization is that of a perfectly conducting material immersed in a dielectric. In contrast, for low frequencies, the ions in solution redistribute and form an induced electrical double layer which screens the particle dipole, cancelling the electro-orientation. Experimentally, however, the low frequency value of the dichroism is not zero, which may be attributed to the dragging of liquid by induced electro-osmotic flows. This can give rise to a slight orientation of the particles that is not due to an electrical polarization, as was also observed in the case of silver nanowires.

While an exact expression for the relaxation frequency is not available in the case of planar geometries (as was the case of very elongated particles), an estimation can be obtained by modelling the relaxation process as the charging of a capacitor [74, 215]. In this manner, the characteristic time can be approximated as  $\tau_{\text{cap}} = RC$ . Here,  $C$  is the capacitance of the induced electric double layer

$$C_{\text{EDL}} = \epsilon_m / \kappa^{-1} = \sqrt{\frac{2e^2 \epsilon_m N_A N_m}{k_B T}} \quad (9.13)$$

being  $N_A$  the Avogadro constant and  $N_m$  the ion molar concentration.  $R$  is the resistance of the circuit, which can be obtained from the electrolyte conductivity,  $K_m$ , as

$$R = \frac{D}{K_m} = \frac{D}{(\lambda_+ + \lambda_-) N_m} \quad (9.14)$$

where  $\lambda_{+(-)}$  is the electrolytic conductivity of the  $K^+$  ( $Cl^-$ ) ions and  $D$  the typical distance that ions travel to counter the particle induced dipole. In this manner, the characteristic relaxation frequency reads:

$$\nu_c = \frac{\lambda_+ + \lambda_-}{D} \sqrt{\frac{k_B T}{2e^2 \epsilon_m N_A}} \sqrt{N_m} \quad (9.15)$$

This law is experimentally checked in Figure 9.9b, where it can be observed that the characteristic relaxation frequency depends linearly on the square root of ion concentration. From the slope value, the mean distance travelled by the ions in solution was estimated to be  $D = 700 \pm 10$  nm, a very reasonable value considering the particle dimensions.

## 9.5. Conclusions

The electro-optical behaviour of graphene oxide flakes provides much information on their interaction with external electric fields, essential for their possible use in applications in which controlled orientation is required. In this work, the electro-orientation of GO was determined in the absence of interparticle interactions, by means of the measurement of linear dichroism. The results were analysed to characterise the geometrical and optical properties, and to determine the polarization mechanisms contributing to the electro-orientation of these particles.

In the first place, from the saturation value of LD, an absorption coefficient of  $760 \text{ mLmg}^{-1} \text{ m}^{-1}$  was obtained for our mildly oxidised GO flakes. Furthermore, the study of the decay of linear dichroism upon removal of the external field by the multi-exponential method furnished a length distribution of the polydisperse GO sample. The results are in good agreement with microscopy determinations. Moreover, from the analysis of the LD build-up after the field is turned on, the polarizability of the GO platelets along their major axis could be calculated.

The measurement of  $\alpha_L^e$  at different field frequencies showed that the polarizability of GO grows significantly above the kHz range. This relaxation of  $\alpha_L^e$  could be explained as follows: For high frequencies, the GO flakes behave as conducting particles suspended in a dielectric medium, and particle polarization is large. On the other hand, for low-frequency fields, the formation of an induced electric double layer screens the particle electric dipole, lowering the overall polarizability. As a conclusion,

the use of high-frequency electric fields enhances the GO response, a fact that must be taken into account to overcome the difficulties of GO electro-orientation.

# 10

## CONCLUSIONS



**Particle shape** has been shown as an important parameter for the description of colloidal systems and for their use in applications. Electric fields are a simple and efficient route to manipulate these particles and control their **orientation**, although much work is still needed to achieve its full potential. In this work, we use **electro-optical techniques** to analyse the interaction of non-spherical particles with external electric fields. Special attention is paid to the polarisation mechanisms of the particles and their electrical double layers, and to the potential that these phenomena possess as characterisation techniques. The main contributions of this dissertation can be summarised as follows:

### **Electric birefringence spectroscopy of montmorillonite particles**

We measured the complete birefringence phenomenology of sodium montmorillonite particles. The analysis of the results demonstrates the positive prospects of this technique and the amount of information that it can provide on such complex systems.

- The spectra of the birefringence permits the observation of well known relaxations of the ionic clouds in EDLs, namely,  $\alpha$  and Maxwell-Wagner.
- ▲ The shape of the spectra suggests that the surface conductivity is not homogeneous, but rather presents an anisotropy associated to the face-edge inhomogeneous charge distribution of these particles.
- ♥ The experimental refractive index of the material is lower than that of bulk montmorillonite, due to particle swelling. The water content could be estimated, and is in good agreement with the literature values.
- For low-frequency fields, the birefringence spectra show anomalous negative values, that is, a tendency of the particles to orient with their faces perpendicular to the applied field, instead of parallel.
- ▲ Such effect is minimized at basic pHs (all surfaces are negatively charged), high ionic strengths (electrostatic screening) and low concentrations.
- ♥ Comparison with previous data on bimodal suspensions suggests that this behaviour is the result of an additional torque induced by

the interaction between the smallest particles of the size distribution of the clay and the largest ones.

### **Electric birefringence of carbon nanotubes: Single- vs double-walled**

The study of the electric birefringence of suspensions of carbon nanotubes allowed the real-time monitoring of their alignment with an external electric field. Two types of particles were compared: single- and double-walled carbon nanotubes (SWNTs and DWNTs respectively).

- DWNTs exhibit a negative birefringence, in contrast to the positive signal found for SWNTs. This anomalous feature could be explained taking into account particle absorbance.
- Both types of nanotubes were shown to undergo almost the same orientation process, because of the cancellation of the  $L^3$ -dependence of the electrical polarizability and the rotational diffusion coefficient at high fields.
- The length of the tubes was obtained from the birefringence decay and from the experimental value of the electrical polarizability anisotropy. The results obtained by these two methods are very similar.
- In the case of the DWNTs, the obtained length differs by a factor 3 from the microscopy results, which suggests that these tubes are more bundled or aggregated when suspended.
- It was possible to prove that the metallic tubes, and not the semiconducting ones, control the electro-optical response of the system, and the refractive index of the particles was obtained.

### **Determination of the size distribution of non-spherical nanoparticles by electric birefringence-based methods**

In this work, we compared the performance of three birefringence-based characterization techniques, namely the stretched-exponential, Watson-Jennings (WJ) and multi-exponential (ME) methods, with electron microscopy and dynamic light scattering measurements.

- The methods were successfully applied to six types of nanoparticles, with very different geometries.
- The ME method furnishes a complete size distribution of the sample, and the results are excellent in most cases. For the goethite needles, the SWNTs or the gibbsite platelets, the obtained distributions are in perfect agreement with the microscopy results.
- For the PTFE and NaMt particles, there are slight differences between the ME method and the microscopy results, but they are not large (below 8%) and can be attributed to the approximations employed in the modelling of the particles.
- ← The WJ method presents larger deviations with respect to the microscopy results in almost all cases, as compared to the ME method, although they remain below 8%. This can be understood taking into account that this method assumes a fixed shape for the size distribution of the sample.
- It can be concluded that the obtained results are excellent, taking into account the very different nature, characteristic sizes and geometries of the selected particles.
- On the other hand, the dynamic light scattering results present strong deviations with respect to the average size found by microscopy, no less than 30% in all cases.

### **Electric birefringence of gold nanorods: Effect of surfactant coating**

We synthesised CTAB-stabilised gold nanorods and studied their electro-optical behaviour, paying special attention to the effect that the surfactant coating plays on the electrical properties of the system.

- It has been experimentally observed that AuNRs exhibit negative electric and flow birefringence. This could be attributed to the strong optical absorbance of gold.
- It has also been shown that the charge of the CTAB layer that stabilises the AuNRs plays a crucial role in their electro-orientation.

- The experimental value of the electrical conductivity of the AuNRs is two orders of magnitude lower than that of bulk gold, as has been previously observed for other gold nano-objects.
- The charge density of the surfactant layer as a function of the ionic strength could be estimated. The results are in good agreement with the values found via the analysis of electrophoretic mobility data with a soft-particle model.
- The study of the AC birefringence spectrum and the transient electric birefringence shows that the rotational diffusion of gold nanorods is slower than expected from their geometry.
- Here, we propose that this field-induced effect is due to the accumulation of CTAB micelles, present in the suspension, around the gold nanorods.

### **Electro-orientation of silver nanowires in alternating fields**

The complete electric birefringence phenomenology of suspensions of commercial silver nanowires was studied in order to obtain information on the polarisation and orientation mechanisms of uncharged metallic particles.

- AgNWs exhibit negative birefringence, a feature also observed for other conducting materials, which could be attributed to particle absorbance.
- The analysis of the transient EB behaviour provided the size distribution of the wires in suspension, in good agreement with that obtained from electron microscopy determinations.
- The high-frequency value of the polarizability is that of a metallic wire. At low frequencies, on the other hand, the polarization decays to a small value due to the appearance of an induced double layer, which screens the particle dipole.
- Moreover, at low frequencies, the hydrodynamic contribution of electro-osmotic fluxes was shown to play a crucial role in particle electro-orientation.

- 🟡 The value of the slip velocity obtained from our measurements is an order of magnitude lower than expected, as observed systematically for other similar systems.

### **Analysis of the electro-optical response of graphene oxide dispersions under alternating fields**

The electro-optical behaviour of graphene oxide flakes provides much information on their interaction with external electric fields. In this work, we study this phenomenology by means of the measurement of linear dichroism.

- 👉 The absorption coefficient of the GO flakes is smaller than the values reported for graphene platelets, due to the effect of the oxidation.
- 👉 The size distribution obtained by the multi-exponential method is in good agreement with microscopy determinations.
- 👉 The saturation of the dichroism impedes working in the Kerr regime, but the polarizability spectra could be determined via the analysis of the LD rise.
- 👉 The electrical polarizability of GO grows significantly above the kHz range, a behaviour which is very similar to the silver nanowire results.
- 👉 The spectral response of the GO flakes indicates that they behave as conducting particles immersed in an electrolyte solution.
- 👉 From the fitting of the dichroism spectra, the average distance that ions travel around the particle could be estimated around 700 nm, a value consistent with particle size.

To sum up, we conclude that the use of electro-optical techniques for the analysis of non-spherical particles in suspension holds a great potential and must be further studied. In this work, its application to very diverse systems has allowed to extract information on their properties and polarisation mechanisms, and to advance in the understanding of not sufficiently explored systems. Hopefully, more publicly funded investigation

will bring about an improvement and dissemination of these techniques, and new applications of particles with controlled geometries.

11

RESUMEN



## 11.1. Introducción y objetivos

A medida que la **ciencia de nanopartículas** avanza, se dispone de nuevos sistemas con propiedades extraordinarias, lo que va inmediatamente seguido de nuevas aplicaciones en diferentes ramas de la técnica y la medicina. De hecho, frecuentemente el potencial de estas partículas se vislumbra incluso antes de que se conozcan con detalle sus propiedades físicas. Sin embargo, aún es necesario seguir trabajando para desarrollar el potencial que estos materiales ofrecen y, sobre todo, para conseguir que estos avances se traduzcan en recursos al alcance de todas las personas, asegurando en todo momento que su conocimiento es público y está al servicio del pueblo.

Aunque frecuentemente se asume que el parámetro fundamental que afecta a las propiedades y aplicaciones de las nanopartículas es su tamaño, cada vez es más evidente que, si bien fundamental, ésta no es la única magnitud relevante. Así, se ha demostrado que la **forma de las partículas**

La forma de las partículas es un parámetro determinante en las propiedades físicas de los sistemas coloidales y sus potenciales aplicaciones.

tiene un efecto sustancial sobre la física de estos sistemas y sus aplicaciones técnicas [1, 2]. Por ejemplo, la forma alargada de los *nanorods* de oro juega un papel fundamental para su uso en sensores de ADN, almacenamiento de datos ópticos de alta densidad o espectroscopía Raman [3–5]. Otros ejemplos son la actividad antibacteriana de las partículas de plata, la toxicidad de los nanotubos de carbono, el comportamiento reológico de las arcillas o las propiedades catalíticas de las nanopartículas de platino [6–9]. Esta es la hipótesis básica del presente trabajo: las nanopartículas de tamaño controlado y forma no esférica poseen características especiales, no suficientemente exploradas y que pueden dar lugar a aplicaciones novedosas en diversos campos.

Además, la posibilidad de controlar la **orientación** de las partículas no esféricas está abriendo nuevas posibilidades, sobre todo en aquellas aplicaciones que explotan propiedades direccionales. Ejemplos de ello pueden encontrarse en el uso de *nanorods* de oro como metamateriales o trampas

de partículas, en la fabricación de electrodos transparentes con nanovarillas de plata, en la implementación de nanotubos de carbono como sensores de ADN, sondas para microscopios o fotodetectores, y en la fabricación de supercondensadores basados en grafeno [10–16]. Una técnica sencilla y eficiente para la manipulación de micro y nanopartículas es el uso de campos eléctricos. Por ejemplo, la dielectroforesis se ha utilizado en la separación de partículas biológicas, como células o bacterias, y en la separación de los nanotubos de carbono metálicos y semiconductores [17–19]. Además, mediante diferentes técnicas basadas en la aplicación de campos eléctricos se ha logrado el ensamblaje y orientación de partículas no esféricas de diferente naturaleza, suspendidas en medio líquido [20–23]. Sin embargo, los mecanismos que dan lugar a este ordenamiento todavía no se entienden completamente, dada la complejidad de los procesos electrohidrodinámicos que lo provocan.

En muchos casos, las micro y nanopartículas se utilizan dispersas en medio acuoso, lo que da lugar a fenómenos interfaciales que gobiernan el comportamiento macroscópico de las suspensiones, complicando su descripción. El presente trabajo se centra en la respuesta de dispersiones de partículas no esféricas bajo el efecto de campos eléctricos, prestando especial atención a los mecanismos de polarización de la partículas y sus dobles capas eléctricas. En el caso de partículas dieléctricas con formas simples, este problema ha sido atajado de forma analítica por Shilov y cols. [24, 25], y numéricamente por Fixman [26]. Además, en la última década, se han desarrollado varios trabajos experimentales [27–32]. Dukhin y cols. estudiaron el caso de partículas metálicas esféricas poco cargadas [33, 34]. Recientemente, estos cálculos se han extendido a otras geometrías [35, 36], y se están llevando a cabo estudios experimentales para este tipo de partículas [37–41].

En este trabajo estudiamos la **polarización de partículas no esféricas en suspensión** mediante el análisis de los fenómenos electro-ópticos, que consisten en la modificación de diferentes propiedades ópticas de las suspensiones por la aplicación de un campo eléctrico [42, 43]. Aquí, nos centramos en dos de ellos: La birrefringencia eléctrica y el dicroísmo lineal, ambos relacionados con la electro-orientación de partículas no esféricas. El análisis

de estos efectos puede proporcionar información útil sobre las propiedades ópticas, eléctricas y geométricas de las partículas en suspensión, y sobre los fenómenos electrocinéticos que tienen lugar en sus interfases. Por lo tanto, tenemos un doble propósito: entender los fenómenos observados y utilizar las técnicas electro-ópticas para la caracterización de partículas de diferentes geometrías.

En este sentido, por ejemplo, la birrefringencia eléctrica transitoria se utiliza desde hace tiempo para obtener información sobre la flexibilidad o el tamaño de partículas no esféricas [44–46]. Sin embargo, sólo

Los fenómenos electro-ópticos consisten en la modificación de las propiedades ópticas de las suspensiones de partículas no esféricas por la aplicación de campos eléctricos, y pueden utilizarse como técnicas de caracterización.

unos pocos trabajos se centran en el análisis de la distribución de tamaños de muestras polidispersas mediante este método [47, 48]. El decaimiento de la birrefringencia depende del cubo del tamaño de las partículas, proporcionando una gran sensibilidad, lo que hace que esta técnica presente un gran potencial. Por otra parte, la espectroscopía de birrefringencia se ha propuesto como una potente herramienta para la medida directa de la polarizabilidad de las partículas en suspensión [49, 50]. Entre otras ventajas, esta técnica es altamente susceptible a la anisotropía de las partículas, a diferencia de otras como la espectroscopía dieléctrica o la electroforesis, que típicamente miden magnitudes promediadas espacialmente. Por lo tanto, puede proporcionar información sobre el efecto de la forma de la partícula y de inhomogeneidades en la distribución de carga o en la estructura interna.

En resumen, este trabajo se centra en el estudio de la **respuesta electro-óptica** de partículas no esféricas de naturaleza muy diferente. Del análisis de los resultados experimentales podemos obtener información sobre las propiedades eléctricas, ópticas y geométricas de las partículas, y sobre sus mecanismos de polarización, muy ligados a la presencia de la doble capa eléctrica. Los principales objetivos pueden resumirse de la siguiente manera:

- La medida y estudio de la fenomenología electro-óptica de partículas

no esféricas con propiedades muy diversas.

- El avance en la comprensión del comportamiento de las partículas metálicas, poco estudiadas en la literatura.
- El progreso en el uso de las técnicas electro-ópticas para la caracterización de nanopartículas, sobre todo en cuanto a las distribuciones de tamaño de muestras polidispersas.

## 11.2. Polarización y electro-orientación de partículas

### 11.2.1. Principios básicos de la polarización

Cuando una partícula cargada se encuentra sumergida en un medio dieléctrico, los iones en torno a la misma se redistribuyen y dan lugar a una estructura conocida como **doble capa eléctrica** (EDL), que determina muchas de las propiedades macroscópicas de las suspensiones coloidales [51–55]. Así, cuando se aplica un campo eléctrico a una dispersión, su comportamiento depende de la respuesta tanto de las partículas como de sus EDLs. Ésta a su vez viene gobernada por diferentes **mecanismos de polarización**, cada uno con un tiempo característico propio. La Figura 11.1 muestra esquemáticamente estos procesos para el caso de partículas esféricas, que describimos a continuación:

- La primera reacción, casi instantánea, del sistema a la aplicación de un campo eléctrico es la **polarización de las nubes electrónicas** [63]. En este caso, la polarizabilidad de las partículas viene dada por el contraste entre la permitividad relativa de la partícula,  $\epsilon_p$ , y del medio  $\epsilon_m$  [62]:

$$\alpha_{\text{perm}} = 3V_p\epsilon_0\epsilon_m \frac{\epsilon_p - \epsilon_m}{\epsilon_p + 2\epsilon_m} \quad (11.1)$$

siendo  $V_p$  el volumen de la partícula y  $\epsilon_0$  la permitividad del vacío.

- Para tiempos más largos, las cargas libres de la partícula y su doble capa tienen tiempo suficiente para desplazarse, y por lo tanto la polarizabilidad pasa a depender del contraste entre conductividades de

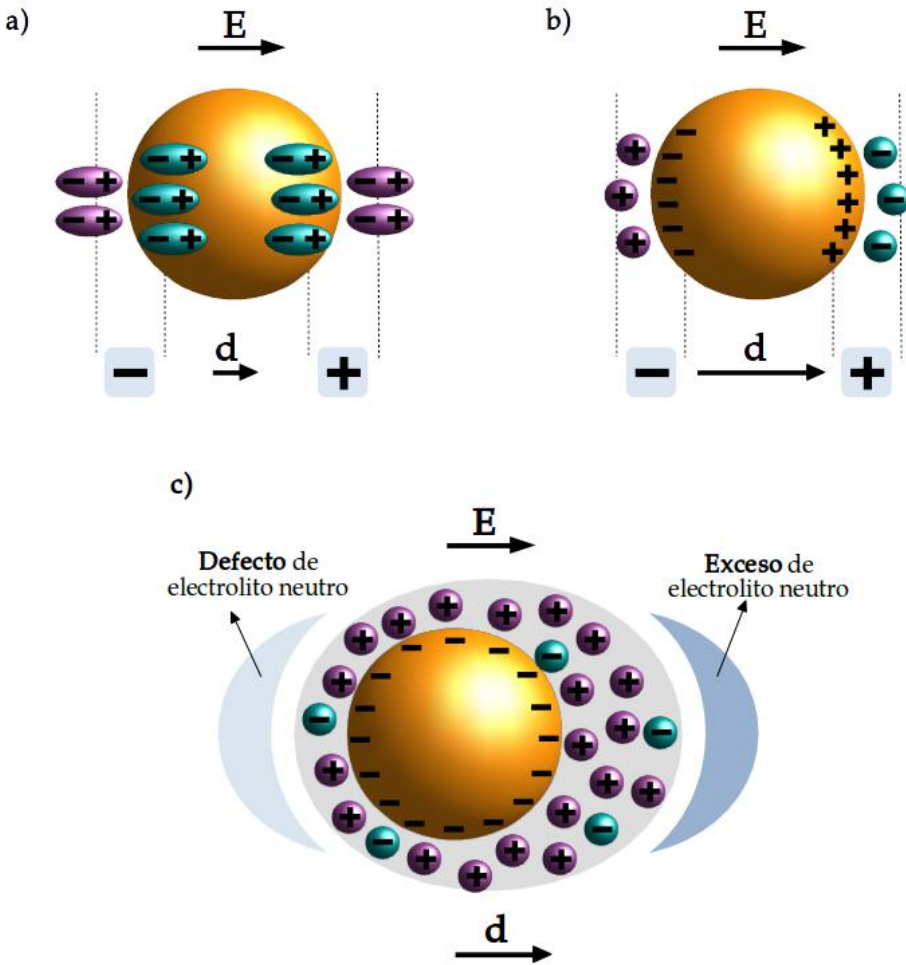


FIGURA 11.1: Representación esquemática de a) la polarización de las nubes electrónicas, b) la polarización de Maxwell-Wagner-O'Konski y c) la polarización de concentración.  $E$  indica el campo eléctrico aplicado y  $d$  el dipolo inducido.

la partícula y el medio [64, 65]. Hay que tener en cuenta en este caso que la presencia de la EDL da lugar a un exceso de conductividad superficial,  $K^\sigma$ , que debe tenerse en cuenta para calcular la conductividad efectiva de la partícula [66]. De esta forma, la polarizabilidad queda [62]:

$$\alpha_{\text{cond}} = 3V_p \epsilon_0 \epsilon_m \frac{K_p^{\text{eff}} - K_m}{K_p^{\text{eff}} + 2K_m} \quad K_p^{\text{eff}} = K_p + 2K^\sigma/a \quad (11.2)$$

donde  $K_m$  es la conductividad del medio,  $K_p$  la de la partícula y  $a$  el radio. Este mecanismo se conoce como **polarización de Maxwell-Wagner-O'Konski**, y presenta un tiempo característico análogo al de carga de un condensador:

$$\tau_{\text{MWO}} = \frac{\epsilon_0 \epsilon_p + \epsilon_0 \epsilon_m}{K_p^{\text{eff}} + K_m} \quad (11.3)$$

- El mecanismo más lento es la **polarización de concentración**, asociada a la deformación de la EDL debido a que los flujos electromigratorios y difusivos de iones no son simétricos dentro y fuera de la misma [52]. Este fenómeno da lugar a una reducción de la polarización de las partículas.

Por otra parte, en el caso de **partículas metálicas** poco cargadas, la estructura de la doble capa eléctrica es bastante débil, mientras que la polarización de la partícula es muy grande. Esto da lugar a fenómenos de redistribución de carga que se traducen en mecanismos de polarización diferentes, representados en la Figura 11.2 [72, 73]:

- Para tiempos cortos, la partícula se polariza como un **conductor perfecto**.

$$\alpha_{\text{cond}} = 3V_p \epsilon_0 \epsilon_m \quad (11.4)$$

- Sin embargo, para tiempos más largos los iones en disolución se redistribuyen y apantallan la carga de la partícula, anulando su efecto. En este caso, el sistema se comporta como un dieléctrico y no se observa polarización total. El tiempo necesario para el establecimiento de este mecanismo viene dado por:

$$\tau_{\text{EDL}} = \frac{aC_{\text{EDL}}}{K_m} \quad (11.5)$$

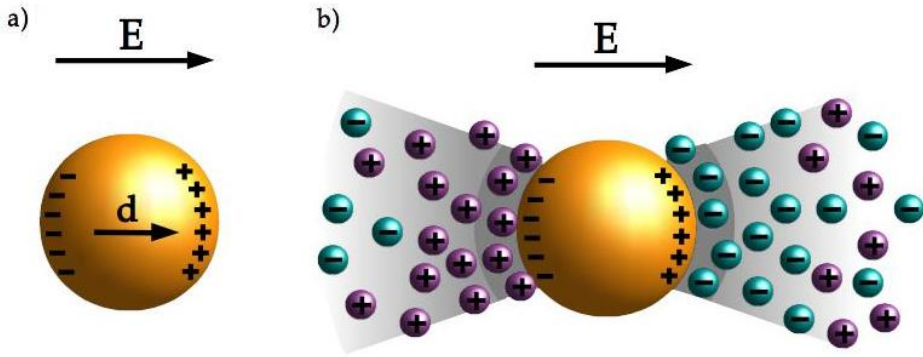


**FIGURA 11.2:** Representación esquemática de la polarización de una partícula metálica a) a tiempos cortos y b) a tiempos largos.  $E$  indica el campo eléctrico aplicado y  $d$  el dipolo inducido.

donde  $C_{EDL}$  es la capacidad de las **EDLs inducidas** por la redistribución de carga.

Esta discusión llevada a cabo en el dominio del tiempo puede extenderse de forma sencilla al **dominio de la frecuencia** mediante la **relajación de la polarizabilidad** [67]. Así, para frecuencias bajas del campo eléctrico, todos los mecanismos de polarización pueden establecerse entre dos inversiones consecutivas del campo. Sin embargo, a medida que la frecuencia aumenta, los mecanismos más lentos dejan de contribuir a la polarización, dado que no tienen suficiente tiempo para establecerse.

### 11.2.2. Electro-orientación y electro-óptica de partículas no esféricas

Los mecanismos de polarización expuestos en el apartado anterior son extensibles al caso de partículas con **geometría no esférica**. Sin embargo, para éstas la polarizabilidad no es isótropa, y en general viene descrita por un tensor [63]. Cuando las partículas tienen simetría axial, sólo dos componentes del mismo son no nulas, y puede definirse la anisotropía de la polarizabilidad como:

$$\Delta\alpha^e = \alpha_{\parallel p}^e - \alpha_{\perp p}^e \quad (11.6)$$

donde  $\alpha_{\parallel p}^e$  y  $\alpha_{\perp p}^e$  son las polarizabilidades a lo largo de las direcciones paralela y perpendicular al eje de simetría de las partículas.

Debido a esta anisotropía, en general, el dipolo inducido en este caso no es paralelo al campo aplicado, lo que da lugar a la aparición de un torque  $\tau$  que obliga a la partícula a rotar hasta que su eje mayor está alineado con el campo [49, 78]. Este fenómeno se conoce como **electro-orientación**, y compete con la difusión rotacional, que tiende a llevar al sistema a una orientación aleatoria. La Figura 11.3 muestra una representación esquemática de este proceso para el caso de una geometría alargada y otra achatada.

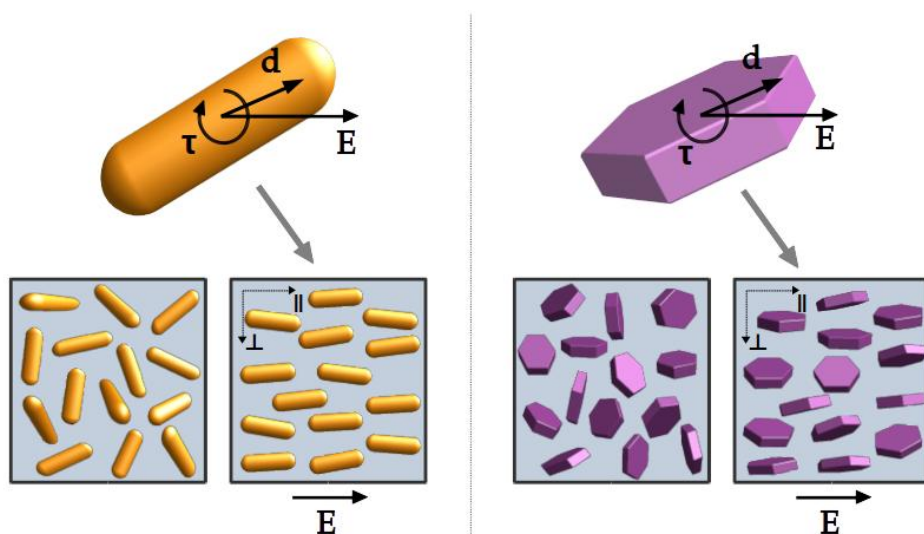


FIGURA 11.3: Representación esquemática del proceso de electro-orientación para partículas alargadas y planas.

La electro-orientación de las partículas de una suspensión da lugar a una anisotropía del sistema a escala macroscópica. Los **fenómenos electro-ópticos** son aquellos relacionados con los cambios en las propiedades ópticas de las suspensiones coloidales debido a la aplicación de campos eléctricos externos [42, 88]. En este trabajo analizamos dos de estos fenómenos:

- **Birrefringencia eléctrica (EB):** Se define como la diferencia entre el índice de refracción de la suspensión a lo largo de las direcciones paralela y perpendicular al campo aplicado,  $\Delta n = n_{\parallel} - n_{\perp}$ .
- **Dicroísmo lineal (LD):** Es la anisotropía que se induce en la absorbancia de la suspensión debido a la electro-orientación de las partículas ( $\Delta A = A_{\parallel} - A_{\perp}$ ).

Ambas magnitudes presentan dependencias muy similares. Así, para sistemas diluidos, la EB y el LD son proporcionales a la concentración de partículas. Además, para campos bajos, ambas magnitudes son proporcionales al cuadrado de la amplitud del campo aplicado, dependencia que se conoce como ley de Kerr [81, 84]. Por otra parte, cuando el campo es muy elevado, casi todas las partículas están orientadas y se llega a la saturación de la EB y el LD, situación en la que no se observa dependencia con la amplitud de campo. Dentro del régimen de Kerr, la EB y el LD son proporcionales a  $\Delta\alpha^e$ , y por lo tanto tienen la misma dependencia espectral que ésta. A su vez, la dependencia de la polarizabilidad con la frecuencia viene dada por la relajación de los diferentes mecanismos de polarización y, por lo tanto, el estudio del comportamiento espectral de los fenómenos electro-ópticos proporciona información directa sobre la polarizabilidad de las partículas y sus dobles capas.

Además, cuando se retira el campo eléctrico, la caída de la EB y el LD, debidas a la difusión rotacional, no son instantáneas, sino que presentan una dependencia temporal directamente relacionada con el tamaño de las partículas. De hecho, se han propuesto varios métodos para la caracterización de las dimensiones de las partículas en suspensión mediante el análisis de estos procesos [46–48, 94].

## 11.3. Principales resultados

### 11.3.1. Espectroscopía de birrefringencia eléctrica de partículas de montmorillonita

La montmorillonita sódica utilizada en este trabajo se obtuvo a partir de bentonita, una arcilla natural, mediante un proceso de homoionización [103]. Estas partículas de geometría aplanada tienen carga negativa fija en sus caras, y dependiente del pH en sus aristas [97, 103]. Además, cuando están en suspensión, las moléculas de agua penetran entre sus capas y dan lugar al hinchado del material. La birrefringencia eléctrica de estas partículas se ha determinado con un equipo casero, capaz de medir la respuesta electro-óptica en un rango espectral amplio.

El espectro de la birrefringencia para diferentes valores del pH se muestra en la Figura 11.4. Los datos se han ajustado con los modelos detallados en [25, 122]. Para describir el espectro experimental es necesario considerar que las partículas presentan una distribución de carga no homogénea. Así, la relación entre la conductividad a lo largo del eje menor y el mayor,  $K_a/K_b$ , es un parámetro libre. Los valores obtenidos se muestran en la Tabla 11.1, donde se observa que a medida que el pH de la muestra aumenta, este cociente se va aproximando cada vez más al valor correspondiente a una carga homogénea, 0.27. Esto es consistente con el hecho de que a pH básico todas las superficies están negativamente cargadas, y la inhomogeneidad de carga disminuye.

**TABLA 11.1:** Valores de la conductividad superficial y la anisotropía de carga obtenidos del ajuste de los datos experimentales al modelo electrocinético.

pH	$K^\sigma$ ( $10^{-8}$ S)	$K_a/K_b$
5	4.4	0.003
7	4.0	0.008
9	3.7	0.009

Además, en la misma tabla se presenta el valor obtenido para la conductividad superficial de la EDL. Los valores son bastante elevados, lo que probablemente sea una manifestación de la presencia de la conductividad

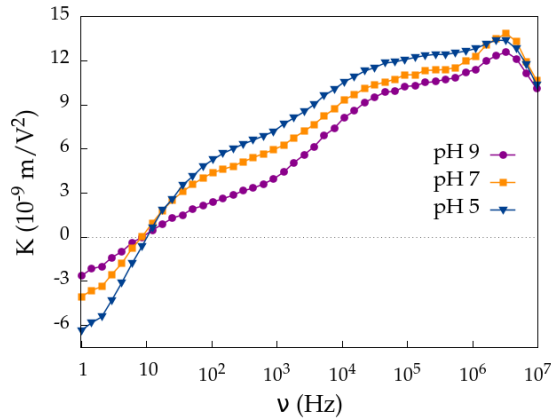


**FIGURA 11.4:** Espectro de birrefringencia de una muestra de montmorillonita sódica a 1 g/L, con 0.3 mM NaCl y diferentes valores del pH. La amplitud del campo aplicado es 10 V/mm.

de la capa de Stern [52, 134, 135], y están en acuerdo con otros valores bibliográficos [136]. Por otra parte, del valor de la birrefringencia se obtuvo experimentalmente la anisotropía óptica de las partículas,  $\Delta\alpha^0 = 4,3 \cdot 10^{-33}$  Fm<sup>2</sup>, correspondiente a un índice de refracción mucho menor que el de la montmorillonita. Este efecto se debe al hinchado del material, y de hecho a partir de los valores experimentales pudo estimarse que el contenido en agua de las partículas es de un 88 %, un porcentaje compatible con los valores bibliográficos (90-93 %) [97, 99].

En la zona de baja frecuencia del espectro se observa que la señal birrefringente pasa a tener signo negativo, lo que se corresponde con una orientación anómala de las partículas, con su eje mayor perpendicular a la dirección del campo aplicado. En la Figura 11.4 se observa que este efecto disminuye a medida que el pH de la muestra aumenta y la carga de toda la partícula se va haciendo más negativa. Por lo tanto, es razonable considerar que este fenómeno anómalo puede deberse a la interacción entre partículas. Por ello, medimos el espectro para muestras con diferentes concentraciones. Los resultados se presentan en la Figura 11.5, donde puede observarse que, en la zona de alta frecuencia, la birrefringencia es proporcional a la concentración, es decir, no hay interacciones entre partículas. Sin

embargo, en la zona de baja frecuencia existe una dependencia importante con la concentración de partículas: el efecto anómalo se ve reforzado a concentraciones altas.

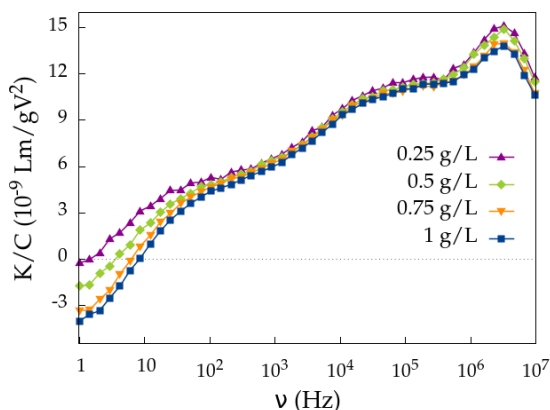


**FIGURA 11.5:** Espectro de birrefringencia, normalizado con la concentración  $C$ , de una muestra de montmorillonita sódica a pH natural, 0.3 mM NaCl y diferentes concentraciones de partícula. La amplitud de campo aplicado es 10 V/mm.

Por lo tanto, concluimos que la orientación anómala a bajas frecuencias se debe efectivamente a la interacción entre partículas. Este efecto es similar al observado en el caso de suspensiones bidispersas de partículas no esféricas (partículas primarias) con otras más pequeñas y esféricas (partículas secundarias). Estos sistemas se han estudiado tanto desde el punto de vista experimental como teórico [26, 50, 80], y se ha concluido que el efecto anómalo se debe a la redistribución asimétrica de las partículas secundarias en torno a las primarias para campos de baja frecuencia, lo que da lugar a un torque hidrodinámico responsable de la orientación anómala. En nuestro caso, el papel de las partículas secundarias lo jugarían las partículas más pequeñas de la muestra polidispersa, mientras que las más grandes serían las partículas primarias.

### 11.3.2. Birrefringencia eléctrica de nanotubos de carbono: comparación entre tubos de pared simple y doble

En este trabajo se ha determinado la respuesta electro-óptica de nanotubos de carbono de pared simple y doble (SWNTs y DWNTs), obtenidos comercialmente de *Carbolex* y *US Research Nanomaterials* respectivamente. Estas muestras presentan una fracción de tubos conductores y otra de tubos semiconductores, en función de la estructura de la hoja de grafeno al cerrarse [111]. Los tubos se suspendieron en 1,2-dicloroetano con la ayuda de una sonda de ultrasonidos. La Figura 11.6 muestra una medida completa de su birrefringencia, donde puede apreciarse que los DWNTs dan una señal negativa, que puede deberse bien al signo de la anisotropía óptica o bien a una orientación anómala. Para estudiar las dos posibilidades, se llevaron a cabo medidas de dicroísmo lineal (misma figura), observándose que el dicroísmo de ambas muestras es positivo, lo que se corresponde con una orientación normal de ambos tipos de partículas, con su eje mayor en la dirección del campo aplicado. Por lo tanto, el signo negativo de los DWNTs se debe a una anomalía en su anisotropía óptica.

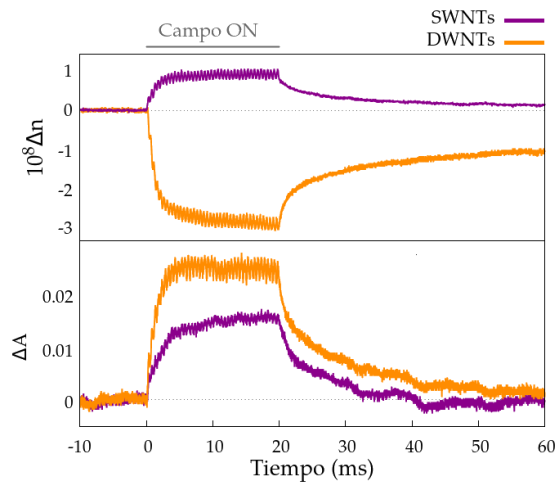


**FIGURA 11.6:** Birrefringencia (arriba) y dicroísmo eléctrico (abajo) de los SWNTs y DWNTs. La concentración de partículas es  $10^{-4}$  wt%, la frecuencia del campo 1 kHz, la amplitud 250 V/mm y la duración del pulso 20 ms.

La dependencia de la birrefringencia con el campo aplicado se muestra en la Figura 11.7, donde puede apreciarse que la ley de Kerr se cumple para campos bajos, y la saturación se alcanza a valores en torno a los 100-200 V/mm. De estos datos experimentales podemos extraer el valor de la anisotropía de la polarizabilidad eléctrica y óptica de las partículas. Los resultados se presentan en la Tabla 11.2. El valor de  $\Delta\alpha^e$  se corresponde con partículas conductoras y, por lo tanto, son los nanotubos metálicos (y no los semiconductores) los que dominan la electro-orientación del sistema. De dicho valor se puede estimar la longitud de los tubos,  $L$ , que se presenta en la misma tabla [63]. Como puede verse, los resultados obtenidos están en buen acuerdo con los que se extraen de la caída de la birrefringencia. Además, para los SWNTs, el valor coincide con el obtenido mediante microscopía. En el caso de los DWNTs, sin embargo, los resultados difieren en un factor 3, lo que podría indicar que estos tubos están más agregados o entrelazados cuando se encuentran en suspensión.

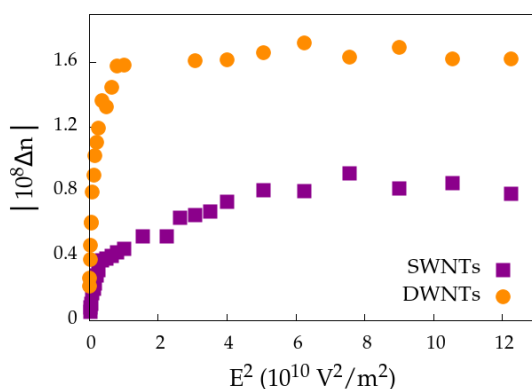


**FIGURA 11.7:** Birrefringencia eléctrica de los SWNTs y DWNTs en función de la amplitud de campo,  $E$ . La concentración de partículas es  $10^{-4}$  wt % y la frecuencia del campo aplicado 1 kHz.

Por otra parte, ha sido posible determinar el origen del signo negativo de  $\Delta\alpha^o$ : los nanotubos de carbono son partículas absorbentes y, por lo tanto, su índice de refracción es complejo, lo que puede dar lugar a valores negativos de la polarizabilidad óptica. Midiendo la absorbancia de los tubos con

**TABLA 11.2:** Valores de diferentes propiedades de los tubos obtenidas a partir de la fenomenología birrefringente de las partículas.

	SWNTs	DWNTs
$\Delta\alpha^e$ ( $10^{-30}$ Fm <sup>2</sup> )	$16.9 \pm 3.1$	$48.7 \pm 3.3$
$\Delta\alpha^o$ ( $10^{-34}$ Fm <sup>2</sup> )	$1.09 \pm 0.18$	$-2.18 \pm 0.13$
L (A partir de $\Delta\alpha^e$ )	$1080 \pm 200$ nm	$1630 \pm 100$ nm
L (Caída de la EB)	1100 nm	2400 nm
L (Microscopía)	$900 \pm 570$ nm	$580 \pm 40$ nm
$n_p$	$2.6 \pm 0.1$	$\approx 2.2$

un espectrofotómetro, fue posible obtener el valor experimental del índice de refracción de las partículas,  $n_p$ , presentado en la Tabla 11.2. El resultado obtenido para los SWNTs es muy parecido a los valores bibliográficos para el grafeno [166, 167]. En el caso de los DWNTs, ha podido explicarse el signo anómalo de la birrefringencia, aunque el valor de  $n_p$  no es muy preciso debido a la incertidumbre en la concentración de la muestra.

### 11.3.3. Determinación de las distribuciones de tamaño de partículas no esféricas mediante métodos basados en la birrefringencia

Una vez las partículas han sido orientadas por la aplicación de un campo eléctrico, al retirarlo, la birrefringencia decae a cero en un tiempo determinado. Este proceso de desorientación de las partículas en suspensión está gobernado por la difusión rotacional, íntimamente relacionada con el tamaño de las partículas. Por lo tanto, el análisis de la caída de la EB puede proporcionar información útil sobre las dimensiones de las partículas en dispersión. En este trabajo analizamos el comportamiento transitorio de la birrefringencia eléctrica mediante tres métodos:

- **Método de la exponencial estirada (SE)** [45, 199]: Bajo ciertas condiciones razonables, el decaimiento de la birrefringencia de una mues-

tra polidispersa toma la forma de una exponencial estirada. El tiempo de caída  $\tau$  de esta función está directamente relacionado con el coeficiente de difusión rotacional  $\Theta$  de las partículas como  $\tau = 1/6\Theta$ . Por lo tanto, mediante el ajuste de la caída de la EB es posible obtener el valor de  $\Theta$ , del cual se puede extraer el tamaño medio de las partículas. Dado que la birrefringencia es proporcional a  $V_p$ , las dimensiones obtenidas mediante este método están promediadas en volumen.

- **Método de Watson-Jennings (WJ)** [48]: En este caso se supone que la distribución de tamaños de las partículas toma la forma de una función log-normal, y se relacionan los parámetros de la distribución con el valor de la derivada logarítmica del decaimiento normalizado a tiempos bajos y del área total bajo la curva.
- **Método multi-exponencial (ME)** [47]: Este método asume que el decaimiento de la birrefringencia puede construirse como una superposición de procesos exponenciales, cada uno correspondiente a una población de tamaño bien definido. El tiempo característico de decaimiento de la población  $i$  se relaciona con su coeficiente de difusión rotacional como  $\tau_i = 1/6\Theta_i$ . De esta forma, a partir de la medida experimental del decaimiento de la birrefringencia se puede obtener la contribución  $C_i$  de la población  $i$  a la señal total. Los coeficientes  $C_i$  proporcionan la distribución de tamaño en volumen de la muestra.

Estos métodos se aplican a 6 materiales diferentes: Varillas de goetita, *rods* de PTFE, nanotubos de carbono de pared simple y doble, nanoplacas de gibsita y partículas de montmorillonita sódica (NaMt). Los resultados obtenidos se presentan en la Figura 11.8, junto con las distribuciones medidas por microscopía electrónica. En el caso de los DWNTs, el tamaño obtenido mediante EB es superior en un factor 2 a los resultados de microscopía, lo que parece indicar que los nanotubos están más agregados o entrelazados en suspensión, lo cual está de acuerdo con los resultados del apartado anterior.

En el resto de los casos, los resultados obtenidos son muy similares a los de microscopía, lo que demuestra el potencial de estos métodos como técnicas de caracterización del tamaño de partículas no esféricas. El método

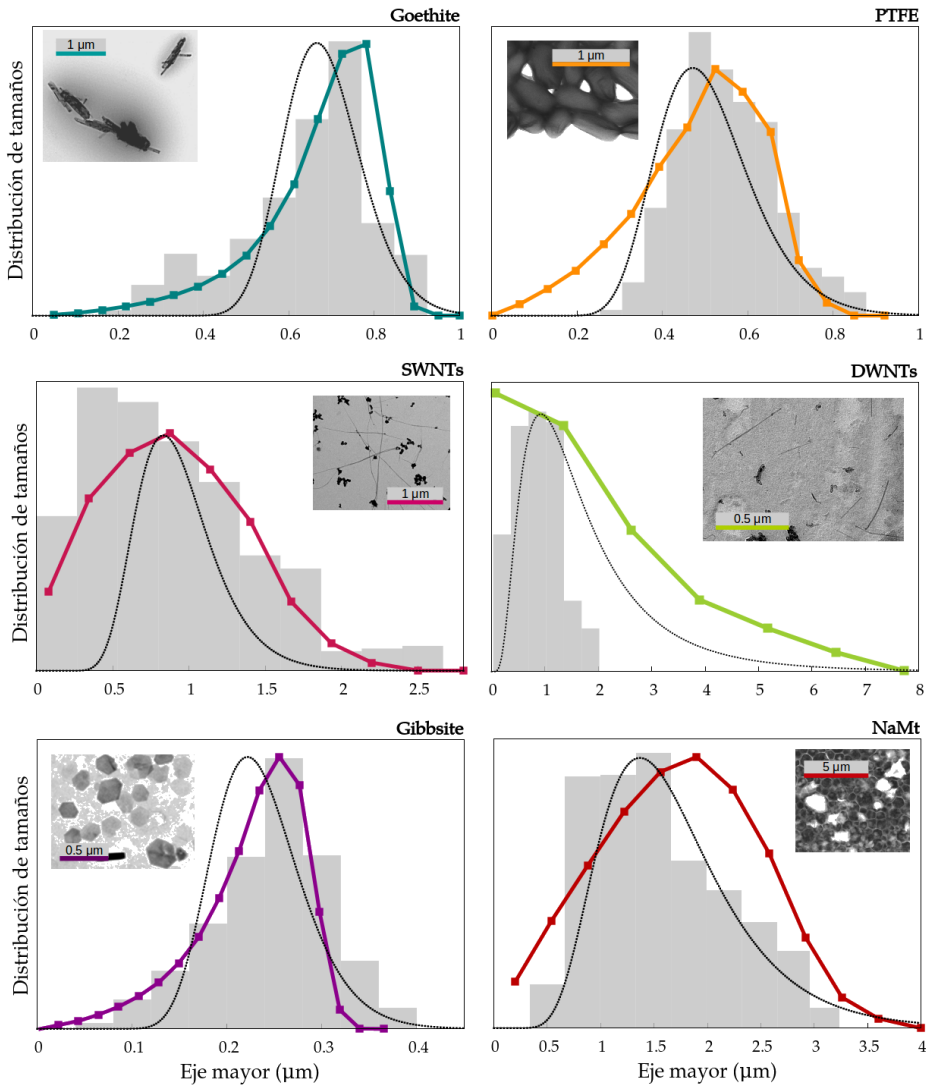


**FIGURA 11.8:** Distribuciones de tamaño en volumen obtenidas con los métodos ME (puntos coloreados), WJ (línea negra discontinua) y microscopía electrónica (barras grises). Los recuadros contiene fotografías de microscopía de las muestras.

SE calcula sólo una longitud media promediada en volumen, siendo sus resultados muy parecidos a los obtenidos mediante el método ME. Por su parte, éste sí proporciona la distribución de tamaños de la muestra, siendo

los resultados excelentes en la mayoría de los casos. Para todos los materiales estudiados, las desviaciones del tamaño medio con respecto al valor de microscopía están por debajo del 8 %. El método WJ presenta desviaciones más significativas, lo que puede entenderse dado que este método asume una forma específica para la distribución de tamaño. Aun así, dichas desviaciones también se mantienen por debajo del 8 %.

#### 11.3.4. Birrefringencia eléctrica de *nanorods* de oro: Efecto del tensioactivo

Los *nanorods* de oro (AuNRs) utilizados en este trabajo han sido sintetizados en nuestro laboratorio por el método descrito en [104]. Las partículas resultantes tienen una longitud media de 56 nm y un diámetro de 16 nm, y están recubiertos por una bicapa compacta de CTAB de unos 3.3 nm de espesor [? ]. La señal birrefringente de estas partículas se muestra en la Figura 11.9, donde se observa que la respuesta de las mismas es negativa. Para esclarecer si este efecto se debe a una orientación anómala o a un signo negativo de  $\Delta\alpha^0$ , se ha medido la birrefringencia de flujo de los AuNRs, mostrada en la misma figura. Como se observa, esta respuesta también es negativa, por lo que podemos concluir que el signo de la EB no se debe a una orientación anómala de los AuNRs.

Esto puede explicarse de la misma forma que para el caso de los DWNTs, teniendo en cuenta que las partículas de oro son altamente absorbentes. Utilizando valores bibliográficos para las constantes ópticas del oro se puede calcular el valor teórico de la polarizabilidad óptica,  $\Delta\alpha^0 = -1,4 \cdot 10^{-33} \text{ Fm}^2$ . Así, el signo experimental puede explicarse teniendo en cuenta las propiedades del material.

La Figura 11.10 muestra el espectro de birrefringencia de los AuNRs para diferentes valores de la fuerza iónica. Aquí puede observarse que la respuesta es muy diferente al comportamiento de otras partículas conductoras, para las que la señal disminuye a frecuencias bajas [74]. Por lo tanto, estas partículas no siguen la dependencia teórica de las partículas metálicas poco cargadas. Esto se debe a la capa de CTAB que recubre y estabiliza los AuNRs, que proporciona una carga elevada, dando lugar a una impor-

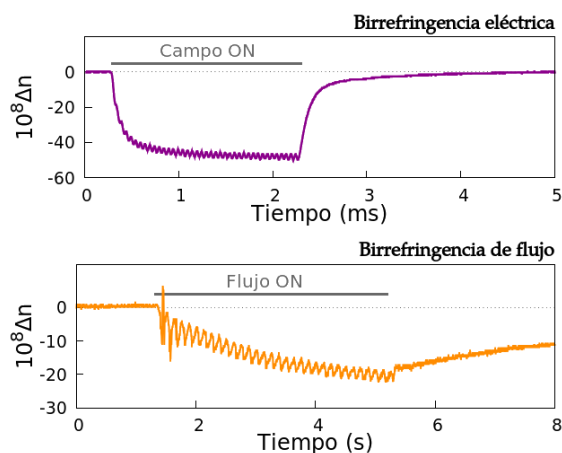


**FIGURA 11.9:** Arriba: Birrefringencia eléctrica de una muestra de AuNRs a 85 mg/L, sometida a un campo de 150 V/mm y 10 kHz durante 20 ms. Abajo: Birrefringencia de flujo de una suspensión a 1400 mg/L bajo un flujo de 0.2 mL/s en un canal de 1 mm<sup>2</sup>.

tante EDL que domina el comportamiento.

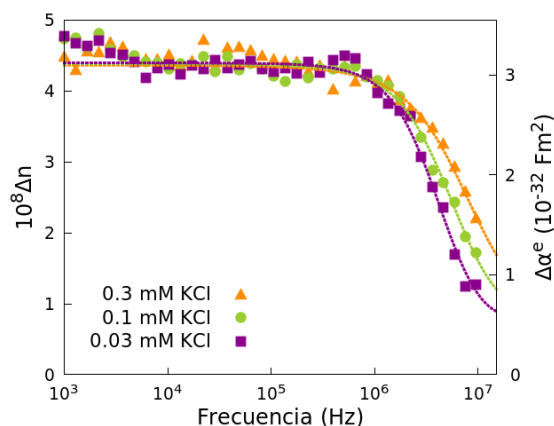


**FIGURA 11.10:** Espectro de la birrefringencia (eje izquierdo) y la polarizabilidad eléctrica (eje derecho) de tres muestras de AuNRs a 88 mg/L y diferentes valores de la fuerza iónica, para un campo de 37 V/mm. Los puntos son los datos experimentales y las líneas discontinuas ajustes al modelo empleado.

Para tener en cuenta en mayor medida el efecto de esta capa, su presencia se introduce en el modelo teórico considerando que las partículas constan

de un núcleo conductor de oro de 56 nm de longitud y 16 nm de diámetro, y una capa dieléctrica de 3.3 nm de grosor. La conductividad del interior se toma de valores bibliográficos para otros nano-objetos de oro, que oscilan entre  $3.5\text{-}440 \cdot 10^5$  S/m. Sólo los valores de este rango por debajo de  $10^6$  S/m son capaces de ajustar nuestros datos experimentales, eligiéndose  $8 \cdot 10^5$  S/m como el valor más adecuado. La conductividad dentro de la capa de CTAB se deja como el único parámetro ajustable.

Como se observa en la figura, el modelo detallado proporciona un buen ajuste de los datos experimentales. El valor de la conductividad del recubrimiento depende ligeramente de la fuerza iónica, obteniéndose 0.15, 0.19 y 0.26 S/m respectivamente para 0.03 mM, 0.1 mM y 0.3 mM KCl. A partir de estos valores puede calcularse la densidad de carga de la capa de CTAB. Como se muestra en la Tabla 11.3, los resultados obtenidos están en buen acuerdo con los calculados a partir de medidas de movilidad electroforética, utilizando un modelo descrito en [233]. Las diferencias cuantitativas permanecen en todo momento por debajo del 20% y en los dos casos se observa la misma tendencia de la densidad de carga a crecer con la fuerza iónica.

**TABLA 11.3:** Densidad de carga de la capa de CTAB ( $\text{MC}/\text{m}^3$ ) obtenida a partir de los experimentos de birrefringencia eléctrica y de las medidas de movilidad electroforética.

Conc. KCl (mM)	0.03	0.1	0.3
Birrefringencia	1.9	2.4	3.3
Movilidad	1.8	2.6	2.8

### 11.3.5. Electro-orientación de nanohilos de plata en campos alternos

Los nanohilos de plata (AgNWs) utilizados en este trabajo se obtuvieron comercialmente de *PlasmaChem*, Alemania, y presentan una carga ligeramente negativa, con un potencial zeta de aproximadamente -30 mV. La Figura 11.11 muestra una imagen de estas partículas, y las distribuciones de tamaño obtenidas mediante microscopía y aplicando el método multi-

exponencial a la caída de la birrefringencia. Los resultados obtenidos están en buen acuerdo, con una diferencia del valor medio de menos del 10%. Sin embargo, puede observarse que la distribución proporcionada por el método ME es ligeramente más estrecha, lo que puede deberse a las dificultades para determinar la longitud a partir de las imágenes de microscopía.

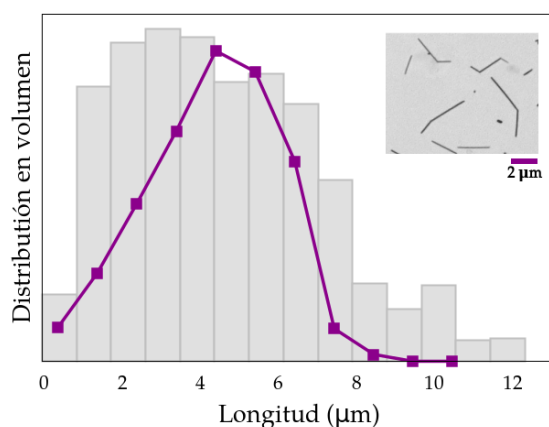


**FIGURA 11.11:** Distribución de longitudes en volumen de la muestra de AgNWs, obtenida por microscopía (barras grises) y aplicando el método multi-exponencial a la caída de la birrefringencia (puntos con líneas). El recuadro contiene una imagen de microscopía de las partículas.

El espectro de birrefringencia de estas partículas se presenta en la Figura 11.12. Los datos experimentales se ajustan al modelo teórico de la electro-orientación de partículas metálicas alargadas [74], teniendo en cuenta los flujos de electro-osmosis por carga inducida (ICEO) que dominan el sistema a frecuencias bajas. Los cálculos de la polarización y los flujos ICEO se realizan numéricamente. Como se observa en la gráfica, el modelo teórico ajusta perfectamente los datos experimentales. Cualitativamente, a frecuencias altas la polarización obtenida es la de una partícula perfectamente polarizable, con las dimensiones determinadas por microscopía. Para frecuencias bajas, las dobles capas inducidas apantallan la polarización de la partícula y el torque eléctrico se anula. Sin embargo, aparece un momento hidrodinámico que orienta ligeramente los AgNWs.

La capacidad obtenida para la doble capa inducida es de 1.4 veces el valor

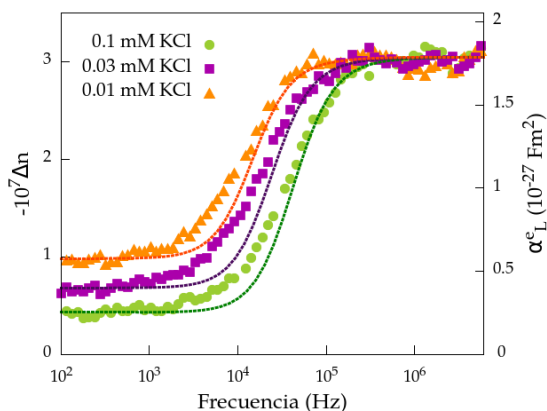


**FIGURA 11.12:** Espectro de la birrefringencia (eje izquierdo) y la polarizabilidad eléctrica (eje derecho) de tres muestras de AgNWs a 100 mg/L y diferentes valores de la fuerza iónica, para un campo de 2 V/mm. Los puntos son los datos experimentales y las líneas discontinuas ajustes al modelo empleado.

de Debye-Hückel, un resultado razonable. La velocidad de los iones es un orden de magnitud menor de lo esperado teóricamente, lo que ya se ha observado en otros trabajos experimentales. El factor de corrección para las curvas a 0.1, 0.03 y 0.01 mM KCl es, respectivamente, 0.08, 0.13 y 0.19. Estos valores son similares a los obtenidos en otras contribuciones, y muestran la misma tendencia a aumentar para fuerzas iónicas menores.

El valor obtenido para  $\Delta\alpha^o$  es negativo, como se espera para la plata, dada su absorbancia. Sin embargo, su valor absoluto es 18 veces menor de lo esperado, lo que se atribuye a una capa de oxidación de las partículas, que ha sido observada mediante XPS. Las constantes ópticas encontradas en la bibliografía para láminas de plata parcialmente oxidadas proporciona valores de  $\Delta\alpha^o$  compatibles con nuestros resultados.

### 11.3.6. Análisis de la respuesta electro-óptica de dispersiones de óxido de grafeno en campos alternos

El óxido de grafeno (GO) utilizado en este trabajo se obtuvo de *Graphenea*, España, y se puso en suspensión acuosa con ayuda de un baño de ultrasonidos. La composición de las partículas se analizó mediante XPS,

observándose un porcentaje del 39 % de oxígeno. El potencial zeta toma valores en torno a los -30 mV. Estas partículas son muy absorbentes, por lo que se estudia su señal dicróica en lugar de la birrefringente. Esto requiere del uso de campos más elevados, por lo que no es posible trabajar dentro del régimen de Kerr. Por ello, la polarizabilidad eléctrica no se obtiene del módulo de  $\Delta A$ , sino a partir del tiempo de subida del dicroísmo, inversamente proporcional a  $\Delta\alpha^e$  a campos altos. Un ejemplo con diferentes subidas para varios valores del campo se muestra en la Figura 11.13.

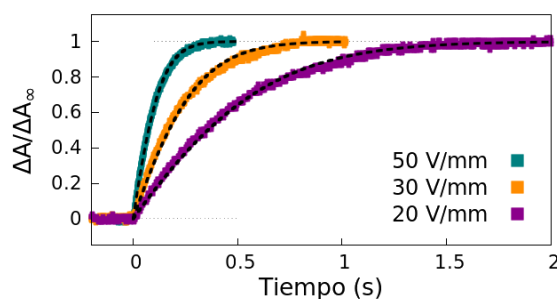


**FIGURA 11.13:** Subida del dicroísmo para una muestra de GO a 50 mg/L y 0.3 mM KCl, para un campo de diferentes amplitudes y 10 kHz de frecuencia.

El espectro de la polarizabilidad obtenido de esta manera se muestra en la Figura 11.14, donde puede observarse que la dependencia es cualitativamente similar al espectro de los nanohilos de plata. Por lo tanto, la respuesta experimental parece indicar que las láminas de GO se comportan como partículas conductoras poco cargadas. Dado que no existen expresiones teóricas para esta geometría, los espectros se ajustan con funciones Cole-Cole, de forma que se obtiene un valor de la polarizabilidad a alta y baja frecuencia, y una frecuencia característica de relajación,  $\nu_c$ .

El valor de la polarizabilidad a alta frecuencia es independiente de la fuerza iónica, lo que puede entenderse teniendo en cuenta que la máxima conductividad del medio es  $10^{-2}$  S/m, un valor muy inferior a la conductividad que se estima para estas láminas (1 S/m [273]). A baja frecuencia, los iones del medio se redistribuyen y apantallan el dipolo de la partícula. La frecuencia característica de este proceso es proporcional a la raíz cuadrada de la concentración iónica, lo que también se espera para las partículas

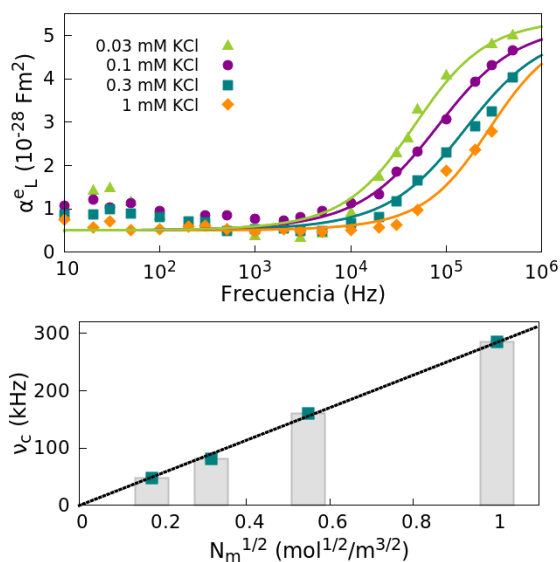


**FIGURA 11.14:** Espectro de la polarizabilidad de las partículas de GO en suspensión, con una concentración de 50 mg/L y diferentes valores de la fuerza iónica. Los puntos son los datos experimentales y las líneas ajustes a una relajación de tipo Cole-Cole. Abajo se muestra la frecuencia característica de la relajación en función de la raíz cuadrada de la concentración iónica ( $N_m$ ), ajustando los datos mediante una recta.

metálicas poco cargadas. Aunque no existe una expresión explícita para formas planas, con los datos obtenidos es posible estimar la distancia típica que viajan los iones, obteniéndose 700 nm, un valor en buen acuerdo con la geometría de las láminas.

## 11.4. Conclusiones

La **forma de las partículas** se ha mostrado como un parámetro importante para la descripción de los sistemas coloidales y sus posibles aplicaciones. El uso de campos eléctricos es una vía sencilla y eficiente para manipular estas partículas y controlar su orientación, aunque todavía es necesario seguir avanzando para alcanzar todo el potencial disponible. En este trabajo utilizamos **técnicas electro-ópticas** para analizar la interacción de micro y nanopartículas no esféricas con campos eléctricos externos. Se presta es-

pecial atención a los mecanismos de polarización de las partículas y sus dobles capas eléctricas, y al potencial que estos fenómenos poseen como técnicas de caracterización.

En primer lugar, medimos la fenomenología birrefringente de partículas de **montmorillonita sódica**, observándose los mecanismos de polarización de las nubes iónicas. La forma de estos espectros sugiere que la conductividad superficial presenta una anisotropía asociada a la carga de la cara y las aristas de estas partículas. Para campos de baja frecuencia se observa que las partículas tienden a alinearse con sus caras orientadas perpendicularmente a la dirección del campo, lo que se ha explicado a partir de un torque adicional originado por la interacción entre las partículas más pequeñas y más grandes de la muestra polidispersa.

A continuación se lleva a cabo el estudio de la respuesta birrefringente de suspensiones no acuosas de **nanotubos de carbono**. Se ha observado que la birrefringencia de los nanotubos de pared doble es negativa, mientras que la de los de pared simple es positiva, lo que se ha podido explicar teniendo en cuenta la absorbancia de estas partículas. La longitud de los tubos se midió de dos maneras: mediante el análisis de la caída de la birrefringencia y a partir del valor de la polarizabilidad eléctrica, obteniéndose en ambos casos resultados muy similares. Ha sido posible comprobar que son los nanotubos metálicos, y no los semiconductores, los que dominan la respuesta electro-óptica.

Además, en este trabajo hemos utilizado el estudio de la caída de la birrefringencia como técnica de **caracterización del tamaño de suspensiones de partículas no esféricas con alta polidispersidad**, mediante varios procedimientos de análisis aplicados a seis tipos de partículas de geometría muy diferente. Todos los métodos empleados proporcionan resultados excelentes, muy similares a los obtenidos por microscopía. De hecho, en todos los casos las desviaciones permanecen por debajo del 8%. Sin embargo, las determinaciones mediante dispersión dinámica de luz presentan desviaciones muy grandes con respecto al tamaño medio encontrado por microscopía, siempre por encima del 30%.

Por otra parte, se ha estudiado el comportamiento de **nanorods de oro estabilizados con CTAB**, sintetizados en nuestro laboratorio. Estas par-

tículas presentan birrefringencia negativa, lo que ha podido atribuirse al efecto de su absorbancia. También se ha comprobado que la capa de CTAB que recubre los nanorods juega un papel esencial en su electro-orientación. La densidad de carga de esta capa calculada mediante nuestras medidas está en buen acuerdo con los valores obtenidos mediante el análisis de la movilidad electroforética.

También se ha estudiado la fenomenología birrefringente de **nanohilos de plata** comerciales. El comportamiento espectral muestra que, a altas frecuencias, la polarizabilidad es la de un hilo metálico. A bajas frecuencias, sin embargo, la orientación decae a un valor pequeño debido a la aparición de las dobles capas inducidas, que apantallan el dipolo de la partícula. Además, en este caso ha sido necesario considerar la contribución hidrodinámica de los flujos electro-osmóticos inducidos, que juegan un papel esencial en la orientación.

Por último, hemos analizado el comportamiento electro-óptico del **óxido de grafeno**, a través de la medida del dichroísmo lineal. La polarizabilidad eléctrica de estas partículas crece significativamente por encima del rango de los kHz, un resultado muy similar al de los nanohilos de plata. La respuesta espectral del sistema indica que estas partículas se comportan como conductoras inmersas en una suspensión electrolítica. La distancia media estimada que los iones viajan para apantallar el dipolo está en buen acuerdo con el tamaño de las partículas.

En resumen, concluimos que el uso de técnicas electro-ópticas para el estudio de partículas no esféricas en suspensión posee un **gran potencial** y debe ser analizado en mayor profundidad. En este trabajo, la aplicación a sistemas muy diversos ha permitido extraer información sobre las propiedades y los mecanismos de polarización de las partículas, y avanzar en la comprensión de los fenómenos físicos implicados. Esperamos que en el futuro se continúe la mejora y extensión de estas técnicas, y que se desarrollen **nuevas aplicaciones** para partículas de geometría controlada, a través de la investigación pública.

## List of Figures

2.1.	Schematic representation of the structure of the electric double layer of a negatively charged spherical colloidal particle. . . . .	12
2.2.	Schematic representation of a) molecular polarization, b) Maxwell-Wagner-O'Konski polarization and c) concentration polarization, of a negatively charged colloidal particle. . . . .	18
2.3.	Dipolar coefficient spectrum for the particle represented in Figure 2.2. . . . .	23
2.4.	Representation of the geometry of a) a prolate and b) an oblate spheroid, together with the electric field and dipole moment components along the symmetry axis and perpendicular to it. . . . .	24
2.5.	Representation of the diffusive (dashed arrows) and electromigrational (solid arrows) flows of the ions inside the EDL for a prolate and an oblate particle, in the cases of orientation of the symmetry axis parallel and perpendicular to the external field. . . . .	27
2.6.	Representation of particles formed by a core and a cover, both with spheroidal shape, in the case of a) prolate and b) oblate geometries. . . . .	28
2.7.	Representation of the EDL structure of a metallic spherical particle with very low negative charge a) at equilibrium and b) under the application of an external electric field. . . . .	31

2.8. Dipolar coefficient spectrum of a spherical metallic particle in an electrolyte solution. The simplified structure of the charges and the field lines around the particle are also shown.	33
2.9. Representation of electro-orientation of non-spherical particles under an external electric field for an elongated and a planar geometry. . . . .	36
2.10. Order parameter as a function of the field amplitude for prolate and oblate axially-symmetric particles. . . . .	39
2.11. Polarizability spectrum of the oblate particles with specific properties. The polarizability along the symmetry and transverse axes and absolute value of the polarizability anisotropy are displayed. . . . .	41
2.12. Schematic representation of the ICEO flows for the case of a) a spherical particle and b) a very elongated particle. . . . .	42
2.13. Birefringence rise and decay of a polydisperse sample under 4 different conditions. The time is given in units of $\tau_d$ . The decay is a stretched exponential function with $\alpha = 0.5$ . In a) and b), $W_{DC} \ll k_B T$ , and hence the rise and the decay are symmetrical. In c) and d), on the other hand, the rise is in the shape of a single exponential function with $\tau_r = \tau_d/4$ . In a) and c), $\omega \gg 3\Theta$ and, as a consequence, the AC component of the birefringence is not observed. In b) and d), in contrast, the birefringence oscillates with twice the frequency of the applied field ( $\omega = \pi/\tau_d$ , $\Delta n_{AC} = 0.2\Delta n_{st}$ ). . . . .	52
3.1. Schematic representation of a sodium montmorillonite particle in an acidic medium. . . . .	57
3.2. a) Environmental scanning electron microscopy picture of the sodium montmorillonite sample. b) Detail of a single particle. . . . .	57
3.3. Schematic representation of a gold nanorod (orange) stabilised by a compact CTAB layer (purple). . . . .	58
3.4. High-resolution TEM picture of the AuNR sample. . . . .	59

---

3.5. Absorption spectrum of a 9.8 mg/L gold nanorod suspension. The inset shows the color of a 98 mg/L AuNR suspension. . . . .	60
3.6. TEM pictures of the AgNWs at two different zoom scales. . .	61
3.7. XPS peaks corresponding to silver and oxygen. . . . .	62
3.8. Absorption spectrum of a 100 mg/L sample of AgNWs in aqueous suspension. The inset is a colour picture of the sample.	62
3.9. Schematic representations of carbon nanotubes. a) Two possibilities for the formation of carbon nanotubes from a graphene layer. The black lines indicate the atoms that coincide after the sheet is rolled. The blue and red configurations correspond to a semiconducting and a metallic tube respectively. b) Structure of a metallic SWNT (purple) and DWNT (orange). . . . .	63
3.10. TEM pictures of the SWNTs. . . . .	64
3.11. TEM pictures of the DWNTs. . . . .	65
3.12. Schematic representation of a possible atomic structure of a GO flake. . . . .	66
3.13. High resolution scanning electron microscopy pictures of the graphene oxide flakes. . . . .	66
3.14. XPS peaks corresponding to carbon and oxygen. . . . .	67
3.15. TEM pictures of a) goethite needles, b) PTFE rods, c) gibbsite platelets, d) sepiolite particles and e) laponite nanodisks. . .	68
3.16. Detail of the electrodes and quartz cell used in the experiments. . . . .	70
3.17. Picture of the experimental setup for electro-optical measurements. The main elements are indicated on the image. .	71
3.18. Optical setup for the determination of linear dichroism. The elements of the schematic representation can be identified in the picture. . . . .	72

3.19. Optical setup for the determination of electric birefringence. The elements of the schematic representation can be identified in the picture. . . . .	74
4.1. Geometrical characterization of the clay particles. a) ESEM picture of a NaMt sample; b) histogram of the largest axis lengths obtained from a). . . . .	87
4.2. Birefringent response (relative to the stationary DC value) of EB measurements of a sample of NaMt 1 g/L and 0.3 mM NaCl when subjected to field pulses of different frequencies, 5 seconds of duration and a field amplitude of 10 V/mm . . .	89
4.3. EB measurements of a sample of NaMt 1 g/L and 0.3 mM NaCl; the field amplitude is 10 V/mm. a) Spectrum of the AC component of the birefringence. The dashed line is a guide to the eye. b) Birefringent response (relative to the stationary DC value) of the sample when subjected to field pulses of different frequencies and 5 seconds of duration. . .	90
4.4. a) Kerr constant of NaMt suspensions (1 g/L particles, 0.3 mM NaCl) as a function of the frequency of the applied field. The points are the experimental data and the line is the electrokinetic prediction. Field strength 10 V/mm. Electrokinetic predictions for the electric polarizability along the major ( $\alpha_b^e$ ) and minor ( $\alpha_a^e$ ) axes of the particles and for the electric polarizability anisotropy ( $\Delta\alpha^e$ ). Two cases are analysed: homogeneous ( $K_a/K_b = 0.27$ ) and heterogeneous ( $K_a/K_b = 0.008$ ) charge distribution. The particles are oblate spheroids with major semiaxis $b = 800$ nm and aspect ratio $b/a = 3$ . Dispersion medium: 0.3 mM NaCl . . . . .	92
4.5. Kerr constant spectra of NaMt suspensions (1 g/L and 0.3 mM NaCl) for the indicated pH values. a) Complete frequency range; b) detail of the high frequency region. The points are the experimental data and the lines correspond to the predictions of the electrokinetic model [25]. . . . .	96

- 4.6. EB spectra of samples of sodium montmorillonite (1 g/L, pH 7) with different values of the ionic strength: a) Complete frequency range, b) zoom in the high frequency range. The points are the experimental data and the lines correspond to the predictions of the electrokinetic model [25]. . . . . 97
- 4.7. a) Birefringence spectra of samples with 0.3 mM NaCl and different concentrations of NaMt. The birefringence is normalized to the particle concentration  $C$ . b) Spectrum of the logarithmic derivative of  $K/C$ . The characteristic frequency of the anomalous behaviour ( $\nu_c = 7$  Hz) is indicated in grey. 99
- 5.1. Electron Transmission Microscopy images of the SWNTs and the DWNTs along with the size distribution obtained from them. . . . . 113
- 5.2. Electro-optic response of suspensions of SWNTs and DWNTs  $10^{-4}$  wt% when subjected to sinusoidal field pulses of 1 kHz, 20 ms of duration and a field amplitude of 250 V/mm. a) Electric birefringence. b) Linear dichroism. . . . . 117
- 5.3. Transient birefringent response of a SWNT suspension  $10^{-4}$  wt% when subjected to sinusoidal field pulses of 20 ms of duration, a field amplitude of 250 V/mm and different frequencies. . . . . 118
- 5.4. Stationary electric birefringence (in absolute value) of SWNT and DWNT suspensions of different concentrations. The field strength is 250 V/mm and the field frequency 1 kHz. . 119
- 5.5. a) Transient electric birefringence (normalised to the stationary value) of the samples of carbon nanotubes  $10^{-4}$  wt% when subjected to field pulses of a duration of 20 ms, a field amplitude of 250 V/mm and a frequency of 1 kHz. The solid line is a fit of the build-up to a single exponential function. The dashed line is a fit of the decay to a stretched exponential function. b) Inverse of the rise time as a function of the square of the field amplitude for the samples in a). The line is a fit of the data to a linear function. . . . . 120

- 5.6. Electric birefringence of the samples as a function of the amplitude of the applied field. The particle concentration is  $10^{-4}$  wt% and the field frequency 1 kHz. a) Full range. b) Zoom in the low-field range. The points are the experimental data and the line is the fit to Kerr's law. . . . . 123
- 6.1. Birefringence signal of the goethite sample subjected to an electric field pulse of 30 ms. The points are the experimental data, and the black line a fitting of the decay to a stretched exponential function. In the inset, the data for short times (points) are presented in logarithmic scale, along with a linear fitting (black line), to show the linear dependence. . . . . 137
- 6.2. a) Electron microscope image of the goethite particles. b) Volume size distribution obtained via the ME method (colored squares and line) and WJ method (dotted black line), compared with the distribution determined from electron microscopy (grey bars). . . . . 139
- 6.3. Same as Fig. 6.2 but for the PTFE rods. . . . . 142
- 6.4. Same as Fig. 6.2 but for the SWNT suspension. . . . . 144
- 6.5. Same as Fig. 6.2 but for the DWNT sample. . . . . 146
- 6.6. Same as Fig. 6.2 but for the gibbsite platelets. . . . . 147
- 6.7. Same as Fig. 6.2 but for the NaMt sample. . . . . 149
- 6.8. Normalized birefringence decays of the studied suspensions. The points are the experimental data, and the black lines fittings to stretched exponential functions. In the insets, the data for short times (points) are presented in logarithmic scale, along with a linear fitting (black line), to show the linear dependence. . . . . 154
- 6.9. Comparison of the size distributions obtained by the ME method for the goethite sample, assuming a constant aspect ratio and a constant particle width. The microscopy result (grey bars) is also shown. . . . . 156

- 7.1. a) Length histogram of the AuNR sample obtained by TEM pictures. The inset shows one of the microscope images. b) Absorption spectrum of a 9.8 mg/L gold nanorod suspension. 163
- 7.2. Electric birefringence signal of the AuNRs subjected 150 V/mm electric field pulses of 2 ms duration, at different field frequencies. The sample has a particle concentration of 85 mg/L and 0.1 mM KCl. . . . . 166
- 7.3. Flow birefringence measurements of a 1400 mg/L sample of AuNRs and a 1 g/L aqueous suspension of sepiolite particles. The 0.2 mL/s flow is maintained for 4 seconds through a channel of 1 mm<sup>2</sup> section. . . . . 167
- 7.4. Electric birefringence of the AuNRs as a function of a) particle concentration and b) square of the field amplitude, for different frequencies of the applied field. The points are the experimental data and the lines fittings to linear functions. In a) the field strength is 37 V/mm, and in b) particle concentration is 88 mg/L. . . . . 169
- 7.5. Kerr constant as a function of the frequency of the applied field, for a sample of gold nanorods at 88 mg/L and three different values of the ionic strength. The points are the experimental data and the lines fittings to the used model. . . 170
- 7.6. a) Decay of the electric birefringence of the AuNRs after the field is turned off. The birefringence is normalised to the initial value. b) Spectrum of the oscillating component of the electric birefringence normalised to the low-frequency value of the DC component. In both cases, the points are the experimental data and the lines, fittings to the theory. . . . . 175
- 7.7. Birefringence signal of two laponite samples a particle concentration of ??? and 0.1 mM KCl. One of the samples is in the presence of 1.5 mM CTAB. The field strength is 60 V/mm. 177
- 8.1. TEM picture of the AgNWs. . . . . 185
- 8.2. Electrophoretic mobility (left axis) and zeta potential (right axis) of the AgNWs as a function of the ionic strength. . . . . 186

- 8.3. a) Zoom-in TEM picture of the AgNWs. b) XPS peaks corresponding to silver and oxygen. . . . . 188
- 8.4. a) Electric birefringence of a 100 mg/L AgNW suspension in 0.03 mM KCl as a function of time. The electric field pulses have an amplitude of 2 V/mm, a duration of 12.5 s and the indicated frequencies. b) Flow birefringence of suspensions of AgNWs at 200 mg/L and sepiolite needles at 2 g/L, as a function of time. . . . . 190
- 8.5. Electric birefringence of a silver nanowire suspension at 0.03 mM KCl a) as a function of particle concentration and b) as a function of the square of the field amplitude, for the indicated field frequencies. In a)  $E_0$  is 2 V/mm and in b) the particle concentration is 100 mg/L. . . . . 192
- 8.6. a) Normalised birefringence of the AgNWs in 0.03 mM KCl solution, as a function of time. b) Length distribution by volume of the AgNW sample as obtained from microscopy pictures (bars) and from the multi-exponential method (line). 193
- 8.7. a) Electric birefringence of AgNW samples with the indicated salt concentrations, as a function of the field frequency. The field strength is 2 V/mm and the particle concentration 100 mg/L. The points are the experimental data and the dotted lines fittings to the model for conducting wires. b) Same as a) but only for 0.03 mM KCl (points), with the electric (dotted grey line) and viscous (dashed red line) contributions given by the model, presented separately. The solid black line is the sum of the two effects. . . . . 195
- 8.8. Schematic representation of the ICEO flows for a very elongated particle. . . . . 197
- 9.1. Transmission electron microscopy pictures of the graphene oxide particles at two different zoom scales. . . . . 208
- 9.2. XPS peaks corresponding to carbon (top) and oxygen (bottom). 209

- 9.3. Linear dichroism measurements of a 50 mg/L aqueous suspension of GO, with 0.3 mM KCl. The field strength is 50 V/mm and the frequency 10 kHz. . . . . 210
- 9.4. Linear dichroism of the GO platelets as a function of particle concentration, under a 10 kHz electric field of 10 V/mm and 50 V/mm. The salt concentration is 0.3 mM KCl. . . . . 211
- 9.5. Linear dichroism of a dispersion of GO particles at 50 mg/L and 0.3 mM KCl as a function of the square of the field strength. The field frequency is 10 kHz. The points are the experimental data, and the solid line a fitting to Equation 9.3. The dashed line indicates the low-field linear behaviour (Equation 9.4) . . . . . 211
- 9.6. Decay of the linear dichroism of a dispersion of GO particles at 50 mg/L and 0.3 mM KCl after the application of a 10 kHz electric field of the indicated amplitude.  $\Delta A$  is normalised to the initial value. . . . . 213
- 9.7. Volume-weighted length distribution of the GO particles, as obtained from microscopy determinations and using the multi-exponential (ME) method for the analysis of the dichroism decay. . . . . 214
- 9.8. Rise dynamics of the the dichroism of a dispersion of GO particles at 50 mg/L and 0.3 mM KCl. The field frequency is 10 kHz. a) Normalised rise of LD for different field amplitudes. The dashed black lines are fittings to Equation 9.10. b)  $1/\tau_r$  as a function of the square of the field amplitude. The black line is a linear fitting. . . . . 216
- 9.9. a) Polarizability spectra of four samples of GO flakes at 50 mg/L, with different values of the ionic strength. The points are the experimental data and the solid lines fittings to Cole-Cole relaxation functions. b) Relaxation frequency as a function of ion concentration. . . . . 217

- 11.1. Representación esquemática de a) la polarización de las nubes electrónicas, b) la polarización de Maxwell-Wagner-O'Konski y c) la polarización de concentración.  $E$  indica el campo eléctrico aplicado y  $d$  el dipolo inducido. . . . . 235
- 11.2. Representación esquemática de la polarización de una partícula metálica a) a tiempos cortos y b) a tiempos largos.  $E$  indica el campo eléctrico aplicado y  $d$  el dipolo inducido. . . . . 237
- 11.3. Representación esquemática del proceso de electro-orientación para partículas alargadas y planas. . . . . 238
- 11.4. Espectro de birrefringencia de una muestra de montmorillonita sódica a 1 g/L, con 0.3 mM NaCl y diferentes valores del pH. La amplitud del campo aplicado es 10 V/mm. . . . . 241
- 11.5. Espectro de birrefringencia, normalizado con la concentración  $C$ , de una muestra de montmorillonita sódica a pH natural, 0.3 mM NaCl y diferentes concentraciones de partícula. La amplitud de campo aplicado es 10 V/mm. . . . . 242
- 11.6. Birrefringencia (arriba) y dicroísmo eléctrico (abajo) de los SWNTs y DWNTs. La concentración de partículas es  $10^{-4}$  wt%, la frecuencia del campo 1 kHz, la amplitud 250 V/mm y la duración del pulso 20 ms. . . . . 243
- 11.7. Birrefringencia eléctrica de los SWNTs y DWNTs en función de la amplitud de campo,  $E$ . La concentración de partículas es  $10^{-4}$  wt% y la frecuencia del campo aplicado 1 kHz. . . . . 244
- 11.8. Distribuciones de tamaño en volumen obtenidas con los métodos ME (puntos coloreados), WJ (línea negra discontinua) y microscopía electrónica (barras grises). Los recuadros contiene fotografías de microscopía de las muestras. . . . . 247
- 11.9. Arriba: Birrefringencia eléctrica de una muestra de AuNRs a 85 mg/L, sometida a un campo de 150 V/mm y 10 kHz durante 20 ms. Abajo: Birrefringencia de flujo de una suspensión a 1400 mg/L bajo un flujo de 0.2 mL/s en un canal de  $1 \text{ mm}^2$ . . . . . 249

- 11.10 Espectro de la birrefringencia (eje izquierdo) y la polarizabilidad eléctrica (eje derecho) de tres muestras de AuNRs a 88 mg/L y diferentes valores de la fuerza iónica, para un campo de 37 V/mm. Los puntos son los datos experimentales y las líneas discontinuas ajustes al modelo empleado. . . . . 249
- 11.11 Distribución de longitudes en volumen de la muestra de AgNWs, obtenida por microscopía (barras grises) y aplicando el método multi-exponencial a la caída de la birrefringencia (puntos con líneas). El recuadro contiene una imagen de microscopía de las partículas. . . . . 251
- 11.12 Espectro de la birrefringencia (eje izquierdo) y la polarizabilidad eléctrica (eje derecho) de tres muestras de AgNWs a 100 mg/L y diferentes valores de la fuerza iónica, para un campo de 2 V/mm. Los puntos son los datos experimentales y las líneas discontinuas ajustes al modelo empleado. . . . . 252
- 11.13 Subida del dicroísmo para una muestra de GO a 50 mg/L y 0.3 mM KCl, para un campo de diferentes amplitudes y 10 kHz de frecuencia. . . . . 253
- 11.14 Espectro de la polarizabilidad de las partículas de GO en suspensión, con una concentración de 50 mg/L y diferentes valores de la fuerza iónica. Los puntos son los datos experimentales y las líneas ajustes a una relajación de tipo Cole-Cole. Abajo se muestra la frecuencia característica de la relajación en función de la raíz cuadrada de la concentración iónica ( $N_m$ ), ajustando los datos mediante una recta. . . . . 254



# List of Tables

4.1.	Values of the surface conductivity and charge anisotropy obtained from the fit of the electrokinetic expressions to the experimental data. The pH dependence is analysed at 0.3 mM NaCl. The ionic strength dependence is studied at pH 7	95
5.1.	Experimental values of the particle length found by microscopy measurements (averaged and volume averaged), by the analysis of the birefringence decay via the stretched exponential method and by the analysis of the electrical polarizability anisotropy. For the microscopy measurements, the error is obtained from the standard deviation of the distribution.	121
5.2.	Experimental values found from the measurements in Figure 9.5: Kerr constant, saturation value of the birefringence, saturation field, electrical and optical polarizability anisotropies and refractive index of the SWNTs and DWNTs.	124
6.1.	Volume-averaged length of the major axis of the particles (and standard deviation of the distribution when available) obtained via EM and DLS measurements and with the SE, ME and WJ methods.	140
6.2.	Expressions of the coefficients $F_D$ and $F_\Theta$ in equations 6.1 and 6.2 for the simplified geometries used in this work.	153

---

7.1. Charge density of the CTAB layer ( $\text{MC}/\text{m}^3$ ) obtained from electric birefringence experiments and electrophoretic mobility determinations, for three different values of the ionic strength. . . . .	173
11.1. Valores de la conductividad superficial y la anisotropía de carga obtenidos del ajuste de los datos experimentales al modelo electrocinético. . . . .	240
11.2. Valores de diferentes propiedades de los tubos obtenidas a partir de la fenomenología birrefringente de las partículas. . . . .	245
11.3. Densidad de carga de la capa de CTAB ( $\text{MC}/\text{m}^3$ ) obtenida a partir de los experimentos de birrefringencia eléctrica y de las medidas de movilidad electroforética. . . . .	250

# Bibliography

- [1] M. L. Jiménez and T. Bellini, "The electrokinetic behavior of charged non-spherical colloids," *Current Opinion in Colloid and Interface Science*, vol. 15(3), pp. 131–144, 2010.
- [2] C. Kinnear, T. L. Moore, L. Rodriguez-Lorenzo, B. Rothen-Rutishauser, and A. Petri-Fink, "Form follows function: nanoparticle shape and its implications for nanomedicine," *Chemical Reviews*, vol. 117(17), pp. 11476–11521, 2017.
- [3] H. John, "Fluorescence properties of gold nanorods and their application for dna biosensing," *Chemical communications*, vol. 31, pp. 3924–3926, 2005.
- [4] J. Chon, C. Bullen, P. Zijlstra, and M. Gu, "Spectral encoding on gold nanorods doped in a silica sol-gel matrix and its application to high-density optical data storage," *Advanced Functional Materials*, vol. 17(6), pp. 875–880, 2007.
- [5] K. Lin, J. Yi, J. Zhong, S. Hu, B. Liu, J. Liu, C. Zong, Z. Lei, X. Wang, J. Aizpurua, R. Esteban, and B. Ren, "Plasmonic photoluminescence for recovering native chemical information from surface-enhanced raman scattering," *Nature Communications*, vol. 8, p. 14891, 2017.
- [6] S. Pal, Y. K. Tak, and J. M. Song, "Does the antibacterial activity of silver nanoparticles depend on the shape of the nanoparticle? a study of the gram-negative bacterium escherichia coli," *Applied and Environmental Microbiology*, vol. 73(6), pp. 1712–1720, 2007.

- [7] K. Yamashita, Yasuo, Y. Yoshioka, K. Higashisaka, Y. Morishita, T. Yoshida, M. Fujimura, H. Kayamuro, H. Nabeshi, T. Yamashita, K. Nagano, Y. Abe, H. Kamada, Y. Kawai, T. Mayumi, and T. Yoshikawa, "Carbon nanotubes elicit dna damage and inflammatory response relative to their size and shape," *Inflammation*, vol. 33(4), pp. 276–280, 2010.
- [8] B. Abu-Jdayil, "Rheology of sodium and calcium bentonite–water dispersions: Effect of electrolytes and aging time," *International Journal of Mineral Processing*, vol. 98(3-4), pp. 208–213, 2011.
- [9] S. Mostafa, F. Behafarid, J. R. Croy, L. K. Ono, L. L. J. C. Yang, A. I. Frenkel, and B. Roldan-Cuenya, "Shape-dependent catalytic properties of pt nanoparticles," *Journal of the American Chemical Society*, vol. 132(44), pp. 15714–15719, 2010.
- [10] V. Shalaev, W. Cai, U. Chettiar, H. Yuan, A. Sarychev, V. Drachev, and A. Kildishev, "Negative index of refraction in optical metamaterials," *Optics Letters*, vol. 30(24), pp. 3356–3358, 2005.
- [11] L. Zhang, J. Xia, Q. Zhao, L. Liu, and Z. Zhang, "Functional graphene oxide as a nanocarrier for controlled loading and targeted delivery of mixed anticancer drugs," *Small*, vol. 6(4), pp. 537–544, 2010.
- [12] Y. Ko, S. K. Song, N. H. Kim, and S. T. Chang, "Slightly transparent and stretchable conductors based on a directional arrangement of silver nanowires by a microliter-scale solution process," *Langmuir*, vol. 32(1), pp. 366–373, 2015.
- [13] J. Li, H. Ng, A. Cassell, W. Fan, H. Chen, Q. Ye, J. Koehne, J. Han, and M. Meyyappan, "Carbon nanotube nanoelectrode array for ultrasensitive dna detection," *Nano Letters*, vol. 3(5), pp. 597–602, 2003.
- [14] J. Hafner, C. Cheung, and C. Lieber, "Growth of nanotubes for probe microscopy tips," *Nature*, vol. 398(6730), pp. 761–762, 1999.
- [15] L. Zhang, Y. Wu, L. Deng, Y. Zhou, C. Liu, and S. Fan, "Photodetection and photoswitch based on polarized optical response of

- macroscopically aligned carbon nanotubes," *Nano Letters*, vol. 16(10), pp. 6378–6382, 2016.
- [16] Y. Zhu, S. Murali, M. D. Stoller, K. J. Ganesh, W. Cai, P. J. Ferreira, A. Pirkle, R. M. Wallace, K. A. Cychosz, M. Thommes, D. Su, E. A. Stach, and R. S. Ruoff, "Carbon-based supercapacitors produced by activation of graphene," *Science*, vol. 332(6037), pp. 1537–1541, 2011.
- [17] A. Ramos, H. Morgan, N. G. Green, and A. Castellanos, "Ac electrokinetics: a review of forces in microelectrode structures," *Applied Physics Letters*, vol. 31(18), p. 2338, 1998.
- [18] R. Pethig, "Dielectrophoresis: using inhomogeneous ac electrical fields to separate and manipulate cells," *Critical Reviews in Biotechnology*, vol. 16(4), pp. 331–348, 1996.
- [19] T. Lutz and K. Donovan, "Macroscopic scale separation of metallic and semiconducting nanotubes by dielectrophoresis," *Carbon*, vol. 43(12), pp. 2508–2513, 2005.
- [20] A. Bezryadin, C. Dekker, and G. Schmid, "Electrostatic trapping of single conducting nanoparticles between nanoelectrodes," *Applied Physics Letters*, vol. 71(9), pp. 1273–1275, 1997.
- [21] P. A. Smith, C. D. Nordquist, T. N. Jackson, T. S. Mayer, B. R. Martin, J. Mbindyo, and T. E. Mallouk, "Electric-field assisted assembly and alignment of metallic nanowires," *Applied Physics Letters*, vol. 77(9), pp. 1399–1401, 2000.
- [22] X. Chen, T. Saito, H. Yamada, and L. Matsushige, "Aligning single-wall carbon nanotubes with an alternating-current electric field," *Applied Physics Letters*, vol. 78(23), pp. 3714–3716, 2001.
- [23] X. Duan, Y. Huang, Y. Cui, J. Wang, and C. M. Lieber, "Indium phosphide nanowires as building blocks for nanoscale electronic and optoelectronic devices," *Nature*, vol. 409(6816), p. 66, 2001.

- [24] S. S. Dukhin and V. N. Shilov, "Kinetic aspects of electrochemistry of disperse systems. Part II. Induced dipole moment and the non-equilibrium double layer of a colloid particle," *Advances in Colloid and Interface Science*, vol. 13(1-2), pp. 153–195, 1980.
- [25] V. N. Shilov, Y. B. Borkovskaja, and S. N. Budankova, "Thin double layer theory of the wide-frequency range dispersion of the polarizability of nonconducting spheroidal particles," in *Molecular and colloidal electro-optics* (S. Stoylov and M. Stoimenova, eds.), pp. 39–57, Boca Raton: CRC Press, 2006.
- [26] M. Fixman, "A macroion electrokinetics algorithm," *Journal of Chemical Physics*, vol. 124, p. 214506, 2006.
- [27] C. Chassagne, F. Mietta, and J. C. Winterwerp, "Electrokinetic study of kaolinite suspensions," *Journal of Colloid and Interface Science*, vol. 336(1), pp. 352–359, 2009.
- [28] R. A. Rica, M. L. Jiménez, and A. V. Delgado, "Electric permittivity of concentrated suspensions of elongated goethite particles," *Journal of Colloid and Interface Science*, vol. 343(2), pp. 564–573, 2010.
- [29] R. A. Rica, M. L. Jiménez, and A. V. Delgado, "Electrokinetics of concentrated suspensions of spheroidal hematite nanoparticles," *Soft Matter*, vol. 8(13), pp. 3596–3607, 2012.
- [30] Y. Tsujimoto, C. Chassagne, and Y. Adachi, "Comparison between the electrokinetic properties of kaolinite and montmorillonite suspensions at different volume fractions," *Journal of Colloid and Interface Science*, vol. 407, pp. 109–115, 2013.
- [31] M. A. González, A. V. Delgado, R. A. Rica, M. L. Jiménez, and S. Ahualli, "Electric permittivity and dynamic mobility of dilute suspensions of platelike gibbsite particles," *Langmuir*, vol. 31(29), pp. 7934–7942, 2015.
- [32] S. Ahualli, M. A. González, A. V. Delgado, and M. L. Jiménez, "Dynamic electrophoretic mobility and electric permittivity of concen-

- trated suspensions of plate-like gibbsite particles," *Journal of Colloid and Interface Science*, vol. 502, pp. 112–121, 2017.
- [33] N. I. Gamayunov, V. A. Murtsovkin, and A. S. Dukhin, "Pair interaction of particles in electric field. 1. Features of hydrodynamic interaction of polarized particles," *Colloid Journal of the USSR*, vol. 48(2), 1986.
- [34] V. A. Murtsovkin and G. I. Mantrov, "Steady flows in the neighborhood of a drop of mercury with the application of a variable external electric field," *Colloid Journal of the USSR*, vol. 53(2), pp. 240–244, 1991.
- [35] T. M. Squires and M. Z. Bazant, "Induced-charge electro-osmosis," *Journal of Fluid Mechanics*, vol. 509, pp. 217–252, 2004.
- [36] M. Z. Bazant, M. S. Kilic, B. D. Storey, and A. Ajdari, "Towards an understanding of induced-charge electrokinetics at large applied voltages in concentrated solutions," *Advances in Colloid and Interface Science*, vol. 152(1-2), pp. 48–88, 2009.
- [37] J. A. Levitan, S. Devasenathipathy, V. Studer, Y. Ben, T. Thorsen, T. M. Squires, and M. Z. Bazant, "Experimental observation of induced-charge electro-osmosis around a metal wire in a microchannel," *Colloids and Surfaces A: Physicochemical and Engineering Aspects*, vol. 267(1-3), pp. 122–132, 2005.
- [38] K. A. Rose, J. A. Meier, G. M. Dougherty, and J. G. Santiago, "Rotational electrophoresis of striped metallic microrods," *Physical Review E*, vol. 75(1), p. 011503, 2007.
- [39] Y. K. Ren, D. Morganti, H. Y. Jiang, A. Ramos, and H. Morgan, "Electrorotation of metallic microspheres," *Langmuir*, vol. 27(6), pp. 2128–2131, 2011.
- [40] P. García-Sánchez, J. J. Arcenegui, H. Morgan, and A. Ramos, "Self-assembly of metal nanowires induced by alternating current electric fields," *Applied Physics Letters*, vol. 106(2), p. 023110, 2015.

- [41] A. Ramos, P. García-Sánchez, and H. Morgan, "Ac electrokinetics of conducting microparticles: A review," *Current Opinion in Colloid and Interface Science*, vol. 79(90), pp. 79–90, 2016.
- [42] C. T. O'Konski, *Molecular electro-optics*. New York: Marcel Dekker, 1976.
- [43] E. Frederiq and C. Houssier, *Electric dichroism and electric birefringence*. Oxford: Clarendon, 1973.
- [44] P. J. Hagerman, "Investigation of the flexibility of dna using transient electric birefringence," *Biopolymers: Original Research on Biomolecules*, vol. 20(7), pp. 1503–1535, 1981.
- [45] T. Bellini, F. Mantegazza, R. Piazza, and V. Degiorgio, "Stretched-exponential relaxation of electric birefringence in a polydisperse colloidal solution," *Europhysics Letters*, vol. 10 (5), pp. 499–503, 1989.
- [46] V. Degiorgio, R. Piazza, F. Mantegazza, and T. Bellini, "Stretched-exponential relaxation of electric birefringence in complex liquids," *Journal of Physics: Condensed Matter*, vol. 2 (S), p. SA69, 1990.
- [47] M. Matsumoto, H. Watanabe, and K. Yoshioka, "A method for determining the relaxation spectrum from the decay curve of electric birefringence of macromolecular solutions," *Kolloid-Zeitschrift und Zeitschrift für Polymere*, vol. 250(4), pp. 298–302, 1972.
- [48] R. M. J. Watson and B. R. Jennings, "Polydisperse size data from single electric birefringence transients," *Powder Technology*, vol. 72(1), pp. 63–69, 1992.
- [49] T. Bellini and F. Mantegazza, "Electric birefringence spectroscopy: A new electrokinetic technique," in *Interfacial electrokinetics and electrophoresis* (A. Delgado, ed.), pp. 401–441, New York: Marcel Dekker, 2002.
- [50] M. L. Jiménez, L. Fornasari, F. Mantegazza, and M. C. Mourad, "Electric birefringence of dispersions of platelets," *Langmuir*, vol. 28(1), pp. 251–258, 2012.

- [51] R. J. Hunter, *Foundations of colloid science*. Oxford University Press, 2001.
- [52] J. Lyklema, *Fundamentals of interface and colloid science, Vol II: Solid-liquid interfaces*. New York: Academic Press, 1995.
- [53] R. J. Hunter, *Zeta potential in colloid science: principles and applications*. New York: Academic Press, 1981.
- [54] J. Lyklema, *Solid/liquid dispersions*. London: Academic Press, 1987.
- [55] A. D. (Ed.), *Interfacial electrokinetics and electrophoresis*. New York: Marcel Dekker, 2002.
- [56] S. Wall, "The history of electrokinetic phenomena," *Current Opinion in Colloid and Interface Science*, vol. 15(3), pp. 119–124, 2010.
- [57] M. Gouy, "Sur la constitution de la charge électrique à la surface d'un électrolyte," *Journal de Physique Théorique et Appliquée*, vol. 9(1), pp. 457–468, 1910.
- [58] D. L. Chapman, "LI. A contribution to the theory of electrocapilarity," *The London, Edinburgh, and Dublin Philosophical Magazine and Journal of Science*, vol. 25(148), pp. 475–481, 1913.
- [59] O. Stern, "The theory of the electrolytic double-layer," *Zeitschrift für Elektrochemie*, vol. 30(508), pp. 1014–1020, 1924.
- [60] S. S. Dukhin and B. V. Derjaguin, "Electrokinetic phenomena," in *Surface and Colloid Science* (E. Matijević, ed.), vol. 7, New York: Wiley, 1974.
- [61] C. Grosse, "Relaxation mechanisms of homogeneous particles and cells suspended in aqueous electrolyte solutions," in *Interfacial electrokinetics and electrophoresis* (A. Delgado, ed.), pp. 277–327, New York: Marcel Dekker, 2002.
- [62] V. N. Shilov, A. V. Delgado, F. González-Caballero, J. Horno, J. J. López-García, and C. Grosse, "Polarization of the electrical double

- layer. time evolution after application of an electric field," *Journal of Colloid and Interface Science*, vol. 232(1), pp. 141–148, 2000.
- [63] L. D. Landau and E. M. Lifshitz, *Electrodynamics of continuous media*. Oxford: Pergamon Press, 1960.
- [64] J. C. Maxwell, *Electricity and magnetism*. Oxford: Clarendon, 1892.
- [65] K. W. Wagner *Archiv für Elektrotechnik*, vol. 2, pp. 371–387, 1914.
- [66] C. T. O'Konski, "Electric properties of macromolecules. v. theory of ionic polarization in polyelectrolytes," *Journal of Physical Chemistry*, vol. 64, pp. 605–619, 1960.
- [67] S. S. Dukhin and V. N. Shilov, *Dielectric phenomena and the double layer in disperse systems and polyelectrolytes*. New York: Wiley, 1974.
- [68] P. J. W. Debye, *Polar molecules*. New York: Dover Publications, 1929.
- [69] K. S. Cole and R. H. Cole, "Dispersion and absorption in dielectrics I. Alternating current characteristics," *The Journal of Chemical Physics*, vol. 9(4), pp. 341–351, 1941.
- [70] C. Grosse, S. Pedrosa, and V. N. Shilov, "Calculation of the dielectric increment and characteristic time of the Ifdd in colloidal suspensions of spheroidal particles," *Journal of Colloid and Interface Science*, vol. 220 (1), pp. 31–41, 1999.
- [71] R. Bilboul, "A note on the permittivity of a double-layer ellipsoid," *Journal of Physics D: Applied Physics*, vol. 2(6), pp. 921–922, 1969.
- [72] M. Z. Bazant and T. M. Squires, "Induced-charge electrokinetic phenomena: theory and microfluidic applications," *Physical Review Letters*, vol. 92(6), p. 066101, 2004.
- [73] J. J. Arcenegui, P. García-Sánchez, H. Morgan, and A. Ramos, "Electro-orientation of a metal nanowire counterbalanced by thermal torques," *Physical Review E*, vol. 89(6), p. 062306, 2014.

- [74] J. J. Arcenegui, P. García-Sánchez, H. Morgan, and A. Ramos, "Electro-orientation and electrorotation of metal nanowires," *Physical Review E*, vol. 88(6), p. 063018, 2013.
- [75] P. García-Sánchez, Y. Ren, J. J. Arcenegui, H. Morgan, and A. Ramos, "Alternating current electrokinetic properties of gold-coated microspheres," *Langmuir*, vol. 28(39), pp. 13861–13870, 2012.
- [76] H. A. Stone, J. R. Lister, and M. P. Brenner, "Drops with conical ends in electric and magnetic fields," *Proceedings of the Royal Society of London A: Mathematical, Physical and Engineering Sciences*, vol. 455(1981), pp. 329–347, 1999.
- [77] M. L. Jiménez, L. Fornasari, F. Mantegazza, M. C. Mourad, and T. Bellini, "Electric birefringence of dispersions of platelets," *Langmuir*, vol. 28(1), pp. 251–258, 2011.
- [78] P. Arenas-Guerrero, G. Iglesias, A. Delgado, and M. Jiménez, "Electric birefringence spectroscopy of montmorillonite particles," *Soft Matter*, vol. 519, pp. 2584–2588, 2016.
- [79] M. Teubner, "The motion of charged colloidal particles in electric fields," *The Journal of Chemical Physics*, vol. 76(11), pp. 5564–5573, 1982.
- [80] F. Mantegazza, M. Caggioni, M. L. Jiménez, and T. Bellini, "Anomalous field-induced particle orientation in dilute mixtures of charged rod-like and spherical colloids," *Nature Physics*, vol. 6, p. 561, 2010.
- [81] C. O'Konski, K. Yoshioka, and W. Orttung, "Electric properties of macromolecules. iv. determination of electric and optical parameters from saturation of electric birefringence in solutions," *Journal of Physical Chemistry*, vol. 63(10), pp. 1558–1565, 1959.
- [82] T. Bellini, V. Degiorgio, and F. Mantegazza, "The electric birefringence of polyelectrolytes: an electrokinetic approach," *Colloids and Surfaces A: Physicochemical and Engineering Aspects*, vol. 140(1-3), pp. 103–117, 1998.

- [83] G. Thurston and D. Bowling, "The frequency dependence of the kerr effect for suspensions of rigid particles," *Journal of Colloid and Interface Science*, vol. 30(1), pp. 34–35, 1969.
- [84] M. J. Shah, "Electric birefringence of bentonite. ii. an extension of saturation birefringence theory," *The Journal of Physical Chemistry*, vol. 67(10), pp. 2215–2219, 1963.
- [85] V. N. Shilov and T. S. Simonova, "Polarization of electric double-layer of disperse particles and dipolophoresis in a steady (dc) field," *Colloid Journal of the USSR*, vol. 43(1), pp. 90–96, 1981.
- [86] T. M. Squires and M. Z. Bazant, "Breaking symmetries in induced-charge electro-osmosis and electrophoresis," *Journal of Fluid Mechanics*, vol. 560, pp. 65–101, 2006.
- [87] H. C. Benoît, "Study of the kerr effect by dilute solutions of rigid macromolecules," *Annals of Physics*, vol. 6, pp. 561–609, 1951.
- [88] S. P. Stoylov and M. V. Stoimenova, *Molecular and colloidal electro-optics*. Boca Raton: CRC Press, 2006.
- [89] P. Arenas-Guerrero, M. Jiménez, K. Scott, and K. Donovan, "Electric birefringence of carbon nanotubes: Single-vs double-walled," *Carbon*, vol. 126, pp. 77–84, 2018.
- [90] K. J. Donovan, K. Scott, and M. Somerton, "Electric linear dichroism. a powerful method for the ionic chromophore colloid system as exemplified by dye and montmorillonite suspensions," *Colloids and Surfaces A: Physicochemical and Engineering Aspects*, vol. 175(1-2), pp. 23–39, 2000.
- [91] A. V. Delgado, F. J. Arroyo, F. González-Caballero, V. N. Shilov, and Y. B. Borkovskaya, "The effect of the concentration of dispersed particles on the mechanisms of low-frequency dielectric dispersion (lfdd) in colloidal suspensions," *Colloids and Surfaces A: Physicochemical and Engineering Aspects*, vol. 140(1-3), pp. 139–149, 1998.

- [92] S. Ahualli, A. V. Delgado, and C. Grosse, "A simple model of the high-frequency dynamic mobility in concentrated suspensions," *Journal of Colloid and Interface Science*, vol. 301(2), pp. 660–667, 2006.
- [93] D. van der Beek, H. Reich, P. van der Schoot, M. Dijkstra, T. Schilling, R. Vink, M. Schmidt, R. van Roij, and H. Lekkerkerker, "Isotropic-nematic interface and wetting in suspensions of colloidal platelets," *Physical Review Letters*, vol. 97(8), p. 087801, 2006.
- [94] P. Arenas-Guerrero, A. V. Delgado, K. J. Donovan, K. Scott, T. Bellini, F. Mantegazza, and M. L. JimÁñez, "Determination of the size distribution of non-spherical nanoparticles by electric birefringence-based methods," *Scientific Reports*, vol. 8(1), p. 9502, 2018.
- [95] O. Levy, "Local field effects on reorientation in suspensions of anisotropic particles," *Physical Review E*, vol. 68(1), p. 011407, 2003.
- [96] K. Donovan and L. Scott, "Transient electric birefringence in suspensions of single-walled carbon nanotubes," *Physical Review B*, vol. 72(19), p. 195432, 2005.
- [97] H. van Olphen, *An introduction to clay colloid chemistry*. New York: Wiley, 1977.
- [98] P. F. Luckham and S. Rossi, "The colloidal and rheological properties of bentonite suspensions," *Advances in Colloid and Interface Science*, vol. 82(1-3), pp. 43–92, 2008.
- [99] H. H. Murray, *Applied clay mineralogy: occurrences, processing and applications of kaolins, bentonites, palygorskite-sepiolite, and common clays*. Amsterdam: Elsevier, 2007.
- [100] S. H. Chang, M. H. Ryan, and R. K. Gupta, "The effect of pH, ionic strength, and temperature on the rheology and stability of aqueous clay suspensions," *Rheologica Acta*, vol. 32(3), pp. 236–269, 1993.
- [101] D. Heath and T. F. Tadros, "Influence of pH, electrolyte, and poly (vinyl alcohol) addition on the rheological characteristics of aqueous

- dispersions of sodium montmorillonite," *Journal of Colloid and Interface Science*, vol. 93(2), pp. 307–319, 1983.
- [102] J. D. G. Durán, M. M. Ramos-Tejada, F. J. Arroyo, and F. González-Caballero, "Influence of ph, electrolyte, and poly (vinyl alcohol) addition on the rheological characteristics of aqueous dispersions of sodium montmorillonite," *Journal of Colloid and Interface Science*, vol. 93(2), pp. 307–319, 1983.
- [103] M. M. Ramos-Tejada, F. J. Arroyo, R. Perea, and J. D. G. Durán, "Scaling behavior of the rheological properties of montmorillonite suspensions: correlation between interparticle interaction and degree of flocculation," *Journal of Colloid and Interface Science*, vol. 235, pp. 251–259, 2001.
- [104] B. Nikoobakht and M. El-Sayed, "Preparation and growth mechanism of gold nanorods (nrs) using seed-mediated growth method," *Chemistry of Materials*, vol. 15(10), pp. 1957–1962, 2003.
- [105] L. Saa, M. Coronado-Puchau, V. Pavlov, and L. M. Liz-Marzán, "Enzymatic etching of gold nanorods by horseradish peroxidase and application to blood glucose detection," *Nanoscale*, vol. 6(13), pp. 7405–7409, 2013.
- [106] K. Park, S. Biswas, S. Kanel, D. Nepal, and R. Vaia, "Engineering the optical properties of gold nanorods: independent tuning of surface plasmon energy, extinction coefficient, and scattering cross section," *The Journal of Physical Chemistry C*, vol. 118(11), pp. 5918–5926, 2014.
- [107] P. Ramasamy, D. M. Seo, S. H. Kim, and J. Kim, "Effects of tio<sub>2</sub> shells on optical and thermal properties of silver nanowires," *Journal of Materials Chemistry*, vol. 22(23), pp. 11651–11657, 2012.
- [108] S. Iijima, "Helical microtubules of graphitic carbon," *Nature*, vol. 354(6234), pp. 461–463, 1995.
- [109] M. Dresselhaus, G. Dresselhaus, and P. A. (Eds.), *Carbon nanotubes: synthesis, structure, properties, and applications*, vol. 80. Springer Science and Business Media, 2003.

- [110] T. Belin and F. Epron, "Characterization methods of carbon nanotubes: a review," *Materials Science and Engineering: B*, vol. 119(2), pp. 105–108, 2005.
- [111] T. Odom, J. Huang, P. Kim, and C. Lieber, "Atomic structure and electronic properties of single-walled carbon nanotubes," *Nature*, vol. 391(6662), pp. 62–64, 1998.
- [112] C. Shen, A. Brozena, and Y. Wang, "Double-walled carbon nanotubes: challenges and opportunities," *Nanoscale*, vol. 3(2), pp. 503–518, 2011.
- [113] K. S. Novoselov, A. K. Geim, S. V. Morozov, D. Jiang, Y. Zhang, S. V. Dubonos, I. V. Grigorieva, and A. A. Firsov, "Electric field effect in atomically thin carbon films. science," *Science*, vol. 306(5696), pp. 666–669, 2004.
- [114] S. Stankovich, D. A. DikinaRichard, R. D. Piner, K. A. Kohlhaas, A. Kleinhammes, Y. Jia, Y. Wu, S. T. Nguyen, and R. S. Ruoff, "Synthesis of graphene-based nanosheets via chemical reduction of exfoliated graphite oxide," *Carbon*, vol. 45(7), pp. 1558–1565, 2007.
- [115] D. Chen, H. Feng, and J. Li, "Graphene oxide: preparation, functionalization, and electrochemical applications," *Chemical Reviews*, vol. 112(11), pp. 6027–6053, 2012.
- [116] R. Su, S. F. Lin, D. Q. Chen, and G. H. Chen, "Study on the absorption coefficient of reduced graphene oxide dispersion," *The Journal of Physical Chemistry C*, vol. 118(23), pp. 12520–12525, 2014.
- [117] K. Krishnamoorthy, R. Mohan, and S. J. Kim, "Graphene oxide as a photocatalytic material," *Applied Physics Letters*, vol. 98(24), p. 244101, 2011.
- [118] J. W. Suk, R. D. Piner, J. An, and R. S. Ruoff, "Mechanical properties of monolayer graphene oxide," *ACS Nano*, vol. 4(11), pp. 6557–6564, 2010.

- [119] J. E. Wijnhoven, D. D. van't Zand, D. van der Beek, and H. N. Lekkerkerker, "Sedimentation and phase transitions of colloidal gibbsite platelets," *Langmuir*, vol. 21(23), pp. 10422–10427, 2005.
- [120] R. Piazza, V. Degiorgio, and T. Bellini, "Matrix analysis of electric birefringence measurements," *Optics Communications*, vol. 58(6), pp. 400–404, 1986.
- [121] B. V. Haeringen, J. P. Dekker, M. Bloemendal, M. R  gner, R. V. Grondelle, and H. V. Amerongen, "Simultaneous measurement of electric birefringence and dichroism. a study on photosystem 1 particles," *Biophysical journal*, vol. 67(1), pp. 411–417, 1994.
- [122] T. Bellini, F. Mantegazza, V. Degiorgio, R. Avallone, and D. A. Saville, "Electric polarizability of polyelectrolytes: Maxwell-wagner and electrokinetic relaxation," *Physical Review Letters*, vol. 82, pp. 5160–5163, 1999.
- [123] D. A. Saville, T. Bellini, V. Degiorgio, and F. Mantegazza, "An extended maxwell-wagner theory for the electric birefringence of charged colloids," *Journal of Chemical Physics*, vol. 113, pp. 6974–6983, 2000.
- [124] R. Sasai and K. Yamaoka, "Electrooptics in dispersed systems. 4. steady-state electric birefringence of disk-shaped particles with various electric moments and the orientation function: case of montmorillonite in aqueous media," *Journal of Physical Chemistry*, vol. 99 (50), pp. 17754–17762, 1995.
- [125] H. Hoffmann and D. Gr  bner, "Electric birefringence anomaly of solutions of ionically charged anisometric particles," *Advances in Colloid and Interface Science*, vol. 216, pp. 20–35, 2015.
- [126] M. C. Fair and J. L. Anderson, "Electrophoresis of nonuniformly charged ellipsoidal particles," *Journal of Colloid and Interface Science*, vol. 127 (2), pp. 388–400, 1989.

- [127] E. Paineau, J. Antonova, C. Baravian, I. Bihannic, P. Davidson, I. Dozov, M. Impèrir-Clerc, P. Levitz, A. Madsen, F. Meneau, and L. J. Michot, "Liquid-crystalline nematic phase in aqueous suspensions of a disk-shaped natural beidellite clay," *The Journal of Physical Chemistry B*, vol. 113 (48), pp. 15858–15869, 2009.
- [128] I. Dozov, E. Paineau, P. Davidson, K. Antonova, C. Baravian, I. Bihannic, and L. J. Michot, "Electric-field-induced perfect anti-nematic order in isotropic aqueous suspensions of a natural beidellite clay," *The Journal of Physical Chemistry B*, vol. 115 (24), pp. 7751–7765, 2011.
- [129] M. J. Shah, D. C. Thompson, and C. M. Hart, "Reversal of electro-optical birefringence in bentonite suspensions," *Journal of Physical Chemistry*, vol. 67 (6), pp. 1170–1178, 1963.
- [130] K. Yamaoka, K. Fukudome, and K. Matsuda, "Electric field orientation of nucleic acids in aqueous solutions. 3. non-kerr-law behavior of high molecular weight dna at weak fields as revealed by electric birefringence and electric dichroism," *Journal of Physical Chemistry*, vol. 96 (17), pp. 7131–7136, 1992.
- [131] S. Holzheu and H. Hoffmann, "Mechanistic origin of transient electric birefringence anomaly of clay mineral dispersion," *Journal of Physical Chemistry B*, vol. 106 (17), pp. 4412–4418, 2002.
- [132] R. Pecora, *Dynamic light scattering: applications of photon correlation spectroscopy*. New York and London: Plenum Press, 1985.
- [133] F. Mantegazza, T. Bellini, M. Buscaglia, V. Degiorgio, and D. A. Saville, "Electrokinetic properties of colloids of variable charge. iii. observation of a maxwell-wagner relaxation mechanism by high-frequency electric-birefringence spectroscopy," *Journal of Chemical Physics*, vol. 113, pp. 6984–6991, 2000.
- [134] C. F. Zukoski and D. A. Saville, "The interpretation of electrokinetic measurements using a dynamic model of the stern layer: I. the dynamic model," *Journal of Colloid and Interface Science*, vol. 114 (1), pp. 32–44, 1986.

- [135] B. R. Midmore and R. J. Hunter, "The effect of electrolyte concentration and co-ion type on the zeta-potential of polystyrene latices," *Journal of Colloid and Interface Science*, vol. 112 (2), pp. 521–529, 1988.
- [136] A. V. Delgado, M. A. Cabrerizo, J. Salcedo, and F. González-Caballero, "On the bulk and surface electric conductivity in montmorillonite suspensions," *Materials Chemistry and Physics*, vol. 20 (3), pp. 233–244, 1988.
- [137] L. Fornasari, F. Mantegazza, M. L. Jiménez, M. Buscaglia, and T. Bellini, "Field-induced clearing in sphere-sphere and rod-sphere binary mixtures of charged colloidal particles," *Physical Review E*, vol. 79 (9), p. 06041, 2009.
- [138] P. Bandaru, "Electrical properties and applications of carbon nanotube structures," *Journal of nanoscience and nanotechnology*, vol. 7(4-5), pp. 1239–1267, 2007.
- [139] K. Ibrahim, "Carbon nanotubes-properties and applications: a review," *Carbon letters*, vol. 14(3), pp. 131–144, 2013.
- [140] R. Baughman, A. Zakhidov, and W. de Heer, "Carbon nanotubes-the route toward applications," *Science*, vol. 297(5582), pp. 787–792, 2002.
- [141] M. de Volder, S. Tawfick, R. Baughman, and A. Hart, "Carbon nanotubes: present and future commercial applications," *Science*, vol. 3396(6119), pp. 535–539, 2013.
- [142] M. Ohfuchi and Y. Miyamoto, "Optical properties of oxidized single-wall carbon nanotubes," *Carbon*, vol. 114, pp. 418–423, 2017.
- [143] P. Avouris, M. Freitag, and V. Perebeinos, "Carbon-nanotube photonics and optoelectronics," *Nature Photonics*, vol. 2(6), pp. 341–350, 2008.
- [144] A. S. Andreev, M. A. Kazakova, A. V. Ishchenko, A. G. Selyutin, O. B. Lapina, V. L. Kuznetsov, and J. B. D. E. de Lacaillerie, "Magnetic and dielectric properties of carbon nanotubes with embedded cobalt nanoparticles," *Carbon*, vol. 114, pp. 39–49, 2017.

- [145] T. Z. Shen, S. H. Hong, and J. K. Song, "Electro-optical switching of graphene oxide liquid crystals with an extremely large kerr coefficient," *Nature Materials*, vol. 13(4), p. 394, 2014.
- [146] A. Sharma, V. Singh, T. L. Bougher, and B. A. Cola, "A carbon nanotube optical rectenna," *Nature Nanotechnology*, vol. 10(12), p. 1027, 2015.
- [147] L. Sun, Y. Zhang, Y. Wang, C. Zhang, C. Min, Y. Yang, S. Zhu, and X. Yuan, "Refractive index mapping of single cells with a graphene-based optical sensor," *Sensors and Actuators B: Chemical*, vol. 242, pp. 41–46, 2017.
- [148] A. Setaro, M. Adeli, M. Glaeske, D. Przyrembel, T. Bisswanger, G. Gordeev, F. Maschietto, A. Faghani, B. Paulus, M. Weitnelt, R. Arenal, R. Haag, and S. Reich, "Preserving  $\pi$ -conjugation in covalently functionalized carbon nanotubes for optoelectronic applications," *Nature Communications*, vol. 8, p. 14281, 2017.
- [149] S. Roche, F. Triozon, A. Rubio, and D. Mayou, "Electronic conduction in multi-walled carbon nanotubes: role of intershell coupling and incommensurability," *Physics Letters A*, vol. 285(1), pp. 94–100, 2001.
- [150] K. Yamamoto, S. Akita, and Y. Nakayama, "Orientation and purification of carbon nanotubes using ac electrophoresis," *Journal of physics D: Applied physics*, vol. 31(8), p. L34, 1998.
- [151] L. Nagahara, A. Islamshah, J. Lewenstein, and R. Tsui, "Directed placement of suspended carbon nanotubes for nanometer-scale assembly," *Applied Physics Letters*, vol. 80(20), pp. 3826–3828, 2002.
- [152] G. Zhang, D. Mann, L. Zhang, A. Javey, Y. Li, E. Yenilmez, Q. Wang, J. McVittie, Y. Nishi, J. Gibbons, and H. Dai, "Ultra-high-yield growth of vertical single-walled carbon nanotubes: Hidden roles of hydrogen and oxygen," *Proceedings of the National Academy of Sciences of the United States of America*, vol. 102(45), pp. 16141–16145, 2005.

- [153] A. A. Khan, G. D. M. Dabera, H. Butt, M. M. Qasim, G. A. Amaratunga, S. Silva, and T. D. Wilkinson, "unable scattering from liquid crystal devices using carbon nanotubes network electrodes," *Nanoscale*, vol. 7(1), pp. 330–336, 2015.
- [154] J. H. Ahn, J. H. Kim, N. F. Reuel, P. W. Barone, A. A. Boghossian, J. Zhang, H. Yoon, A. C. Chang, A. J. Hilmer, and M. S. Strano, "Label-free, single protein detection on a near-infrared fluorescent single-walled carbon nanotube/protein microarray fabricated by cell-free synthesis," *Nano Letters*, vol. 11(7), pp. 2743–2752, 2011.
- [155] S. Fan, M. Chapline, N. Franklin, T. Tomblor, A. Cassell, and H. Dai, "Self-oriented regular arrays of carbon nanotubes and their field emission properties," *Science*, vol. 283(5401), pp. 512–514, 1999.
- [156] R. Krupke, F. Hennrich, H. Löhneysen, and M. Kappes, "Separation of metallic from semiconducting single-walled carbon nanotubes," *Science*, vol. 301(5631), pp. 344–347, 2003.
- [157] K. Bubke, H. Gnewuch, M. Hempstead, J. Hammer, and M. Green, "Optical anisotropy of dispersed carbon nanotubes induced by an electric field," *Applied Physics Letters*, vol. 71(14), pp. 1906–1908, 1997.
- [158] T. Robb-Smith, K. Donovan, L. Scott, and M. Somerton, "Induced electro-optic effects in single-walled carbon nanotubes. i. polarizability of metallic nanotubes," *Physical Review B*, vol. 83(15), p. 155414, 2011.
- [159] T. Robb-Smith, K. Donovan, L. Scott, and M. Somerton, "Induced electro-optic effects in single-walled carbon nanotubes. ii. hydrodynamics of nanotubes in viscous media," *Physical Review B*, vol. 83(15), p. 155415, 2011.
- [160] A. Ortega and J. G. de la Torre, "Hydrodynamic properties of rodlike and disklike particles in dilute solution," *Journal of Chemical Physics*, vol. 119(18), pp. 9914–9919, 2003.

- [161] C. Wilhelm, F. Gazeau, J. Roger, J. N. Pons, M. F. S. R. Perzynski, and J. C. Bacri, "Binding of biological effectors on magnetic nanoparticles measured by a magnetically induced transient birefringence experiment," *Physical Review E*, vol. 65(3), p. 031404, 2002.
- [162] Q. Lu, G. Keshar, R. Ciocan, R. Rao, R. B. Marthur, A. M. Rao, and L. L. Larcom, "Determination of carbon nanotube density by gradient sedimentation," *Journal of Physical Chemistry B*, vol. 110(48), pp. 24371–24376, 2006.
- [163] K. J. Donovan, K. Scott, and M. Somerton, "Anomalous intrinsic viscosity of octadecylamine-functionalised carbon nanotubes in suspension," *The Journal of Chemical Physics*, vol. 138(24), p. 244902, 2013.
- [164] N. M. Shtykov, A. D. L. Chandani, A. V. Emelyanenko, A. Fukuda, and J. K. Vij, "Two kinds of smectic- $c_{\alpha}^*$  subphases in a liquid crystal and their relative stability dependent on the enantiomeric excess as elucidated by electric-field-induced birefringence experiment," *Physical Review E*, vol. 71(2), p. 021711, 2005.
- [165] S. Reich, C. Thomsen, and P. Ordejón, "Electronic band structure of isolated and bundled carbon nanotubes," *Physical Review B*, vol. 65(15), p. 155411, 2002.
- [166] J. W. Weber, V. E. Calado, and M. C. M. van de Sanden, "Optical constants of graphene measured by spectroscopic ellipsometry," *Applied Physics Letters*, vol. 97(9), p. 091904, 2010.
- [167] S. Cheon, K. D. Kihm, H. goo Kim, G. Lim, J. S. Park, and J. S. Lee, "How to reliably determine the complex refractive index (ri) of graphene by using two independent measurement constraints," *Scientific reports*, vol. 4, 2014.
- [168] N. Daum, C. Tscheka, A. Neumeyer, and M. Schneider, "Novel approaches for drug delivery systems in nanomedicine: effects of particle design and shape," *Wiley Interdisciplinary Reviews: Nanomedicine and Nanobiotechnology*, vol. 4(1), pp. 52–65, 2012.

- [169] Z. Wen, L. Zhu, Z. Zhang, and Z. Ye, "Fabrication of gas sensor based on mesoporous rhombus-shaped zno rod arrays," *Sensors and Actuators B: Chemical*, vol. 208, pp. 112–121, 2015.
- [170] M. M. Ramos-Tejada, M. J. Espin, and R. P. dn A. V. Delgado, "Electrorheology of suspensions of elongated goethite particles. journal of non-newtonian fluid mechanics," *Journal of Non-Newtonian Fluid Mechanics*, vol. 159(1), pp. 34–40, 2009.
- [171] B. Reiser, L. González-García, I. Kanelidis, J. H. M. Maurer, and T. Kraus, "Gold nanorods with conjugated polymer ligands: sintering-free conductive inks for printed electronics," *Chemical Science*, vol. 7, pp. 4190–4196, 2016.
- [172] T. Prodver, "Challenges in particle size distribution measurement past, present and for the 21st century," *Progress in organic coatings*, vol. 32(1), pp. 143–153, 1997.
- [173] R. Xu and O. A. D. Guida, "Comparison of sizing small particles using different technologies," *Powder Technology*, vol. 132(2), pp. 145–153, 2003.
- [174] M. Li and D. Wilkinson, "Determination of non-spherical particle size distribution from chord length measurements. part 1: Theoretical analysis," *Chemical Engineering Science*, vol. 60(12), pp. 3251–3265, 1997.
- [175] W. Anderson, D. Kozak, V. A. Coleman, Å. K. Jämting, and M. Trau, "A comparative study of submicron particle sizing platforms: accuracy, precision and resolution analysis of polydisperse particle size distributions," *Journal of Colloid and Interface Science*, vol. 405, pp. 322–330, 2013.
- [176] R. Mathaes, G. Winter, J. Engert, and A. Besheer, "Application of different analytical methods for the characterization of non-spherical micro-and nanoparticles," *International Journal of Pharmaceutics*, vol. 453(2), pp. 620–629, 2013.

- [177] M. Lotya, A. Rakovich, J. J. Donegan, and J. N. Coleman, "Measuring the lateral size of liquid-exfoliated nanosheets with dynamic light scattering," *Nanotechnology*, vol. 24(26), p. 265703, 2013.
- [178] A. D. Levin, E. A. Shmytkova, and K. N. Min'kov, "Determination of the geometric parameters of gold nanorods by partially depolarized dynamic light scattering and absorption spectrophotometry," *Measurement Techniques*, vol. 59(7), pp. 709–714, 2016.
- [179] M. Li, D. Wilkinson, and K. Patchigolla, "Determination of non-spherical particle size distribution from chord length measurements. part 2: Experimental validation," *Chemical Engineering Science*, vol. 60(18), pp. 4992–5003, 2005.
- [180] B. Krause, M. Mende, P. Pötschke, and G. Petzold, "Dispersability and particle size distribution of cnts in an aqueous surfactant dispersion as a function of ultrasonic treatment time," *International Journal of Pharmaceutics*, vol. 48(10), pp. 2746–2754, 2010.
- [181] C. Backes, R. J. Smith, N. McEvoy, N. C. Berner, D. McCloskey, H. C. Nerl, A. O'Neill, P. J. King, T. Higgings, D. Hanlon, N. Scheuschner, J. Maultzsch, L. Houben, G. S. Duesberg, J. F. Donegan, V. Nicolosi, and J. N. Coleman, "Edge and confinement effects allow in situ measurement of size and thickness of liquid-exfoliated nanosheets," *Nature Communications*, vol. 5, p. 4576, 2014.
- [182] R. Pecora, "Dynamic light scattering measurement of nanometer particles in liquids," *Journal of Nanoparticle Research*, vol. 2(2), pp. 123–131, 2000.
- [183] M. Zhang, S. Bradford, J. Šimůnek, H. Vereecken, and E. Klumpp, "Roles of cation valance and exchange on the retention and colloid-facilitated transport of functionalized multi-walled carbon nanotubes in a natural soil," *Water research*, vol. 109, pp. 358–266, 2017.
- [184] L. Reinert, M. Zeiger, S. Suarez, V. Presser, and F. Mücklich, "Dispersion analysis of carbon nanotubes, carbon onions, and nanodiamonds for their application as reinforcement phase in nickel metal

- matrix composites," *RSC Advances*, vol. 5(115), pp. 95149–95159, 2015.
- [185] Z. Saunders, C. Noack, D. Dzombak, and G. Lowry, "Characterization of engineered alumina nanofibers and their colloidal properties in water," *Journal of Nanoparticle Research*, vol. 17(3), p. 140, 2015.
- [186] A. Nelson and T. Cosgrove, "Dynamic light scattering studies of poly (ethylene oxide) adsorbed on laponite: Layer conformation and its effect on particle stability," *Langmuir*, vol. 20(4), pp. 10382–10388, 2004.
- [187] C. Kinnear, H. Dietsch, M. Clift, C. Endes, B. Rothenäcker, and A. Petriäcker, "Gold nanorods: Controlling their surface chemistry and complete detoxification by a two-step place exchange," *Angewandte Chemie International Edition*, vol. 52(7), pp. 1934–1938, 2013.
- [188] Y. Boluk and C. Danumah, "Analysis of cellulose nanocrystal rod lengths by dynamic light scattering and electron microscopy," *Journal of Nanoparticle Research*, vol. 16(1), p. 2174, 2014.
- [189] X. Liu, Q. Dai, L. Austin, J. Coutts, G. Knowles, J. Zou, H. Chenan, and Q. Huo, "A one-step homogeneous immunoassay for cancer biomarker detection using gold nanoparticle probes coupled with dynamic light scattering," *Journal of the American Chemical Society*, vol. 130(9), pp. 2780–2782, 2008.
- [190] T. Liu and Z. Xiao, "Dynamic light scattering of rigid rods—a universal relationship on the apparent diffusion coefficient as revealed by numerical studies and its use for rod length determination," *Macromolecular Chemistry and Physics*, vol. 213(16), pp. 1697–1705, 2012.
- [191] B. Khlebtsov and N. G. Khlebtsov, "On the measurement of gold nanoparticle sizes by the dynamic light scattering method," *Colloid Journal*, vol. 73(1), pp. 118–127, 2011.

- [192] A. Levin, E. Shmytkova, and B. Khlebtsov, "Multipolarization dynamic light scattering of nonspherical nanoparticles in solution," *The Journal of Physical Chemistry C*, vol. 121(5), pp. 3070–3077, 2017.
- [193] M. Zimbone, E. Messina, G. Compagnini, M. Fragalà, and L. Calcagno, "Resonant depolarized dynamic light scattering of silver nanoplatelets," *Journal of Nanoparticle Research*, vol. 17(10), p. 402, 2015.
- [194] S. Badaire, P. Poulin, M. Maugey, and C. Zakri, "In situ measurements of nanotube dimensions in suspensions by depolarized dynamic light scattering," *Langmuir*, vol. 20(24), pp. 10367–10370, 2004.
- [195] D. Bossert, J. Natterodt, D. Urban, C. Weder, and A. P.-F. S. Balog, "Speckle-visibility spectroscopy of depolarized dynamic light scattering," *The Journal of Physical Chemistry B*, vol. 121(33), pp. 7999–8007, 2017.
- [196] A. Shetty, G. Wilkins, J. Nanda, and M. Solomon, "Multiangle depolarized dynamic light scattering of short functionalized single-walled carbon nanotubes," *The Journal of Physical Chemistry C*, vol. 113(17), pp. 7129–7133, 2009.
- [197] I. Martchenko, H. Dietsch, C. Moitzi, and P. Schurtenberger, "Hydrodynamic properties of magnetic nanoparticles with tunable shape anisotropy: Prediction and experimental verification," *The Journal of Physical Chemistry B*, vol. 115(49), pp. 14838–14845, 2011.
- [198] D. Lehner, H. Lindner, and O. Glatter, "Determination of the translational and rotational diffusion coefficients of rodlike particles using depolarized dynamic light scattering," *Langmuir*, vol. 16(4), pp. 1689–1695, 2000.
- [199] V. Degiorgio, R. Piazza, F. Mantegazza, and T. Bellini, "Stretched-exponential relaxation of electric birefringence in complex liquids," *Journal of Physics: Condensed Matter*, vol. 2(S), p. SA69, 1990.

- [200] M. M. Tirado, C. L. Martínez, and J. G. de la Torre, "Comparison of theories for the translational and rotational diffusion coefficients of rod-like macromolecules. Application to short DNA fragments," *Journal of Chemical Physics*, vol. 81(4), pp. 2047–2052, 1984.
- [201] V. Marangoni, J. Cancino-Bernardi, and V. Zucolotto, "Synthesis, physico-chemical properties, and biomedical applications of gold nanorods—A review," *Nature Communications*, vol. 12(6), pp. 1136–1158, 2016.
- [202] X. Huang, S. Neretina, and M. ElâĀřSayed, "Gold nanorods: from synthesis and properties to biological and biomedical applications," *Advanced Materials*, vol. 21(48), pp. 4880–4910, 2009.
- [203] L. Vigderman, B. Khanal, and E. Zubarev, "Functional gold nanorods: synthesis, selfâĀřassembly, and sensing applications," *Advanced Materials*, vol. 24(36), pp. 4811–4841, 2012.
- [204] N. Li, P. Zhao, and D. Astruc, "Anisotropic gold nanoparticles: synthesis, properties, applications, and toxicity," *Angewandte Chemie International Edition*, vol. 53(7), pp. 1756–1789, 2012.
- [205] J. Pérez-Juste, I. Pastoriza-Santos, L. Liz-Marzán, and P. Mulvaney, "Gold nanorods: synthesis, characterization and applications," *Coordination Chemistry Reviews*, vol. 249(17-18), pp. 1870–1901, 2005.
- [206] X. Xiong, A. Busnaina, S. Selvarasah, S. Somu, M. Wei, J. Mead, C. Chen, J. Aceros, P. Makaram, and M. Dokmeci, "Directed assembly of gold nanoparticle nanowires and networks for nanodevices," *The Journal of Physical Chemistry B*, vol. 91(6), p. 063101, 2007.
- [207] L. Cai, H. Skulason, J. Kushmerick, S. Pollack, J. Naciri, R. Shashidhar, D. Allara, T. Mallouk, and T. Mayer, "Nanowire-based molecular monolayer junctions: Synthesis, assembly, and electrical characterization," *The Journal of Physical Chemistry B*, vol. 108(9), pp. 2827–2832, 2004.

- [208] B. Gierhart, D. Howitt, S. Chen, R. Smith, and S. Collins, "Frequency dependence of gold nanoparticle superassembly by dielectrophoresis," *Langmuir*, vol. 23(24), pp. 12450–12456, 2007.
- [209] J. Boote and S. Evans, "Dielectrophoretic manipulation and electrical characterization of gold nanowires," *Nanotechnology*, vol. 16(9), p. 1500, 2005.
- [210] B. van der Zande, G. Koper, and H. Lekkerkerker, "Alignment of rod-shaped gold particles by electric fields," *The Journal of Physical Chemistry B*, vol. 103(28), pp. 5754–5760, 1999.
- [211] A. Zhivkov, B. van der Zande, and S. Stoylov, "Electro-optics of metal particles: electric birefringence of gold rods," *Colloids and Surfaces A: Physicochemical and Engineering Aspects*, vol. 209(2-3), pp. 299–303, 2002.
- [212] W. Ahmed, E. Kooij, A. V. Silfhout, and B. Poelsema, "Quantitative analysis of gold nanorod alignment after electric field-assisted deposition," *Nano Letters*, vol. 9(11), pp. 3786–3794, 2009.
- [213] P. Zijlstra, M. van Stee, N. Verhart, Z. Gu, and M. Orrit, "Rotational diffusion and alignment of short gold nanorods in an external electric field," *Physical Chemistry Chemical Physics*, vol. 14(13), pp. 4584–4588, 2012.
- [214] J. J. Arcenegui, A. Ramos, P. García-Sánchez, and H. Morgan, "Electrorotation of titanium microspheres," *Electrophoresis*, vol. 34(7), pp. 979–986, 2013.
- [215] J. J. Arcenegui, P. García-Sánchez, H. Morgana, and A. Ramos, "Electric-field-induced rotation of brownian metal nanowires," *Physical Review E*, vol. 88(3), p. 033025, 2011.
- [216] R. Chhetri, K. Kozek, A. Johnston-Peck, J. Tracy, and A. Oldenburg, "Imaging three-dimensional rotational diffusion of plasmon resonant gold nanorods using polarization-sensitive optical coherence tomography," *Physical Review E*, vol. 83(4), p. 040903, 2011.

- [217] J. Huang, J. Park, W. Wang, C. Murphy, and D. Cahill, "Ultrafast thermal analysis of surface functionalized gold nanorods in aqueous solution," *ACS Nano*, vol. 7(1), pp. 589–597, 2012.
- [218] S. Gómez-Graña, F. Hubert, F. Testard, A. Guerrero-Martínez, I. Grillo, L. Liz-Marzán, and O. Spalla, "Surfactant (bi)layers on gold nanorods," *Langmuir*, vol. 28(2), pp. 1453–1459, 2011.
- [219] T. Sau and C. Murphy, "Self-assembly patterns formed upon solvent evaporation of aqueous cetyltrimethylammonium bromide-coated gold nanoparticles of various shapes," *Langmuir*, vol. 21(7), pp. 2923–2929, 2005.
- [220] J. Gao, C. Bender, and C. Murphy, "Dependence of the gold nanorod aspect ratio on the nature of the directing surfactant in aqueous solution," *Langmuir*, vol. 19(21), pp. 9065–9070, 2003.
- [221] J. Rodríguez-Fernández, J. Pérez-Juste, L. Liz-Marzán, and P. Lang, "Dynamic light scattering of short Au rods with low aspect ratios," *The Journal of Physical Chemistry C*, vol. 111(13), pp. 5020–5025, 2007.
- [222] J. McLachlan, D. Smith, N. Chmel, and A. Rodger, "Calculations of flow-induced orientation distributions for analysis of linear dichroism spectroscopy," *Soft Matter*, vol. 9(20), pp. 4977–4984, 2013.
- [223] M. Trebin, D. Steinhauser, D. Perlich, A. Buffet, S. Roth, W. Zimmermann, J. Thiele, and S. Förster, "Anisotropic particles align perpendicular to the flow direction in narrow microchannels," *Proceedings of the National Academy of Sciences*, vol. 110(17), pp. 6706–6711, 2013.
- [224] K. McPeak, S. Jayanti, S. Kress, S. Meyer, S. Iotti, A. Rossinelli, and D. Norris, "Plasmonic films can easily be better: rules and recipes," *ACS Photonics*, vol. 2(3), pp. 326–333, 2015.
- [225] J. C. Maxwell, *Treatise on electricity and magnetism*. Oxford: Clarendon, 1881.
- [226] K. Critchley, B. Khanal, M. Górzny, L. Vigdeman, S. Evans, and E. Z. N. Kotov, "Near-field bulk conductivity of gold nanowires as

- nanoscale interconnects and the role of atomically smooth interface," *Advanced Materials*, vol. 22(21), pp. 2338–2342, 2010.
- [227] E. Menke, M. Thompson, C. Xiang, L. Yang, and R. Penner, "Lithographically patterned nanowire electrodeposition," *Nature Materials*, vol. 5(11), p. 914, 2006.
- [228] A. Walton, C. Allen<sup>1</sup>, K. Critchley, M. GÅsyrzny, J. McKendry, R. Brydson, B. Hickey, and S. Evans, "Four-probe electrical transport measurements on individual metallic nanowires," *Nanotechnology*, vol. 18(6), p. 065204, 2007.
- [229] S. Valizadeh, M. Abid, F. Hernández-Ramírez, A. Rodríguez, and K. H. J. Schweitz, "Template synthesis and forming electrical contacts to single au nanowires by focused ion beam techniques," *Nanotechnology*, vol. 17(4), p. 1134, 2006.
- [230] C. Wang, Y. Hu, C. Lieber, and S. Sun, "Ultrathin au nanowires and their transport properties," *Journal of the American Chemical Society*, vol. 130(28), pp. 8902–8903, 2008.
- [231] J. Song, Y. Wu, B. Messer, H. Kind, and P. Yang, "Metal nanowire formation using mo<sub>3</sub>se<sub>3</sub>-as reducing and sacrificing templates," *Journal of the American Chemical Society*, vol. 123(42), pp. 10397–10398, 2001.
- [232] Y. Peng, T. Cullis, and B. Inkson, "Accurate electrical testing of individual gold nanowires by in situ scanning electron microscope nanomanipulators," *Applied Physics Letters*, vol. 93(18), p. 183112, 2008.
- [233] S. Ahualli, M. JimelÀnez, F. Carrique, and A. Delgado, "Ac electrokinetics of concentrated suspensions of soft particles," *Langmuir*, vol. 25(4), pp. 1986–1997, 2009.
- [234] Z. Lin, J. J. Cai, L. E. Scriven, and H. T. Davis, "Electric birefringence of dispersions of platelets," *The Journal of Physical Chemistry*, vol. 98(23), pp. 5984–5993, 1994.

- [235] M. Pelton, J. Aizpurua, and G. Bryant, "Metal-nanoparticle plasmonics," *Laser and Photonics Reviews*, vol. 2(3), pp. 136–159, 2008.
- [236] S. K. Dondapati, T. K. Sau, C. Hrelescu, T. A. Klar, F. D. Stefani, and J. Feldmann, "Label-free biosensing based on single gold nanostars as plasmonic transducers," *Acs Nano*, vol. 4(11), pp. 6318–6322, 2010.
- [237] A. W. Sanders, D. A. Routenberg, B. J. Wiley, Y. Xia, and E. R. D. M. A. Reed, "Observation of plasmon propagation, redirection, and fan-out in silver nanowires," *Nano Letters*, vol. 6(8), pp. 1822–1826, 2006.
- [238] R. M. Dickson and L. A. Lyon, "Unidirectional plasmon propagation in metallic nanowires," *The Journal of Physical Chemistry B*, vol. 104(26), pp. 6095–6098, 2000.
- [239] V. K. Sharma, R. A. Yngard, and Y. Lin, "Silver nanoparticles: green synthesis and their antimicrobial activities," *Advances in Colloid and Interface Science*, vol. 145(1-2), pp. 83–96, 2009.
- [240] K. Ellmer, "Past achievements and future challenges in the development of optically transparent electrodes," *Nature Photonics*, vol. 6(12), p. 809, 2012.
- [241] J. B. Pendry, "Negative refraction makes a perfect lens," *Physical Review Letters*, vol. 85(18), p. 3966, 2000.
- [242] V. M. Shalaev, "Optical negative-index metamaterials," *Nature Photonics*, vol. 1(1), p. 41, 2007.
- [243] M. L. Brongersma, J. W. Hartman, and H. A. Atwater, "Electromagnetic energy transfer and switching in nanoparticle chain arrays below the diffraction limit," *Physical Review B*, vol. 62(64), p. R16356, 2000.
- [244] L. A. Sweatlock, S. A. Maier, H. A. Atwater, J. J. Penninkhof, and A. Polman, "Highly confined electromagnetic fields in arrays of strongly coupled ag nanoparticles," *Physical Review B*, vol. 71(23), p. 235408, 2005.

- [245] N. G. Loucaides and A. Ramos, "Wall effects on the electrical manipulation of metal nanowires," *Electrophoresis*, vol. 36(13), pp. 1414–1422, 2015.
- [246] K. V. Erin, "Study of the kinetics of space charge formation in colloidal magnetic nanoparticles in liquid dielectrics," *Surface Engineering and Applied Electrochemistry*, vol. 53(4), pp. 327–332, 2017.
- [247] C. C. Kathrein, C. Pester, M. Ruppel, M. Jung, M. Zimmermann, and A. Böker, "Reorientation mechanisms of block copolymer/cdse quantum dot composites under application of an electric field," *Soft Matter*, vol. 12(40), pp. 8417–8424, 2016.
- [248] M. P. Petrov, V. N. Shilov, A. A. Trusov, A. V. Voitylov, and V. V. Voitylov, "Electro-optic research of polarizability dispersion in aqueous polydisperse suspensions of nanodiamonds," *Colloids and Surfaces A: Physicochemical and Engineering Aspects*, vol. 506, pp. 40–49, 2016.
- [249] D. Saintillan, E. S. Shaqfeh, and E. Darve, "Stabilization of a suspension of sedimenting rods by induced-charge electrophoresis," *Physics of Fluids*, vol. 18(12), p. 121701, 2006.
- [250] H. Ohshima, "Approximate analytic expression for the electrophoretic mobility of moderately charged cylindrical colloidal particles," *Langmuir*, vol. 31(5), pp. 13633–13638, 2015.
- [251] M. Z. Bazant and T. M. Squires, "Induced-charge electrokinetic phenomena," *Current Opinion in Colloid and Interface Science*, vol. 15(3), pp. 203–213, 2010.
- [252] A. B. D. Brown, C. G. Smith, and A. R. Rennie, "Pumping of water with ac electric fields applied to asymmetric pairs of microelectrodes," *Physical Review E*, vol. 63(1), p. 016305, 2000.
- [253] N. G. Green, A. Ramos, A. González, H. Morgan, and A. Castellanos, "Fluid flow induced by nonuniform ac electric fields in electrolytes on microelectrodes. i. experimental measurements," *Physical Review E*, vol. 61(4), p. 4011, 2000.

- [254] M. Z. Bazant, J. P. Urbanski, J. A. Levitan, K. Subramanian, M. S. K. A. Jones, and T. Thorsen, "Electrolyte dependence of ac electroosmosis," in *Proceedings of 11th international conference on miniaturized systems for chemistry and life sciences*, pp. 2875–2878, MicroTAS, 2006.
- [255] X. Y. Gao, S. Y. Wang, J. L. Y. X. Zheng, R. J. Zhang, P. Zhou, and Y. N. Y. L. Y. Chen, "Study of structure and optical properties of silver oxide films by ellipsometry, xrd and xps methods," *Thin Solid Films*, vol. 455, pp. 438–442, 2004.
- [256] Y. Zhu, S. Murali, W. Cai, X. L. X, J. W. Suk, J. R. Potts, and R. S. Ruoff, "Graphene and graphene oxide: synthesis, properties, and applications," *Advanced Materials*, vol. 22(35), pp. 3906–3924, 2010.
- [257] S. Park and R. S. Ruoff, "Chemical methods for the production of graphenes," *Nature Nanotechnology*, vol. 4(4), p. 217, 2009.
- [258] S. Pei, Q. Wei, K. Huang, H. M. Cheng, and W. Ren, "Green synthesis of graphene oxide by seconds timescale water electrolytic oxidation," *Nature communications*, vol. 9(1), p. 145, 2018.
- [259] R. K. Joshi, P. Carbone, F. C. Wang, V. G. Kravets, Y. Su, I. V. Grigorieva, H. A. Wu, A. K. Geim, and R. R. Nair, "Precise and ultrafast molecular sieving through graphene oxide membranes," *Science*, vol. 343(6172), pp. 752–754, 2014.
- [260] G. Eda, G. Fanchini, and M. Chhowalla, "Large-area ultrathin films of reduced graphene oxide as a transparent and flexible electronic material," *Nature Nanotechnology*, vol. 3(5), p. 270, 2008.
- [261] K. P. Loh, Q. Bao, G. Eda, and M. Chhowalla, "Graphene oxide as a chemically tunable platform for optical applications," *Nature Chemistry*, vol. 2(12), p. 1015, 2010.
- [262] I. Jung, D. A. Dikin, R. D. Piner, and R. S. Ruoff, "Tunable electrical conductivity of individual graphene oxide sheets reduced at 'low' temperatures," *Nano Letters*, vol. 8(12), pp. 4283–4287, 2008.

- [263] H. K. Jeong, M. H. Jin, K. P. So, S. C. Lim, and Y. H. Lee, "Tailoring the characteristics of graphite oxides by different oxidation times," *Journal of Physics D: Applied Physics*, vol. 42(6), p. 065418, 2009.
- [264] K. Krishnamoorthy, M. Veerapandian, K. Yun, and S. J. Kim, "The chemical and structural analysis of graphene oxide with different degrees of oxidation," *Carbon*, vol. 53, pp. 38–49, 2013.
- [265] P. Blake, P. D. Brimicombe, R. R. Nair, T. J. Booth, D. Jiang, F. Schedin, L. A. Ponomarenko, S. V. Morozov, H. F. Gleeson, E. W. Hill, A. K. Geim, and K. S. Novoselov, "Graphene-based liquid crystal device," *Nano Letters*, vol. 8(6), pp. 1704–1708, 2008.
- [266] Q. Wu, Y. Xu, Z. Yao, A. Liu, and G. Shi, "Supercapacitors based on flexible graphene/polyaniline nanofiber composite films," *ACS Nano*, vol. 4(4), pp. 1963–1970, 2010.
- [267] Q. Zheng, W. Ip, X. Lin, N. Yousefi, K. K. Yeung, Z. Li, and J. K. Kim, "Transparent conductive films consisting of ultralarge graphene sheets produced by langmuir–blodgett assembly," *ACS Nano*, vol. 5(7), pp. 6039–6051, 2011.
- [268] L. Wu, M. Ohtani, M. Takata, A. Saeki, S. Seki, Y. Ishida, and T. Aida, "Magnetically induced anisotropic orientation of graphene oxide locked by in situ hydrogelation," *ACS Nano*, vol. 8(5), pp. 4640–4649, 2014.
- [269] J. E. Kim, T. H. Han, S. H. Lee, J. Y. Kim, C. W. Ahn, J. M. Yun, and S. O. Kim, "Graphene oxide liquid crystals," *Angewandte Chemie International Edition*, vol. 50(13), pp. 3043–3047, 2011.
- [270] S. H. Hong, T. Z. Shen, and J. K. Song, "Electro-optical characteristics of aqueous graphene oxide dispersion depending on ion concentration," *The Journal of Physical Chemistry C*, vol. 118(45), pp. 26304–26312, 2014.
- [271] J. Y. Kim and S. O. Kim, "Liquid crystals: Electric fields line up graphene oxide," *Nature Materials*, vol. 13(4), p. 325, 2014.

- [272] J. Nguyen, J. G. Underwood, and I. L. García, "Orienting lipid-coated graphitic micro-particles in solution using ac electric fields: A new theoretical dual-ellipsoid laplace model for electro-orientation," *Colloids and Surfaces A: Physicochemical and Engineering Aspects*, vol. 549, pp. 237–251, 2018.
- [273] N. Morimoto, T. Kubo, and Y. Nishina, "Tailoring the oxygen content of graphite and reduced graphene oxide for specific applications," *Scientific Reports*, vol. 6, p. 21715, 2016.
- [274] Y. Hernandez, V. Nicolosi, M. Lotya, F. M. Blighe, Z. Sun, S. De, I. T. McGovern, B. Holland, M. Byrne, Y. K. Gun'Ko, J. J. Boland, P. Niraj, G. Duesberg, S. Krishnamurthy, R. Goodhue, J. Hutchison, V. Scardaci, A. C. Ferrari, and J. N. Coleman, "High-yield production of graphene by liquid-phase exfoliation of graphite," *Nature Nanotechnology*, vol. 3(9), p. 563, 2008.
- [275] M. Lotya, Y. Hernandez, P. J. King, R. J. Smith, V. Nicolosi, L. S. Karlsson, F. M. Blighe, S. De, Z. Wang, I. T. McGovern, G. S. Duesberg, and J. N. Coleman, "Liquid phase production of graphene by exfoliation of graphite in surfactant/water solutions," *Journal of the American Chemical Society*, vol. 131(10), pp. 3611–3620, 2009.
- [276] U. Khan, A. O'Neill, M. Lotya, S. De, and J. N. Coleman, "Concentration solvent exfoliation of graphene," *Small*, vol. 6(7), pp. 864–871, 2010.
- [277] M. Lotya, P. J. King, U. Khan, S. De, and J. N. Coleman, "High-concentration, surfactant-stabilized graphene dispersions," *ACS Nano*, vol. 4(6), pp. 3155–3162, 2010.
- [278] U. Khan, H. Porwal, A. O'Neill, K. Nawaz, P. May, and J. N. Coleman, "Solvent-exfoliated graphene at extremely high concentration," *Langmuir*, vol. 27(5), pp. 9077–9082, 2011.
- [279] I. Jung, M. Vaupel, M. Pelton, R. Piner, D. A. Dikin, S. Stankovich, J. An, and R. S. Ruoff, "Characterization of thermally reduced gra-

---

phene oxide by imaging ellipsometry," *The Journal of Physical Chemistry C*, vol. 112(23), pp. 8499–8506, 2008.